**Instituut voor**
**Kern- en Stralingsfysica**
Departement Natuurkunde
Faculteit Wetenschappen


# DECAY OF $^{66}$Fe STUDIED WITH A NEW $\beta$-$\gamma$-DETECTION SET-UP AT LISOL

Promotoren:
Prof. Dr. M. Huyse
Prof. Dr. P. Van Duppen

Proefschrift ingediend tot
het behalen van de graad van
doctor in de wetenschappen
door

**Oleg V. Ivanov**

**Leuven 2007**

ISBN 978-90-8649-144-5
D/2007/10.705/66

*To my Parents, with everlasting gratitude and true love.*

*There are only two mistakes*
*one can make along the road to truth.*
*Not going all the way, and not starting.*
Buddha

*I hear and I forget.*
*I see and I remember.*
*I do and I understand.*
Confucius

*Make everything as simple as possible,*
*but not simpler.*
Albert Einstein

# Acknowledgements

I would like to express my sincere gratitude to those people, who helped me to reach this goal and make this work possible:

- First of all, to my promoters:
  *Prof. Dr. Mark Huyse* and *Prof. Dr. Piet Van Duppen* for presenting me with an opportunity to start my Ph.D. study in the Nuclear Spectroscopy group and providing me with their patient help and valuable inspiration;

- To the members of the jury:
  *Prof. Dr. Nathal Severijns*, *Prof. Dr. Chris Van Haesendonck*, *Prof. Dr. Andrei Andreyev*, and *Dr. Yuri Kudryavtsev* for their valuable and insightful comments on the first manu-script of my thesis;

- To the former and present members of the Nuclear Spectroscopy group:
  *Dieter Pauwels*, *Dmitry Smirnov*, *Farouk Aksouh*, *Hilde De Witte*, *Irina Stefanescu*, *Ivan Mukha*, *Jan Van Roosbroeck*, *Jan Ponsaers*, *Jan Diriken*, *Jarno Van de Walle*, *Jean-Charles Thomas*, *Jeroen Buscher*, *Karen Van de Vel*, *Maria Sawicka*, *Marius Facina*, *Nick Bree*, *Nikolas Patronis*, *Pascale Mayet*, *Riccardo Raabe*, *Sarah Dean*, *Shelly Lesher*, *Tetsu Sonoda*, and *Thomas Cocolios* for making it a wonderful and productive group;

- To our engineers at the LISOL facility:
  *Johnny Gentens* and *Paul Van den Bergh* for their wonderful work, professional help, and productive cooperation during our numerous experiments;

- To the engineers from the Louvain-La-Neuve Cyclotron Center:
  *Guido Ryckewaert* and *Marc Loiselet* for providing the LISOL facility with primary beams and for their willingness to meet our requirements;

- To all former and present members of the MINIBALL Collaboration and especially to *Dirk Weisshaar*, *George Pascovici*, *Heiko Scheit*, *Heinz-Georg Thomas*, and *Nigel Warr* for helping me with my first steps in the MINIBALL business;

- To the IKS personnel:
  the members of the secretariat — *Josee Pierre*, *Katia Cools*, *Sally Vetters* and to the IT-team — *Luc Verwilst* and *Bert Keyaerts* for providing me with everything needed for my study at the IKS and letting me concentrate fully on my work;

- To the IKS engineer *Willy Schollaert* and the members of the mechanical and electronical workshops for their professional work on various hardware that I had to order for our detection set-up;

- To the Russian friends some of who once were the IKS members:
  *Nadezhda Smirnova*, *Valentin Kozlov*, *Nataliya Egorova*, *Ilya Krayev*, *Victor Golovko*, *Rustem Shakhmuratov*, and *Alexey Aladyshkin* for their helpful advice during my stay in Leuven and interesting time together;

- Above all, to my Parents:

  MY FATHER — *Valeriy Vasilyevich Ivanov*
  AND
  MY MOTHER — *Ludmila Anatolyevna Ivanova*

  for giving me their zest to learn and for their endless love, immense support, and strong belief in me;

- To my loving wife *Aneliya* and my sister *Ekaterina* for their quiet and profound support. My special thanks to my wife for her great patience throughout this work.

*Oleg Valeryevich Ivanov*

November, 2007
Leuven, Belgium

# Contents

# Chapter 1

# Introduction

The nucleus is a complex quantum-mechanical entity governed by the strong, weak, and electromagnetic forces acting between the constituent nucleons, which can be finally bound into various finite nuclear systems. The aim of nuclear-structure research is to obtain experimental information that can be confronted with results from theoretical models in order to improve these models and as such improve our understanding of the atomic nucleus. A broad spectrum of experimental techniques exists to obtain this crucial information. One of them is the radioactive decay, which will be the subject of this thesis.

So far, our current understanding of nuclear structure has been largely limited to nuclear systems at or close to the valley of stability. The proton and neutron drip-lines have been reached only at low-mass nuclei with most of success being done on the less-extending proton-rich side through the use of complete fusion-evaporation reactions. Various theoretical predictions and actual experimental evidence indicate that the nuclear structure very far from stability may not be as what one would conclude from extrapolating our knowledge on nuclear systems at or close to stability.

So, how do we proceed after having charted the nuclear systems at or close to the valley of stability? Obviously, in order to improve our understanding of the atomic nucleus one should investigate regions of the nuclear chart with nuclear systems, whose properties provide a critical test for the predictions of various nuclear models. Systematic studies of nuclei at or in the vicinity of closed proton and/or neutron shells provide an important testing ground for the nuclear shell-model. Both the experimental and theoretical studies will allow us to further assess and map the evolution within the whole nuclear landscape.

Due to the technological advance in production of radioactive nuclear beams in the last two decades the horizon of our knowledge of the nuclear landscape has been widely extended to nuclear systems far from stability. Many of the possibly doubly-magic nuclei with large proton or neutron excess — $^{48}$Ni, $^{78}$Ni,

$^{100}$Sn, $^{132}$Sn — have been produced and even studied in many different laboratories all over the World. Our fellow scientists have even reached the long-expected region of super-heavy nuclei. Nevertheless, many regions of the nuclear landscape remain largely unexplored. One of such places is the neutron-rich Ni region and especially below the $Z$=28 proton shell down to the $Z$=20 shell. More specifically, without even going very far from stability, the nuclear structure of the neutron-rich $^{66-68}$Co isotopes right below the semi-doubly-magic $^{68}$Ni nucleus still remains largely unknown. Low-energy excited states in neutron-rich Co nuclei can be successfully studied in $\beta^-$-decay of the corresponding Fe isobars. However, since Fe is a refractory-type element, production of its isotopes becomes challenging by the conventional Isotope-Separator-On-Line method.

For already more than a decade, the nuclear-structure studies in the neutron-rich Ni region have been one of the main subjects at the Leuven-Isotope-Separator-On-Line (LISOL) facility. Recent developments of the laser ion source allowed to produce beams of radioactive Fe isotopes and, thus, study their $\beta$-decay at LISOL. As a consequence, new experiments aimed at studies of the neutron-rich $^{65,66,67}$Co nuclei in $\beta$-decay of the corresponding $^{65,66,67}$Fe isobars were performed. The physics goal of this work is a detailed nuclear-structure study of the $^{66}$Co nucleus in $\beta$-decay of $^{66}$Fe.

There has long been a need for a high-sensitivity high-selectivity detection system at LISOL to be used in combination with purified laser-ionized low-intensity radioactive beams. Thus, the technical goal of this work is to develop and implement a new high-efficiency high-resolution high-granularity $\beta$-$\gamma$-detection set-up for our experiments.

Chapter 2 starts with a brief description of the current understanding of nuclear structure by means of various nuclear models with a strong accent on the shell-model and defines the main incentives for our nuclear-structure studies in the lower part of the neutron-rich Ni region. Chapter 3 defines the main problems in registration of $\beta$- and $\gamma$-radiations using conventional detection set-ups and presents a solution based on implementation of highly-segmented detectors. Chapter 4 describes the current status in development and construction of the new $\beta$-$\gamma$-detection set-up at LISOL and demonstrates its performance at low production rates of nuclei of interest. Chapter 5 presents the results from the experiment on $\beta$-decay of $^{66}$Fe and offers the interpretation of the obtained decay scheme of the $^{66}$Co nucleus. The thesis concludes with a summary and outlook in the closing Chapter 6.

# Chapter 2

# Nuclear structure in the neutron-rich Ni region

## 2.1 Nuclear models

### 2.1.1 From the characteristic properties of the nucleon-nucleon interaction to the description of nuclear systems: the need for nuclear models

As we all know, the atomic nucleus consists of charged protons and neutral neutrons, called nucleons[1] due to distinct similarity of their properties. While a free neutron is unstable against $\beta^-$-decay with a half-life of 10.25 min, when both types of nucleons are combined together they can form a rich variety of stable nuclear systems. This is manifested by an astoundingly large number of possible bound nuclear systems — around 6000, out of which 287 nuclides are stable or primordial[2]. So far, only about 3000 unstable nuclides have been produced and identified in nuclear experiments. Each nucleus is identified by its proton and neutron numbers $Z$ and $N$, respectively, and has the atomic mass number $A = Z + N$. By placing all nuclides in a two-dimensional ($Z$,$N$) diagram, we get the so-called chart of the nuclides, also known as the Segre

[1] In particle physics neutron and proton are considered to be, respectively, an excited and ground state of nucleon.

[2] Due to nucleon-nucleon pairing effect, discussed later, there may be only one stable nuclide per each set of odd-$A$ isobars and there are no odd-$Z$ odd-$N$ stable nuclides heavier than $^{14}$N. However, when $\beta$-decay energy is very small and/or nuclear spin is quite high relative to that of neighboring isobars, the life-time of such nuclear systems can be so extremely large, that they could have even survived since their very creation in violent cosmic environments. Since these nuclides had to be created in the same period of time as the stable nuclear systems, they are called *primordial* and have a half-life of more than $10^9$ y.

chart. The main question that unalterably drives nuclear physics is: "What is behind such a rich variety of possible nuclear systems with clearly distinctive structural differences?"

While charged protons of the nucleus interact with each other through the *electromagnetic* force and the transformation between the nucleonic states is governed by the *weak* interaction, there is clearly an additional and rather pronounced interaction that binds all nucleons into a bound nuclear system. This interaction is called the *strong* interaction. In order to describe any given nuclear system as a whole we must understand its underlying nuclear structure, which is not possible to embrace without defining and knowing all major aspects of the strong inter-nucleon interaction:

- It acts only in a very short range of ∼3–4 fm[3] and becomes very weak beyond it. An evident implication of this would be a pronounced saturation of the strong nuclear force in multi-nucleon configurations.

- It is predominantly attractive, becoming repulsive at nucleon separation of less than ∼1 fm (which is approximately the size of a free nucleon at rest). Its strength is by a factor of 137 and ∼$10^4$ higher than that of the electromagnetic and weak interactions, respectively. This allows to easily overcome the repulsive Coulomb force between protons and create nuclear systems that are stable against $\beta$-decay;

- Its potential includes a noncentral or, in mathematical terms, tensor component;

- Since nucleons have an intrinsic spin of $\frac{1}{2}\hbar$ and, thus, are Fermions (subject to the Fermi-Dirac statistics), its strength depends on the alignment (parallel or anti-parallel) of the nucleon spins;

- It is nearly charge-independent, implying that proton-proton and neutron-neutron interactions must have the same strength taking into account the correction for a repulsive Coulomb interaction between charged protons;

- Considering the experimental fact that two-proton or two-neutron configurations do not form a bound nuclear system, while the proton-neutron system — $^2$H called deuteron — has only one bound state, and applying the isospin formalism unavoidably coupled with the Pauli principle, it is evident that the proton-neutron interaction (more precisely with the total isospin coupling $T$=0) is the strongest.

[3] 1 femtometer (fm) = $10^{-15}$ m is a convenient unit of length for nuclear dimensions and is colloquially known as 1 fermi in honor of the Italian-born American nuclear physicist Enrico Fermi.

Clearly, in order to describe a nuclear system as a whole and obtain its properties, we must consider all inter-nucleon interactions together. This implies having a dynamical description of each individual nucleon in the many-body nuclear system. Such a direct or, in other words, *ab initio* approach can be used only with the help of numerical methods. But dealing with a huge number of different nucleon-nucleon combinations brings a danger of getting lost in tedious and complex numerical calculations. With the current computer technologies at hand, *ab initio* calculations can reproduce only light nuclei with masses up to $A \sim 10$. Instead, knowing all major aspects of the inter-nucleon interaction, we must be able to arrive at a description by means of a *nuclear model*. This means that simple (understandable and tractable) physical and/or mathematical phenomena can be taken as a joint basis that would allow to reproduce main properties of the nuclear system, while additional refinements can be represented through different conditional terms within the model. It is already quite obvious that there are two vital consequences that can make such a description feasible and reliable, namely: i) the inter-nucleon force saturates, meaning that a nucleon will "feel" hardly more than its immediate neighbors and, as a result, the density of nuclear matter (or, in classical physics terms, all separate nucleons) must be rather constant within most of the nuclear volume, and ii) the nucleon-nucleon interaction must be predominantly a two-body interaction, substantially simplifying the overall description. All this leads to the first major implication: the intra-nuclear force is obviously a resultant of all inter-nucleon interactions within the nuclear system, and each nucleon can be considered as interacting with the overall intra-nuclear field generated by all nucleons in the nucleus. The second implication is the fermionic nature of the nucleon-nucleon interaction firmly anchored with the Pauli principle. In essence, these two major points stem almost explicitly through virtually any nuclear model.

All existing nuclear models can be subdivided into four almost independent groups, namely: collective (geometrical), shell, algebraical, and ab-initio (numerical) models. But historically, in the course of attaining a clear understanding on a puzzling nature of intra-nuclear interaction, nuclear scientists have always been concerned with one, although largely forgotten or simply lost through complex formalisms of nuclear models, but rather important question: "How is it possible that there is enough room for evidently moving nucleons to "safely" exist in so heavily-packed and highly-interactive nuclear environments?" From this perspective it is vital to follow the actual evolution of our understanding of nuclear structure through a short description of nuclear models as they evolved.

### 2.1.2 Collective approach: the liquid-drop model

Since Ernest Rutherford's hypothesis on the atomic nucleus in 1911 that gave the actual start to nuclear physics, it took years of essentially experimental work to gather all kinds of scientific information, including James Chadwick's discovery of the neutron (originally predicted by Rutherford), before the first ever nuclear model was developed and introduced by Niels Bohr in 1937. As followed from numerous scattering experiments at that time the nuclear density was "seen" to be rather constant and, thus this semiclassical macroscopic model was based on an assumption that nucleus can be described as an incompressible, viscous, charged liquid drop with its volume proportional to the number of nucleons $A$ and, thus, radius $R = R_0 \cdot A^{\frac{1}{3}}$, where $R_0$=1.27 fm. The expression for the nuclear binding energy, known as the semi-empirical Bethe-Weizsäcker mass equation, in terms of the liquid-drop description with additional correction terms to account for the loss of symmetry energy due to the effect of the Pauli principle and an additional energy stabilization due to nucleon pairing is given in the following form:

$$\begin{aligned} B(A,Z) &= [B_v - B_s - B_c] + [-B_A \pm B_p] \\ &= a_v A - a_s A^{\frac{2}{3}} - a_c Z(Z-1)A^{-\frac{1}{3}} - a_A(A-2Z)^2 A^{-1} \pm \delta a_p A^{-\frac{1}{2}}, \end{aligned} \tag{2.1}$$

where $B_v$, $B_s$, $B_c$, $B_A$, $B_p$ are volume, surface, Coulomb repulsion, asymmetry, and nucleon pairing terms, respectively, and the corresponding constants have the following values: $a_v$=15.85 MeV, $a_s$=18.34 MeV, $a_c$=0.71 MeV, $a_A$=23.21 MeV, and $a_p$=12 MeV. This equation reproduces relatively well the dependence of nuclear binding energy on the atomic mass number for the majority of nuclides at or near the $\beta$-stability line, see Fig. 2.1.

In 1952 Aage Bohr and Ben Mottelson proposed a description of excited states of a nucleus in terms of vibrational or rotational energy of the (deformed) liquid drop. The reasons that may cause a nucleus to collectively vibrate or rotate for certain originate from a change in collective motion of some nucleons (especially at the surface) and must be considered purely macroscopically in the current approach. Deformation of the incompressible liquid drop or, mathematically speaking, deviation of the nuclear surface radius at a coordinate [$\theta$,$\phi$] (spherical coordinate system) from an average value $R_{av}$ can be described in terms of spherical harmonics[4]:

$$R(\theta,\phi) = R_{av} + \Delta R(\theta,\phi) = R_{av} + \sum_{\lambda \geq 1} \sum_{\mu=-\lambda}^{+\lambda} \alpha_{\lambda\mu} Y_{\lambda\mu}(\theta,\phi), \tag{2.2}$$

where $\lambda$ is the multipole order, see Fig. 2.2a, and $\alpha_{\lambda\mu}$ are spherical harmonic amplitudes. The constant term $\lambda$=0 is incorporated in $R_{av}$, and, thus, $\lambda \geq 1$.

[4]The spherical harmonics $Y_{\lambda\mu}(\theta,\phi)$ are the angular portion of the solution to Laplace's equation in spherical coordinates where azimuthal symmetry (on $\phi \in [0, 2\pi]$) is not present.

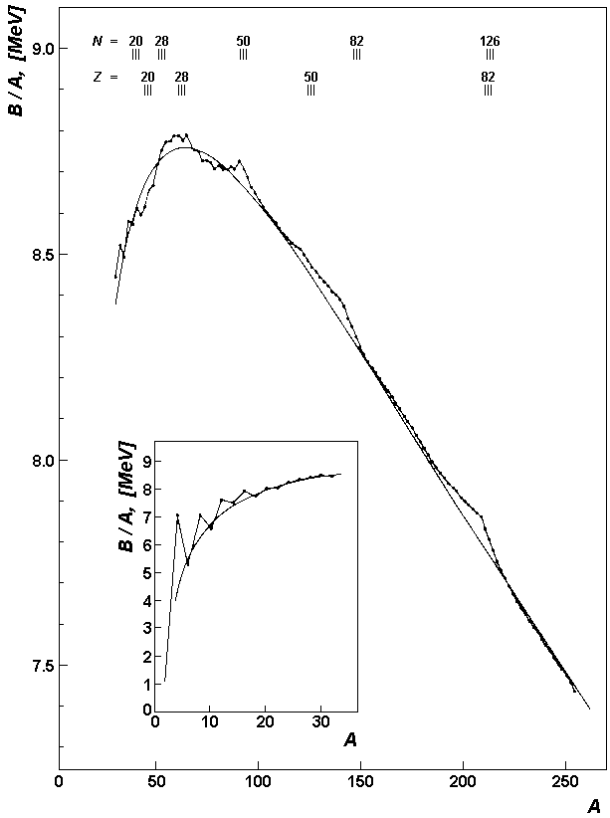


**Figure 2.1:** Nuclear binding energy per nucleon as a function of the atomic mass number. The full curve represents the result from the pure liquid-drop model (without the correction term for nucleon pairing). The inset shows the region of light-mass nuclides.

The dipole term ($\lambda$=1) corresponds to a geometrical shift in the center of mass of the nucleus, and cannot be induced through collective motion in terms of the liquid-drop model, but rather originates from an oscillation of protons relative to neutrons in the nucleus, giving rise to giant dipole resonances at considerable energies, typically in the range from 8 to 20 MeV. This multipole order is of little concern for nuclear-structure that is characterized mainly in terms of lower-lying excited energy states. So, the most common shape corresponds to the quadrupole deformation ($\lambda$=2).

The corresponding spherical harmonic amplitudes can be expressed in terms of Euler angles yielding two intrinsic variables $\beta$ and $\gamma$:

$$\alpha_{20} = \beta\cos\gamma, \quad \alpha_{21} = \alpha_{21} = 0, \quad \alpha_{22} = \alpha_{2-2} = \beta\sin\gamma, \tag{2.3}$$

where $\beta$ represents the extent of the quadrupole deformation and $\gamma$ gives the degree of axial asymmetry. By representing the quadrupole shape in Cartesian coordinate system with the $Z$ axis chosen as a symmetry axis, one gets two distinct cases of deformation: 1) prolate deformation with $\beta >0$ and corresponding to an expansion in one and compression in two directions (rugby ball), and 2) oblate deformation with $\beta <0$ and corresponding to an expansion in two and compression in one directions (frisbee disc), see Fig. 2.2b. The angle $\gamma$ ranges from 0° for an axially symmetric shape to 30° corresponding to a maximum axial asymmetry. As an example, for axially symmetric ($\gamma$=0°) quadrupole deformations all $\alpha_{2\mu}$ except $\alpha_{20}$ vanish, and the resulting shape has a cylindrical symmetry ($R(\theta,\phi)$ in Equation 2.2 is independent of $\phi$). This way, the nucleus has an elongated form of a prolate ellipsoid for $\beta >0$ and a flattened form of an oblate ellipsoid for $\beta <0$. The deformation parameter $\beta$ is then related to the eccentricity of the ellipsoid as

$$\beta = \frac{4}{3}\sqrt{\frac{4}{\pi}}\frac{\Delta R}{R_{av}} \tag{2.4}$$

The presence of a deformation implies that along with a non-spherical distribution of nuclear matter of the nucleus there is a resulting non-sphericity in the distribution of the overall electric charge of the protons, leading, in case of the quadrupole deformation, to the existence of the electric quadrupole moment

$$Q_0 = \frac{3}{\sqrt{5\pi}}R_{av}^2 Z\beta(1+0.16\beta) \tag{2.5}$$

Here, $Q_0$ is known as the *intrinsic* quadrupole moment that would only be observed in the frame of reference in which the nucleus was at rest.

Vibrational motion can be described as an oscillation of the nucleus through a series of shapes of multipole order $\lambda$ and, thus, $R(\theta,\phi)$ becomes time dependent, see Fig. 2.2c. The small-amplitude oscillations of $\alpha_{\lambda\mu}(t)$ can be described

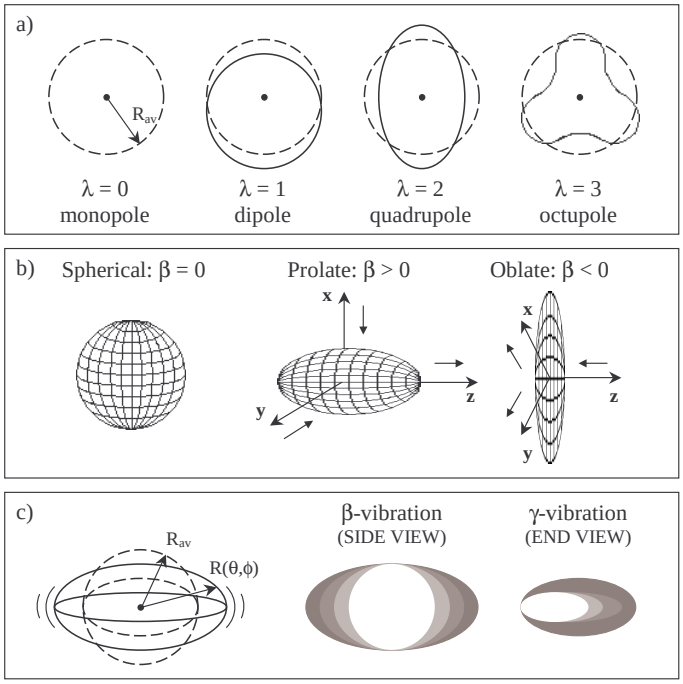


**Figure 2.2:** a) A representation of equal potential surfaces for the first four multipole order distortions. b) A schematic illustration of the two quadrupole-deformation shapes. c) An illustration of vibrational motion.

in terms of a harmonic oscillator approximation, resulting in a Hamiltonian of the form

$$H = T + V = \frac{1}{2}B\sum_{\mu}\left|\frac{d\alpha_{2\mu}}{dt}\right|^2 + \frac{1}{2}C\sum_{\mu}\left|\alpha_{2\mu}\right|^2, \tag{2.6}$$

where $B$ from the kinetic energy part plays a role of the mass parameter and $C$ from the potential energy part is a restoring force. By differentiating $H$ and solving the resulting differential equation of motion of a harmonic oscillator, we obtain that each of the amplitudes $\alpha_{2\mu}$ undergoes oscillations with a frequency $\omega = \sqrt{\frac{C}{B}}$, giving the vibrational energy $\hbar\omega$. A quantum of vibrational energy is called *phonon*. One quadrupole phonon carries two units of angular momentum and adding its vibrational energy to the ground state $0^+$ of an even-even nucleus results in the first excited state with the total spin and parity of $2^+$. An addition

of a second quadrupole phonon creates a triplet of states $0^+$, $2^+$, $4^+$ and, since two identical phonons carry twice the energy of one phonon, these states must be situated at a level of twice the energy of the first $2^+$ state. By using the $m$-scheme (see textbooks), one gets that a combination of three quadrupole phonons yields a quintuplet of states $0^+$, $2^+$, $3^+$, $4^+$, and $6^+$ at an energy level of three times that of one phonon. The resulting multi-phonon multiplets of states are not degenerate due to residual interactions between phonons not considered in this simple approach. Since the quadrupole phonon is described by the five-dimensional harmonic oscillator (five values of $\mu$), one can obtain an expression for the vibrational energy $E_{vibr}$ as a linear combination of the number of phonons $N_{ph}$:

$$E_{vibr} = \hbar\omega \left( N_{ph} + \frac{5}{2} \right) \tag{2.7}$$

The energy at $2_1^+$ of the first phonon cannot be predicted by this model, and, thus, it is an adjustable parameter. Drawing a parallel with the independent-particle approach discussed later, a destruction of one collective-excitation phonon does not correspond to a change of orbit of an individual nucleon. The total wave function of a collective excitation can be represented as a coherent linear combination of various particle–hole excitations, and therefore $\gamma$-ray transitions between different phonon levels are permitted and the strength of such transitions depends on the degree of coherence. An immediate implication is that, since a two-phonon excitation represents a superposition of two linear combinations of single-particle excitations, the destruction of two phonons would require a simultaneous destruction of two particle-hole excitations. Such transitions are clearly forbidden, and, therefore, the selection rule for transitions between multi-phonon states can be written as

$$\Delta N_{ph} = 0, \pm 1 \tag{2.8}$$

The predictions from such a simple approach are in a relatively good agreement with experimental results for many even-even nuclei with $A$ <150 and especially through the fact that in such cases $E(4_1^+)/E(2_1^+)$ ∼2.2. Another important prediction of this model is the fact that if the equilibrium nuclear shape is spherical then the quadrupole moment of the $2_1^+$ state should vanish, which is in agreement with experiment. In general, any discrepancies or *anharmonicities* with a resulting description in terms of vibrational motion must arise from additional three-body interactions, the exclusive and restricting nature of the Pauli principle for the case of multi-phonon states, or from interactions with other types of excitations.

The second mode of collective motion is the rotational motion, which can only be observed in deformed nuclei and especially in the mass ranges 150<

$A$ <190 and $A$ >220. The existence of a deformation in these nuclei is immediately observed through a presence of a noticeably large electric quadrupole moment (note that since the nucleus is rotating, the observed total electric quadrupole moment is to differ from the rest-frame intrinsic moment through an additional dependence on the total nuclear angular momentum). The shape of nuclei under rotational motion can be rather successfully represented as an ellipsoid of revolution. With the total angular momentum $\ell = \mathcal{J}\omega$, where $\mathcal{J}$ is a moment of inertia and $\omega$ is the angular velocity around the body-fixed axis, the total kinetic energy of a rotating nucleus is given as

$$E_{rot} = \frac{1}{2}\mathcal{J}\omega^2 = \frac{\ell^2}{\mathcal{J}} = \frac{\hbar^2}{2\mathcal{J}} I(I+1), \tag{2.9}$$

where $I$ is the intrinsic angular momentum quantum number. This way, increasing the value of $I$ corresponds to adding rotational energy to the nucleus, resulting in the formation of nuclear excited states known as a *rotational band*. In the case of an even-even nucleus, the ground state is always a $0^+$ state, and for a rotational band built on top of it we obtain that $E(4^+)/E(2^+)$ ~3.33, which is in a remarkable agreement with experiment. It is worth noting here, that in order to obtain the same spacing between the resulting energy levels of rotational bands, the actual moment of inertia must be chosen from the range between two extreme cases — $\mathcal{J}_{fluid}$ when the nucleus is considered to be somewhat like a fluid of weakly-bonded nucleons and $\mathcal{J}_{rigid}$ when the nucleus is regarded as a rigid object brought together by tightly-bonded nucleons:

$$\mathcal{J}_{fluid} < \mathcal{J} < \mathcal{J}_{rigid}, \quad \mathcal{J}_{fluid} = \frac{9}{8\pi} M R_{av} \beta, \quad \mathcal{J}_{rigid} = \frac{2}{5} M R_{av} (1 + 0.31\beta), \tag{2.10}$$

where $M$ is the mass of the rotating nucleus.

It is possible to build rotational bands on top of different types of intrinsic excited states which correspond to a change in the intrinsic structure of the nucleus — ,e.g., pair-breaking particle excitations or vibrational states arising from vibrations around a deformed equilibrium shape. The vibrational states in deformed nuclei are of two types: $\beta$-vibrations when the deformation parameter $\beta$ oscillates while the nucleus preserves its cylindrical symmetry and $\gamma$-vibrations when the cylindrical symmetry is temporarily violated, see Fig. 2.2c.

### 2.1.3 Independent-particle approach: the shell model

Although the liquid-drop model is rather extensively used to calculate nuclear binding energies, to describe various phenomena, such as nuclear fission, and to reproduce certain nuclear excited states in terms of collective motion for a large variety of nuclear systems, quite often it cannot achieve a needed degree of quality and clearly fails in providing a description for many nuclear transitions observed in experiment. Probably the best example, as follows from Fig. 2.1, is a noticeably-large extra amount of binding energy in nuclear systems with the proton and/or neutron numbers 2, 8, 20, 28, 50, 82, and 126 that cannot be accounted for even through the inclusion of an additionally-binding pairing energy. As a result, nuclides with $Z$ and/or $N$ at or near these "magic" numbers are often stable and more abundant, and can be characterized by a substantially low neutron-capture cross-sections, substantially high one- and two-neutron(proton)-separation energies, and much higher energies of the $2_1^+$ state of several MeV. All this provided a hint on a prevalence of a single-particle rather than collective nature of the increased stability in such nuclear systems. This way, each nucleon must rather be considered as a quasi-independent particle moving in a certain orbital (to avoid collisions) within the overall potential generated by all weakly-interacting nucleons altogether. The nucleon-nucleon interaction to a relatively good degree of accuracy at "normal" distances between nucleons can be approximated by a two-body interaction. The constant of motion — Hamiltonian for a system of $A$ nucleons can be written as

$$H = T + V = \sum_{i=1}^{A} \frac{\mathbf{p}_i^2}{2m_i} + \sum_{i>k=1}^{A} V_{ik}(\mathbf{r}_i - \mathbf{r}_k), \tag{2.11}$$

where $V_{ik}$ is a nucleon-nucleon potential generated through the interaction between the $i$-th and $k$-th nucleons. By directly introducing this Hamiltonian in the Schrödinger equation of motion, the resulting differential equations can only be solved by means of numerical methods, and this has been done only for a few lightest nuclei so far. Instead, all nucleon-nucleon potentials in Equation 2.11 can be transformed altogether into a total nuclear potential with a dominant spherically-symmetric part by adding and subtracting a one-body potential $\sum_{i=1}^{A} U(\mathbf{r}_i)$, which is experienced by all $A$ nucleons and which approximates the combined effects of all $A(A-1)/2$ two-body interactions:

$$H = \sum_{i=1}^{A} \left[ \frac{\mathbf{p}_i^2}{2m_i} + U(\mathbf{r}_i) \right] + \left[ \sum_{i>k=1}^{A} V_{ik}(\mathbf{r}_i - \mathbf{r}_k) - \sum_{i=1}^{A} U(\mathbf{r}_i) \right] = H_0 + H_{residual} \tag{2.12}$$

Here, the Hamiltonian $H_0$ describes the system of nearly independent nucleons orbiting in spherically-symmetric mean-field potential $U_i(\mathbf{r})$, while $H_{residual}$ is a small perturbation term. The mean-field potential $U(\mathbf{r})$, generated by all $A$

nucleons, must be obtained through the two-body interaction convoluted with the nuclear density $\rho$ at $\mathbf{r}_i$ and integrated over the nuclear volume:

$$U(\mathbf{r}_i) = \int V_{ik}(\mathbf{r}_i - \mathbf{r}_k)\rho(\mathbf{r})d\mathbf{r} = \sum_k \int \psi_k^*(\mathbf{r})V_{ik}(\mathbf{r}_i - \mathbf{r}_k)\psi_k(\mathbf{r})d\mathbf{r}, \qquad (2.13)$$

where $\psi_k$ is a wave function of a single nucleon (in an orbit $k$). This results in an unavoidable paradox that in order to know the single-particle wave functions we need to know the potential in which they move and which is generated by the particle wave functions themselves. A certain aforethought choice of the mean-field potential cannot guarantee that resulting wave functions would minimize the total energy of the system. Instead, as a basis of the generalized Hartree-Fock-Bogoliubov method, for a given $V_{ik}(\mathbf{r}_i - \mathbf{r}_k)$ an initial guess is taken on $\psi_k$ to calculate $U(\mathbf{r})$. The resulting $U(\mathbf{r})$ is then used to obtain $\psi_k$ and the whole process is continued until a self-consistent convergence and energy minimization are achieved.

In the Hamiltonian $H_0 = \sum_{i=1}^{A} H_0^i$ each $H_0^i$ describes the motion of an individual $i$-th particle in the stationary Schrödinger equation:

$$H_0^i\psi_i(\mathbf{r}) = E_i\psi_i(\mathbf{r}), \qquad (2.14)$$

where $\psi_i(\mathbf{r})$ is a wave function of an individual nucleon in the potential $U(\mathbf{r})$ with a single-particle energy $E_i$. The total wave function of the nuclear system is $\psi(\mathbf{r}_1, \mathbf{r}_2, .., \mathbf{r}_A) = \prod_{i=1}^{A} \psi_i(\mathbf{r})$ and corresponds to a total energy $E_0 = \sum_{i=1}^{A} E_i$.

In essence, the nuclear potential provides a spacial confinement of the nucleons that results in formation of bound nuclear systems. Its "real" depth must be on the level of ∼50 MeV. As a starting point, one can use a simple-form potential, such as a square-well or a harmonic-oscillator potential.

The nucleons are characterized by their spacial coordinates, intrinsic spin, and isospin (proton or neutron). Being fermions, the nucleons are subject for the Pauli principle[5], which has profound consequences on nuclear structure by, first of all, allowing two nucleons of the same type to be in "the same place" only if their spins are opposite and, secondly, not considering the repulsive Coulomb force between protons, allowing both types of nucleons to equally occupy the same energy levels.

The nuclear shell model was proposed in the late 1940's and was based on an assumption that nucleons move in orbitals clustered into shells in analogy with

[5]For fermions, as particles with a half-integer spin, the nuclear wave function must be totally anti-symmetric, which means that it must change its sign when all the coordinates (spacial, spin, isospin) are interchanged. This implies that the probability to find two nucleons in the same quantum state must always vanish, and, thus, no two nucleons can have identical quantum numbers. This is known as the Pauli principle.

electron shells in atom. Apart from the intrinsic spin and isospin, each single-particle wave function is then characterized by its radial quantum number $n$, orbital angular momentum quantum number $\ell$, and the eigenvalue $m$ of the $z$-projection $\ell_z$ of the orbital angular momentum. In analogy with the atomic physics, the values of $\ell$=0, 1, 2, 3, 4, 5, 6,... were assigned the historical letter names s (sharp), p (principal), d (diffuse), f (fundamental), g (from here alphabetically), h, i,..., respectively. Both types of nucleons sequentially fill the energy levels for a given $n$ and $\ell$. Since the nuclear potential is spherically symmetric, $\ell$ is a good quantum number and, equally for each type of nucleons, each level has a degeneracy of $2(2\ell + 1)$, where $(2\ell + 1)$ arises from the $m$ degeneracy ($(2\ell + 1)$ values of $m$) and the factor of 2 stems from the intrinsic spin degeneracy (two possible values). For nuclear levels, $n$ is not a principal quantum number and simply counts the number of levels with certain $\ell$ values. Since the equation of motion is separable in radial and angular coordinates, the single-particle wave functions can be written in spherical coordinates as

$$\psi_{nlm}(\mathbf{r}) = \psi_{nlm}(r\theta\phi) = \frac{1}{r}R_{nl}(r)Y_{lm}(\theta\phi), \tag{2.15}$$

where $R_{nl}(r)$ and $Y_{lm}(\theta\phi)$ are radial and angular parts, respectively. For a radial solution, with each angular momentum $L$ there is an associated centrifugal force, which generates an additional centrifugal part of the nuclear potential:

$$U_{cent} = \int F_{cent}dr = \int \frac{L^2}{mr^3}dr = -\frac{\hbar^2\ell(\ell+1)}{2mr^2} \tag{2.16}$$

The radial part of the Schrödinger equation then becomes

$$\frac{\hbar^2}{2m}\frac{d^2R_{nl}(r)}{dr^2} + \left[E_{nl} - U(r) - \frac{\hbar^2}{2m}\frac{\ell(\ell+1)}{r^2}\right]R_{nl}(r) = 0 \tag{2.17}$$

The radial wave functions $R_{nl}(r)$ are expressed in terms of Laguerre polynomials in $r^2$ while the angular part can be represented as a multipole expansion, thus, determining the parity of the single-particle wave function $\pi_{nlm} = (-1)^l$. Independent of the nuclear potential form, the centrifugal force raises the energy levels by squeezing the overall shape of the potential and, additionally, creates a centrifugal barrier. For a three-dimensional harmonic-oscillator potential, the single-particle energies are obtained as $E_{nl} = (2n+\ell-\frac{1}{2})\hbar\omega$, which creates an additional degeneracy of levels with $\Delta\ell = -2\Delta n$. This is due to a profound result of the interplay of the harmonic-oscillator and centrifugal potentials that creates groupings of degenerate levels at equidistant energies of $\sim$8 MeV as on the left in Fig. 2.3.

In reality, the nuclear potential must have a rather uniform distribution in the interior of the nucleus due to an obvious saturation of the nuclear force

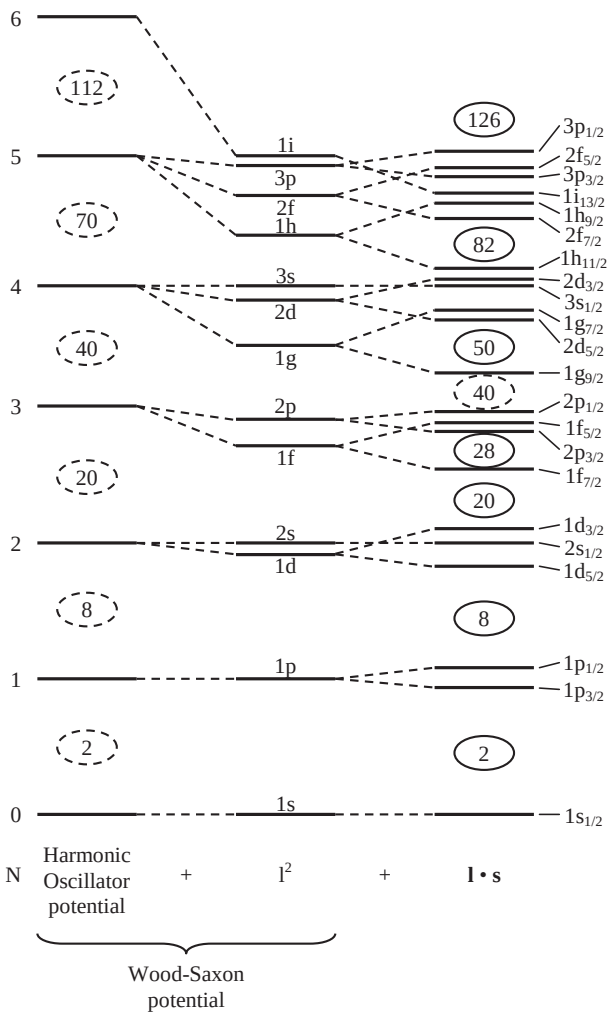


**Figure 2.3:** The sequence of single-particle energies for the harmonic-oscillator potential, with an inclusion of an additional orbit-orbit $l^2$ term or by simply using a Wood-Saxon potential, and with an addition of the spin-orbit term. $N$ labels the harmonic oscillator shell: $N = 2(n-1)+l$.

and a stronger attractive interaction between high angular momentum particles that lowers their energies, and an additional flattening at larger radii due to the centrifugal force that causes particles to spend more time closer to the surface of the nucleus. An evident solution would be an introduction of an additional $\ell^2$ term in the nuclear potential, but it is much more practical to use a more realistic Wood-Saxon potential of the form $U(r) = -U_0 \frac{1}{1+e^{\frac{r-R}{a}}}$, where $U_0$ is the depth of the nuclear potential corresponding to its value at the very center of the nucleus, $R = R_0 \cdot A^{-\frac{1}{3}}$ with $R_0$=1.27 fm is the radius of the nucleus, and $a$=0.67 fm is the diffuseness (or skin thickness) of the nuclear surface. This results in a noticeable decrease, up to several MeV, in single-particle energies, which depends on the value of the orbital angular momentum and the distance from the center of the nucleus, and, thus, leads to a spread between the levels of different $\ell$ as in the middle in Fig 2.3.

At this point, the shell model could reproduce only the first three shell closures and hardly any experimental sequence of levels. It was a rather fascinating suggestion from Maria Göppert-Mayer and independently from Otto Haxel, J. Hans D. Jensen, and Hans E. Suess in 1949 to introduce a spin-orbit interaction term[6][7] in analogy with the electromagnetic interaction of the atomic electron's magnetic moment with the magnetic field generated by its motion around the nucleus. The additional spin-orbit term $U_{\mathbf{l}\cdot\mathbf{s}}$ for the nuclear potential $U(r)$ can be written in the form $U_{\mathbf{l}\cdot\mathbf{s}} = -U_{\ell s}\frac{\partial U(r)}{\partial r}\mathbf{l}\cdot\mathbf{s}$, where $U_{\ell s}$ is a strength constant. The spin-orbit component of the nuclear force arises naturally from the relativistic effects of the nucleonic motion and, in general, is a surface phenomenon. This way, the nuclear force felt by a nucleon depends on the value of the orbital angular momentum and on whether its spin $\mathbf{s}$ and orbital angular momentum $\mathbf{l}$ are aligned parallel or antiparallel. As a result,

[6]It was Enrico Fermi who asked Maria Göppert-Mayer the key question: "Is there any indication of spin-orbit coupling?", whereupon she immediately realized that that was the answer she was looking for, and thus was born the spin-orbit coupling shell model of nuclei. Her husband Joseph Mayer gives the following description of this episode: "Fermi and Maria were talking in her office when Enrico was called out of the office to answer the telephone on a long distance call. At the door he turned and asked his question about spin-orbit coupling. He returned less than ten minutes later and Maria started to "snow" him with the detailed explanation. You may remember that Maria, when excited, had a rapid fire oral delivery, whereas Enrico always wanted a slow detailed and methodical explanation. Enrico smiled and left: "Tomorrow, when you are less excited, you can explain it to me.""

[7]While Maria Göppert-Mayer was preparing the spin-orbit coupling model for publication, she learned of a paper by other physicists presenting a similar explanation. As a courtesy, she asked the Editor of the Physical Review to hold her brief Letter to the Editor in order that it appear in the same issue as that paper. As a result of this delay, her work appeared one issue following publication of an almost identical interpretation of the magic numbers by Otto Haxel, J. Hans D. Jensen, and Hans E. Suess. Jensen, working completely independently in Heidelberg, had almost simultaneously realized the importance of spin-orbit coupling for explaining the shell structure, and the result had been this joint paper.

each *nl* level becomes split into two levels, as on the right in Fig 2.3, with the lowest ones corresponding to the parallel alignment and therefore experiencing a stronger spin-orbit interaction. The magnitude of the spin-orbit term of the nuclear potential is quite substantial: the energy splittings produced by it are comparable with the energy differences between the adjacent multiplets of the harmonic oscillator potential. As can be seen, this immediately results in a re-arrangement of levels into new groupings or "shells" with substantial energy gaps of a few MeV in between, corresponding to all known "magic" numbers. It must be realized, however, that since the nuclear potential and, thus, the extent of spacial confinement are determined by the number of nucleons in the system, the actual values and also the sequence of single-particle energies are mass-dependent, scaling as $E_{s.p.e.} \sim \frac{1}{r^2} \sim A^{-\frac{2}{3}}$.

Starting from the grouping of levels that is between the magic-number gaps 28 and 50, each shell contains a majority of levels of one parity, called *normal-parity orbits*, and one level of the opposite parity, called *unique-parity orbits*. Neglecting the very weak parity-nonconserving part of the weak interaction and taking into account the fact that the unique-parity orbits are situated quite far away from its original multiplets, whatever configuration mixing does occur between different levels, it cannot mix levels of different parity. For this reason, the unique-parity orbits provide pure and distinct configurations amidst a usually enormous complexity of mutually mixed states, and clearly provide an ideal testing ground for various nuclear models.

Finally, the issue of an independent-particle motion in a heavily-packed and strongly-interacting bound nuclear system can be properly addressed and explained in the framework of the shell model. First of all, it relates to the sheer fact that the strong nuclear force is rather "weak" compared to the kinetic motion of nucleons inside the nucleus — just consider the binding energy of the deuteron ($^2$H) of 2.23 MeV or the highest binding energies of the most stable Fe and Ni nuclides of ∼8.8 MeV and an average kinetic energy of a nucleon inside the nucleus of at least 20 MeV. Secondly, if a collision were due to occur deep inside the nucleus, the Pauli principle would simply prohibit a "scattered" particle to occupy any higher levels which are already fully filled with other particles. Thirdly and vaguely, the relativistic effects of the nucleonic motion and the Pauli principle should bring into play an additional spacial "confinement" of the nucleonic matter.

A singly- or doubly-magic nucleus then corresponds to a configuration where one of or both types of nucleons, respectively, completely fill major shells. Since for any closed (completely filled) shell the sum of all magnetic substates $m$ is coupled to zero, the ground state of any doubly-magic nucleus is always $0^+$. Extending this case to a configuration with one particle outside or one hole (all but one particles) inside a closed shell, the spin and parity of the ground state will then be determined by the last filled particle or unfilled hole, respectively.

For simple configurations, when a particle (hole) is outside (inside) the major shell in an orbital $j_1$, the shell model can immediately provide the energies of excited states corresponding to configurations with the particle (hole) in an orbital $j_2$ in terms of single-particle energies as $E^{ex.}_{j_2} = E_{j_2} - E_{j_1}$. Quite often it is mistakenly or rather ignorantly stated that the influence of a closed shell on a single particle (hole) outside (inside) can be ignored, which is not exactly true and especially for "magic" nuclei far off stability. The fact that the closed shell has $J$=0 means that its total wave function is spherically symmetric (with no preferred direction in space) and, thus, its interaction with a single particle (hole) is independent of the particle's (hole's) magnetic substate $m$. The interaction does exist but in a sense that it arises from a change in the spherically-symmetric central potential, and as a result the single-particle energies can be altered.

By further extending the model to configurations with two or more nucleons outside a closed-shell core we must properly deal with the residual part of nuclear interaction. Considering two valence nucleons of both types ($\pi$-$\pi$, $\nu$-$\nu$, $\pi$-$\nu$) in non-equivalent orbits $j_1m_1$ and $j_2m_2$ outside a closed-shell core, the resulting values of $J$ are simply integer values ranging from $|j_1 - j_2|$ to $|j_1 + j_2|$. For equivalent orbits $j_1 = j_2$ ($n_1l_1j_1 = n_2l_2j_2$), there are two distinct cases, namely, of identical and nonidentical nucleons. In the first case (isospin T=1: $\pi$-$\pi$, $\nu$-$\nu$) the Pauli principle puts a restriction on the occupation of identical $m$ states and, therefore, $J$ takes only on even integer values $J$=0, 2,...(2$j$-1), while for the second case ($T$=0: $\pi$-$\nu$) there is no such restriction and, thus, $J$ takes on all even (T=1) and odd (T=0) integer values $J$=0..2$j$. Without any additional interactions in such multiparticle configurations all $J$ values would be degenerate. But the existing residual interactions of predominantly short-range character induce energy shifts for different $J$ states relative to the degenerate case and clearly affect scattering of particles from one orbit to another (the so-called *configuration mixing*). Whereas the overall scale of the interaction and its strength depend on the radial behavior of the wave functions, the relative energies of different $J$ states depend on the angular structure of the corresponding wave functions. In the case of two identical nucleons the Pauli principle requires that their intrinsic spins be anti-aligned and, thus, the affected levels would have the intrinsic spin coupling $S$=0. It can be generally stated that in case of identical nucleons for positive-/negative parity configurations only even-/odd-$J$ levels are affected (lowered), respectively, while the rest of levels (odd-/even-$J$, respectively) are left unperturbed. And the more oriented the orbits are relative to each other, the more overlap there is between the particles, and, thus, the more affected the corresponding level $J$ is. It is an extremely important result and especially for a configuration of two identical particles in an equivalent orbit: the $J^\pi$=$0^+$ state is lowered the most, thus becoming the ground state, and quite often there is a large spacing to the

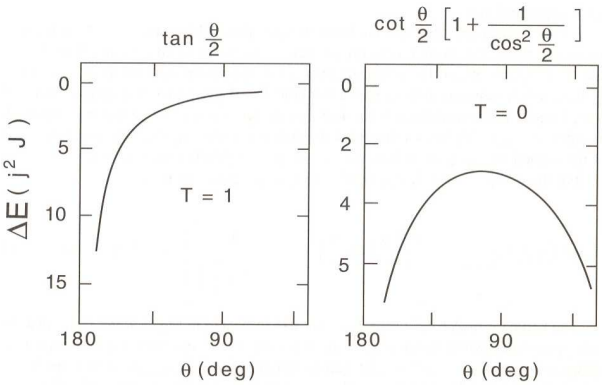


**Figure 2.4:** Angular dependence of the energy shifts due the $\delta$-function residual interaction for two identical ($T$=1) and nonidentical ($T$=1 and $T$=0) particles in equivalent orbits. The corresponding trigonometric expressions are given above the respective plots with an assumption, for simplicity, that $j, J \gg 0$. The figure is taken from [1].

$2_1^+$ level. The residual interaction can be approximated as a $\delta$-interaction in terms of the mathematical $\delta$-function, that is the interaction vanishes unless the particles occupy the same spacial position. Using a semiclassical geometrical interpretation of a nucleon as orbiting inside the nucleus with a certain orbital angular momentum under the influence of a $\delta$-interaction with another nucleon in the same orbit, the angular dependence of the residual interaction strength and, thus, the energy shifts for different $J$ states can be represented as in Fig. 2.4. This approach can be further extended to a two-particle configuration in nonequivalent orbits, see [1]. It is rather clear that the attractive residual interaction is stronger for a $\pi$-$\nu$ system than that for a $\pi$-$\pi$ or $\nu$-$\nu$ configuration. This formalism can be equally applied for particle-hole or hole-hole systems, but in the former case the interaction will be repulsive while for the latter configurations it will reverse to become attractive again.

Residual interaction clearly depends on the separation between two particles and, thus, can be expanded in terms of spherical harmonics as

$$V(|\mathbf{r}_1 - \mathbf{r}_2|) = \sum_k \nu_k(r_1 r_2) P_k(cos\theta) = \sum_{km} \nu_k(r_1 r_2) \frac{4\pi}{2k+1} Y^*_{km}(\theta_1 \phi_1) Y_{km}(\theta_2 \phi_2), \tag{2.18}$$

where $P_k(cos\theta)$ are Legendre polynomials and $\nu_k(r_1 r_2)$ can be written in terms of a $\delta$-interaction as

$$\nu_k(r_1 r_2) = \frac{2k+1}{4\pi} \frac{\delta(|\mathbf{r}_1 - \mathbf{r}_2|)}{r_1 r_2} \tag{2.19}$$

A more detailed analysis would require an additional separation of the two-particle wave function into radial and angular parts, but this is not strictly necessary within the scope of this work for just underlying the key points about the residual interaction. For the case of two identical particles in equivalent orbits, the antisymmetrization requirement allows only even integer values of $k$, while for other configurations $k$ may take on all integer values. In addition, $k \leq min[2l_1,2l_2,2j_1,2j_2]$.

Since the monopole component $P_0(cos\theta)$=$const$ over all angular space depending only on the overlap of the corresponding radial wave functions of the two particles, it does not contribute to any splittings in a multiplet of different $J$ values but can only result in an overall shift of the multiplet as a whole. The dipole component $k$=1 of the residual interaction is of no importance for low-energy excitations and can be omitted in our discussion. The next important and, actually, major component is the quadrupole part $k$=2 of the residual interaction, which leads to the splittings between corresponding levels. Since $P_2(cos\theta) \sim cos^2\theta$ ($P_2(cos\theta) = \frac{1}{2}(3cos^2\theta - 1)$), the splitting for each $J$ level relative to the unperturbed position is $\Delta E \sim J(J+1)$, thus, giving a parabolic dependence for the energy distribution of different $J$ states of a multiplet as in Fig. 5.12. This way, the quadrupole component is strongest for $J$ values corresponding to anti-aligned and aligned couplings and actually changes its sign in the middle. This means that the quadrupole interaction lowers the energies of the extreme values of $J$ the most while raising the energies of intermediate values.

In the framework of the shell model, the description of the two-particle configuration relative to the closed-shell core can be extended to multiparticle ($n > 2$) configurations of valence nucleons. The most physically-transparent and easiest way, based on the Pauli exclusion principle, is by means of the so-called $m$-scheme, which provides permissible values of total angular momentum $J$ from a consideration of possible $m$-substate occupations for all $n$ particles in a state $j$. The maximum angular momentum for a configuration $j^n$ is given as $J_{max} = nj - \frac{n(n-1)}{2}$. Certain values of $J$ will be made in several distinct ways resulting from different couplings between the valence particles. The total wave function of a certain state $J$ must be represented as a totally-antisymmetric linear combination of these basis states. The normalized coefficients in such a combination are called coefficients of fractional parentage (CFP) with their squares being the probability that a given final state is constructed from a certain parent coupling of valence particles. By using two-particle CFP coefficients an $n$-particle state can be described in terms of ($n$−2)-particles wave functions. All this means that a nuclear structure of a complex nuclear system with a configuration $j^n$ relative to the inert closed-shell core can be at least qualitatively understood from nuclear spectra of the neighboring even-even nucleus with a configuration $j^{n-1(2)}$, where 1 and 2 represent the odd and even values of $n$,

respectively. The particles from the same state $j$ have a tendency to couple to $J{=}0^+$ and the nuclear force is effectively measured by the number of such pairs. This property is explicitly exploited in the so-called seniority scheme. Here, seniority is defined as the smallest value of $n{=}\nu$ that can produce a given value $J$ in the configuration $j^n$ or, in physical terms, it is simply the number of unpaired particles in a state $j$. Clearly, the states with lower seniority will lie lower in energy. This is why the ground state of all even-even nuclei is $J^\pi{=}0^+$. Similarly, the ground state of odd-mass nuclei must normally have the seniority $\nu{=}1$. A powerful implication is that the two-body matrix elements in the configuration $j^n$ can be linked to those in the configuration $j^\nu$. Thus, in the $n$-particle configuration, the energy differences of seniority $\nu{=}0$ and $\nu{=}2$ states are identical to those in the two-particle system and are independent of $n$. This is a crucial result that makes the shell model applicable in a simple way to nuclei with more than two nucleons away from the closed shells. A rather important characteristic feature of even-even nuclei at or near closed shells arises from the framework of the seniority scheme: since the energy spacings between different seniority states are (rather) independent on the number of nucleons in a given equivalent orbit and due to the fact that $J^\pi{=}0_1^+$ is lowered the most, such nuclei are characterized by the ratio $E(4_1^+)/E(2_1^+) < 2$. Seniority is generally a good quantum number for at least the nuclei with $A < 80$, but it can be broken in deformed nuclei due to the presence of a strong proton–neutron residual interaction.

The whole discussion would not be complete without mentioning the pairing interaction and profound implications of it on nuclear structure. It is defined as an attractive interaction that acts between two identical nucleons in total angular momentum $0^+$ states, in which the two particles have extremely high spacial overlaps. In comparison with the $\delta$-interaction, the pairing interaction for a configuration of two identical particles in equivalent orbits leads to lowering of only the $0^+$ state with the rest of the energy levels of the multiplet staying unperturbed. By forming pairs of particles coupled to $J{=}0$, the pairing interaction clearly favors sphericity. As a consequence, near closed shells, it may lead to a sudden onset of deformation.

The pairing interaction is defined in terms of its matrix elements as

$$\langle j_1 j_2 J|V_{pair}|j_3 j_4 J'\rangle = -G\left(j_1+\frac{1}{2}\right)^{\frac{1}{2}}\left(j_3+\frac{1}{2}\right)^{\frac{1}{2}}\delta_{j_1 j_2}\delta_{j_3 j_4}\delta_{J0}\delta_{J'0}, \quad (2.20)$$

where $G$ is the so-called strength of the pairing force. This way, the pairing interaction is defined to act only on identical nucleons in equivalent orbits $j_1{=}j_2$ and $j_3{=}j_4$ all coupled to $J^\pi{=}0^+$. Additionally, it is not just an interaction between two nucleons in the same $j$ state. The pairing interaction is equally strong for matrix elements connecting the $|j_1^2 J = 0^+\rangle$ and $|j_3^2 J' = 0^+\rangle$ states, which corresponds to a scattering of pairs of particles from the orbit $j_1$ to

the orbit $j_3$. Without these nondiagonal components the excited states would be formed by just raising both particles to the next unoccupied orbit and the energy gap in even-even nuclei would be just twice the average energy spacing of low-lying levels in neighboring odd nuclei and not 5–10 times larger as observed experimentally. Although the pairing force is orbit-independent, it is identical for each magnetic substate and, thus, scales for an orbit $j$ as $2j + 1$. This implies that it is stronger for higher $j$ orbits. In our region of interest, it may be an important factor for nuclei at or near the $N$=40 neutron subshell gap, separating the $\nu 2p_{1/2}$ and $\nu 1g_{9/2}$ orbits. The strength $G$, although being orbit-independent, decreases with $A$ due to the fact that in heavier nuclei the outer nucleons are further apart from each other and, thus, have smaller spatial overlaps. Additionally, it is lower for protons because of the Coulomb repulsion. The commonly used values are $G_p = \frac{17}{A}$ MeV and $G_n = \frac{23}{A}$ MeV.

In the absence of pairing the energy levels would be occupied up to some point, called the Fermi energy, with all levels above it being completely empty. Due to the pairing interaction such occupation sequence is smeared out resulting in partial occupation of energy levels $\varepsilon_i$ above and below the Fermi level $\lambda$ as in Fig. 2.5a. This way, a single-particle excitation energy $(\varepsilon_i - \lambda)$ is replaced by a quasi-particle energy $E_i = \sqrt{(\varepsilon_i - \lambda)^2 + \Delta^2}$, where $\Delta = G \sum_{i,j} U_i V_j$ is the gap parameter, given as a sum over partially occupied orbits $i, j$. Here, $U$ and $V$ are the so-called emptiness and fullness factors, respectively, given as

$$U_i^2 = \frac{1}{2}\left[1 + \frac{(\varepsilon_i - \lambda)}{\sqrt{(\varepsilon_i - \lambda)^2 + \Delta^2}}\right], \quad V_j^2 = \frac{1}{2}\left[1 - \frac{(\varepsilon_j - \lambda)}{\sqrt{(\varepsilon_j - \lambda)^2 + \Delta^2}}\right], \quad (2.21)$$

where $U_i^2$ and $V_i^2$ give the probability that the $i$-th orbit is, respectively, empty and full, so that $U_i^2 + V_i^2 = 1$.

This way, the particles and holes are replaced by quasiparticles representing partially filled levels. In even nuclei the simplest particle–hole excitation corresponds to breaking one pair and raising one of the particles to the next higher orbit. Due to pairing it appears as a two quasi-particle excitation, when one quasi-particle represents the hole and the other is the created particle excitation. The total excitation energy is then given by

$$E_{ij}^{2qp} = E_i^{qp_1} + E_j^{qp_2} = \sqrt{(\varepsilon_i - \lambda)^2 + \Delta^2} + \sqrt{(\varepsilon_j - \lambda)^2 + \Delta^2} \geq 2\Delta \quad (2.22)$$

This shows an almost universal feature of even-even nuclei — the presence of the pairing gap $2\Delta$, see Fig. 2.5b, which is ∼1.5–2 MeV, and the fact that few two quasi-particle excitations may appear below it. In odd-mass nuclei, excited levels are obtained by replacing the quasi-particle of the ground state with a quasi-particle in a different single-particle level. The excitation energy is then

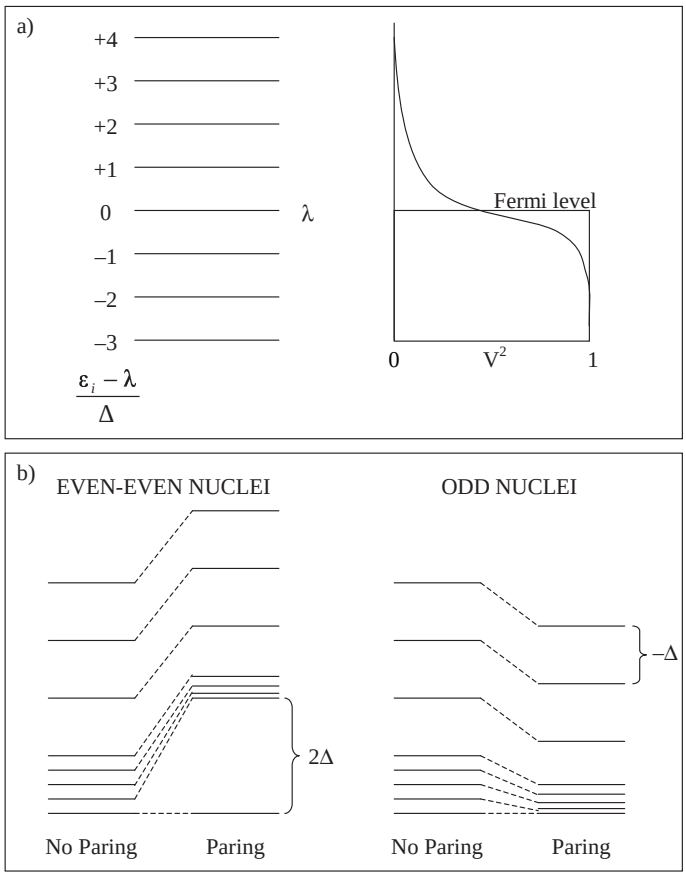


**Figure 2.5:** Pairing interaction. a). A schematic representation of the pair scattering between different orbits resulting in partial occupancies of single-particle states around the Fermi level. b). The effect of pairing in even-even and odd nuclei. The notations are taken from the text, where $\varepsilon_i$ is the energy of the $i$-th single-particle level; $\lambda$ is the Fermi level; $\Delta$ is the gap parameter; and $V$ is the occupation or fullness factor giving the occupation probability $V^2$.

given by

$$E_i^{qp} = E_i - E_0 = \sqrt{(\varepsilon_i - \lambda)^2 + \Delta^2} - \sqrt{(\varepsilon_0 - \lambda)^2 + \Delta^2} \quad \overset{(\varepsilon_i - \lambda) \gg \Delta}{\longrightarrow} \quad (\varepsilon_i - \lambda) - \Delta, \tag{2.23}$$

where $\varepsilon_0$ is the quasi-particle energy of the orbit nearest to the Fermi level. This shows the opposite effect of pairing in odd-mass nuclei — the compression of the low-lying energy levels and the decrease in the excitation energies of the higher states by an amount of $\sim \Delta$ as in Fig 2.5b.

The introduction of pairing results in quite significant simplifications in shell model calculations for nuclei with many valence nucleons. Instead of constructing all possible values of total angular momentum within a major shell, a physically-meaningful truncation based on the occupation probabilities can be imposed by considering quasi-particle excitations relative to the Fermi surface. This new shell-model approach is based on Monte Carlo methods and, by making use of the pairing interaction, exploits the fact that most of the billions of resultant configurations are not important for general nuclear properties and, therefore, only a subset of relevant configurations need to be sampled [2][3]. As an example from [3], the energy change of a single-particle level of a single valence proton due to the residual interaction with neutrons from the partially-occupied orbits of the configuration space around the Fermi level can be given as

$$\epsilon_{j_\pi}^{res} = \sum_{j_\nu} E_{j_\pi j_\nu} (2j_\nu + 1) v_{j_\nu}^2, \tag{2.24}$$

where $E_{j_\pi j_\nu}$ is the average matrix element of a proton-neutron interaction and $v_{j_\nu}^2$ is the occupation probability of the neutron orbital $j_\nu$. However, in spite of all these developments, the shell model cannot be used for description of a huge variety of nuclei far from closed shells. These nuclei are mainly characterized by a presence of a strong deformation and must be treated within the framework of collective models where such shapes arise naturally.

### 2.1.4 Unified approach: the deformed shell model

Both the macroscopic compound-nucleus and microscopic independent-particle approaches are limited to only certain suitable sets of nuclei and cannot provide a complete full-scale description of the huge multitude of various nuclear systems. On the other hand, in many nuclei there is a clear distinction between collective and single-particle degrees of freedom and, therefore, none of the approaches can be abandoned but rather both of them must be unified. An ideal and most physically-transparent way would be to consider an independent-particle motion in the deformed mean field of the nucleus. Such early attempt to develop a unified approach was made by Sven Nilsson in 1955.

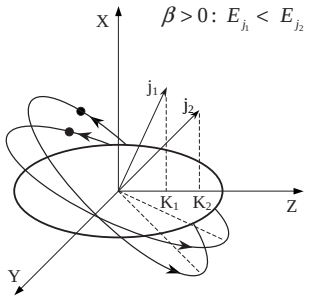


**Figure 2.6:** A simplified illustration of two single-particle orbits at different inclinations to the main bulk of nucleus with a prolate deformation.

Clearly, in such a description of deformed nuclei there is a conceptual difficulty in separation of the single-particle motion from the collective motion of the nucleus. An approximate separation can be achieved if the frequency of the nucleonic motion is much larger than the rotational frequency of the nucleus. If that is not the case, then in order to describe the effects of the nuclear rotation on the single-particle motion an abstract Coriolis force must be introduced.

In the case when the central part of the nuclear potential is spherical, the energy levels of each single-particle state have a degeneracy of $2j+1$. In the presence of a deformed potential, the energies of the levels depend on the spacial orientation of the orbit relative to the symmetry axis and, therefore, the orbital angular momentum is no longer a good quantum number. The energy level of a single valence nucleon moving in a deformed mean-field lies lower if its orbit is situated closer to the bulk of the nucleus as in Fig. 2.6. As a result, the energy levels of each single-particle state become split depending on the orientation of the corresponding single-particle orbits, which is specified by the projection $K$ of the total angular momentum on the symmetry axis. Since the orientation angle upon symmetry reflection relative to the symmetry axis is the same for orbits with opposite directions of orbital momentum, two nucleons with opposite angular momenta but having the same $K$ may occupy the same level. The rotational angular momentum of axially-symmetric nuclei is perpendicular to the symmetry axis and, thus, does not contribute to $K$.

Each orbit, called *Nilsson orbit*, is labeled as $K^\pi[Nn_z\Lambda]$, where $K^\pi$ gives the total angular momentum and parity; $N$ is the principal quantum number that denotes the major shell; $n_z$ is the number of nodes in the wave function in the $z$ direction (along the symmetry axis); and $\Lambda$ is the component of the orbital angular momentum along the $z$ axis. The evolution of single-particle

levels with deformation can be represented in a diagram, colloquially known as the *Nilsson diagram*, as shown in Fig. 5.14 for both proton and neutron levels in our region of interest. As can be seen, each Nilsson state, originally straight, starts sloping upwards or downwards for both prolate ($\beta > 0$) and oblate ($\beta < 0$) deformations, depending on the angle of the orbit relative to the main bulk of the nucleus. For small deformations this dependence of the level energies scales as $\sim K^2$. Further on, in the presence of the deformed field, there is a characteristic single-particle configuration mixing of different $j$ values, which is now additionally superimposed on the $K$-splitting. From the antisymmetrization requirement no two levels with the same quantum numbers (here with the same $K^\pi$ values) may cross, and, thus, the corresponding Nilsson states must repel from each other upon approach. Thus, there are three major factors that constitute the Nilsson diagram: the initial (shell-model) single-particle energies, the $K$-splitting, and identical-level repulsion.

The wave functions for Nilsson orbits are rarely pure because of single-$j$ configuration mixing, mainly caused by the quadrupole interaction. It is only at very small deformations, that the nuclear wave functions can be nearly pure in $j$, but with the increase in the deformation the configuration mixing becomes more pronounced. Not the least role here is played by the nondiagonal matrix elements of the quadrupole interaction, which can mix configurations differing by two units of angular momentum and without change in nucleon spin orientation, as, e.g., possibly $\pi$1f7/2 and $\pi$2p3/2, $\nu$1f5/2 and $\nu$2p1/2 in our region of interest. In contrast, the unique-parity orbits, such as $K$=7/2 and $K$=9/2 from the initial $g_{9/2}$ orbit, are far away from $j$ shells with the same $K$-values and parity and, thus, are extremely pure and appear virtually straight in the Nilsson diagram. Concerning the form of the Nilsson wave functions, because of the configuration mixing involved, they can be expanded in the spherical basis as $\psi^i_{Nilsson} = \sum C^i_j \phi_j$, where $\phi_j$ are solutions to the spherical independent-particle model and $C^i_j$ are configuration-mixing coefficients.

In conclusion, apart from the fact that the Nilsson model provides an unified description of (collectively-) deformed nuclei in terms of their single-particle structure, it also gives a remarkable simplification to the enormous complexity of the spherical shell model. For instance, in nuclei with many valence nucleons outside closed shells, instead of considering $2j+1$ degeneracy of several levels of the configuration space — albeit substantially simplified through the pairing interaction, the Nilsson model, allowing only two nucleons in each level in the deformed basis, simply retains the single-particle description of orbits as a relatively simple mixture of spherical $j$-orbits. Without any rebate whatsoever, the Nilsson model proved to be a grand success.

## 2.2 Nuclear structure

### 2.2.1 Main physics incentives for this work

The physics goal of this work, namely $\beta$-decay of the neutron-rich $^{66}$Fe isotope, is in fact part of the project that has been successfully carried on at LISOL for almost a decade and that can be defined in general terms as "Nuclear-structure studies in the neutron-rich Ni region". The whole region of interest, as approximately specified in Fig. 2.7, draws a great deal of attention due to the closed proton shell at $Z$=28 and a remarkable span over several neutron shells: from the magic $N$=28 closure on the neutron-deficient side, through the semi-magic $N$=40 and to the magic $N$=50 closures on the neutron-rich side. Thus, it provides an important and convenient testing ground for various nuclear models and especially the shell model, bringing a better understanding of and new insights into the overall issue of nuclear structure.

Taking recent works on the most neutron-rich part of the region, many of these nuclei have been extensively investigated in numerous experiments by our group: $^{66,67,68,70}$Ni in $\beta$-decay of $^{66,67,68,70}$Co [4][5] and $^{68-74}$Cu in $\beta$-decay of $^{68-74}$Ni [6][7] at LISOL [8][9], $^{68-74}$Zn in $\beta$-decay of $^{68-74}$Cu [10][11] and $^{68,70}$Cu [12], $^{67,69,71,73}$Cu [13], $^{74,76,78,80}$Zn [14] in Coulomb excitation at ISOLDE [15]; as well as other groups: the corresponding isobars from the $\beta$-decay of $^{59-62}$V, $^{61-64}$Cr, $^{63-66}$Mn, $^{65-68}$Fe, $^{67-70}$Co [16] and $^{60-62}$V, $^{62-66}$Cr, $^{64-68}$Mn, $^{67-70}$Fe, $^{69-71}$Co [17] at GANIL [18], $^{61-69}$Fe in $\beta$-decay of $^{61-69}$Mn [19] at ISOLDE, and a few more which will be cited whenever needed in the course of this section. Due to the fact that Fe, Co, and Ni are refractory-type elements[8], their isotopes are difficult to produce by the conventional Isotope-Separator-On-Line method, based on high-temperature target – ion source system. The production capabilities of short-lived neutron-rich Fe beams at LISOL, see section 4.2, combined with a new detection set-up for $\beta$-decay studies, see section 4.4, allows to perform new studies in the region below the $Z$=28 closed proton shell.

The physics goal of this work can be summarized in nuclear-structure terms as follows:

- to contribute to the current understanding of the evolution of nuclear structure along the $Z$=28 proton shell-closure;
- to study the persistence of the semi-magic $N$=40 neutron shell-closure around $^{68}$Ni;
- to investigate possible indications to the onset of deformation;
- to investigate the decay properties of nuclides from the produced isobaric chains;

[8] The elements with a low vapor pressure at high temperature.

**Figure 2.7:** A part of the chart of the nuclides, representing the region of interest for this work.

### 2.2.2 Evolution of nuclear structure along the $Z$=28 proton shell-closure

A global overview of the nuclear structure along the closed $Z$=28 proton shell is given in Fig. 2.8. The energy of the first $2^+$ and $4^+$ states in the even-even Zn ($Z$=30), Ni ($Z$=28) and Fe ($Z$=26) isotopes is shown together with the $E(4_1^+)/E(2_1^+)$ ratio. Fig. 2.9 shows the systematics of the $B(E2)$ values[9] and the two-neutron separation energy[10] $S_{2n}$ for these even-even nuclei. Although the excitation energy of the $2_1^+$ in the doubly-magic $^{56}$Ni nucleus hints to a good closed shell character, the relatively high $B(E2 : 2_1^+ \rightarrow 0_1^+)$ value of 9.4(1.9) W.u. [20] indicates the opposite in comparison with other doubly-magic $N$=$Z$ nuclei of lower mass, as, e.g., 3.3(3) W.u. for $^{16}$O, 2.3(4) W.u. for $^{40}$Ca, 1.6(5) W.u. for $^{48}$Ca. Recent large-scale shell-model calculations [21] confirm that the wave function of the ground and $2_1^+$ states in $^{56}$Ni is constructed from particle-hole excitations across the $Z$=28 and $N$=28 closed shell gaps. Following the systematics from the $^{56}$Ni nucleus towards the heavier Ni isotopes, the excitation energy of the $2_1^+$ state as well as the $E(4_1^+)/E(2_1^+)$ ratio indicate a typical behavior of a semi-closed shell nucleus. At the $N$=40 neutron sub-shell closure in $^{68}$Ni the $2_1^+$ state rises in energy and the $B(E2)$ goes down to value of 3.2(7) W.u. [24]. Although these two observables are fingerprints for an increased magicity, it has been explained using large-scale

[9] Since the electromagnetic interaction in the nucleus only weakly perturbs by-far the dominant nuclear interaction, the $\gamma$-ray reduced transition probability between the two nuclear states, being simply a change in charge (electric) and current (magnetic) distributions in the nucleus, can provide an almost pure quantitative notion of the difference between the corresponding nuclear wave functions. It is defined as $B(^E_M\lambda : I_i \rightarrow I_f) = \frac{1}{2I_i+1}|\langle\Psi_f||M(^E_M\lambda)||\Psi_i\rangle|^2$, where $^E_M\lambda$ is the electric/magnetic transition multipolarity; $M(^E_M\lambda)$ is the electric/magnetic multipole operator; $I_i$ and $I_f$ are the initial and final nuclear states with the total wave-functions $\Psi_i$ and $\Psi_f$, respectively. This way, $B(E2 : 2^+ \rightarrow 0^+)$ is the quadrupole electric transition probability between the nuclear states with total angular momenta $2^+$ and $0^+$. It is measured in units of $e^2fm^{2\lambda}$=$e^2fm^4$=$0.01{\cdot}e^2b(arn)^2$. Alternatively, since the change in the nuclear wave-function is related to the change in the nuclear-matter density distribution, the transition between two nuclear states, involving a redistribution of single nucleons, can be expressed in pure single-particle units, called Weisskopf Units: $B(E2 : 2^+ \rightarrow 0^+)$[W.u.]=$\frac{16.8}{A^{4/3}} \cdot B(E2 : 2^+ \rightarrow 0^+)[e^2fm^4]$, where 1 W.u. corresponds to the transition involving one single nucleon.

[10] Obviously, the two-proton or two-neutron separation energy is the energy, required to remove two protons or two neutrons, respectively, from a given nucleus. Being an important nuclear-structure parameter for even-even nuclei in the vicinity of closed shells, it can be effectively defined as a remaining difference in binding energy as $S_{2p/2n} = B(^A_ZX_N) - B(^{A-2}_{Z-2}X_N/^{A-2}_ZX_{N-2}) + B(2p/2n)$. Since the pairing interaction between identical nucleons is orbit-independent in the first-order approximation, it is commonly accepted to provide immediately the first derivatives of the $S_{2p/2n}$ curves, yielding peaks at closed shells. However, since such an assumption is not accurate and especially in highly-mixed many-particle valence configurations involving single-particle orbits with different orbital angular momenta, it is more correct to provide pristine values.

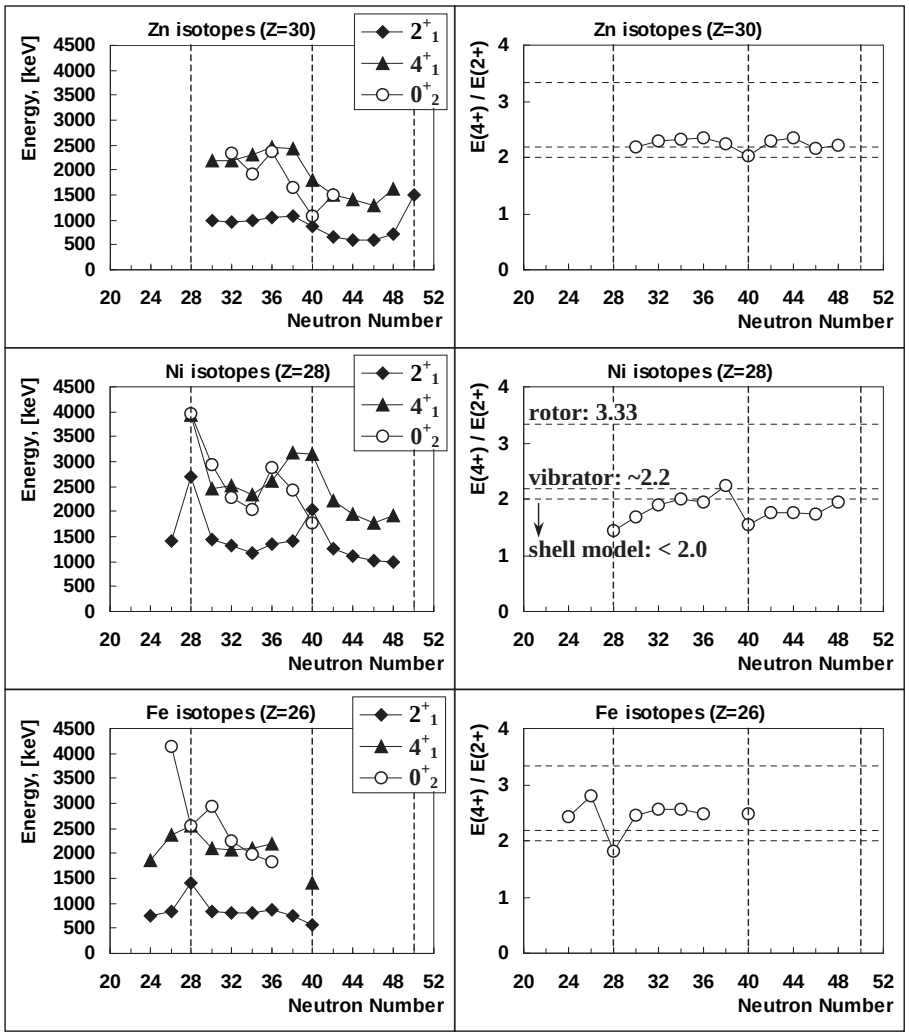


**Figure 2.8:** Systematics of the energies of $2^+_1$, $4^+_1$, $0^+_2$ states (on the left) and the ratio $E(4^+_1)/E(2^+_1)$ (on the right) for even-even Zn, Ni, and Fe isotopes. The given data represent the currently adopted experimental values, see, e.g., [22], with $E(2^+_1)$, $E(4^+_1)$ for $^{64,66}$Fe$_{38,40}$ taken from [19] and $E(2^+_1)$ for $^{80}$Zn$_{50}$ taken from [14].

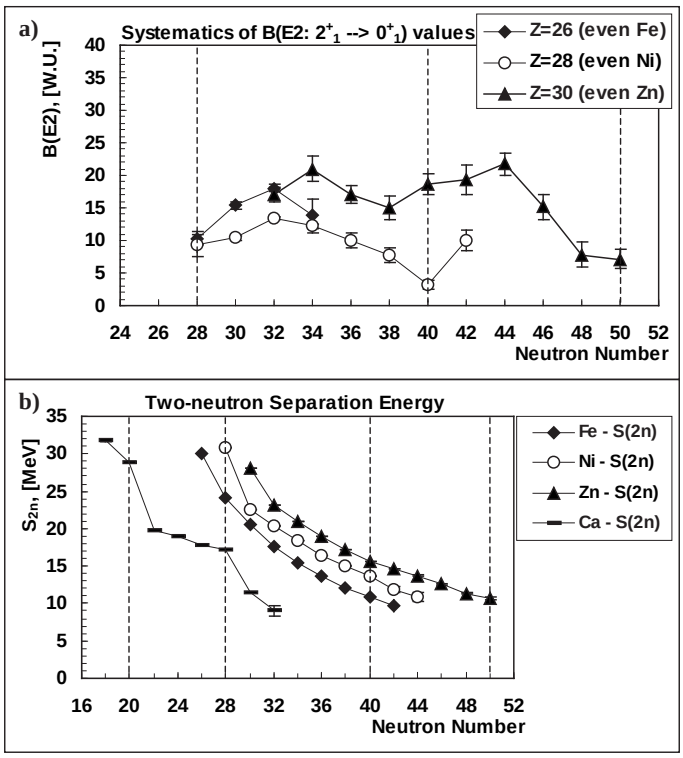


**Figure 2.9:** Major nuclear-structure characteristics describing its evolution along and near singly- and doubly-closed shells: a) systematics of the $B(E2 : 2_1^+ \rightarrow 0_1^+)$ transition rate in even-even Fe, Ni, and Zn isotopes; b) systematics of the two-neutron separation energy in even-even Fe, Ni, Zn, and, for comparison purposes, Ca isotopes. The given data represent the currently adopted experimental values, see, e.g., [22], with $B(E2 : 2_1^+ \rightarrow 0_1^+)$ values for $^{76,78,80}$Zn taken from [14] and for $^{70}$Ni taken from [23].

shell-model calculations [24][25] as arising from the fact that the $2_1^+$ state can not be built from re-coupling of two neutrons in the $\nu p_{1/2}$ orbital. As explicitly pointed out in [25], the small $B(E2)$ value simply reflects the fact that the lowest $2^+$ state in $^{68}$Ni is primarily a neutron excitation involving a pair scattering across the $N$=40 neutron sub-shell gap into the $\nu g_{9/2}$ orbital and most of the $B(E2)$ strength resides in higher lying excited states created through proton

excitations. From the systematic trend of the two-neutron separation energy, no strong indication of a $N$=40 sub-shell closure is present. The iron ($Z$=26) and zinc ($Z$=30) isotopes with two protons away from the $Z$=28 shell-closure show a drop in the energy of the first excited $2^+$ state at $N$=40. Unfortunately, the $B(E2)$ values for the Fe isotopes have only been reported up to $N$=34. As suggested in [19] from the energy systematics of the Fe isotopes, an unexpected increase in collectivity takes place near the $N$=40 neutron sub-shell closure. Furthermore, the same conclusion is supported in [19] by the comparison of the experimental half-life values of the neutron-rich Mn isotopes with the results from the QRPA (Quasi-particle Random-Phase Approximation) calculations. The onset of collectivity in this region is largely explained as arising from the increased proton-neutron residual interaction.

### 2.2.3 Persistence of the semi-magic $N$=40 neutron shell-closure: is $^{68}$Ni a good core?

Although the doubly-magic character of $^{68}$Ni has been questioned, it appears to be a good core for the description of nuclear structure of nuclei in its immediate neighborhood. The excitation spectra of the neighboring $^{67,69}$Ni and $^{68,69,70}$Cu nuclei were interpreted as coupling of proton and/or neutron particles (holes) to the $^{68}$Ni core [26][5][11][7]. However, it was realized that a similar description for the $^{66,70}$Ni and $^{70}$Zn nuclei as, respectively, two neutron and two proton particles (holes) coupled to the $^{68}$Ni core failed [4]. Clearly, the persistence of the underlying $^{68}$Ni core vanishes when two or more nucleons of the same type are coupled to it. The experimental low-lying excited states in nuclei in the immediate neighborhood of $^{68}$Ni are shown in Fig. 2.10, which can be summarized as follows:

- **$Z$=28 $^{67,69}$Ni isotopes** Some of the low-lying levels in the $^{67}_{28}\mathrm{Ni}_{39}$ [5] and $^{69}_{28}\mathrm{Ni}_{41}$ [26] nuclides can be explained in single-particle terms of a single neutron hole and particle, respectively, outside the $^{68}$Ni core [27]. Coupling with the $^{68}$Ni ground and $2^+_1$ states have been suggested and, additionally, the states, involving neutron excitations across the $N$=40 sub-shell gap, were also considered.

- **$Z$=29 $^{68-70}$Cu isotopes** The presence of the underlying core can be observed in the nuclear structure of $^{69}_{29}\mathrm{Cu}_{40}$, where the main components of the nuclear wave functions for many of the lowest levels correspond to a single proton particle coupled to the $^{68}$Ni core. The excitation spectra of $^{68,70}_{29}\mathrm{Cu}_{39,41}$ can be relatively well explained as multiplets of states created through residual interaction between the valence proton and neutron outside $^{68}$Ni core [6][7][27][12][13].

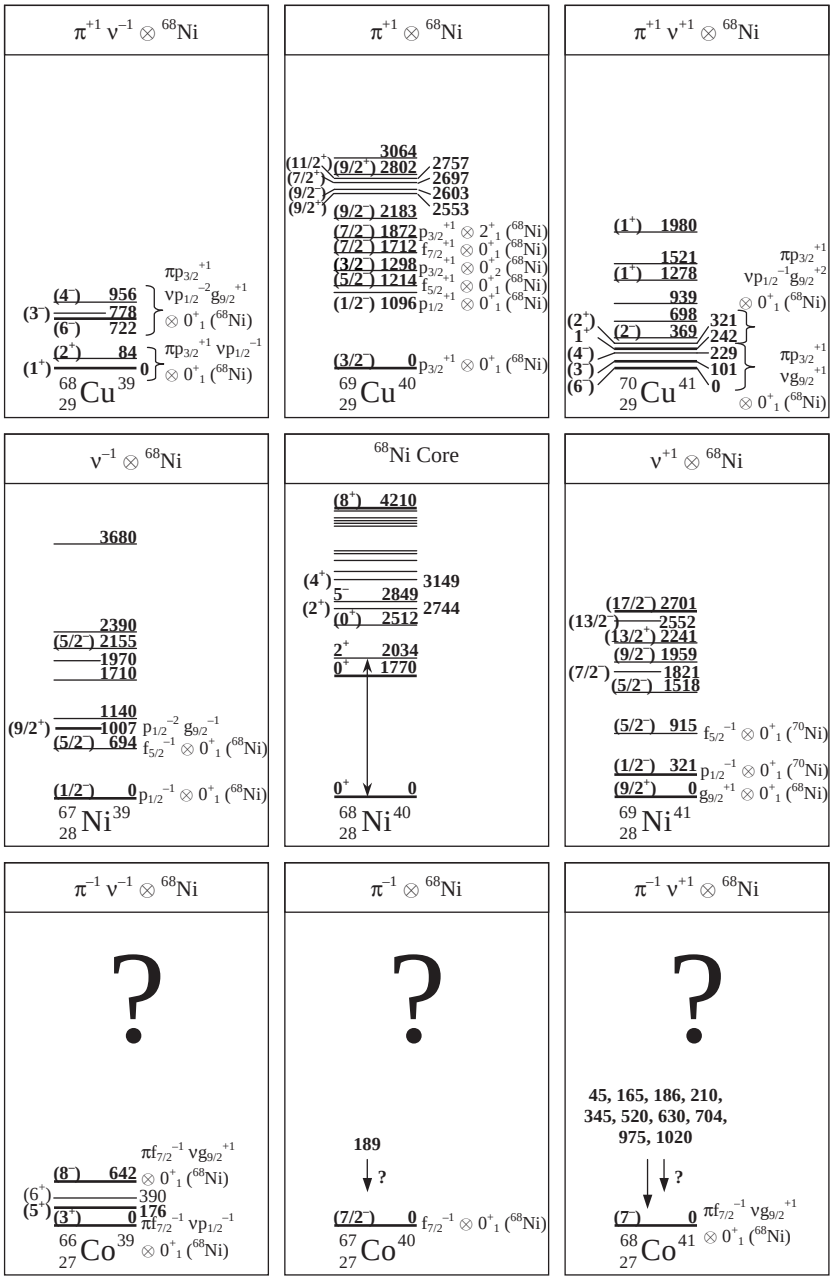


**Figure 2.10:** The experimental low-energy excitation spectra of nuclei with $Z$=27–29, $N$=39–41 compiled from various up-to-date sources [22]. See the text for more discussion. Whenever possible, suggestions for dominant configurations are given for the available states.

- **$Z$=29 $^{66-68}$Co isotopes** Apart from a few levels and several unplaced $\gamma$-transitions, very little is known [28][29][17] about neutron-rich Co isotopes starting from $^{66}$Co. It is logical to suggest that the structure of these nuclei might be dominated by a presence of the $^{68}$Ni core similar to the case of Cu isotopes. However, a stronger residual interaction between the proton hole in the $\pi f_{7/2}$ level and neutrons in the fpg-shell and especially the $\nu g_{9/2}$ level might lead to a substantial configuration mixing and an onset of deformation, most likely diminishing the structural presence of the $^{68}$Ni core and even obliterating the $Z$=28 proton shell gap.

Clearly, one of the aims of the present study is to obtain experimental information on the level structure in $^{66}$Co in order to test the persistence of the $N$=40 neutron sub-shell closure below $^{68}$Ni.

### 2.2.4 The onset of deformation

As already addressed in the previous section, in terms of the independent-particle approach, deformation in nuclei can take place as a result of the proton-neutron residual interaction. In our region of interest, an onset of deformation has been suggested in neutron-rich nuclei close to and well below the $Z$=28 proton shell-closure already not very far from stability — in nuclei with $Z$=24–26 and $N$ up to ∼40, see [19], [29], and [30].

Since the axially-symmetric quadrupole deformation constitutes the most common and usually main component of the overall deformed nuclear shape, nuclear deformation is usually quantified by the quadrupole deformation parameter $\beta_2$, see Eqs 2.2, 2.3, and 2.4. Although the deformation parameter is not a direct observable in experiment, the presence of deformation can be invoked and even quantified from various nuclear-structure parameters, as, e.g., the electric quadrupole moment, lifetimes of shape isomers, transition probabilities. As described in [31], the deformation parameter $\beta$, similar to the quadrupole deformation parameter $\beta_2$, can be extracted from the quadrupole electric transition probability $B(E2: 2^+ \rightarrow 0^+)$ in units of $e^2b^2$ as follows:

$$\beta = \left(4\pi/3ZR^2\right)\left[B(E2)\uparrow/e^2\right]^{1/2}, \tag{2.25}$$

where $Z$ is the atomic number of the given nucleus and $R = 1.2A^{1/3}$ fm is the radius of the nucleus with $A$ being the atomic mass number. Using the available experimental $B(E2)$ values from Fig. 2.9b, the obtained deformation parameters for even-even nuclides from our region of interest are given in Fig. 2.11. More extensive quantitative results for all nuclides must be obtained from theoretical calculations. For neutron-rich nuclei from and somewhat below our region of interest, as in [29] and especially [19], from the variety of the existing theoretical tabulations, as, e.g., [33],[32], and [34], the most sensible agreement with experiment in terms of the deformation parameter is achieved

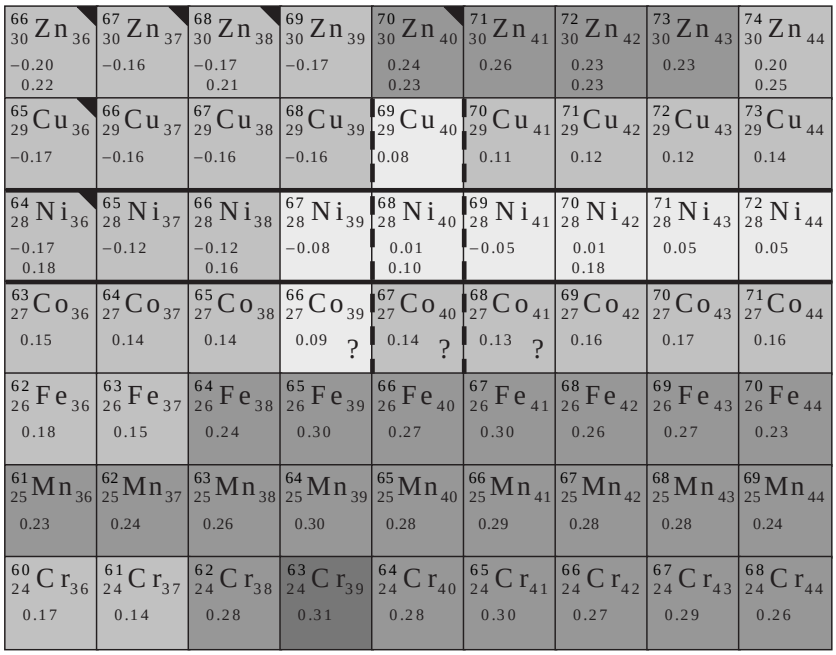


**Figure 2.11:** Calculated quadrupole deformation parameter $\beta_2$ for the ground states of the nuclides from the part of the neutron-rich Ni region and below not very far from stability. For each nuclide the first number on the left is taken from the calculations in [32] and for some even-even nuclides the second number on the left corresponds to the deformation parameter extracted from the known $B(E2 : 2_1^+ \rightarrow 0_1^+)$ values in Fig. 2.9b according to [31].

with the calculations based on the Extended Thomas-Fermi with Strutinski Integral approach (ETFSI) in [32], given in Fig. 2.11. In addition, the existence of the isomeric transition in $^{67}$Fe [30], supported by theoretical calculations from the same reference, provides an indication that there is an onset of deformation in this nucleus with $\beta_2 \approx 0.3$.

As can be seen from the Fig. 2.11, the Ni isotopes, as well as the neighboring Cu and Co isotopes, exhibit only a small deformation with $\beta_2 < 0.2$. From theoretical predictions, the ground states of $^{68-72}$Ni isotopes can be even considered as almost spherical. However, as early as in Zn and Fe isotopes with, respectively, two proton particles and holes away from the $Z$=28 closed proton shell, an onset of deformation clearly starts taking place, reaching $\beta_2 \approx 0.3$ in $^{65-67}$Fe isotopes. The fact that deformation is more pronounced in nuclei below the $Z$=28 closed shell can be explained by a stronger proton-neutron residual interaction between the proton holes in the $\pi f_{7/2}$ orbital and the neutrons in the fpg-shell. One can also see that the semi-doubly magic $^{68}$Ni core has very little stabilizing effect on the nuclides in its immediate neighborhood.

### 2.2.5 Decay properties

As presented in Chapter 5, this work concentrates fully on the $\beta$-decay of $^{66}$Fe. The decay schemes of the $^{66}$Fe and $^{66}$Co nuclei, as known prior to our experiments, are given in Fig. 2.12.

#### $^{66}$Fe

The $\beta$-decay half-life of 440(60) ms is known from [35] and [29]. The proposed level scheme is based on the work by Grzywacz *et al* [28]. In all of the three works, the $^{66}$Co nuclei were produced in fragmentation reactions. The In-Flight separation technique, see section 4.1, used in [28], allowed to identify $\mu$s isomeric transitions, resulting in the observation of 175 keV ($T_{1/2}$=1.21(1) $\mu$s) and 252 keV ($T_{1/2}$ >100 $\mu$s) transitions. The subsequent level scheme is shown in Fig. 2.12b. As discussed in [28], the isomeric nature of these metastable states is related predominantly to the occupation of the neutron $\nu g_{9/2}$ orbital, creating intruder levels in the neutron $\nu$fp-shell. Clearly, if the assigned spin and parities are correct, the $8^-$ and $6^+$ states in $^{66}$Co cannot be populated in $\beta$-decay of the $0^+$ ground state of $^{66}$Fe. Finally, a 471 keV $\gamma$-line was observed in the $\beta$-decay chain of $^{66}$Fe [29], but its placement was not defined.

#### $^{66}$Co

The first decay scheme of $^{66}$Co was presented in [36]. Only four $\gamma$-lines, namely at 471, 1020, 1246, and 1426 keV, were observed. Over a decade later, another experiment was performed, as presented in [4], using the ISOL method, see

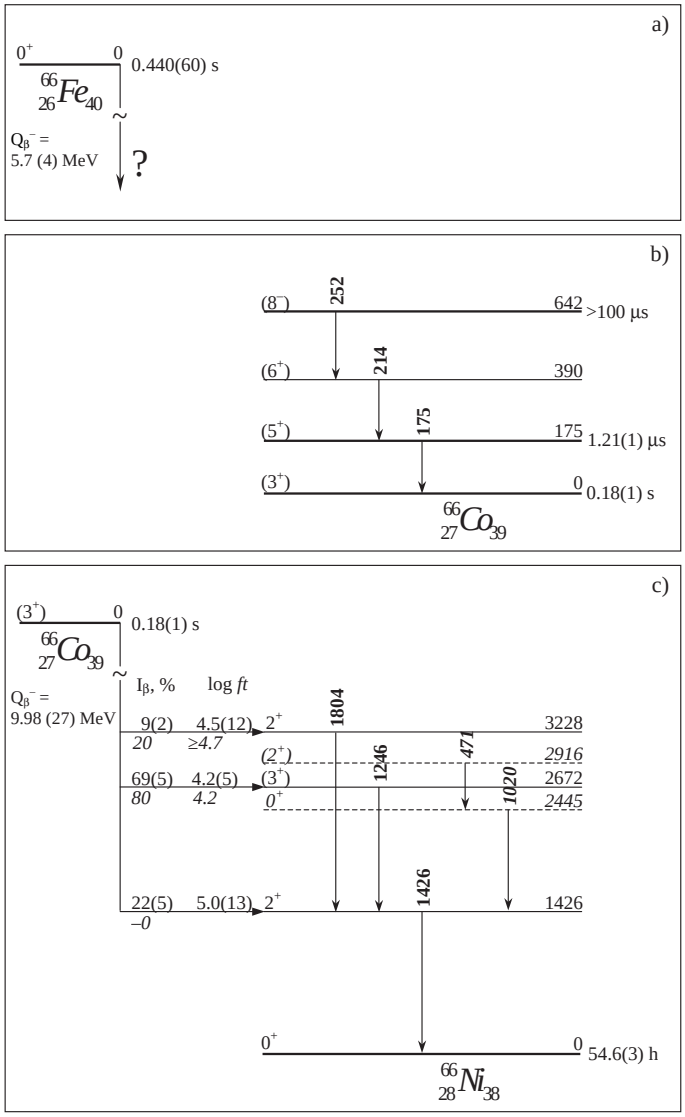


**Figure 2.12:** a) The $\beta^-$-decay half-life of $^{66}$Fe known from [35] and [29]; b) The level scheme of $^{66}$Co as deduced from [28]; c) The decay scheme of $^{66}$Co. The experimental information noted in italic font is taken from [36], while the rest of the data is taken from [4]. Apart from the $\gamma$-transitions at 1426 and 1246 keV, the information from [36] was not confirmed by the study in [4].

section 4.1. Only the 1246 and 1426 keV $\gamma$-transitions were confirmed to exist in the level scheme from [36], with the $\gamma$-lines at 471 and 1020 keV being unobserved, see Fig. 2.12c. A new $\gamma$-line at 1804 keV was assigned to the decay of $^{66}$Co. The $\beta$-decay half-life of 0.18(1) s was obtained. As pointed out in [36], the 471 keV $\gamma$-transition exhibited a larger decay half-life time of 0.4(2) s compared to 0.23(2) s from the same reference for the 1246 and 1426 keV $\gamma$-transitions.

In conclusion, apart from the $\beta$-decay half-life and three $\gamma$-transitions originating from two $\mu$s isomeric states in $^{66}$Co, there is no further information on the decay scheme of $^{66}$Fe. Clearly, there is a need for an experiment on $\beta$-decay of $^{66}$Fe. A similar situation takes place in higher-mass Fe nuclides.

# Chapter 3

# $\beta$-decay studies with highly-segmented HPGe $\gamma$-detectors

## 3.1 $\beta$ decay

### 3.1.1 The concept of $\beta$ decay

Since this work mainly deals with $\gamma$-ray spectroscopy in $\beta$-decay as an experimental tool for nuclear structure studies, let us briefly describe the main concept behind the process of $\beta$-decay.

The binding energy $B(A, Z)$ between all nucleons in a nucleus determines stability of this nuclear system against decay, or, in other words, against transformation into a more stable system:

$$B(A, Z) = \left\{ M\left({}^{A}_{Z}X_{N}\right) - [Z \cdot M_p + (A - Z) \cdot M_n] \right\} \cdot c^2 \tag{3.1}$$

where $M\left({}^{A}_{Z}X_{N}\right)$ is the mass of the nucleus $X$ with $Z$ protons and $N$ neutrons, $A = Z + N$, $M_p$ and $M_n$ are proton and neutron masses, respectively. Stability is described in terms of particular relationships between $Z$ protons and $N$ neutrons, where the charge-independent nuclear force favors $N = Z$ configurations, while the repulsive Coulomb force leads to $N > Z$ systems to account for larger separation between protons. Since the binding energy is negative, the most stable nuclear systems with different combinations of $Z$ protons and $N$ neutrons are at the bottom of the so-called "valley of stability", while less stable systems build its sides. So, the difference in binding energy or, as alternatively called following the Equation 3.1, the mass difference is the driving force for any nuclear transformation, and it is obvious, that the dominant

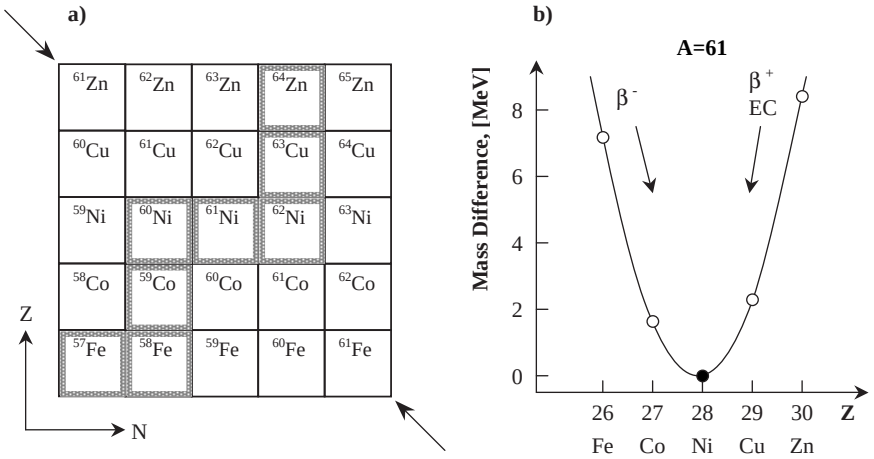


**Figure 3.1:** $\beta$ decay: a) A part of the Chart of the Nuclides around the most stable isotopes of Ni. Heavy boxes indicate stable nuclides; b). The energy parabola for the isobar $A = 61$. For the sake of representation, the difference in binding energy or mass difference is taken relative to the most bound isobar, thus, yielding positive values. $^{61}$Ni is stable, other nuclides are $\beta$-active.

form of radioactive decay is movement directly down the hillsides of the valley. Apart from $\alpha$-decay and spontaneous fission, this corresponds to the process of $\beta$ decay, when the nuclear system corrects its neutron or proton excess by converting a neutron into a proton or a proton to a neutron, respectively. In this process, both $Z$ and $N$ change by one unit, while the total mass number $A = Z + N$ always remains constant. In other words, it corresponds to transitions along an isobar or line of constant $A$. If we take a diagonal slice of the "valley of stability" at any particular $A$ as in Fig. 3.1, the values of the binding energy for different isobars will constitute a parabola, with the lowest point corresponding to the most stable nucleus of given $A$. And there are theoretical grounds for such parabolic behavior, based on the liquid-drop nuclear model. The energy difference between any two neighboring points of the parabola will correspond to the energy released in this form of decay.

To conserve electric charge, the process of converting one type of nucleons to another must involve another charged particle — originally called $\beta$-particle but later shown to be electrons or positrons (antielectrons). This process can occur in three possible ways:

- $\beta^-$ **decay** — In case when for two neighboring isobars

$$M(A, Z) > M(A, Z + 1),$$

the nucleus ${}^A_Z X_N$ is unstable against $\beta^-$ decay, also known as negative $\beta$ or electron (negatron) decay, in which a neutron gets converted into a proton:

$${}^A_Z X_N \longrightarrow {}^A_{Z+1} X'_{N-1} + e^- + \tilde{\nu},$$

involving the creation and emission of a $\beta^-$-particle (an ordinary electron $e^-$) and antineutrino $\tilde{\nu}$.

- $\beta^+$ **decay** — In case when for two neighboring isobars

$$M(A, Z + 1) > M(A, Z) + 2m_e,$$

where $m_e$ is the electron rest mass, the nucleus ${}^A_{Z+1} X_{N-1}$ is unstable against $\beta^+$ decay, also known as positive $\beta$ or positron decay, in which a proton gets converted into a neutron:

$${}^A_{Z+1} X_{N-1} \longrightarrow {}^A_Z X'_N + e^+ + \nu,$$

involving the creation and emission of a $\beta^+$-particle (an antielectron $e^+$) and neutrino $\nu$. $\beta^+$ decay is only possible if the difference in binding energy of the two consecutive isobaric nuclides exceeds a critical value $2m_0c^2 \simeq 1022\ keV$, which is twice the rest mass of an electron. In essence, it is as a threshold energy needed to create an electron–positron pair. The positron is rapidly slowed down within surrounding matter until it has almost no kinetic energy left. Once it inevitably appears near an electron, the process of annihilation takes place when the total mass of both positron and electron is converted into two annihilation photons, each with energy being equal to the electron rest mass of ∼511 keV. To conserve momentum these two photons will be emitted at 180° angle relative to each other.

- **Electron capture (EC)** — This is an alternative mode of decay for nuclei that are unstable to $\beta^+$-decay, and this is the only mode available when the mass difference between two adjacent isobars is less than 1022 keV. So, when for two neighboring isobars

$$M(A, Z + 1) > M(A, Z) + \frac{\varepsilon}{c^2},$$

where $\varepsilon$ is binding energy of an electron in the atom and $c$ is the speed of electromagnetic radiation in vacuum, an electron from one of the shells

may be captured by the nucleus ${}^{A}_{Z+1}X_{N-1}$ and, as a result, a proton gets converted into a neutron:

$$ {}^{A}_{Z+1}X_{N-1} + e^{-} \longrightarrow {}^{A}_{Z}X'_{N} $$

Since the largest overlap between the wave functions of the nucleus and the electrons in the atom is for K-shell electrons, it is more likely that a K-shell electron will be captured, thus giving the process an alternative name *K-capture*. The probability of capture from the less strongly bound higher shells L, M, etc. increases as the decay energy decreases. The loss of an electron from one of the shells leaves a vacancy, which is filled by an electron dropping in from one of the higher, less tightly bound, shells. The energy released in this way often appears as an $X$-ray, or, alternatively, is transferred to one of the electrons and sets it free from the atom as a whole. These monoenergetic electrons, called *Auger electrons*, are usually emitted from atomic orbitals with low binding energies.

It is obvious that in nuclear transformations between two adjacent isobaric nuclear systems neutron-rich unstable nuclei will decay by means of the $\beta^{-}$-decay process and neutron-deficient unstable nuclei will proceed through $\beta^{+}$- or EC decay, as in Fig. 3.1. However, some odd-odd nuclear systems in the middle of the valley of stability may decay by both $\beta^{-}$- and $\beta^{+}$-/EC decay processes when both of the two even-even adjacent isobars have larger absolute value of binding energy due to pairing.

### 3.1.2 Fermi theory of $\beta$ decay

In $\beta^{-/+}$ decay, electron/positron and antineutrino/neutrino are created out of the decay energy according to the relation $m = E/c^2$ and, thus, do not exist inside the nucleus before the decay. The process of $\beta$-decay corresponds to a transition of the nuclear system between two (initial and final) discrete energy states. The final energy state may be a ground state or an excited state of the daughter nucleus, and in the latter case the excitation energy is then removed by emission of $\gamma$-rays or through the processes of internal conversion and pair production. The difference between the initial and final (corresponding to the final state in $\beta$ decay) nuclear mass energies, called the $Q$-value, represents the kinetic energy shared between the $\beta$-particle, the neutrino (or the antineutrino), and negligibly the daughter nucleus. This gives rise to a continuous energy distribution of emitted $\beta$-particles with a characteristic shape as in Fig. 3.2, where the maximum value $E^{max}$, called the end-point energy, corresponds to a decay in which the $\beta$-particle carries away all of the decay energy. Such a distribution has a maximum at $E^{(m)} \approx \frac{1}{3}E^{max}$. Neutrino, proposed by Wolfgang Pauli to explain the shape of $\beta$-particle energy spectrum, and later

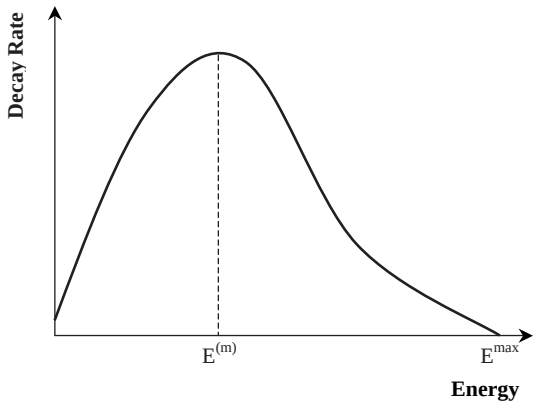


**Figure 3.2:** A schematic representation of characteristic distribution of $\beta$-particle energies.

given its name by Enrico Fermi, is a highly-penetrating radiation represented by a particle with a negligibly-small rest mass.

The whole process is successfully described by the Fermi theory of $\beta$-decay, based on the Pauli neutrino hypothesis. The probability of a transition between the initial and final nuclear states in $\beta$-decay or, in other words, the decay rate is the reciprocal of the mean lifetime of the initial state. As follows from the Fermi theory, the total decay rate is given as

$$\lambda = \frac{g^2\, m_e^5\, c^4\, |M_{fi}|^2}{2\pi^3\, \hbar^7}\, f(Z, E_e^{max}), \tag{3.2}$$

where $g = 0.88 \times 10^{-4}$ MeV·fm$^3$ is the $\beta$-decay strength constant; $m_e$ is the electron rest mass; $c$ is the speed of electromagnetic radiation in vacuum; $\hbar$ is the reduced Plank's constant; $M_{fi}$ is the reduced matrix element for a transition between the initial $\psi_i$ and final $\psi_f$ states interacting through a Hamiltonian $H_{int}$:

$$M_{fi} = \langle \psi_f | H_{int} | \psi_i \rangle \tag{3.3}$$

Finally, $f(Z, E_e^{max})$, known as the Fermi integral, is the integral over all values of momentum $p_e$ of the emitted electron ($\beta$-particle):

$$f(Z, E_e^{max}) = \frac{1}{(m_e c)^3\, (m_e c^2)^2} \int_0^{p_e^{max}} F(Z, p_e)\, p_e^2\, (E_e^{max} - E_e)^2\, dp_e, \tag{3.4}$$

where $Z$ is the number of protons in the nuclear system after the decay and $F(Z, p_e)$ is the so-called Fermi function that corrects for a distortion of the electron wave function due to its interaction with the electrostatic field of the nucleus. There are tabulations of this integral for different values of $Z$ and $E_e^{max}$. An important piece of information for spectroscopists is that for low $Z$ and large end-point energies $E_e^{max}$ the Fermi integral and, thus, the transition probability are fairly well approximated as being proportional to $\sim [E_e^{max}]^5$.

This way, in the expression for the total decay rate in Equation 3.2 there are two distinct components, namely, $M_{fi}$, which represents the interaction between the nucleons in the nuclear system that results in the decay process, and $f(Z, E_e^{max})$, which accounts for the kinematics of the decay products, governed by the requirements of the energy and momentum conservation. Since $\lambda = \ln 2/t_{1/2}$, where $t_{1/2}$ is the half-life of the $\beta$-decaying nuclear system, we get

$$ft_{1/2} = \ln 2 \frac{2\pi^3\,\hbar^7\,c^3}{g^2\,m_e^5\,c^4|M_{fi}|^2} \approx \frac{6000}{|M_{fi}|^2}, \tag{3.5}$$

where the quantity on the left is called the *comparative half-life* or *ft value*. It somehow cancels out the fact that the farther we go from the bottom of the valley of stability, the steeper the hillsides become resulting in higher $Q_\beta$ values, and thus the higher is the probability for the nuclear system to decay resulting in smaller half-life values. So, what we are left with is a pure dependence on the nuclear matrix element representing the degree of the overlap between the wave functions of the nuclear system before and after the decay. Because the half-lives in $\beta$-decay span a huge range of values (from the order of milliseconds to about $10^{15}$ a), what is usually quoted is a common logarithm $\log ft$ ($\log_{10} ft$), where $t_{1/2}$ is always given in seconds. Considering only the overlap between the initial and final wave functions, it would be almost impossible to account for such a huge range of $\beta$-decay half-lives differing by more than twenty orders of magnitude. In fact, the real source of variation in possible half-lives is due to a difficulty to create a $\beta$ particle and a neutrino in an angular momentum state with $l > 0$.

Both the electron and neutrino are fermions with the intrinsic spin $s = \frac{1}{2}\hbar$. Considering the spin coupling between them (total spin $\overrightarrow{S} = \overrightarrow{s_e} + \overrightarrow{s_\nu}$) during the decay process, there are two distinctive possibilities:

- **Fermi decay**, corresponding to the antiparallel coupling of the electron and neutrino spins: $S = 0$;

- **Gamow-Teller decay**, corresponding to the parallel coupling of the electron and neutrino spins: $S = 1$.

### 3.1.3 Allowed and forbidden $\beta$ decays

The most probable $\beta$-decay transitions, called *allowed* transitions, take place when the electron and neutrino carry no orbital angular momentum ($\Delta L = 0$) and, thus, the only change in the total angular momentum of the nuclear system ($\overrightarrow{I} = \overrightarrow{L} + \overrightarrow{S}$) results from the intrinsic spins of the electron and neutrino. This way, $\Delta I = |I_i - I_f| = 0$ *or* 1, where $\Delta I = 0$ and $\Delta I = 0$ *or* 1 correspond to the Fermi $S = 0$ and Gamow-Teller $S = 1$ decays, respectively. The selection rules for the allowed $\beta$-transitions can be stated as follows:

$$\Delta I = 0, 1 \quad \Delta\pi = 0$$

The condition $\Delta I = 1$ cannot be satisfied for the case $I_i = I_f = 0$ when only the Fermi transition can take place. These pure Fermi transitions $0^+ \rightarrow 0^+$ are called *superallowed*, taking place between the so-called *isobaric analogue states* (IAS), which differ only in the interchange between proton and neutron, and thus have analogous wave functions except for the Coulomb effects. A characteristic feature of such IAS multiplets comes from the fact, that, since $\Delta I = \Delta L + \Delta S = 0$, the change in the nuclear isospin $\Delta T = 0$, and, thus, these states will differ only in the values of the isospin projection, constituting a multiplet of states with $T_z$ ranging from $-T$ to $T$.

It is much less probable that $\beta$ particle and neutrino are created in an angular momentum state $l > 0$. E.g., for 1 MeV $\beta$-particle the maximum expectation value of the orbital angular momentum is $\sim 0.04\,\hbar$, corresponding to the separation between the $\beta$ particle and neutrino by a typical nuclear radius of $\sim$6 fm. But if the allowed matrix elements happen to vanish, the only transitions that become possible are those when the $\beta$ particle and neutrino carry away an orbital angular momentum $\Delta L > 0$. Such transitions are called *forbidden*. The decay, that corresponds to $\Delta L \geq n\,\hbar$ where $n$ is the difference in orbital angular momentum between the initial and final nuclear states, is called $n$-th forbidden. Coupling $\Delta S = 0, 1$ and $\Delta L = n$ we get $\Delta I = n-1, n+1$, taking into account the fact that it would be extremely unlikely that the electron and neutrino carry away an orbital angular momentum of $\Delta L > n$ if they can be much easier created in a state $l = n$. If the electron and neutrino are to carry away an odd value $n$ of the nuclear orbital angular momentum, this would require a change in parity of the initial state $\Delta\pi = (-1)^n = -1$. So, the selection rules, e.g, for the first forbidden transitions are

$$\Delta I = 0, 1, 2 \quad \Delta\pi = -1$$

Concerning higher orders of forbiddenness, we must consider the fact the change in the nuclear angular momentum by $\Delta I = 0, n-1$ will satisfy the selection rules for the allowed or lower-order forbidden decays, which are by far much more probable. So, the selection rules, e.g., for the second forbidden transitions

**Table 3.1:** Summary of characteristic log $ft$ values for allowed and forbidden decays.

| Transition | log $ft$ |
|---|---|
| Superallowed | 2.9–3.7 |
| Allowed | 4.4–6.0 |
| 1-st forbidden | 6–10 |
| 2-nd forbidden | 10–13 |
| 3-d forbidden | >15 |

can be stated as

$$\Delta I = 2, 3 \quad \Delta\pi = 0$$

The same considerations are applied for extremely rare third and fourth forbidden transitions. Each degree of forbiddenness is equivalent to a reduction in transition probability by a factor of $\sim 10^4$, corresponding to the increase in the log $ft$ value by $\sim$4 units. The characteristic log $ft$ values for allowed and forbidden decays are summarized in the Table 3.1.

### 3.1.4 $\beta$ decay in the neutron-rich Ni region

It is worth closing this section with a brief discussion on $\beta^-$-decay of the neutron-rich nuclei along and in the close vicinity of the magic $Z$=28 proton shell-closure and from the neighborhood of the semi-magic $N$=40 neutron shell up to the supposedly magic $N$=50 neutron shell gap. The configuration space in terms of the spherical shell-model level sequence can be limited from $f_{7/2}$ to $g_{9/2}$ for both protons and neutrons as in Fig 3.3a. This representation, being stuffed with various possible transitions, is a generalization for the whole range of nuclei in this region, whereas in reality each nuclide has one or two major $\beta$-decay paths. Possible $\beta^{+/-}$-decay transitions in both neutron-deficient and neutron-rich Fe isotopes not very far from the bottom of the valley of stability are shown in Fig 3.3b in terms of spherical shell-model level sequence.

At this point it is worth mentioning the key issues that influence the transition probability in $\beta$-decay:

- The degree of overlap between the initial and final wave functions: it is higher for higher angular momentum states. In our region of interest this implies that, e.g., $\nu$f $\rightarrow$ $\pi$f must be more probable than $\nu$p $\rightarrow$ $\pi$p. Additionally, the wave functions with different number of nodes have a poor degree of overlap and, thus, the transitions 1f(2p)$\rightarrow$2p(1f) are much less probable than the transitions 1f(2p)$\rightarrow$1f(2p) provided that the latter channels are available, see Fig 3.4b.

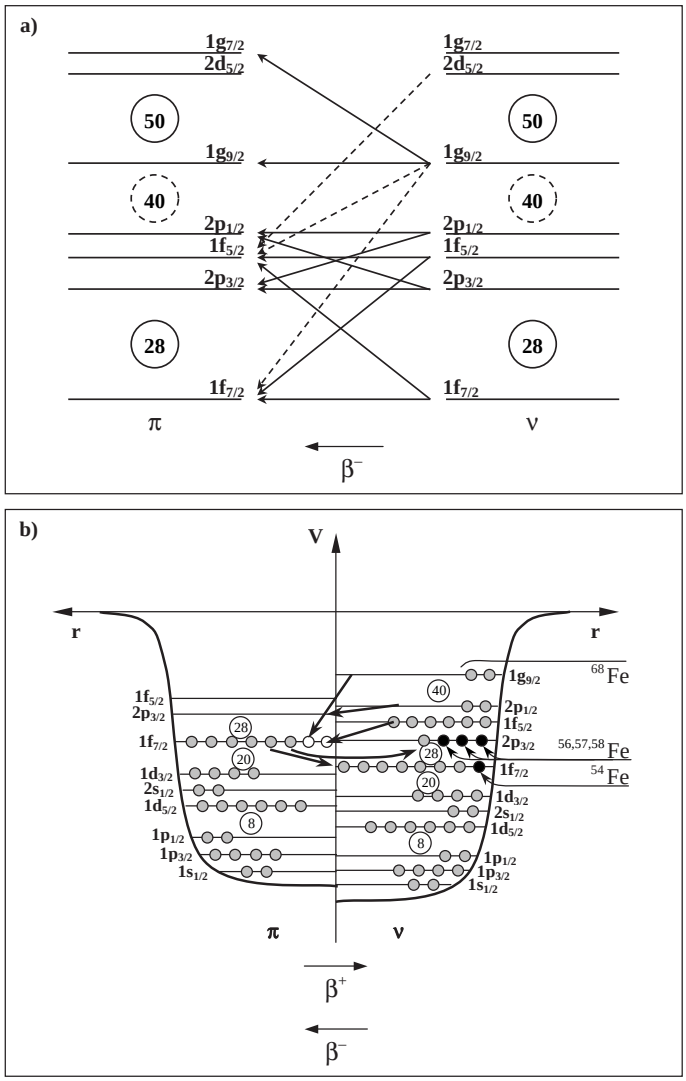


**Figure 3.3:** a). A schematic representation of possible $\beta$-decay transitions in neutron-rich nuclei from the Ni region. The solid and dashed arrows represent the allowed and forbidden transitions, respectively. b). A schematic representation of $\beta^{+/-}$-decay transitions in Fe isotopes between spherical single-particle levels in a realistic potential. $^{54,56,57,58}$Fe isotopes are stable.

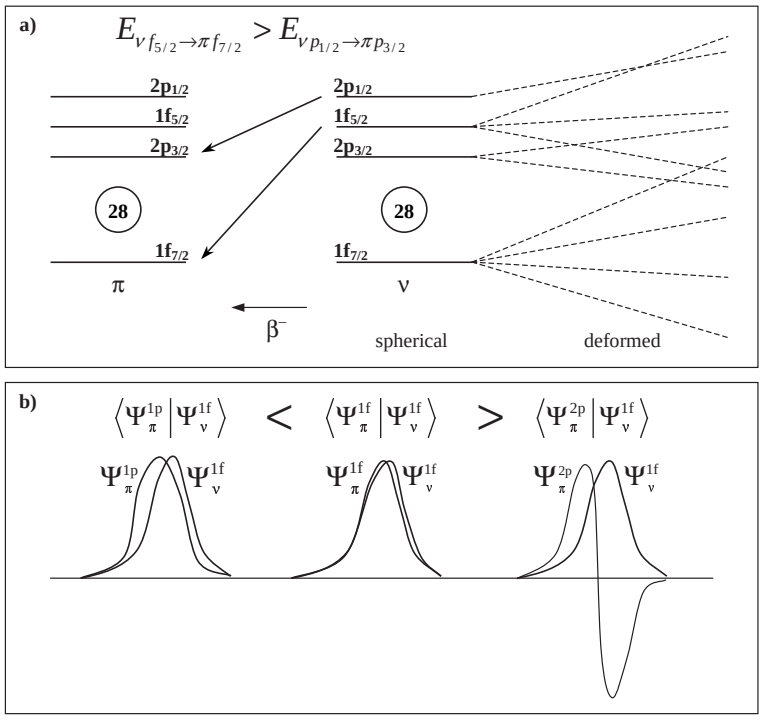


**Figure 3.4:** A schematic representation of various factors that influence $\beta$-decay transition rate.

- The energy difference between the initial and final states: as already mentioned earlier, the Fermi integral and, thus, the transition probability scale as the fifth power of the decay energy to a fairly good degree of approximation. The result is obvious: $\beta$-decay transitions between the levels with higher energy difference are more probable. This means that $\nu 1f_{5/2} \rightarrow \pi 1f_{7/2}$ must be more dominant than $\nu 2p_{1/2} \rightarrow \pi 2p_{3/2}$, see Fig 3.4a.

- The occupancies of the levels that are available for transition: higher occupancies of the initial states and lower occupancies of the final states result in higher transition probabilities.

The IAS in the daughter nuclides are not available in this region, and, therefore, the Fermi transitions are not possible at all. It is rather safe to

suggest that allowed Gamow-Teller transitions must be predominant for nuclides not very far away from the bottom of the valley of stability. Indeed, as can be seen from various experimental [6][7][26][4][5][10][11][19] and predicted [37][38][39] decay schemes, the nuclei at and in the immediate vicinity of the $Z$=28 proton shell-closure and well before the $N$=50 neutron shell gap undergo by-far predominant fast high-energy Gamow-Teller transitions involving simple shell-model configurations $\nu 1f_{5/2,7/2} \rightarrow \pi 1f_{5/2,7/2}$, $\nu 1g_{9/2} \rightarrow \pi 1g_{7/2,9/2}$, and $\nu 2p_{1/2,3/2} \rightarrow \pi 2p_{1/2,3/2}$. Possible first-forbidden decay channels are mainly due to transitions $\nu 1g_{9/2} \rightarrow \pi 1f_{7/2}$ and, when crossing the $N$=50 shell gap in nuclei with $Z$ >28, $\nu 2d_{5/2} \rightarrow \pi 1f_{5/2}$. It is only when matrix elements for a large variety of allowed transitions happen to vanish that these forbidden decay channels start playing an important role even when the initial and final wave functions have different number of nodes. It must be realized however, that the sequence of levels strongly depends on various aspects of nuclear structure involved. This can be due to residual and pairing interactions that may lower or raise certain levels or due to a presence of deformation that removes the degeneracy on orbital momentum and drastically alters the subsequent ordering of states. In the latter case, in the presence of deformation each spherical shell-model state becomes split into several Nilsson states bringing different values of total angular momentum into play, see Fig 3.4a. As a result of all these effects, certain decay channels may be completely blocked, while other channels may become available.

Nevertheless, all those simple considerations given above, are explicitly present in any, whatever sophisticated, phenomenological calculations, and must be firmly set in the experimentalist's mind. As a vivid example, we can take a look at the most dominant decay channels in the nuclei from our region of interest. In Ni and Cu isotopes, having 28 and 29 protons, respectively, the $Z$=28 proton shell-closure is completely filled, and, thus, in, e.g., $^{68-74}$Ni [6][7] and the corresponding Cu isobars [10][11], the most dominant decay channel is the Gamow-Teller $\nu 2p_{1/2} \rightarrow \pi 2p_{3/2}$ transition. Starting from $^{70}$Ni, there is an additional available decay channel, albeit less energetically-favorable but anyway existing, which is the allowed $\nu 1g_{9/2} \rightarrow \pi 1g_{9/2}$ transition. In Co isotopes, having 27 protons, there is one hole in the $\pi 1f_{7/2}$ level, and, thus, the most favorable decay channel in, e.g., $^{66,67,68}$Co [26][4][5] is the Gamow-Teller $\nu 1f_{5/2} \rightarrow \pi 1f_{7/2}$ transition. Concerning forbidden-decay transitions in our region of interest, it is rather obvious to suggest that due to a presence of the unique-parity level $1g_{9/2}$ above the opposite-parity fp shell there is a possibility for the first-forbidden decay channel $\nu 1g_{9/2} \rightarrow \pi 1f_{7/2}$. As an example, due to an admixture of the $\pi 1f_{7/2}^{-1}$ ground and $\pi 1f_{7/2}^{-1} \nu 2p_{1/2}^{-2} \nu 1g_{9/2}^{2}$ excited configurations in $^{67}$Co, there is an additional weak $\nu 1g_{9/2} \rightarrow \pi 1f_{7/2}$ $\beta$-decay transition with $I_\beta$=3(3)% and $\log ft$=6.3, populating the 13.4 $\mu$s isomer at 1007 keV with the $\nu 2p_{1/2}^{-2} \nu 1g_{9/2}^{1}$ configuration in $^{67}$Ni [5]. It is worth adding here, that

according to the calculations in [37][38], when crossing the supposedly-magic $N$=50 neutron shell-gap in, e.g., Ni and Cu isotopes, the first-forbidden transitions start providing a dominant contribution to the total $\beta$-decay half-lives of these nuclides. As a result, these calculations predict a rather substantial reduction in the neutron-emission probabilities for these and neighboring nuclei with $A \geq$80 lasting for a certain number of isotopes.

Further below the $Z$ =28 proton shell closure, as, e.g., in $^{61-69}$Mn isotopes ($Z$ =25) [19], the most favorable $\beta$-decay channel is again the allowed Gamow-Teller $\nu 1f_{5/2} \rightarrow \pi 1f_{7/2}$ transition. It is somehow obvious to suggest the same decay path for our nuclei of interest — the neutron-rich $^{65,66,67}$Fe. But, as discussed in the previous chapter, the experimental information is rather scarce, which implies that one must be fully open-minded before having an at least partial level scheme at hand. To reiterate what was already mentioned and shown in Fig 3.4a, the whole picture in terms of spherical shell-model level sequence may drastically change with a possible onset of deformation. This can be a collective phenomenon as in many nuclei far from both proton and neutron closed shells or a consequence of single-particle configurations leading to residual and pairing interactions in nuclei near closed shells. Special attention must be drawn to the $^{67}$Fe isotope where the onset of deformation may already become quite significant. Additionally, it is bound to have at least one neutron in the $\nu 1g_{9/2}$ level and, coupled with neutrons in the negative-parity levels of the fp-shell as in many neighboring nuclides, this may easily result in configurations for both mother and daughter nuclei that produce isomeric transitions. Next to this, if for some reasons the allowed decay channels become hampered in such configurations, this may easily enhance the transition probability of the first-forbidden $\nu 1g_{9/2} \rightarrow \pi 1f_{7/2}$ channel.

Unfortunately, any further discussion on $\beta$-decay of $^{65,66,67}$Fe is bound to end up as pure speculations if not supported by any calculations like, e.g., in [37][38][39][40]. In essence, these models are based on the Fermi theory of $\beta$-decay with various extensions and can predict half-lives and even single-particle states. All of these models are phenomenological and need proper experimental input. But, as shown in the next chapter, due to experimental difficulties in selective production of neutron-rich isotopes of the refractory Ni, Co, and especially Fe elements, the existing experimental information is scarce. Thanks to the innovative and rather unique LISOL facility, many of the neutron-rich Ni and Co isotopes were successfully produced and studied in $\beta$-decay experiments. In the Ni region, the neutron-rich nuclei with $Z$ >28 are easier to produce and, therefore, their isotopes are studied in much more detail at already the $N$=50 shell gap and even beyond. Now, it is the right time to perform consistent and systematic $\beta$-decay studies of the neutron-rich nuclei below the $Z$=28 proton shell-gap.

## 3.2 Choice of detectors for $\beta$-decay $\gamma$-ray spectroscopy

By $\gamma$ radiation we call an electromagnetic radiation which is emitted when the nuclear system undergoes a transition from an excited state to another state of lower energy. The radiated $\gamma$-ray carries away an energy which is equal to the energy difference between the initial and final nuclear states. Additionally, $\gamma$-radiation can be created in the process of annihilation, as described in paragraph 3.1.1. Since the $\gamma$-transitions are by far the main source of information on any changes in nuclear structure, this can be most successfully done by means of $\gamma$-ray spectroscopy using $\gamma$-radiation detectors. This requires complete knowledge on how $\gamma$-radiation interacts with matter and what are the most efficient ways of detecting the full energy of $\gamma$-rays.

### 3.2.1 Interaction of $\gamma$ radiation with matter

To register the full energy of a $\gamma$-ray implies that it must be fully absorbed within the detector material. Since $\gamma$ radiation has electromagnetic nature, it is obvious, that $\gamma$-rays will interact with "charge-holders" of matter, like, e.g., electrons of the atoms, atoms as a whole, or charges within nuclei. This will result in the excitation and ionization of the atoms of the material. This way, it is expected that $\gamma$-ray attenuation and absorption as measures of the degree of interaction of $\gamma$-radiation with matter will depend on the atomic number of the detector material and the $\gamma$-ray energy. There are three main mechanisms of interaction of $\gamma$-radiation with matter:

- **Photoelectric absorption**, when the $\gamma$-ray photon interacts with one of the bound electrons in an atom. The full energy of the $\gamma$-ray $E_\gamma$ is then transferred to this electron, which gets ejected with a kinetic energy

$$E_e = E_\gamma - E_b, \tag{3.6}$$

  where $E_b$ is the binding energy of this electron in its shell. The atom is left in an excited state with an excess energy of $E_b$ and recovers its equilibrium through emission of the characteristic $X$-rays and/or release of Auger electrons, as already mentioned in the paragraph 3.1.1. The emitted $X$-rays will then undergo the photoelectric absorption or, if the original interaction takes place close to the detector surface, they may completely escape from the detector. The photoelectric absorption cross-section depends on the atomic number $Z$ and $\gamma$-ray energy $E_\gamma$ in the following manner:

$$\sigma_{pe} \propto \frac{Z^n}{E_\gamma^m}, \tag{3.7}$$

where $n$ and $m$ are within a range of ∼3–5. The best quoted functions are $Z^5/E_\gamma^{3.5}$ and $Z^{4.5}/E_\gamma^3$.

- **Compton scattering**, when the $\gamma$-ray photon interacts with one of the electrons of an atom, transferring only part of its original energy. The energy imparted to the recoil electron is given by the following equation:

$$E_e = E_\gamma - E'_\gamma - E_b = E_\gamma \left\{ 1 - \frac{1}{(1 + E_\gamma[1 - \cos\theta]/m_e c^2)} \right\} - E_b, \quad (3.8)$$

where $E'_\gamma$ is the the energy of the $\gamma$-ray photon after the interaction and $\theta$ is the scattering angle. At 0° scattering angle (direct forward scattering) no energy is transferred to the electron, while 180° angle (backscattering) corresponds to the maximum fraction of $\gamma$-ray energy that can be absorbed in one incidence. The resultant $\gamma$-ray photon may undergo yet another instance of Compton scattering until it is finally absorbed through the photoelectric effect or it may completely escape the detector. The absorption cross-section in this process depends on the atomic number $Z$ and $\gamma$-ray energy $E_\gamma$ in the following manner:

$$\sigma_{cs} \propto \frac{A}{Z} \cdot \frac{1}{E_\gamma}, \quad (3.9)$$

where $A$ is the atomic mass of the absorber material. Since the ratio $A/Z$ changes only fractionally throughout the periodic table, the Compton scattering cross-section is almost independent of the atomic number of the detector material.

- **Pair production**, when the $\gamma$-ray photon with an energy of at least two electron rest-masses interacts with an atom as a whole. The interaction takes place within the Coulomb field of the nucleus, resulting in the creation of an electron-positron pair. This way, the $\gamma$-ray energy is converted into the rest-mass and kinetic energy of the created particles. As described in the paragraph 3.1.1, the positron annihilates with an electron and their rest-mass energy is converted into two ∼511 keV $\gamma$-rays which are emitted in the opposite direction relative to each other. The net kinetic energy imparted to both the electron and positron is

$$E_e = E_\gamma - 2m_e c^2 \quad (3.10)$$

The two 511 keV annihilation $\gamma$-rays, representing the term $2m_e c^2$, will be absorbed through the processes of Compton scattering and photoelectric effect or they can escape independently from the detector. The cross-section for this process depends on $Z$ and $E_\gamma$ in the following manner:

$$\sigma_{pp} \propto Z^2 f(Z, E_\gamma), \quad (3.11)$$

where $f(Z, E_\gamma)$ represents an additional continuously increasing dependence (mostly on the $\gamma$-ray energy) that accounts for higher probability of this process to take place at higher energies.

The degree of attenuation and absorption by these processes within the material with the atomic number $Z$, atomic mass $A$, and density $\rho$ as a function of the $\gamma$-ray energy can be expressed in terms of linear attenuation and absorption coefficients:

$$\mu_{at} = \rho \frac{N_A}{A}(\sigma_{pe} + \sigma_{cs} + \sigma_{pp} + \sigma_{es}) \tag{3.12}$$

$$\mu_{ab} = \rho \frac{N_A}{A}(f_{pe}\sigma_{pe} + f_{cs}\sigma_{cs} + f_{pp}\sigma_{pp}), \tag{3.13}$$

where $N_A$ is the Avogadro's number and $\sigma_{es}$ represents an additional loss of $\gamma$-ray intensity by elastic scattering. Here, the linear attenuation coefficient $\mu_{at}$, as a measure of reduction in $\gamma$-ray intensity, defines the probability that a $\gamma$-ray of a particular energy will interact with a given material, while the linear absorption coefficient $\mu_{ab}$, as a measure of reduction in energy, also takes into account the fact that only a certain part of the $\gamma$-ray energy will be absorbed in the interaction, expressed by the factors $f$. The intensity $I_0$ of $\gamma$-ray photons of a given energy, passing through an absorbing material of a thickness $t$ and with a linear attenuation coefficient $\mu$, is reduced exponentially and the transmitted intensity is then given by

$$I = I_0 e^{-\mu t} \tag{3.14}$$

The linear attenuation coefficient of germanium, as one of the best detector materials in $\gamma$-ray spectroscopy, is given in Fig. 3.5. As expected, the process of photoelectric absorption is dominant for low-energy $\gamma$-rays — in germanium it is up to an energy of ∼150 keV, the process of pair production starts dominating at very high energies — from ∼8 MeV in germanium, with the Compton scattering being the main interaction process for a wide energy range in between.

### 3.2.2 Interaction of charged particles with matter

Charged particles interact with matter mainly through Coulomb interaction with the charge of the orbital electrons within the atoms of the absorbing material. By interacting simultaneously with many electrons the charged particle loses its energy by exciting and ionizing the atoms in the close proximity to its path. The rate of this collisional or, alternatively, impact-ionization energy loss is described by the Bethe formula, which has the following form for fast

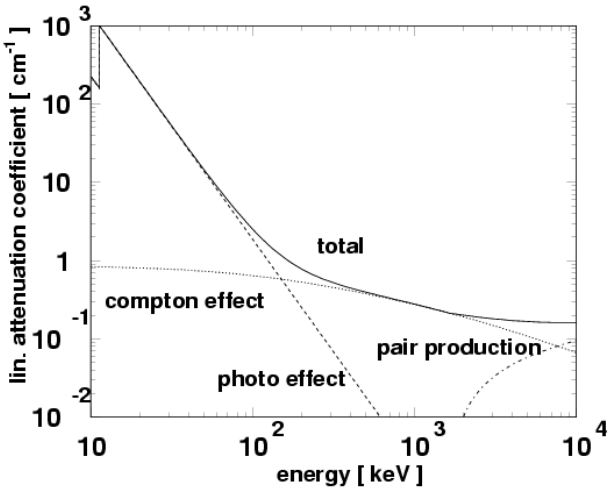


**Figure 3.5:** The linear attenuation coefficient of $\gamma$-rays in germanium.

electrons:

$$-\left(\frac{dE}{dx}\right)_i = \frac{2\pi e^4 nZ}{m_e v^2} \times$$
$$\left[\ln\frac{m_e v^2 E}{2I^2(1-\beta^2)} - (2\sqrt{1-\beta^2} - 1 + \beta^2)\ln 2 + (1-\beta^2) + \frac{1}{8}(1-\sqrt{1-\beta^2})^2\right], \tag{3.15}$$

where $v$ is the velocity of the primary electron; $m_e$ is the electron rest mass; $e$ is the electronic charge; $Z$ is the atomic number of the absorber atoms; $n = \rho\frac{N_A}{A}$ is the number of absorber atoms per unit of volume, where $N_A$ is the Avogadro's number, $\rho$ is the density of the absorber material, and $A$ is the atomic mass of the absorber atoms; $I$ is the average excitation and ionization potential of the absorber atoms; $\beta = \frac{v}{c}$ with $c$ being the speed of electromagnetic radiation in vacuum.

In contrast to heavy charged particles, such as $\alpha$-particles, light charged particles like electrons may also lose their energy through radiative processes. The major component of such losses is Bremsstrahlung[1], which is an electromagnetic radiation produced by the interaction of fast electrons with the

[1] *Bremsstrahlung* is a German word meaning "slowing-down radiation".

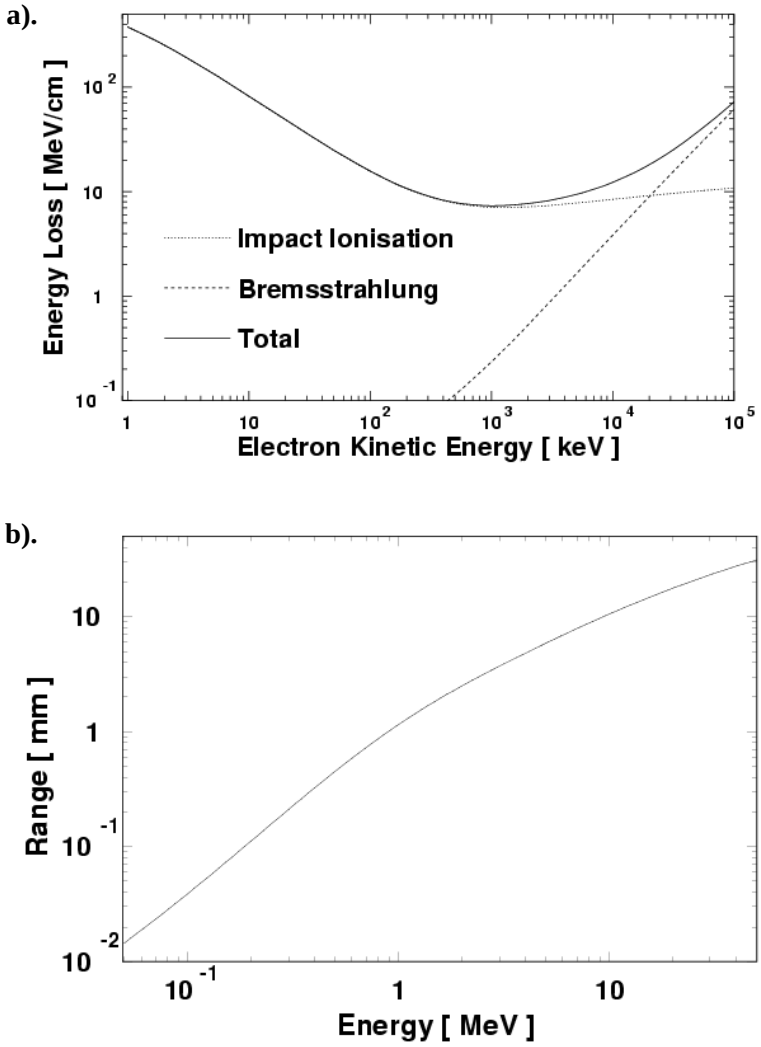


**Figure 3.6:** a) Energy loss of electrons in germanium; b) Mean range of electrons in germanium. (The *mean range* is defined as as the absorber thickness that reduces the intensity of charged particles to one-half of its initial value.) Both figures are taken from [41].

Coulomb field of a nucleus in the absorbing material and can be emitted from any position along the electron track. It arises from a simple fact that a charged particle must radiate energy when accelerated — in this case it is the deflected electron. The rate of this radiative energy loss is given by

$$-\left(\frac{dE}{dx}\right)_r = \frac{4e^4 nZ(Z+1)E}{137 m_e^2 c^4}\left[\ln\frac{2E}{m_e c^2} - \frac{1}{3}\right] \tag{3.16}$$

The total linear energy loss for electrons is given as the sum of the impact-ionization and radiative losses:

$$-\left(\frac{dE}{dx}\right)_t = -\left[\left(\frac{dE}{dx}\right)_i + \left(\frac{dE}{dx}\right)_r\right] \tag{3.17}$$

The ratio between these two corresponding components is given approximately by

$$\frac{(dE/dx)_r}{(dE/dx)_i} \cong \frac{EZ}{700}, \tag{3.18}$$

where $E$ is in units of MeV. As can be seen, for electrons of typical energies of a few MeV the radiative losses represent only a small fraction of the total energy loss, see Fig. 3.6.

### 3.2.3 Choice of detectors

The primary electrons and positrons, being $\beta^{-/+}$-particles or produced through various mechanisms of interaction of $\gamma$-radiation with matter, continuously lose their kinetic energy in the detector absorber material through the impact-ionization and radiative processes by transferring it to the secondary electrons of the absorber atoms. This results in the excitation of an electron from the valence band and its elevation to the conduction band or levels just below, thus leaving a hole behind and creating the so-called electron-hole pair. This brings two distinctive options of measuring the energy of the incident $\beta$-particle or $\gamma$-ray photon:

- By the scintillation process in insulator materials with a characteristic band-gap (the energy gap between the valence and conduction bands) up to ∼10 eV. In this process, the energy given to the secondary electron may not be sufficient enough to elevate it all the way through the band-gap, but rather to an extra band just below and continuous with the conduction band. This way, the electron just below the conduction band and the hole in the valence band will remain electrostatically attracted to each other as an entity called an exciton until the de-excitation process takes place, when the electron falls back to the valence band and releases its excitation energy by emitting electromagnetic radiation. Now, if this

radiation is in, or rather near, optical wavelengths (naturally or through the use of scintillation activator impurities) it can be detected by a light-measuring device, such as photomultiplier, to provide the output detector signal. However, scintillation detection is subject to a large variety of different statistical and intrinsic uncertainties, such as disproportionality of the number of emitted photons to the number of created electron-hole pairs and non-linearity in conversion of the exciton energy to the photon energy, respectively, resulting in an overwhelming non-linearity and uncertainty of the detector response. This is the basis behind the operation of any scintillation detector. The most prominent examples of scintillation materials are sodium/caesium iodide(telluride) NaI(Te)/CsI(Te), caesium/calcium/barium fluoride CsF/$CaF_2$/$BaF_2$, bismuth germanate or BGO $Bi_4Ge_3O_{12}$, and cadmium tungstate $CdWO_4$.

- By using semiconductor material with a characteristic band-gap of ∼1 eV and applying an external electric field to collect the created charge of secondary electrons/holes. Because of a by-far smaller band-gap of semiconductors, the energy imparted by the primary electron to the secondary electron will be large enough for the latter one to be elevated even from the deep energy levels well below the valence band into the energy levels well above the base of the conduction band. Now, a strong and homogeneous electric field applied across the semiconductor material will prevent the excited secondary electrons from falling back into the valence band, and, instead, the charge of all secondary electrons/holes will be collected at the corresponding electrodes. This way, the amount of collected net charge $Q_n$ is given by the number of created electron-hole pairs $n_{e-h}$, which is proportional to the fully absorbed kinetic energy of the primary electron (positron) $E^e_{abs}$:

$$Q_n \propto n_{e-h} = \frac{E^e_{abs}}{\epsilon_{e-h}}, \tag{3.19}$$

where $\epsilon_{e-h}$ is the energy needed to create one electron-hole pair (e.g., 3.62 eV in silicon, 2.96 eV in germanium). Evidently enough, the smaller band-gap means smaller $\epsilon_{e-h}$, which results in a higher number of electron-hole pairs $n_{e-h}$ and, thus, in a higher precision with which the absorbed energy can be measured. On the other hand, a too small band-gap will result in a higher probability of thermal excitations. As a consequence, to reduce the detector leakage current, the detector material may need substantial cooling. To fully sustain such a proportionality between the collected net charge and absorbed energy, it is extremely vital that the charge-carriers (secondary electrons and holes) be not trapped by various impurities within the detector material. This implies the use of materials with a very high purity and as perfect as possible

cristalline state. The most suitable semiconductor materials for nuclear spectroscopy are silicon Si, germanium Ge, cadmium telluride CdTe, mercury/lead iodide $HgI_2/PbI_2$, gallium arsenide GaAs, bismuth sulfide $Bi_2S_3$, gallium/cadmium selenide GaSe/CdSe, aluminum antimonide AlSb.

To summarize comparatively for semiconductor and scintillator detectors, there are several requirements to be addressed when choosing the right detector:

- Proportionality of the detector output to the absorbed energy of the incident $\beta$-particle or $\gamma$-ray photon: high-purity semiconductor detectors with the linear dependence of the collected net charge on the absorbed energy, compared to the scintillation detectors with a substantially non-linear detector response, are by far much more suitable;
- Good efficiency, i.e high absorption coefficient: the scintillation $\gamma$-detectors are up to $\sim$10 times more efficient than the semiconductor $\gamma$-detectors;
- Good energy resolution: at 1332 keV $\gamma$-ray energy a standard sodium iodide detector has a poor energy resolution of $\sim$80 keV compared to a good resolution of $\sim$2 keV of a typical high-purity germanium detector;
- Easy mechanism of collecting the energy information: it is much easier to collect charge in case of semiconductor detectors rather than light in case of scintillation detectors;
- Fast detector response: collection of light in transparent scintillator materials compared to collection of charge carriers drifting under the influence of an external electric field in semiconductor materials indisputably results in more precise timing information;
- Good stability over time, temperature, and operating parameters: stability of scintillation detectors is subject to changes in ambient temperature, operating parameters, such as high-voltage, compared to a good stability of semiconductor detectors;
- Reasonable cost: semiconductor detectors are very much costly;
- Reasonable size: scintillation detectors can be much more compact compared to, e.g., germanium semiconductor detectors, which require installation of a liquid-nitrogen dewar for cooling.

It is clear that in $\gamma$-ray spectroscopy the whole comparison boils down to the choice between high-efficiency, fast-timing-response, low-cost but bad-resolution scintillation detectors and high-resolution but low-efficiency, mediocre-timing-response, high-cost semiconductor detectors. When a relatively large

number of $\gamma$-transitions must be identified, the resolution becomes almost the main factor and therefore most of $\gamma$-spectrometers make use of semiconductor detectors. The only drawback is a relatively small efficiency and especially for high energy $\gamma$-rays, but, as shown later in this work, there is an arduous but accomplishable way to successfully tackle this problem. When detection efficiency is more important than resolution and especially for high-energy $\gamma$-rays, scintillator detectors can be successfully used: in $\beta$-decay to obtain full transition probabilities, e.g., using the so-called Total Absorption Gamma Spectrometer [42], in high-energy Coulomb excitation to study giant resonances, or in numerous $\gamma$-spectrometers as charged-particle detectors and anti-Compton shielding. Additionally, scintillator detectors with ultra-fast timing response are successfully applied in $\gamma$-ray spectroscopy for measuring lifetimes of nuclear states [43].

From the choice of available semiconductor materials, taking into account all major criteria, germanium represents the best option as a material for semiconductor $\gamma$-radiation detector. It has the lowest band-gap, which implies the best resolution, a relatively high atomic number and high density, which means relatively high attenuation and absorption coefficients, the highest mobility of both electrons and holes, which results in the best charge collection and less requirements for operating bias voltage. But it also brings along some huge disadvantages to deal with, such as a need for encapsulation due to the hydrophilic nature of the crystal and a strong requirement for extremely low impurity concentrations, which altogether results in a very high cost, an unique requirement for operation at very low temperature due to the small band-gap, which means that the detector will be quite large in size and will require an additional degree of proper handling. Even though there is great deal of research aimed at a relatively easy production of alternative semiconductor materials with comparable properties, germanium is by far a truly unique material for high-resolution $\gamma$-radiation spectroscopy.

For registration of $\beta$-particles, both semiconductor and scintillator detectors can be used with choice criteria being essentially the same as those for $\gamma$-registration. When energy resolution is of primary importance then semiconductor materials again represent the best option. Conversely, if $\beta$-detector signals are needed only as triggers in $\beta\gamma$-coincidences, scintillator detectors with fast timing response are a much better choice.

## 3.3 β-delayed γ-ray spectroscopy with highly-segmented detectors

### 3.3.1 Nuclear-structure studies in β-decay experiments

The goal of $\beta$-decay experiments aimed at nuclear-structure studies is to register the $\gamma$-transitions following the $\beta$-decay of a nucleus of choice. This means that we must be able to measure rather efficiently the energy of the emitted $\gamma$-rays and register at least a part of the $\beta$-particle energy. Through $\beta$-$\gamma$ and $\gamma$-$\gamma$ coincidences we can establish nuclear level schemes and through time behavior of $\beta$-gated $\gamma$-transitions we can extract half-lives of nuclei of interest. If full energy of $\beta$-particles can be registered, $Q_\beta$ values can be obtained from end-point energies of the $\beta$-particle energy spectrum. This may require additional $\gamma$-energy-gated $\beta$-$\gamma$-coincidences. The final most difficult step is to extract $\gamma$-ray intensities, $\beta$-branching ratios, $\log ft$ values and assign spins and parities to established states of the level scheme. This must be done in conjunction with nuclear-structure considerations.

### 3.3.2 The optimal β-γ-detection set-up

Let us now briefly describe how an optimal $\beta$- and $\gamma$-radiation detection set-up for $\beta$-decay experiments should look like. Optimal means having the highest efficiency of both $\beta$- and $\gamma$-registration that it can possibly deliver but, on the other hand, being rather simple to use and having a configuration that would be most suitable for $\beta$-delayed $\gamma$-ray spectroscopy.

Obviously, a very important requirement is that timing information of registered $\beta$-particles and $\gamma$-rays be as precise as possible in order to establish reliable $\beta\gamma$-coincidences. $\beta$ particles, being physical precursors of subsequent $\gamma$-ray cascades, usually constitute by far smaller statistics in corresponding $\beta$-detectors compared to that of $\gamma$-rays from $\gamma$-detectors. Additionally, commonly-used scintillator detectors for $\beta$-particle registration allow to achieve a much more precise timing information. Therefore, the signals from $\beta$-detectors must be considered as triggers for possible $\beta\gamma$-coincidences. But the main emphasis must be made on the detection of both types of radiation with a few simple requirements to meet:

- To create a point-like source of radiation of interest. This will help to avoid an unwanted decrease in absolute efficiencies and reduce the uncertainty on the geometrical solid-angle coverage of the detectors and, thus, remove an undesirable systematic error in the absolute efficiencies of both $\beta$- and $\gamma$-detectors.

- Since $\beta$-particles have a relatively short range in dense materials in comparison to $\gamma$-rays, the $\beta$-detectors must be placed first around the source

of radiation. This immediately necessitates the use of rather thin and compact $\beta$-detectors to avoid any additional attenuation of $\gamma$-rays passing through them. On the other hand, this should be done without any substantial trade-off in $\beta$-registration efficiency. It is easily achievable by means of thin plastic scintillator or semiconductor $\Delta$E $\beta$-detectors. This way, only a part of the $\beta$-particle kinetic energy will be registered in such detectors. In case when the total $\beta$-particle energy needs to be measured, a thick $\beta$-detector or rather a $\Delta$E-E telescope must be introduced. Such a telescope, which can also be used to register other charged-particles, such as protons in the proton- and two-proton-decay, or any other additional detectors, such as neutron detectors, should not be placed between the source and a $\gamma$-detector but rather separately.

- Both $\beta$- and $\gamma$-detectors must be placed as close as possible to the source to get maximum efficiencies.

- To arrange an exact geometry: i) all detectors must be centered with respect to the source (this would correspond to the maximal and more precise geometrical efficiency); ii) both $\beta$- and $\gamma$-detectors should better be aligned relative to each other and the source. Here, the latter condition arises from the simple fact that a $\beta$-particle can be incident on a $\gamma$-detector, and, having a sufficient energy, it can easily penetrate through the end-cap and dead layer of this detector. As a result, the $\gamma$-detector signal may represent the energy of the remaining $\beta$-particle and/or possible associated Bremsstrahlung radiation summed together with a partial or full energy of an incident $\gamma$-ray. There are three solutions to this problem: i) to put a rather thick bulk of dense material between the $\gamma$- and $\beta$-detectors to fully stop all incoming $\beta$-particles, but that again would mean a noticeable degree of absorption of $\gamma$-rays in such material and an unjustified decrease in $\gamma$-ray efficiency due to a farther position of the $\gamma$-detector from the source; ii) to use the $\beta$-detector as a veto detector to dismiss such $\beta$-$\gamma$-coincidences; iii) to distinguish between $\gamma$-detector signals generated by $\beta$-particles and/or $\gamma$-rays, thus introducing additional requirements to the $\gamma$-detectors discussed later.

- To arrange multi-layer shielding against natural radioactivity and cosmic background radiation and possibly other sources of background related to the beam production and transportation, like, e.g., $X$-rays, Bremsstrahlung, neutrons, fast particles. The layers of shielding against background $\gamma$-radiation and subsequent $\gamma$-induced $X$-rays can be arranged either as a passive shielding made of a thick, dense, high-$Z$ absorbing material or an active shielding constructed out of several low-resolution but high-efficiency scintillator detectors, such as, e.g., BGO. Signals from an active shielding detector can be used as veto triggers to

discard any coincident signals from its corresponding main $\gamma$-detector. This corresponds not only to the situations when background $\gamma$-rays pass through the shielding detector leaving part of their energy there and then get finally absorbed in the main detector, but also to very often cases when $\gamma$-rays from the source of interest get partially absorbed in the main detector finally escaping from it and leaving the rest or a part of their energy in the shielding detector.

- Finally, to install as many and efficient $\beta$- and $\gamma$-detectors as possible in configuration of interest.

It is rather clear that with an obvious emphasis on the detection efficiency in each of the given steps a final optimal configuration corresponds to a close-geometry $\beta$-$\gamma$-detection set-up.

### 3.3.3 The main experimental challenges in $\gamma$-radiation detection in the context of $\beta$-decay experiments

From the description of a common optimal $\beta$-$\gamma$-detection set-up for $\gamma$-radiation spectroscopy in $\beta$-decay studies it is clear that there are some experimental difficulties associated purely with detection, as schematically represented in Fig. 3.7, which can be summarized briefly as follows:

- *Low photopeak efficiency*[2] of $\gamma$-registration. As an example, in our previous detection set-up the absolute photopeak $\gamma$-registration efficiency of one of the most-efficient coaxial HPGe[3] detectors was only some ∼5–7% at its highest value for low energies, dropping down to less than ∼2% for 1.33 MeV $\gamma$-rays, see the lower curve in Fig. 4.15. This is mainly due to the *incomplete energy absorption* of incident $\gamma$-rays or, in other words, *escapes*: as mentioned in the paragraph 3.2.1, these can be $X$-ray escapes in the photoelectric absorption, Compton escapes in Compton scattering, and annihilation-radiation escapes in pair production. As an example, for 1 MeV $\gamma$-rays incident on a typical large coaxial HPGe detector (a cylinder of ∼7 cm in diameter and ∼8 cm in length) ∼10% of the $\gamma$-rays will traverse the detector without any interaction and the rest ∼90% will undergo a series of interactions via Compton scattering (four instances on average), representing only some ∼20% of cases when they were totally absorbed by the detector and ∼70% of cases when they completely es-

[2]Since photoelectric effect corresponds to at least the final stage of full-energy absorption of an incident $\gamma$-ray of any energy, the efficiency of registering full $\gamma$-ray energy is often called *photopeak efficiency*. As shown later, it is better to use the more general term "full-energy peak efficiency", especially for cluster detectors.

[3]High- or Hyper-Purity Germanium

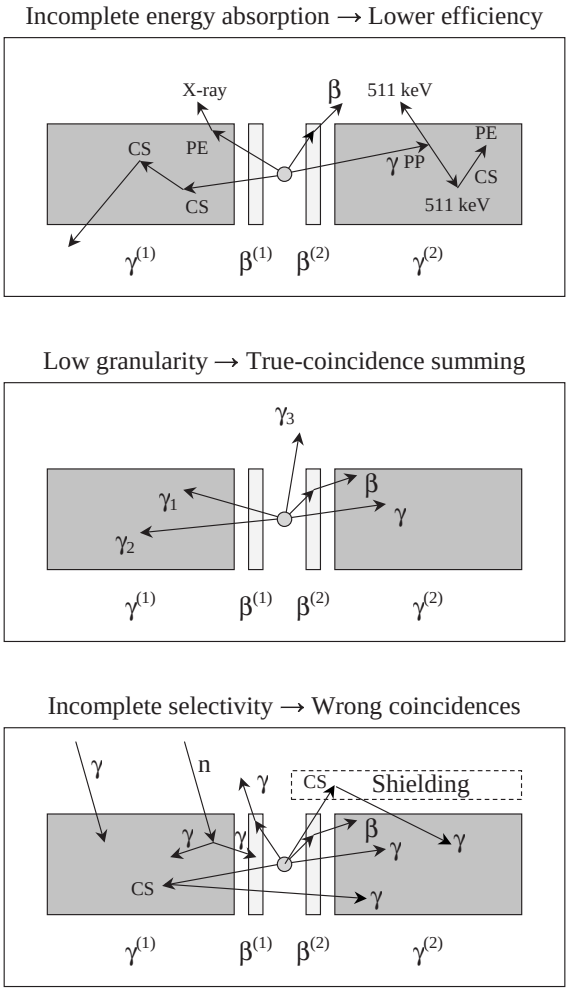


**Figure 3.7:** A schematic representation of the main experimental difficulties in $\beta$-$\gamma$-detection. Here $\beta^{(1)}$,$\beta^{(2)}$ and $\gamma^{(1)}$,$\gamma^{(2)}$ are two $\beta$- and two $\gamma$-detectors, respectively; the abbreviations PE, CS, and PP represent interaction instances of photoelectric absorption, Compton scattering, and pair production, respectively.

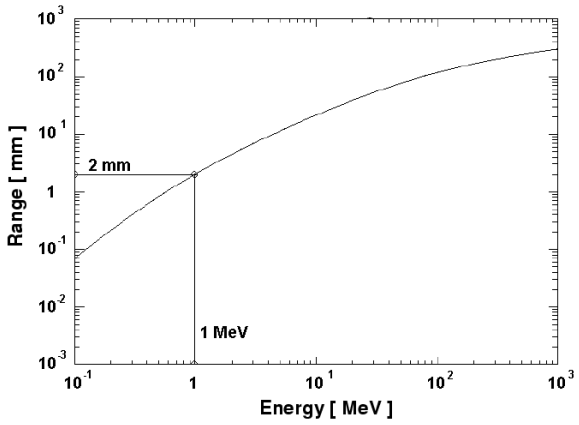


**Figure 3.8:** Mean range of electrons in aluminum.

caped from it. This constitutes the so-called peak-to-total ratio[4], which in this case is $\varepsilon_{peak}/\varepsilon_{total} = 100\% \cdot (0.2/0.9) = 22\%$. It is quite logical to suggest that in order to increase $\gamma$-ray energy absorption and eventually $\gamma$-detection efficiency, the germanium crystals must be grown as large as possible. But due to the fact that there is a substantial radial increase in impurity concentrations and crystalline structure anisotropy during the process of growing, the performance and resolution of a very large germanium detector would not be satisfactory at all. Thus, largest HPGe coaxial detectors have a relative efficiency[5] of only ∼90–110%.

- *True coincidence summing* (TCS) when two or more $\gamma$-rays from the same cascade are incident on and registered by the same detector. For $\gamma$-ray cascades following $\beta$-decay or electron capture, TCS may involve other additional sources of $\gamma$-detector signals, which arise from the same decay, namely $\beta$-particles or associated Bremsstrahlung, annihilation radiation in $\beta^+$-decay, and $X$-rays in electron capture. In close-geometry configurations, $\gamma$-rays which are backscattered from an opposite $\gamma$-detector or any

[4] In more stringent detector terms this is the definition of the *intrinsic photopeak efficiency* (see later in the text), which defines the ability of the detector to absorb a $\gamma$-ray energy of interest, while a more wider term *peak-to-total ratio* also incorporates an additional ability to remove unwanted incomplete energy absorption (escape) or intruder continuum events, e.g., by means of an additional active shielding.

[5] *Relative efficiency* is one of the performance measure standards, that relates the efficiency of full-energy detection of the $^{60}$Co $\gamma$-ray at 1332.5 keV at 25 cm distance to that of a standard 76×76 mm (3" x 3") cylindrical NaI detector.

surrounding material, such as shielding (especially high-density material of any passive shielding), must also be taken into account. This way, TCS corresponds to a situation when the detector signal represents a sum of a fully-absorbed $\gamma$-ray energy and at least partially-absorbed energy of another incident $\gamma$-ray or another member of the decay cascade, thus, resulting in a loss of counts in photopeaks in the final $\gamma$-spectra. The extent of losses due to TCS depends on the solid-angle coverage of the detectors and the multiplicity of the decay cascade, and can be as high as a several tens of percents. It is worth noting here, that in contrast to *random coincidence summing*, TCS does not depend on the count rate from the source. In detector terms, this overall issue can be described as *low granularity* of the total detector array. Considering TCS of only $\gamma$-rays from a cascade of multiplicity $M_\gamma$ incident on a $\gamma$-detector array of granularity $\mathcal{G}$ with each grain supposedly having the same solid-angle coverage and the same intrinsic efficiency[6], the real absolute photopeak $\gamma$-efficiency is

$$\varepsilon_{ph.}^{\gamma} = \mathcal{G} \cdot \varepsilon_{ph.}^{\gamma(s)} \cdot \prod_{i=2}^{M_\gamma} (1 - \frac{\varepsilon_{tot.}^{\gamma_i(s)}}{\mathcal{G}}), \tag{3.20}$$

where $\varepsilon_{ph.}^{\gamma(s)}$ and $\varepsilon_{tot.}^{\gamma(s)}/\mathcal{G}$ are photopeak and total $\gamma$-efficiencies of each grain for a single $\gamma$-ray, respectively. Extending our example from the previous item to a cascade of $\gamma$-rays, each of 1 MeV in energy, incident on two HPGe coaxial detectors of 2% absolute photopeak efficiency and $\sim 2 \cdot \frac{90}{20} = 9\%$ total efficiency at 1 MeV $\gamma$-ray energy, the true absolute photopeak $\gamma$-efficiency is reduced by factors of $\sim$1.2 and $\sim$1.3 for $\gamma$-ray multiplicities 3 and 4, respectively. This can lead to wrong intensity balances between different cascades of various $\gamma$-multiplicities. In addition, since it may be important to distinguish between $\gamma$-detector signals due to incident $\gamma$-rays and $\beta$-particles, poor granularity of both $\beta$- and $\gamma$-detectors results in a substantial decrease in photopeak statistics of $\beta$-gated $\gamma$-events when $\beta$-$\gamma$-vetoing needs to be performed.

- *Incomplete selectivity* as a measure of capability to discriminate the radiation of interest out of overall events. There are two major factors that may strongly influence this parameter. First of all, it is clear that in an ideal situation the $\beta$- and $\gamma$-detectors must be sensitive[7] only to $\beta$- and

[6] Full-energy peak or total *intrinsic efficiency* is the ratio of, respectively, the full-energy peak or total number of registered counts to the number of $\gamma$-rays incident on the detector. Thus, the intrinsic efficiency is independent of the detector–source geometry and serves as one of the standard parameters of the detector.

[7] In wider terms, sensitivity somehow encompasses all previous issues. E.g., geometrical sensitivity is defined as a ratio of the number of radiation events incident on the detector to the total number of emitted radiation events, bringing into play such parameters as detector

$\gamma$-radiation, respectively. In reality however, both types of radiation can easily generate signals in either of the detectors. As mentioned before, this is one of the reasons that necessitates the use of thin $\beta$-detectors to reduce their sensitivity to $\gamma$- and $X$-rays, Bremsstrahlung, cosmic radiation, and neutrons. For example, as quoted in [44], plastic scintillator $\beta$-detectors of $\sim$1 mm in thickness and $\sim$25 cm$^2$ in area, which were used in our experiments, have a $\sim$1–2% sensitivity to $\gamma$-rays depending on their energy. An even more serious problem appears with an unwanted registration of incident $\beta$-particles by $\gamma$-detectors. Since, the most common material that usually separates the actual germanium crystal and the $\beta$-detector is aluminum of the $\gamma$-detector end-cap, a 1 MeV $\beta$-particle will be stopped in only some $\sim$2 mm of the material, see Fig. 3.8, not to mention the highly-penetrating associated Bremsstrahlung. This translates into the reduced $\gamma$-detector sensitivity to the incident $\beta$-particles of more than 50%. Secondly, the registration, albeit not fully efficient, of a $\beta$-particle followed by a cascade of $\gamma$-rays of interest can be drastically interfered by unwanted events, originating from i) the randomly-coincident natural-radioactivity, cosmic, and beam-related (e.g. neutron-induced) background or the source itself and ii) the truly-coincident scattered events from the same decay of interest, such as Compton-scattered $\gamma$-rays (forward-scattering from the neighboring detector or shielding and back-scattering from an opposite detector or shielding) or scattered $\beta$-particles. The overall issue is especially important for retrieving true $\beta$-$\gamma$ and $\gamma$-$\gamma$-coincidences and, therefore, it is crucial to have as precise as possible timing information on registered $\beta$-particles and $\gamma$-rays in order to remove at least randomly-coincident events.

For the purpose of this work, these long-standing issues are given in the context of $\gamma$-ray spectroscopy in $\beta$-decay studies. But more or less the same problems are faced in other applications with probably the best example being in-beam $\gamma$-ray spectroscopy, such as Coulomb excitation [41][14]. In these experiments nuclei of interest moving at high velocities de-excite in-flight and, as a result, registered $\gamma$-transitions appear Doppler-broadened and Doppler-shifted. To properly correct for this effect the exact position information of incident $\gamma$-rays as well as scattered nuclei must be known, which means that high-granularity detector arrays must be used. It is obvious that all these experimental difficulties cannot be properly addressed with conventional detection set-ups and there is clearly an urgent need for yet a new and better concept that would bring registration of both $\beta$- and $\gamma$-radiations to yet another level.

solid-angle coverage and granularity. The same way, the intrinsic sensitivity, given as a ratio of the number of registered full-energy events to the number of total emitted events, is almost always called efficiency. But in our discussion the term sensitivity is used only to describe discrimination between different types of radiation.

### 3.3.4 Solution: highly-segmented detectors

The main problems in $\beta$-$\gamma$-detection as described in the previous paragraph have already been addressed in one way or another in the past. An extensive progress has already been done and especially for the in-beam-detection applications. The main goals of any $\beta$-$\gamma$ detection set-up are to achieve a) high efficiency, b) high granularity, and c) high selectivity. To fully explain how all this can be done, it is worth following three major evolutional steps in detector development with the main emphasis on $\gamma$-detection:

1. Let us take as a starting point the conventional $\beta$-$\gamma$-detection set-up as described in the paragraph 3.3.2. To pursue a close-geometry configuration, hardly more than two large HPGe coaxial detectors, together with a shielding around each of them, can be put near the source as in Fig. 3.9a. In essence, this represents our previous detection set-up at LISOL. For the purpose of the discussion, the lower curve in Fig. 4.15 is taken as an absolute full-energy peak efficiency of each $\gamma$-detector. The main experimental parameters of such a detection set-up for $\beta$-decay studies are indicated in Fig. 3.9a.

Understandably, in order to increase detection efficiency and/or be able to extract $\gamma$-ray angular distributions, the first evolutional step was to install more single $\gamma$-detectors around the source, thus, constructing an almost $4\pi$ multi-detector germanium array. In order to achieve higher peak-to-total ratio for $\gamma$-registration, an active anti-Compton shielding must be installed around each detector. This led to introduction of a whole number of different $\gamma$-spectrometers around the World in the 1980's, such as a series of TESSA arrays in Niels Bohr Institute (Denmark)/University of Liverpool (UK), HERA in LBNL (USA), OSIRIS (German collaboration), the Canadian $8\pi$ Spectrometer, NORDBALL (Scandinavian collaboration), and several more of the kind. These "so-called" first-generation Ge-arrays had an absolute photopeak efficiency of $\sim$1% and due to higher granularity, of the order of a few tens of crystals, allowed to successfully register high-multiplicity $\gamma$-cascades.

2. While the first $4\pi$-spectrometers employed relatively small germanium crystals of $\sim$25% relative efficiency, the second-generation Ge-arrays made use of larger detectors with $\sim$45–70% relative efficiency, which together with anti-Compton shielding covered whole $4\pi$ area. Some of the early examples are GASP in the LNL laboratory in Legnaro (Italy) and EXOGAM in GANIL (France). Additionally, to further increase the detector granularity, some of the first low-segmentation detectors, like, e.g., Gammasphere in LBNL (USA), were introduced at this stage. Alternatively, another approach was employed, when several detectors were stacked side-by-side to each other to constitute a clover or a cluster detector. In order to obtain as much of a solid angle coverage as possible, it is required that germanium crystals be partially (clover) or fully (cluster) tapered and placed very close to each other. As a result of this development, first $\gamma$-spectrometers using clover detectors were introduced

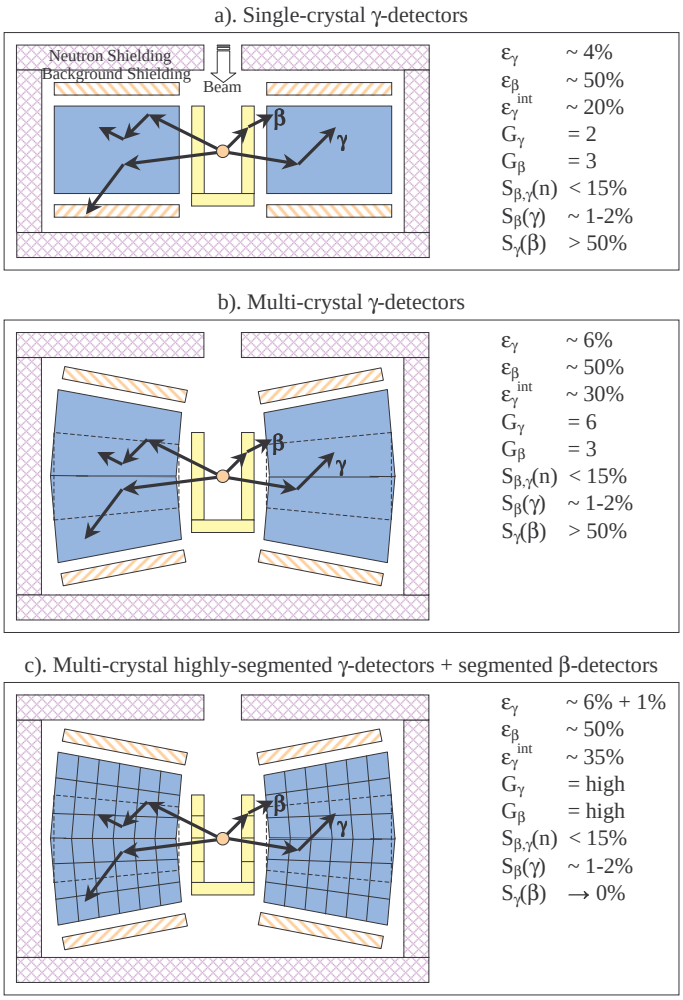


**Figure 3.9:** A schematic representation of the three major steps in the $\gamma$-detection evolution with an emphasis on $\gamma$-ray spectroscopy in $\beta$-decay studies at LISOL. Here $\varepsilon_\gamma/\varepsilon_\beta$ are absolute photopeak/total $\gamma$-/$\beta$-registration efficiencies; $\varepsilon_\gamma^{int}$ is the intrinsic photopeak $\gamma$-registration efficiency; $\mathcal{G}^\gamma$ and $\mathcal{G}^\beta$ are $\gamma$- and $\beta$-detector granularity, respectively; $S_\mathcal{D}(\mathcal{R})$ is the reduced sensitivity of $\mathcal{D}$-detector to $\mathcal{R}$-radiation. Since these three stages somehow reproduce the development of our $\beta$-$\gamma$-detection set-up at LISOL, all given values represent the actual or projected experimental numbers, where the $\gamma$-registration efficiencies are given for 1 MeV $\gamma$-rays.

— EUROGAM II in Strasbourg (France) and early EUROBALL (European collaboration). The difficulty to operate several (up to 7) crystals in a single cryostat of a cluster detector triggered the first introduction of encapsulated HPGe detectors when each crystal is placed in a separate capsule. As soon as this technique became available, new EUROBALL cluster detectors, comprising seven hexagonally-tapered crystals, were successfully put into operation. As can be concluded from our discussions in this chapter, the main reason for low photopeak $\gamma$-efficiency is the inability to provide enough volume of germanium material that would efficiently absorb incoming $\gamma$-rays, thus resulting in a dominant fraction of incompletely-absorbed $\gamma$-ray energies. So, it is obvious that by stacking more germanium material together in one cluster, the intrinsic and, thus, absolute photopeak $\gamma$-efficiency of a cluster is higher than the sum of efficiencies of each crystal. In order to reproduce the $\gamma$-ray energy absorption by one cluster, as if being one continuous bulk of material, the coincident detector signals, representing incident $\gamma$-rays that are inter-scattered within more than one crystal, must be summed together. In cluster detector terms it is called the "add-back" mode.

Concerning our close-geometry $\beta$-$\gamma$-detection set-up in the experimental conditions at LISOL, an introduction of, for instance, a triple cluster, comprising three closely-stacked germanium crystals each of 50–60% relative efficiency, would result in an increase of the intrinsic and absolute photopeak $\gamma$-efficiency by a factor of $\sim$1.5, see Fig. 3.9b, which is simply an increase in the volume of the germanium material. Further on, each crystal is additionally surrounded by $<1/3{\cdot}4\pi$ with germanium material of other two crystals. So, in our original example an intrinsic photopeak efficiency of a large (70–90%) detector of $\sim$20% at 1 MeV can be further increased at maximum by $1/3{\cdot}70\%$ in add-back mode if three such crystals were stacked together to constitute a cluster. Since the relative efficiency of a tapered germanium crystal is at maximum $\sim$80%, as follows from [41], in a case of a triple cluster of a relative efficiency of $\sim$50–60% for each crystal, in add-back mode the efficiency is increased by only $\sim$15% at 1 MeV. This translates into an increase of 1% in the absolute photopeak (or rather full-energy) efficiency or 5% in the intrinsic photopeak (full-energy) efficiency. However, it must be realized that by considering a cluster detector as a single detector in the add-back mode, the granularity is substantially reduced. As a result, taking the previous example of a cascade of three 1 MeV $\gamma$-rays, this gain in efficiency will be completely lost due to true coincidence summing.

3. It is clear at this point that, depending on the $\gamma$-ray multiplicity, there is a distinct choice to increase the detection efficiency and sensitivity whether through clustering of detectors for the add-back mode or through a mere increase in granularity. At this stage all active shielding between the single-crystal or cluster detectors could be removed to constitute a full $4\pi$ germanium ball. It is logical to suggest though that by constructing a ball of a large

enough radius the add-back mode would become possible without any substantial loss in granularity. But this would immediately require a large number of costly germanium detectors. Instead, by segmenting the detectors in the transverse plane, a close-geometry high-granularity $4\pi$ Ge-ball configuration can be achieved. The segmentation is achieved by electrically separating the outer contact where the charge-carriers of an opposite sign are collected. This way, the sum of segment energies should be equal to the core energy of the central contact[8]. As a result, instead of an add-back between adjacent crystals, the fired neighboring (from the same crystal) and adjacent (from two neighboring crystals) segments can be considered as individual groups of segments to extract the incident $\gamma$-ray energy. Alternatively, by performing the pulse-shape analysis through the use of the segment information, a relatively exact position with $\sim$5 mm resolution in the transverse plane of $\gamma$-ray main interaction can be extracted, thus further increasing the detector granularity. To avoid a problem of true coincidence summing in one crystal and to separate the first and main interaction points, an additional longitudinal segmentation must be introduced. This way, by means of the so-called "$\gamma$-ray tracking" algorithms through the use of the full-scale pulse-shape analysis the incident high-multiplicity $\gamma$-rays can be tracked down and relatively easily separated from each other. Since $\gamma$-rays can inter-scatter between adjacent crystals, all detectors must be considered as a continuous highly-segmented germanium shell, thus allowing to perform a proper and final $\gamma$-ray tracking in a later software reconstruction. The very first highly-segmented HPGe cluster detectors of the third generation Ge-arrays were six-(with only transverse segmentation: $6\times1$) and, later on, twelve-fold (with an additional two-fold longitudinal segmentation: $6\times2$) segmented MINIBALL detectors (European collaboration), which were successfully employed in the experiments at LISOL presented in this work. Two independent projects, aimed at the production of Ge-arrays of still higher segmentation, are currently being carried out at the moment of writing, namely GRETA (USA) and AGATA (Europe). In both cases the $4\pi$ Ge-shells will be comprised of $6\times6$-segmented triple clusters.

The introduction of highly-segmented HPGe detectors in our $\beta$-$\gamma$-detection set-up at LISOL, see Fig. 3.9c, would result in the same 15% increase in intrinsic and absolute full-energy $\gamma$-registration efficiencies at 1 MeV when the add-back is performed without a substantial loss in granularity due to true coincidence summing. Generally speaking, this is achieved if all segments of a cluster are considered as a collectively continuous hit-pattern, thus allowing to perform

[8]It must be realized however, that due to a lower mobility of the holes (usually the electrons are collected on the central contact), increasing anisotropy and impurity concentrations at larger distances from the central contact, a slightly worse charge collection in the so-called weak electric-field regions at the corners of tapered crystals, an additional capacitance between the outer contact and the wall of the capsule, the registration efficiency and the energy resolution of segments is slightly worse than that of a core signal.

the add-back only if adjacent segments are fired as well as to separate several $\gamma$-rays incident on the same crystal. The alternative approach of pulse-shape analysis will not yield any increase in efficiency without additional longitudinal segmentation.

The very high sensitivity of our $\gamma$-detectors to the incident $\beta$-particles, of more than 50%, is usually removed through the additional use of $\beta$-detectors as veto detectors in $\beta$-$\gamma$-coincidences. This means that both $\beta$-particle and subsequent coincident $\gamma$-rays should result from opposite $\beta$- and $\gamma$-detectors only. Although the $\gamma$-detector peak-to-total ratio is drastically improved, this also leads to a substantial loss in $\beta$-gated $\gamma$-event statistics. All this can be easily avoided by introducing segmented $\beta$-detectors. This way, the fired $\gamma$-detector segments, which cover the same solid angle from the source as the fired $\beta$-detector segments in front, can be taken out of the consideration. This means that a $\beta$-particle was registered in a $\beta$-detector segment, passed through the $\gamma$-detector front-end material, and then was finally absorbed in germanium. Obviously, the higher the segmentation of both $\beta$- and $\gamma$-detectors is, the lower the $\gamma$-detector reduced sensitivity to incident $\beta$-particles will be. In other words, the $\beta$-$\gamma$-veto efficiency can be expressed as

$$\varepsilon_{veto}^{\beta\gamma} = \sum_{i}^{\mathcal{G}^{\gamma}} \varepsilon_i^{\gamma} \cdot \sum_{j}^{\mathcal{G}^{\beta}} \varepsilon_j^{\beta} - N^{\beta-\gamma} \cdot \frac{\sum_{i}^{\mathcal{G}^{\gamma}} n_i^{\gamma}\varepsilon_i^{\gamma} \cdot \sum_{j}^{\mathcal{G}^{\beta}} n_j^{\beta}\varepsilon_j^{\beta}}{\mathcal{G}^{\gamma} \cdot \mathcal{G}^{\beta}}, \qquad (3.21)$$

where the first and second terms represent the total and removed $\beta$-$\gamma$-coincidence efficiency, respectively. Here $\mathcal{G}^{\gamma}$ and $\mathcal{G}^{\beta}$ are $\gamma$- and $\beta$-detector granularity, respectively; $\varepsilon_i^{\gamma}/\varepsilon_j^{\beta}$ are absolute photopeak/total $\gamma$-/$\beta$-registration efficiency of the $i$-th/$j$-th $\gamma$-/$\beta$-detector segment (grain); $n_i^{\gamma}/n_j^{\beta}$ are the number of the $i$-th/$j$-th $\gamma$-/$\beta$-detector segments fully covering one $\beta$-/$\gamma$-detector segment; and, finally, $N^{\beta-\gamma}$ is the number of solid-angle-coupled pairs of $\beta$- and $\gamma$-detectors. As can be seen, with $\mathcal{G}^{\gamma}, \mathcal{G}^{\beta} \to \infty$ or $N^{\beta-\gamma} \to 0$ we get $\varepsilon_{veto}^{\beta\gamma} \to \varepsilon_{total}^{\beta\gamma}$. In case $\gamma$-detectors have many-fold longitudinal segmentation, another feasible possibility would be to discriminate the $\gamma$-detector signals that originated only from one of the front segments (which obviously means that these would be $\beta$-induced $\gamma$-detector events) and with a condition that both $\beta$-particle and coincident $\gamma$-rays were registered by the same solid-angle-coupled pair of $\beta$- and $\gamma$-detectors. Alternatively, due to a substantial difference in ranges of $\beta$-particles and $\gamma$-rays in germanium, such a discrimination can be achieved through the use of full-scale pulse-shape analysis.

It would not be practical to fully describe the evolution and all ongoing developments in $\gamma$-detection with HPGe detectors in full detail within the scope of this work. Interested readers are strongly referred to [45] and the references therein.

### 3.3.5 The needs and perspectives for application of highly-segmented detectors for β-delayed γ-ray spectroscopy

To conclude this rather lengthy discussion on $\beta$- and $\gamma$-detection with highly-segmented detectors, let us briefly summarize on their application for $\beta$-delayed $\gamma$-ray spectroscopy. By introducing such a $\beta$-$\gamma$-detection set-up for our experiments at LISOL we are aiming to achieve our main goals through the following steps:

- To increase both $\beta$- and $\gamma$-detection efficiency by i) increasing the geometrical efficiency, which simply means introducing more detectors or through the use of cluster detectors, and ii) improving the intrinsic efficiency, which implies using more efficient detector material;
- To increase the granularity of $\gamma$-detectors to reduce to a sheer minimum the effects of true coincidence summing and/or to further increase the intrinsic full-energy $\gamma$-registration efficiency by up to 20% (depending on the incident $\gamma$-ray energy) by using cluster detectors in the add-back mode;
- To further increase the $\gamma$-detector granularity by introducing highly-segmented cluster detectors. The segment signals from a whole cluster can be reconstructed as a pattern of groups of fired neighboring (from the same crystal) and adjacent (from neighboring crystals) segments. The segment energies should be taken into account to provide a certain degree of feasibility on inter-segment scattering. The reconstruction algorithm must be coupled with the add-back mode. This way, the $\gamma$-detection efficiency will be increased without any losses due to true coincidence summing. With an additional manifold longitudinal segmentation a full-scale pulse-shape analysis can be performed resulting in $\gamma$-ray tracking;
- To increase the $\gamma$-detection selectivity (or, in detector terms, peak-to-total ratio) by reducing its sensitivity to $\beta$-particles and associated Bremsstrahlung using highly-segmented $\beta$-detectors. A substantial reduction of veto solid angle would immediately result in an almost negligible loss in $\beta$-gated $\gamma$-event statistics. An alternative approach would be the use of $\gamma$-detector longitudinal segmentation to discriminate $\beta$-induced $\gamma$-detector signals.

To fully achieve these, although seemingly simple, tasks would require a good knowledge in different fields of physics, a great deal of experimental skills, an arduous passion for work, and, of course, a high-degree teamwork. With all these qualities at hand, the needs must not be just satisfied, the needs must be converted into perspectives.

# Chapter 4

# Experimental set-up

## 4.1 Production of radioactive ion beams

Nuclides with large proton or neutron excess are most successfully produced in nuclear reactions resulting from collisions at very high energies, ranging from tens of MeV to a few GeV per nucleon, as in the case of multi-nucleon transfer reactions, induced fission, spallation, and fragmentation reactions. The choice of reaction mechanisms for production of radioactive nuclei strongly depends on the region of interest. The next important step after the production stage is to properly separate the nuclei of interest from other reaction products. There are two major separation techniques — In-Flight Separation [46] and Isotope Separator-On-Line [47], which can also be complementary to each other.

#### In-Flight Separation

The use of fragmentation reactions provides a good example when the In-Flight separation technique (IF) can be applied. In this reaction a usually heavy nucleus accelerated to very high energies, typically 50 - 500 MeV per nucleon, impinges on a thin target (less than a gram/cm$^2$). The result of such a collision is the fragmentation of the projectile ions into separate nuclear systems that "continue" traveling preferentially in the forward direction at almost the same relativistic speed as the incident projectile. The target should be as thin as possible to avoid absorption of the reaction products and to narrow down their energy distributions. At this stage the reaction kinematics is used to separate the nuclei of interest from other reaction products. In other words, the products of interest are separated while in flight, giving the technique its name. By using magnetic fields, eventually further combined with electrical fields and/or with solid degraders, where the energy loss is dependent on the atomic number, the nuclei of interest can be separated from other reaction products and focused

into beams. In essence, the IF separation technique provides us with so-called "cocktail" beams and specific nuclides can be selected out according to their atomic number and atomic mass.

Production of radioactive nuclear beams by the IF method gives us certain advantages:

- The produced nuclei are available instantly, on the order of microseconds, which is, indeed, instantaneous on the time scale of most $\beta$ decays;
- No chemical selectivity introduced by the choice of target material due to very high energies of reaction products;
- Both neutron-deficient and neutron-rich nuclear species can be produced.

The disadvantages of this method are mostly related to the beam energy and quality:

- The high energies of produced beams (hundreds of MeV per nucleon) are well suited for nuclear reaction studies, but, on the whole, are too high for most of the nuclear structure studies (0 – 15 MeV per nucleon is required);
- Very broad energy distribution of produced beams;
- Very large angular divergence;
- Relatively modest beam purities.

A schematic representation of this method is given in Fig. 4.1. There are a number of facilities operational worldwide, which are based on the IF technique. Some of the most advanced and notable of them are the FRS facility at GSI (Darmstadt, Germany), LISE at GANIL (France), COMBAS at FLNR (Dubna, Russia), the fragmentation facilities at MSU (Michigan, USA) and at RIKEN (Japan).

**Isotope Separator-On-Line**

The idea behind the Isotope Separator-On-Line (ISOL) technique is to produce good-quality beams of only nuclei of interest. This can be achieved best if all reaction products are stopped and only certain nuclei of interest are extracted. Induced fission and spallation are most common reaction mechanisms, which are used in this method. In these reactions, compared to the projectile fragmentation, the roles of projectile and target are inversed. A common case is when a target of intermediate- or heavy-mass nuclei is bombarded with a light beam (neutrons, protons or low-mass ions). At low energies of the primary beam (a few tens of MeV per nucleon), various types of nuclear reactions

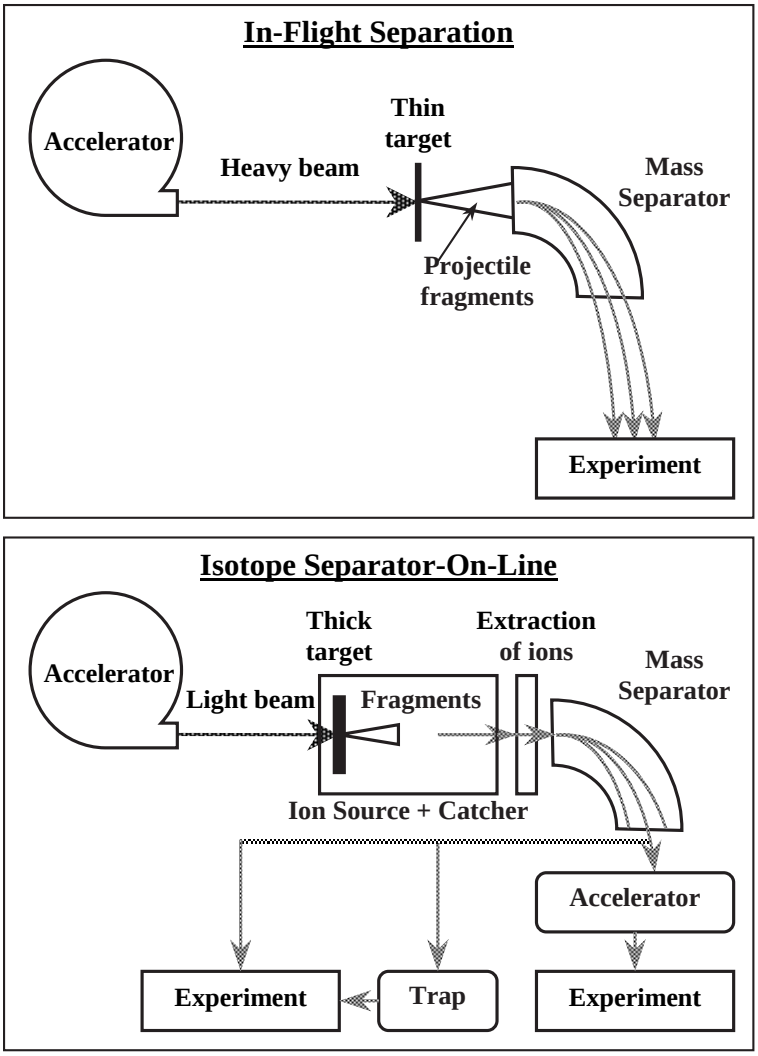


**Figure 4.1:** A Schematic representation of the In-Flight Separation and Isotope Separator-On-Line methods.

between the incident projectile and the target nuclei take place — such as fusion-evaporation, induced fission, and multi-nucleon transfer reactions. At higher energies of the projectiles (e.g. a few hundreds of MeV for neutrons or around 1 GeV for protons), a huge amount of energy brought into the nucleus triggers other types of reactions within the target, such as fragmentation and spallation.

In some cases, as, e.g., at ISOLDE [15], to achieve high production yields, the target is made very thick — several tens of grams/cm$^2$. The thermalized reaction products diffuse and desorb within the material and eventually reach its surface, where they become available for ionization and extraction. Another possibility is to arrange a target – catcher link. In most situations, the target or catcher material should be heated to high temperatures.

The next steps are to extract and accelerate the ions, separate them based on their mass-over-charge ratio by means of an electromagnetic separator, and finally deliver them to an experiment. Alternatively, instead of acceleration, the exotic species of interest can be collected for studies of their decay or introduced into an ion or atom trap for specific experiments. All this, with open options, is schematically represented in Fig. 4.1.

The mass-separated beams will be contaminated with single- or double-charge isobars. Thus, another important issue is to provide an additional element separation. And that is where the ISOL technique has an advantage over IF. It is realistically achievable if one uses chemical properties of produced atoms. This can be done by using chemical selectivity during transfer to the ion source or by a suitable choice of the target material. But probably the best option is photo-ionization by laser light.

The ISOL method has the following advantages:

- The beam of interest is pre-selected (mass selection and often element selection) which results in relatively pure beams;
- A very low energy spread, which allows for a possibility of post-acceleration of the beam;
- Very small angular divergence, which leads to small beam spots.

The disadvantages of this method are:

- A relatively large scale of extraction times, which makes the study of many short-lived nuclear species almost impossible;
- Chemical selectivity introduced by the choice of target and catcher material;
- Contaminants in the beam, e.g., surface-ionized isobars.

In order to deal with both the problem of long extraction times, resulting from the slow evacuation stage, and the problem of chemical selectivity, introduced by the target and catcher materials, the production target can be made thin. This would allow reaction products to easily recoil out of the target material, which then can be stopped in a gas catcher confined together with the target in a cell. By a proper choice of gas, e.g. a noble gas, one can avoid any chemical selectivity of the catcher material. The next step is to neutralize and re-ionize the reaction products, which can be achieved through charge-exchange mechanisms with the atoms of the gas. By engaging a constant flow of the buffer gas, the reaction products can be easily evacuated to the ion-extraction stage. This gas-cell technique within the framework of the ISOL method allows to produce rather efficiently short-lived radioactive nuclei with half-lives as low as evacuation times, which normally vary from a few milliseconds to a few hundred milliseconds. It was successfully applied in our radioactive beam facility, which is described in detail in the next section.

A simpler production of proton beams made the ISOL technique to be developed first, resulting in construction of a whole variety of different radioactive beam facilities. Some of the most known and advanced are ISOLDE at CERN (Switzerland), LISOL at Louvain-La-Neuve (Belgium), IGISOL at Jyväskilä (Finland), HRIBF at ORNL (Oak-Ridge, USA), SPIRAL at GANIL (France), ISAC at TRIUMF (Vancouver, Canada).

## 4.2 The LISOL facility

### 4.2.1 Layout of the facility

The experiments presented in this work were carried out at LISOL [8], [9], standing for Leuven Isotope Separator-On-Line, which is situated at Louvain-La-Neuve cyclotron center in Belgium. As follows from its name, the facility is based on the ISOL technique. The current layout of the facility is given in Fig. 4.2 with its schematic representation in Fig. 4.3. Production and acceleration of primary beams is provided by the Louvain-La-Neuve ion sources and cyclotrons, respectively.

Radioactive beams at LISOL can be produced by induced fission [48] and fusion-evaporation [49][50] reactions. The $^{65,66,67}$Fe isotopes, partly presented in this work, were produced at LISOL by proton-induced fission of $^{238}$U.

### 4.2.2 The gas cell

The proton beam, accelerated in the K=110 Cyclone cyclotron to the energy of 30 MeV, impinges on two thin 10 mg/cm$^2$ $^{238}$U targets, tilted at 20° angle relative to the beam to increase their effective thickness. The Fe isotopes

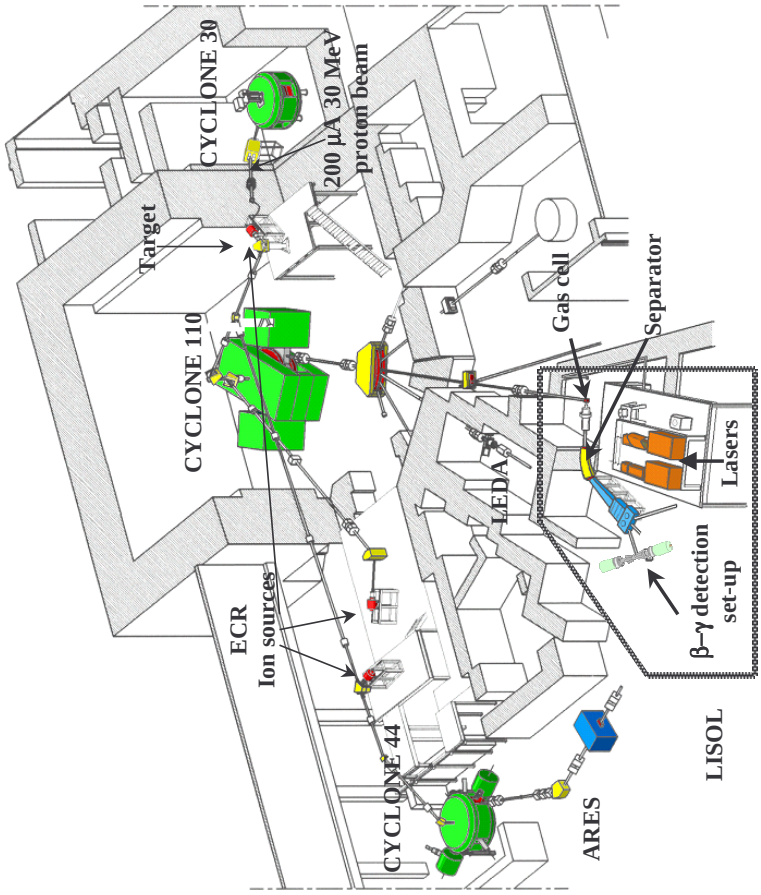


**Figure 4.2:** The layout of the LISOL facility at Louvain-La-Neuve.

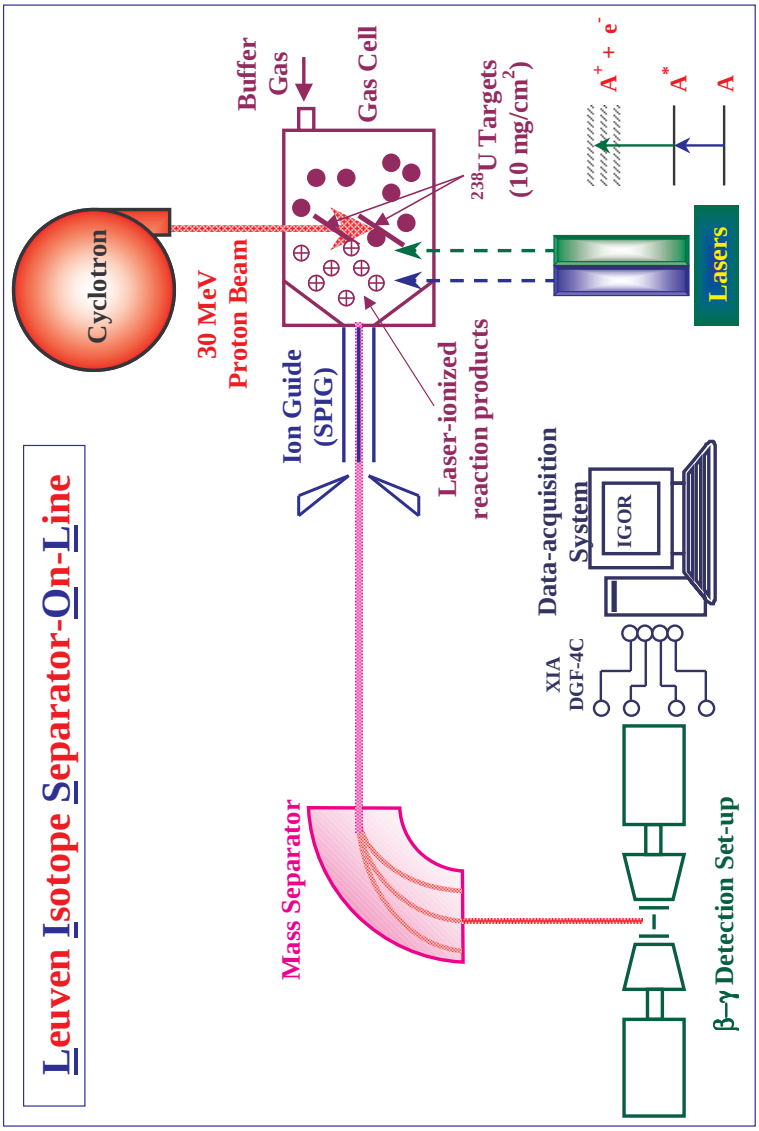


**Figure 4.3:** A schematic representation of the LISOL facility.

produced as proton-induced fission products of $^{238}$U have a maximum kinetic energy of approximately 125 MeV.

Contrary to the common ISOL method, as described in section 4.1, the target is made thin enough to let the fission products easily recoil out of it. But too thin target may result in the loss of the production yield. Such substitution of a thick bulk of target material with a thin foil was suggested as a solution to address two main problems of the ISOL method. First of all, avoiding slow processes like diffusion and desorption, which take seconds and even minutes, makes the production much faster. Secondly, this eliminates dealing with chemical properties of the target material. This immediately gives a possibility to produce the refractory elements, like e.g. Ni, Co, and Fe.

The fission products, isotropically recoiling out of the targets, have rather wide energy distributions and still need to be thermalized in a catcher medium. As was suggested in [51], the ions can be stopped and quickly evacuated to the extraction region by use of a buffer gas. Such a technique became known as Ion Guide Isotope Separator-On-Line or IGISOL for short. It should be a noble gas to avoid chemical reactions with the produced nuclei, and it is preferred to have as high atomic mass as possible to create more stopping power. Another important reason for using the noble gases is that they have high ionization potentials and this results in smaller cross-sections for charge-exchange between the ions of interest and the atoms of the buffer gas, which in turn leads to longer ion survival times. The buffer gas must also be pure and available in reasonable quantities. For these reasons we chose argon. It is confined in a cell and kept at a pressure of $\sim$500 mbar. It is worth mentioning here, that not all fission products like Fe or Ni isotopes can be stopped in the current volume of the cell at this pressure of the buffer gas.

On the scale of microseconds the produced ions collide with atoms of the gas and through charge-exchange reactions acquire a low charge state, predominantly 1+. Due to high first ionization energy of noble gases the ions keep this state for several milliseconds, long enough to evacuate and extract them from the cell. It is important to add here, that the proton beam on its impact with the buffer gas creates a low-density plasma, leading to recombination of the produced ions. For this reason, the region around the targets is screened from ions produced in the gas cell by means of 3 $\mu$m thick aluminum foils. Finally, by engaging a constant flow of the buffer gas, the reaction products are evacuated to the exit hole of the cell.

One can see that apart from thermalization and evacuation of the reaction products the use of a gas cell configuration offers two additional options:

- The surviving ions, produced through charge-exchange reactions with the atoms of the buffer gas, can be directly extracted;
- Alternatively, the produced ions can be neutralized in the buffer gas and then re-ionized by means of external selective ionization.

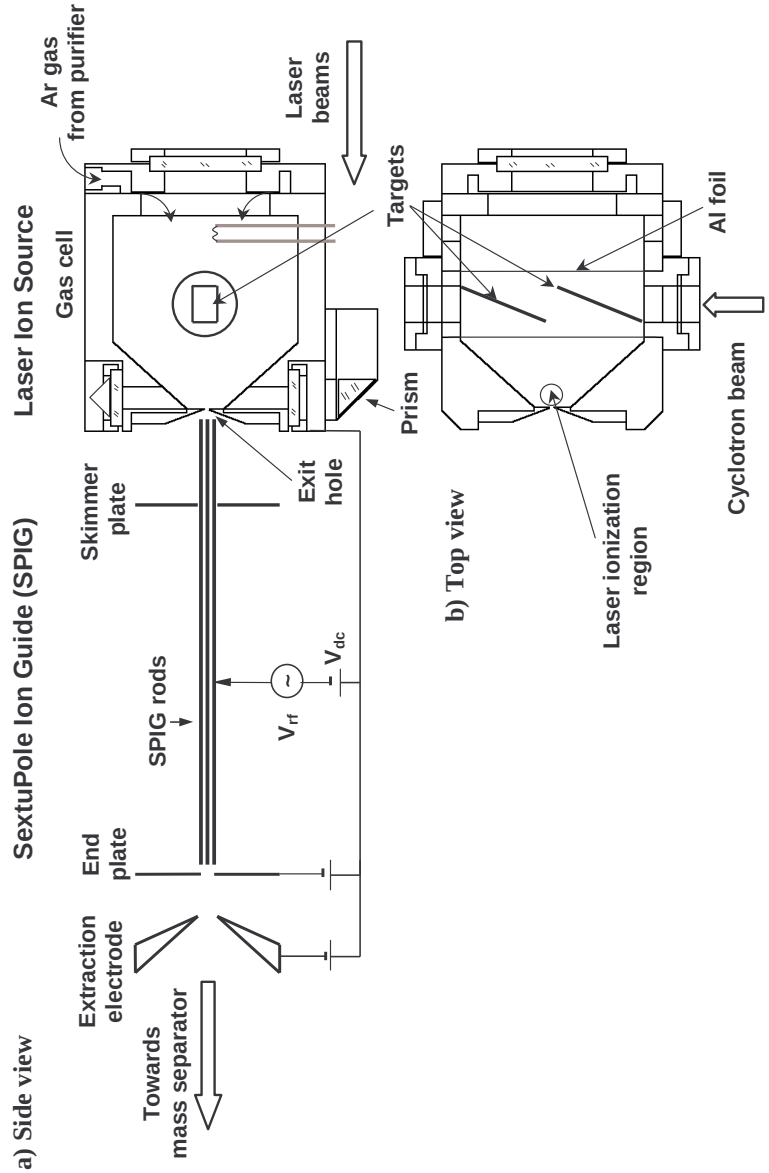


**Figure 4.4:** The drawing of the gas cell for induced fission experiments, coupled with laser ionization and extraction stages.

Given that there is an external selective source of ionization, the second approach provides a much better degree of selectivity and, thus, gives more pure beams. This option is fully pursued at the LISOL facility by coupling the gas cell configuration with the selective resonant laser ionization.

The gas cell for induced fission reactions, used in our experiments, together with the laser ionization and extraction stages is presented in Fig. 4.4 taken from [9]. For more detailed information on different gas cells used at LISOL see [52]. Without laser ionization the short ion survival time will become the main limiting factor. Next to this, processes like deposition of ions on the cell walls further degrades the efficiency. A fraction of ions of interest can also take part in chemical reactions with the impurities present in the buffer gas. The reader is referred to [53] for a more detailed description of gas cell efficiency limitations.

The reaction products are driven with a constant laminar flow of the buffer gas to the exit hole of the gas cell of 0.5 mm in diameter. At this stage a huge negative gradient of the gas pressure is achieved by means of differential pumping, thus engaging this flow of gas. The average evacuation time from the center of the gas cell is about 0.5 s.

### 4.2.3 Resonant laser ionization

As discussed in the previous paragraph, the produced ions can acquire a low charge state through charge-exchange reactions with the atoms of the buffer gas. This way, the nuclei of interest constitute only a certain fraction among many other much more abundantly produced and ionized reaction products. Evidently enough, there is a need to selectively ionize the products of interest using their atomic properties, thus giving an additional element separation. This can be successfully achieved by means of resonant photo-ionization using intense laser light [54], [55], [9]. Such coupling of the laser ionization with the production stage is called the Laser Ion Source (LIS).

With a choice of intense laser beams at hand and ionization energies of atoms of interest, for most cases it is achievable only by multi-step laser ionization. Each element will require its own and almost unique ionization scheme. As an example, the laser-ionization scheme for iron is presented in Fig. 4.5. The first ionization potential for iron is 7.87 eV, so we have to use two laser beams to ionize the Fe atoms to the 1+ state in two steps. With our lasers, the optimum yield of Fe isotopes was found to correspond to laser beam wavelengths of 229.82 nm and 493.80 nm, respectively. A photon of the first laser beam promotes one of the outer electrons of the Fe atom to an excited state. A photon from the second laser promotes the electron from this excited state to another excited state, which is degenerate with a continuum state. This leads to a new state, being a mixture of the bound and the continuum states, i.e. an auto-ionizing state. These states are situated at the beginning of the contin-

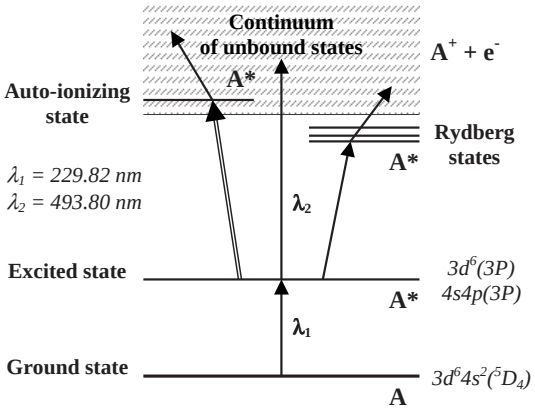


**Figure 4.5:** The laser ionization scheme for iron.

uum, and relaxate by setting the electron free. A second possibility would be promoting the electron from the first excited state directly to the continuum of unbound states. There is a third possibility, however. The second photon can bring the electron from the excited state to one of the orbitals with high principal quantum number. Such bound states, called Rydberg states, correspond to putting an electron into an orbit whose dimensions are very large compared to the rest of the ion core. As a result these states are situated shortly below the continuum and the electrons are easily knocked off from these states by collisions with the atoms of the buffer gas.

The laser optical system [9] consists of two tunable dye lasers pumped by two time-synchronized excimer XeCl (308 nm) lasers. The frequency of the first step laser radiation is doubled in the second harmonic generator in order to get UV light. The laser beams are directed near the outlet of the gas cell as in Fig. 4.4. The maximum laser pulse repetition rate is 200 Hz, to make sure that most of the atoms, driven with the flow of the buffer gas, will pass across the laser beams at least once. For the case of Fe isotopes the lower limit for the laser ionization selectivity, which is the ratio of the number of laser-produced ions to the number of ions produced without laser ionization, was estimated to be about 25.

It is worth to mention here that a fraction of laser-produced ions will be lost in three body collisions or appear as molecular complexes with impurities present in the gas or even with the buffer gas atoms. In the experiments on $\beta$-decay of $^{65,66,67}$Fe isotopes the latter case was especially pronounced for double-

mass double-charge contaminants like $(^{98}YO_2)^{++}$, $(^{100}YO_2)^{++}$, $(^{100}NbO_2)^{++}$, $(^{102}NbO_2)^{++}$, $(^{94}Y^{40}Ar)^{++}$, $(^{94}Sr^{40}Ar)^{++}$, which got ionized by charge-exchange reactions with the buffer gas atoms due to low ionization potentials of Y, Nb, and Sr atoms. Although the laser ionization is a very selective tool, the atoms can be ionized by other processes, like, e.g., already mentioned ionization due to charge-exchange reactions with the atoms of the buffer gas, re-ionization by radiation and fast electrons produced in the proton-induced fission reaction inside the cell, and to a small degree ionization and neutralization by plasma created on the proton beam impact and due to radioactivity of the target itself (mainly due to $\beta$-decay of various fission products). All these non-laser-related processes will lead to ionization of many different atoms in the cell, thus deteriorating the overall laser ion source selectivity.

### 4.2.4 The sextupole ion guide

The next step is to extract the ions from the gas jet, which can be achieved by applying a constant electric field in the region next to the exit of the cell. This is done by introducing the SextuPole Ion Guide (SPIG) [56] and applying a DC voltage of about 200 V between it and the gas cell, see Fig. 4.4. The SPIG is a structure of six metallic rods, each of 1.5 mm in diameter and 124 mm in length, placed parallel to the beam and side by side to each other to form a hexagonal shape cross-section with the innermost diameter of 2.5 mm. It is situated at a distance of 1.5 mm from the cell. At this stage, slightly accelerated ions undergo frequent collisions with the neutral atoms of the buffer gas. This leads to dissociation of a fraction of molecules bound as produced ions and atoms of the gas, thus increasing the overall efficiency of the ion source. The extracted ions are driven by the field and then introduced into the SPIG. A voltage of 150 V amplitude with a frequency of 4.7 MHz is applied to each SPIG rod in antiphase with its two neighboring rods. As a result, the ions are radially confined inside by the electromagnetic field created by the rods.

The extracted ions progress along inside the SPIG, while the neutral gas still present inside gushes out through the open spaces between the rods and is further pumped away. The remaining small pressure of the buffer gas at the entrance of the SPIG allows to reduce the kinetic energy spread of the ions by collisions with the atoms of the gas. Such "cooling" leads to a very narrow energy distribution of the ion beam at the exit of the SPIG. A skimmer plate was introduced at a distance of 29 mm from the entrance of the SPIG to separate the volumes around the structure and, thus, enable differential pumping. This way, the remnants of the buffer gas can reach the volume behind the skimmer only through the SPIG. High-vacuum pumping is engaged after the skimmer plate to ensure a very good vacuum at the entrance into the separator. Finally, the extraction electrodes are placed after the SPIG to accelerate the beam to 40 keV in energy.

### 4.2.5 The mass separator

At this stage the beam represents not only laser-ionized nuclei of interest, but also the whole variety of reaction products that get ionized by various means in the gas cell. In addition, various nuclei of the beam can form heavier molecules together with atoms and molecules of impurities present in the gas cell or with the very atoms of the buffer gas, thus further extending the composition of the beam. And more often than not we have to deal with production of nuclei farther away from the $\beta$-stability line, which simply means that the nuclei of interest will constitute just a small fraction of our beam. So, the need for a precise mass separation brings us to a very important stage in the production of radioactive beams. Since, in essence, our beam consists of moving ions of certain mass and charge, it can be decomposed based on mass-over-charge ratio of its different components by applying magnetic fields on its way.

In our case the ions, extracted from the laser ion source, are delivered to the 55° dipole magnet of 1.5 m radius, where they are separated based on their mass-over-charge ratio. At present, the mass-resolving power $M/\Delta M$ of LISOL is around 1450. And this is mainly due to a good quality of the beam delivered by the SPIG.

### 4.2.6 Beam time structure

Production of radioactive beams at LISOL is not a continuous process but rather has a certain time structure for the following reasons. First of all, in the presence of the proton beam on the targets, a lot of charges are created inside the gas cell, resulting in a large decrease of the ion source selectivity. Additionally, there is a beam-related background radiation due to prompt neutrons from the production reaction. Consequently, provision of the primary beam and extraction of ions from the gas cell should be done in anti-phase, relative to each other. Secondly, in most cases one needs to study the decay properties of produced nuclei of interest or detect very weak transitions in the absence of the beam. So, it is also important to have a time structure of the secondary beam. All this can be achieved by proper time synchronization of different components of the set-up. The secondary beam time structure evolves through the time structure of different stages of the set-up, as schematically presented in Fig. 4.6.

The proton beam is delivered onto the targets for 100 ms. Then, during the next 100 ms, it is switched off internally by lowering the HF power of the cyclotron. As it was already mentioned, the extraction of the ions from the gas cell takes place in the absence of the proton beam. Switching the proton beam on generates a signal for the SPIG to switch off both the RF and DC voltages till the proton beam is off again. There is, however, a manually set delay of 2 ms to have sufficient time for the ion source to relaxate from the ionization

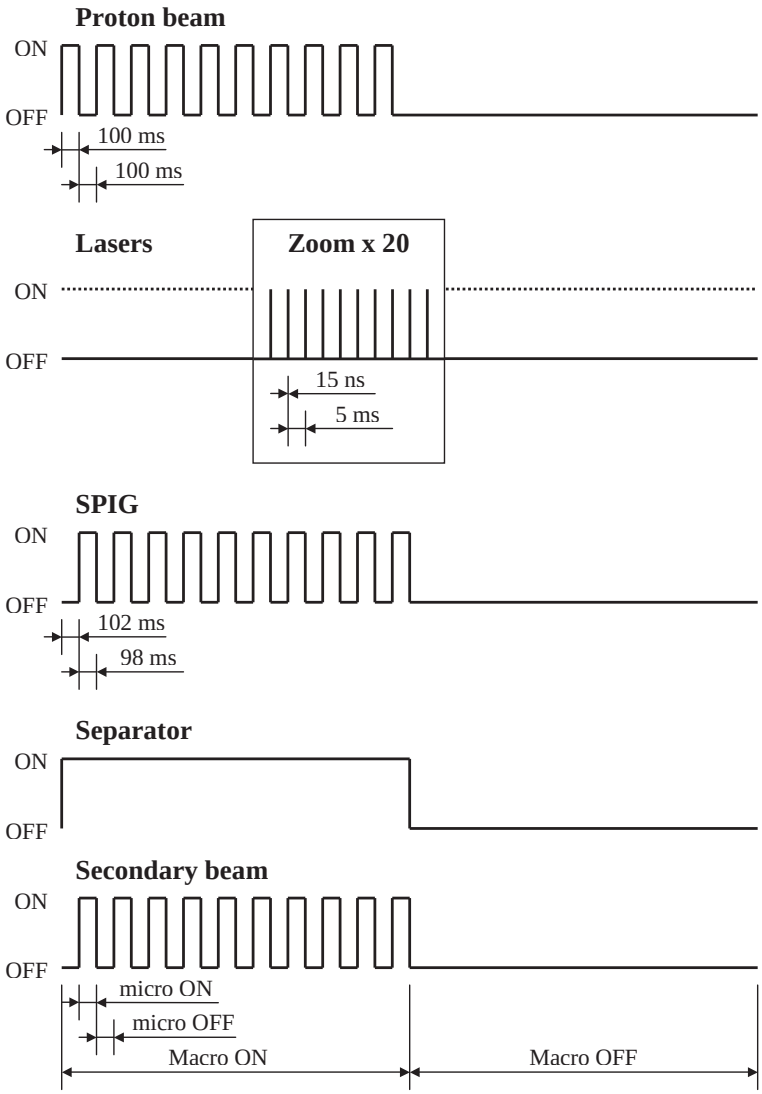


**Figure 4.6:** The time structure of the LISOL beam.

effects taking place in the gas cell on the proton beam impact. So, the SPIG stays switched off for 102 ms. Consequently, after 2 ms since the proton beam was switched off, the RF and DC voltages on the SPIG are applied again, and the extraction of ions lasts for 98 ms. At this point the whole cycle is repeated again. The proton beam cycle, and as a result the SPIG operation cycle, can be changed depending on the experimental needs.

As for the laser beams, it is not practical to switch them off during periods of time when there is no secondary beam production, since that would cause some change in temperature of the laser hardware and, as a result, a change in the stability of the system. So, the laser beams are constantly delivered into the gas cell at a repetition rate of about 200 Hz. The duration of the laser pulse is 15 ns.

To be able to study the decay properties of nuclei of interest, one needs a certain macro-time structure of the secondary beam. This is especially important for the half-life determination. In most cases when the half-life is not too long, the secondary beam is provided for a period of time equal to two–four half-lives. This beam "macro on" part is then followed by a subsequent beam "macro off" part, usually chosen to be of the same duration of time. During this period of time, when the secondary beam should not be delivered to the experiment, the proton beam is switched off, both the RF and DC voltages on the SPIG are not applied, and the remnants of the beam are deflected away from the separator. This macro-time structure is then repeated all over again, constituting the so-called macrocycle.

### 4.2.7 The advantages of the LISOL facility

While having all the advantages characteristic of any ISOL-based facility, the LISOL set-up clearly addresses the main problems of the ISOL technique, as described in section 4.1. In the present conditions the main limitation is imposed by availability and energy of the primary beams, thus reducing the possible choice of reaction mechanisms. As extensively described in the next section, the energy of the primary beams is not an issue, e.g., for the light-particle-induced fission, but the use of reaction mechanisms like, e.g., projectile fragmentation or target spallation is impossible.

The use of a gas cell configuration puts the LISOL set-up into a somewhat special position amongst a number of standard ISOL-based facilities and makes it a very competitive tool in production of radioactive beams. To summarize, the main advantages of the LISOL facility are:

- Considerably smaller scale of extraction times, allowing to produce short-lived nuclei with half-lives down to a few hundred milliseconds;
- Almost no chemical selectivity, which immediately gives a possibility to produce

  - refractory elements, like, e.g., Tc, Ru, Rh;
  - slowly-releasing elements, like, e.g., Fe, Ni;

- Enhanced ion-source selectivity due to application of resonant laser ionization, which, in turn, leads to higher-purity beams;
- Flexibility in choosing a suitable reaction mechanism by simply employing different gas-cell configurations. As a result, the subjects of the current spectroscopy studies at LISOL can be outlined as follows:
  - neutron-deficient nuclei in the vicinity of the $N = Z$ line, produced in light-ion and heavy-ion fusion-evaporation reactions (e.g., Ni, Co and Tc, Ru, Rh isotopes, respectively);
  - neutron-rich nuclei in the region around the $Z = 28$ proton shell closure (e.g. Fe, Co, Ni, Cu isotopes), produced in proton-induced fission reaction;

For information on further developments at the LISOL facility the reader is referred to [57].

## 4.3 Production of neutron-rich Fe isotopes at LISOL

### 4.3.1 Choice of reaction: proton-induced fission of $^{238}$U

The neutron-rich intermediate-mass nuclei are produced at LISOL in spontaneous fission, a form of radioactive decay, or induced fission, a form of nuclear reaction. In both cases the same mechanism of nuclear fission is involved. The nuclear fission is an exothermal process, when a massive nucleus attains an amount of potential energy enough to break it into two separate nuclear systems [58]. The process takes place because the sum of the binding energies of produced fission fragments is greater then the binding energy of the original nucleus. The process of nuclear fission is described by a macroscopic representation of splitting of a charged incompressible liquid drop with an addition of microscopic shell and pairing corrections, the so-called macroscopic-microscopic model.

The probability of the nuclear fission in the simplest case of spontaneous fission is determined by the quantum mechanical penetrability of the potential barrier. For example, for nuclei with $Z > 90$ and $A > 230$ the height of the barrier is around 6 MeV and stays almost constant. The mechanism of induced fission suggests the creation of an excitation energy in a nuclear system. Examples of induced fission reactions are photofission, Coulomb fission, and induced fission by light and heavy ($A > 10$) projectiles. The latter case proceeds

through the mechanism of creation of a compound nucleus, when a relatively large number of projectile nucleons are absorbed by a target nucleus. This leads to the so-called fusion-fission reactions. The total energy release in fission is the sum of the total kinetic energy of the fragments and the energy emitted by the prompt and delayed radiations. For example, in thermal-neutron-induced fission of $^{235}$U, the total fission energy is about 203 MeV, out of which about 170 MeV is the total kinetic energy of fission fragments, and approximately 12 MeV and 21 MeV are taken away by the prompt and delayed radiations, respectively. Since the total kinetic energy of both fission fragments is generated mainly by the Coulomb repulsion between them, it is almost independent of the excitation energy and can be approximately calculated as

$$E^K \approx 0.1189 \frac{Z^2}{A^{\frac{1}{3}}} + 7.3, \tag{4.1}$$

where $Z$ and $A$ are the atomic number and atomic mass of the fissioning nucleus, respectively. From kinematics considerations the kinetic energy of an individual fragment is then given as

$$E_F \approx E^K \frac{A - A_F}{A} \tag{4.2}$$

Considering $^{67}$Fe as one of the fission fragments in proton-induced fission of $^{238}$U, its original kinetic energy right after the fission is approximately 125 MeV.

A very wide range of nuclei is produced in nuclear fission. Because of the curvature of the $\beta$-stability valley, neutron-rich fission fragments are formed. The shape of the mass distribution of fission fragments depends on the atomic number, atomic mass, and the excitation energy of the fissioning nucleus. There are two distinctive types of mass distribution:

1. Symmetric distribution with a maximum at approximately one half of the atomic mass of the fissioning nucleus. It is characteristic for all nuclei at excitation energies higher than 40 MeV and for nuclei with $Z < 88$ at all excitation energies. It is also observed in spontaneous fission of some heavy nuclei like e.g. $^{258}$Fm, $^{259}$Fm, $^{259}$Md, $^{258}$No, and $^{260}$Rf.

2. Asymmetric distribution with two distinctive maxima (light and heavy fragments). It is characteristic for nuclei with $Z > 90$ at low excitation energies, except for those mentioned above. At moderate excitation energies of 20–40 MeV or for nuclei with $88 \geq Z \leq 90$ a superposition of these two types is observed.

Since we are interested in the production of very neutron-rich nuclei, the target material must have as high atomic number as possible. Additionally, the heavier the nuclear system is the less bound it becomes, which means that less energy is required to induce the process of nuclear fission. This leaves out

the use of induced fission of middle-mass nuclei. With these considerations at hand, very neutron-rich nuclides from the Ni region can be produced best in a fission of heavy nuclei with the predominantly asymmetric mass distribution. The use of spontaneously-fissioning nuclei results in low production yields due to small fission probabilities and would require a substantial amount of material. However, we used a rather strong 20 MBq source of $^{252}$Cf, but only to produce radioactive nuclei with atomic masses close to or at maxima of the fission-fragment mass distribution. So far in this project, we mainly concentrated on production of $^{113,115}$Ru, $^{112-116}$Rh, and $^{114}$Pd isotopes to study the decay properties of $\beta$-decaying nuclides along the corresponding isobaric chains. A similar grand project has been started recently at Argonne National Laboratory, USA, aimed at using an extremely strong $\sim$37 GBq $^{252}$Cf source in a gas cell to produce and accelerate the whole variety of very neutron-rich nuclei, such rare as $^{132}$Sn, with final beam intensities being as high as $10^5$ ions/s [59]. Taking into account considerations of availability in reasonable amounts, we are left with a choice of primordial U and Th isotopes as a target material. For just this reason, the best option is $^{238}$U.

The fission probability strongly depends on the excitation energy. With the choice of the primary beams in Louvain-La-Neuve and their energies and intensities at hand, the simplest option is the proton-induced fission. The dependence of the total fission cross-section on the incident proton energy for the $^{238}$U(p,f) reaction is shown in Fig. 4.7a. At first the fission cross-section grows exponentially with the increase in the incident proton energy, then at approximately 30 MeV starts saturating, and within the range of $\sim$40–60 MeV approaches the full cross-section that corresponds to the maximum fission probability. The fission fragment mass distribution curves at different proton energies between 18.2 and 45.1 MeV in the $^{238}$U(p,f) reaction are shown in Fig. 4.7b. As expected, the cumulative yield from the dominant asymmetric fission mode grows with the increase in the incident proton energy and starts saturating at around 30 MeV. Another important issue for the choice of incident projectile and its energy is to use a maximum yield from the asymmetric fission mode. As follows from the same figure, the yield from the symmetric fission mode also grows with proton beam energy and after 30 MeV or so its contribution relative to that of the asymmetric fission starts increasing. As a result, at proton beam energies of more than 30 MeV one would expect a slightly more rapid saturation in cross-section for production of our nuclei of interest, which are situated quite far down at the left wing of the asymmetric distribution. However, there is a rather severe restriction on the incident proton beam energy that arises from the simple fact that higher proton energies result in higher fluxes of originally fast neutrons produced in the fission process inside the gas cell and in various nuclear reactions of protons of the beam with different materials of the beam dump. As a consequence, there is a dramatic increase in intensity

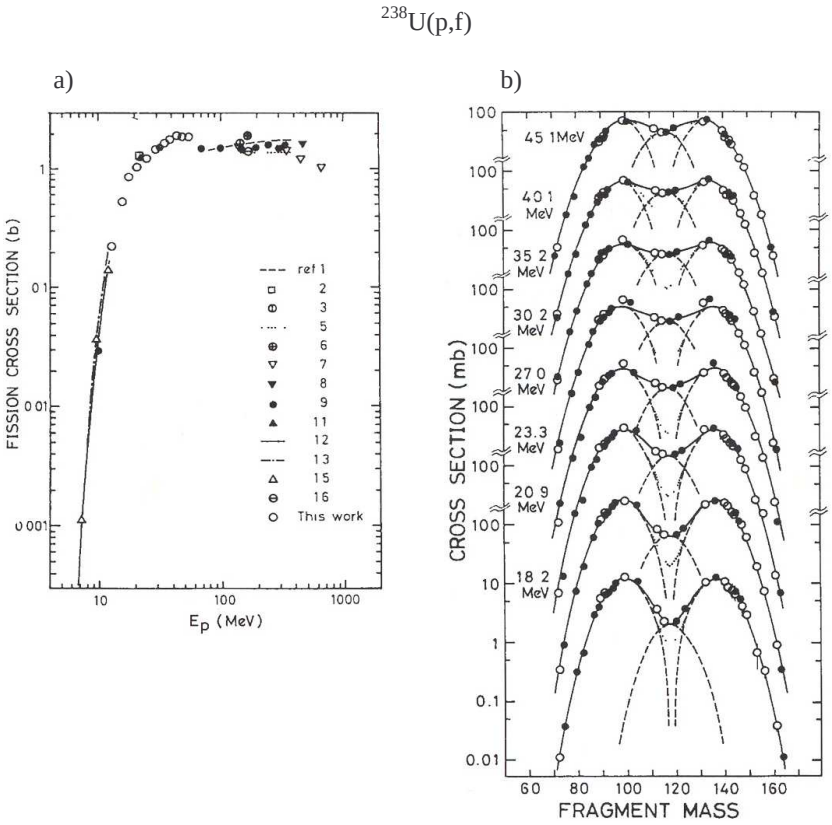


**Figure 4.7:** The $^{238}$U(p,f) reaction: a) The dependence of the total fission cross-section on the incident proton energy; b) The fission fragment mass distribution curves at different proton energies. The figures are taken from [60].

of neutron-induced background $\gamma$-radiation at the detection set-up. With all these considerations at hand, the proton beam energy of 30 MeV was chosen as an optimum for induced fission of $^{238}$U in our present experimental conditions.

Summarizing the whole discussion, the optimum fission reaction for production of nuclei from the neutron-rich Ni region at LISOL is induced fission of $^{238}$U by 30 MeV protons.

### 4.3.2 Production of neutron-rich Fe isotopes in the induced fission of $^{238}$U by 30 MeV protons

The experimental isotopic cross-sections for production of nuclei from the neutron-rich Ni region in induced fission of $^{238}$U by low-energy protons are scarcely available. After several years of production at LISOL of neutron-rich nuclei in the vicinity of the closed proton shell $Z = 28$ [4][5][6][7][61], the experimental yields of neutron-rich $^{65-70}$Co, $^{68-74}$Ni, $^{70-76}$Cu, and $^{74-81}$Ga isotopes were extracted, as summarized in Table 4.1 taken from [62]. The extracted values are based on registered $\gamma$-ray intensities or, in cases of low production rates, on counting rates from $\beta$-detectors with a subtraction of normalized off-resonance (without resonant laser ionization) statistics and correction for cumulative $\beta$-counting rates from the isobaric daughter and double-charge double-mass contaminant activities.

As reported in [62], calculations based on a semi-empirical description of the fission process were performed by Benlliure *et al* [63] for our reaction of interest. The macroscopic-microscopic model was used as a basis. To simplify the description of the process and approximate both macroscopic and microscopic parts of the potential some input parameters, like e.g. widths of fission fragment mass distributions, were taken from various experiments. The calculated isotopic cross-sections for production of neutron-rich Co, Ni, Cu, and Ga isotopes in induced fission of $^{238}$U by 30 MeV protons are shown in Fig. 4.8a together with the experimental values obtained at LISOL. The shape of isotopic and isobaric fission yields is fairly well described by the Gaussian distribution. The experimental values were scaled by matching the experimentally extracted and calculated data for Ni isotopes. This scaling factor between the experimental production yields and the calculated cross-sections represents the absolute ion-source efficiency, which is $\sim$0.01% for laser-ionized Co, Ni, and Cu isotopes and $\sim$0.02% for Ga isotopes produced without laser-ionization. Here, although the laser-ionization selectivity for Co, Ni, and Cu was on the level of $\sim$100, the ion survival probability for Ga ions was by a factor of $\sim$40 higher. The agreement between the experimental and calculated values is on the level of the experimental error bars — the centroids and the widths of the respective distributions match very well.

To extract the isotopic cross-sections for production of Fe isotopes in the same reaction the centroids and the widths of the calculated distributions for Co, Ni, and Cu isotopes were linearly extrapolated one unit of atomic number. The resulting distribution for Fe isotopes is shown in Fig. 4.8b together with the calculated curves for Co and Ni isotopes from Fig. 4.8a. By using inversely the same scaling factor that was applied for Co, Ni, and Cu isotopes the expected production rates for $^{65-69}$Fe isotopes are extracted, as shown in Table 4.1.

**Table 4.1:** Experimental production rates in atoms/$\mu$C for neutron-rich $^{65-69}$Fe, $^{65-70}$Co, $^{68-74}$Ni, $^{70-76}$Cu, and $^{74-81}$Ga isotopes produced at LISOL in induced fission of $^{238}$U by 30 MeV protons. Except for the Fe isotopes, the values are taken from [62]. The corresponding values for the Fe isotopes are extracted by extrapolating Gaussian distribution parameters for Co, Ni, and Cu isotopes and, thus, the error bars are not provided. See text for more detail.

| Atomic mass | Fe | Co | Ni | Cu | Ga |
|---|---|---|---|---|---|
| 65 | 6.6 | 7 (3) | | | |
| 66 | 4.3 | 10 (4) | | | |
| 67 | 1.7 | 16 (5) | | | |
| 68 | 0.4 | 11 (3) | 16 (3) | | |
| 69 | 0.06 | 7 (3) | 23 (4) | | |
| 70 | | 1.3 (3) | 28 (5) | 12 (2) | |
| 71 | | | 14 (3) | 25 (7) | |
| 72 | | | 5 (1) | 65 (14) | |
| 73 | | | 1.4 (3) | 45 (10) | |
| 74 | | | 0.20 (5) | 21 (5) | 5(2) |
| 75 | | | | 8 (4) | 33 (8) |
| 76 | | | | 2 (1) | 76 (6) |
| 77 | | | | | 119 (21) |
| 78 | | | | | 102 (8) |
| 79 | | | | | 79 (8) |
| 80 | | | | | 26 (4) |
| 81 | | | | | 9(2) |

Although the experimental results are discussed at full length in Chapter 5, we can already present the experimentally extracted production rate for the $^{66}$Fe isotope using the strongest registered $\gamma$-ray from its decay scheme. The Fe isotopes presented in this work were produced using resonant laser ionization and, as shown in Chapter 5, the $\gamma$-transitions from the excitation spectrum of $^{66}$Co isotopes were not observed in the off-resonance mode. Otherwise, the normalized off-resonance statistics would have to be subtracted from the corresponding on-resonance spectrum. For any given nuclide of interest the production rate per unit of charge is then obtained as

$$\mathcal{P} = \frac{\kappa_l \kappa_d \kappa_c \mathcal{A}}{\eta_p \eta_s \varepsilon_\beta \varepsilon_\gamma I_\gamma I_p \Delta t_{meas}}, \tag{4.3}$$

where $\mathcal{A}$ is the registered activity of the $\beta$-gated $\gamma$-ray of choice; $\kappa_l$, $\kappa_d$, and $\kappa_c$ are the correction factors to account for the secondary beam decay losses, dose, and cycle, respectively; $\eta_p$ and $\eta_s$ are the primary proton and secondary separator beam transport efficiencies, respectively; $\varepsilon_\beta$ and $\varepsilon_\gamma$ are the $\beta$- and $\gamma$-detector efficiencies for the activity of choice, respectively; $I_\gamma$ is the abso-

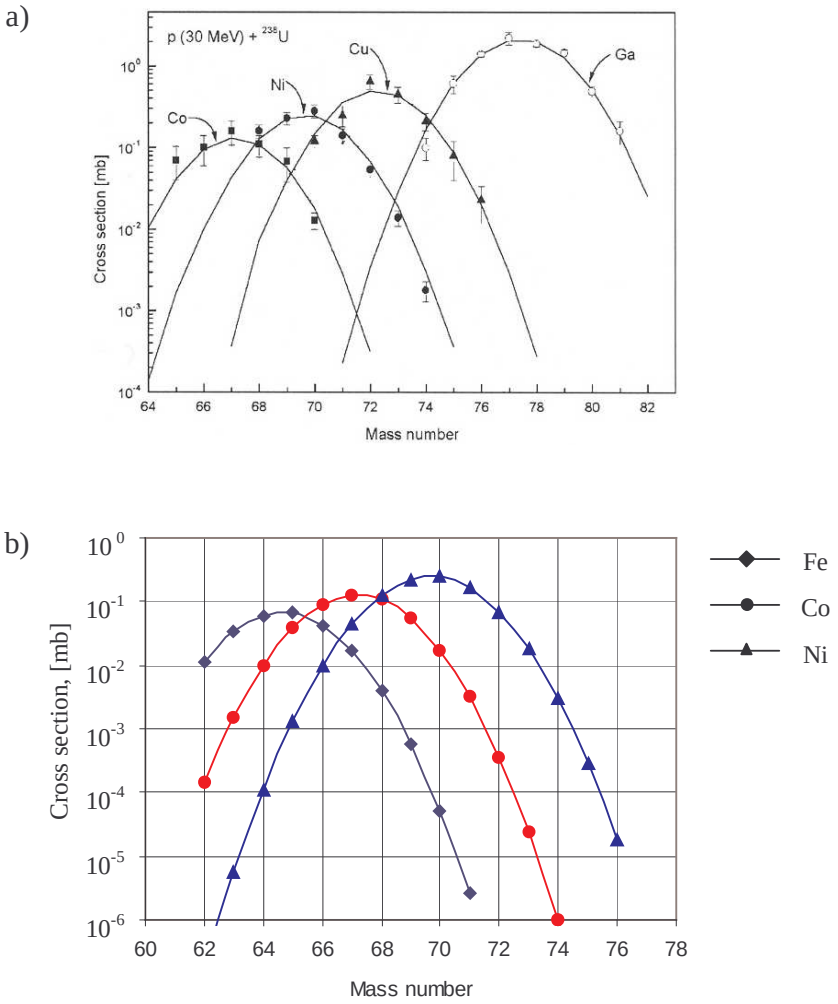


**Figure 4.8:** Calculated isotopic cross-sections for production of neutron-rich nuclei in the vicinity of the closed proton shell $Z = 28$ in the induced fission of $^{238}$U by 30 MeV protons: a) calculated distributions from [63] (solid line) together with the experimental values for $^{65-70}$Co, $^{68-74}$Ni, $^{70-76}$Cu, and $^{74-81}$Ga isotopes. The figure is taken from [62]; b) Gaussian distributions of the calculated cross-sections for Co and Ni isotopes and the extrapolated values for Fe isotopes. See text for more detail.

lute intensity of the given $\gamma$-ray; $I_p$ is the proton beam current in DC mode; and $\Delta t_{meas}$ is the total measurement time during which the activity of choice was accumulated, provided that there were no particular changes in the performance of both the beam production facility and the detection set-up. This way, we obtain the production rate for nuclei of interest that are produced and effectively ionized in the gas cell.

Because of the relatively short half-lives of the nuclei of interest, a certain part of produced ions decays during the evacuation from the gas cell. The transportation time is very small compared to the evacuation time from the gas cell, and, therefore, can be safely disregarded. In order to account for this effect, the correction factor for the decay losses is introduced and given as

$$\kappa_l = e^{\lambda T_{evac}}, \quad \lambda = \frac{\ln 2}{T_{1/2}}, \tag{4.4}$$

where $T_{evac}$ is the mean evacuation time from the gas cell and $T_{1/2}$ is the half-life of the produced nuclei of interest. In our current ion-source configuration the mean evacuation time is at the level of $\sim$500 ms.

As described in the paragraph 4.2.6, the secondary beam is not continuous but rather has a certain predefined time structure. In order to correct for such noncontinuous secondary-beam dose, the corresponding correction factor is introduced and given as

$$\kappa_d = \frac{T_\mu^{ON} + T_\mu^{OFF}}{T_\mu^{ON}} \cdot \frac{T_M^{ON} + T_M^{OFF} + \dfrac{T_{tape}}{N_M}}{T_M^{ON}}, \tag{4.5}$$

where $T_\mu^{ON}$ and $T_\mu^{OFF}$ are, respectively, the "micro on" and "micro off" parts of the primary proton beam; $T_M^{ON}$ and $T_M^{OFF}$ are, respectively, the "macro on" and "macro off" parts of the secondary beam; $T_{tape}$ is the average time needed to move the implantation tape, see 4.4.2; and $N_M$ is the number of macrocycles that defines the period of time during which the activity from the implanted secondary beam is accumulated before the tape is moved. As already mentioned in 4.2.6, the secondary beam from the ion source is provided in antiphase with the primary proton beam and, therefore, $T_\mu^{ON}$ and $T_\mu^{OFF}$ represent the microstructure of the secondary beam. In essence, this factor is the reciprocal of the ion-source duty cycle which is defined as the ratio of the working time to the total (working plus idle) time.

It is clear that, on one hand, the ion-source duty cycle must be kept as high as possible, while, on the other hand, the "macro off" part of the macrocycle must be long enough to allow the nuclei of interest to decay and, thus, their corresponding activity to be registered. Since an optimum case is usually chosen to correspond to a "macro off" part duration of 2–4 half-lives of interest, a

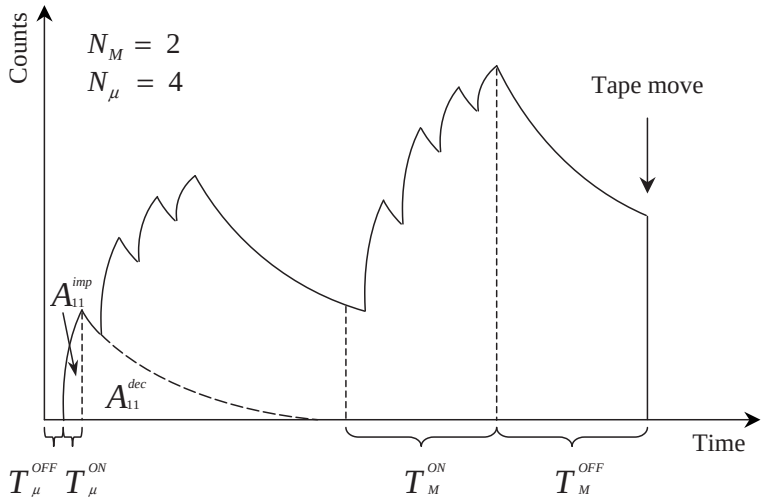


**Figure 4.9:** A schematic representation of the time distribution of an activity of choice generated in the decay of implanted nuclei of interest during $N_M$ successive macrocycles of noncontinuous implantation before the tape is moved at the end of the last macrocycle.

certain amount of nuclei of interest is bound to be still left at the end of the macrocycle and, thus, be withdrawn when the tape is moved, see Fig. 4.9. For this reason, a correction must be introduced as the reciprocal of the fraction of implanted nuclei of interest, that decayed during $N_M$ successive macrocycles of noncontinuous implantation before the tape was finally moved. This correction factor is then given as

$$\kappa_c = N_M \frac{T_\mu^{ON}}{T_\mu^{ON} + T_\mu^{OFF}} T_M^{ON} \frac{P_M}{A_{N_M}} = N_M N_\mu T_\mu^{ON} \frac{P_M}{A_{N_M}}, \tag{4.6}$$

where $N_\mu$ is the number of microcycles per each macrocycle; $P_M$ is the production rate of nuclei of interest per one macrocycle and, when provided for the time interval $N_M N_\mu T_\mu^{ON}$, it yields the number of nuclei of interest that are implanted during $N_M$ macrocycles; $A_{N_M}$ is the number of nuclei of interest that decayed during this period of time, represented by the total resultant activity

of choice that is available for registration. As can be seen in Fig. 4.9, the total activity accumulated during $N_M$ macrocycles before the tape is moved can be represented as a sum of activities accumulated during $N_M N_\mu$ microcycles with an extension of each decay time interval till the end of the last macrocycle:

$$A_{N_M} = \sum_{i=1}^{N_M} \sum_{j=1}^{N_\mu} (A_{ij}^{imp} + A_{ij}^{dec}), \tag{4.7}$$

where $A_{ij}^{imp}$ is the activity accumulated during the "micro on" implantation part of the $j$-th microcycle of the $i$-th macrocycle and must be the same for all $N_M N_\mu$ microcycles; $A_{ij}^{dec}$ is the activity accumulated during the rest of the available decay time extending till the end of the last macrocycle when the tape is moved. Since each macrocycle starts with the "micro off" part, that has no preceding "micro on" implantation part, the index $j$ in each $A_{ij}^{dec}$ starts from the second microcycle. This means that for each $ij$-th curve both the implantation and decay parts, although starting in different microcycles, have the same index $j$. It is rather clear that only in cases when $T_M^{OFF} \gg T_{1/2}$ that the difference between different activities $A_{ij}^{dec}$ can be ignored, thus, resulting in $\kappa_c \simeq 1$. For the number of nuclei $n_{ij}^{imp}$ that is produced during the $ij$-th implantation part and is still available for the decay at a time $t$ within the corresponding time interval $[t_{ij}^0, t_{ij}^0 + T_\mu^{ON}]$ we have

$$\frac{n_{ij}^{imp}(t)}{dt} = P_M - \lambda n_{ij}^{imp}(t) \tag{4.8}$$

Taking into account that $n_{ij}^{imp}(t_{ij}^0) = 0$, the solution to this equation is

$$n_{ij}^{imp}(t) = \frac{P_M}{\lambda}(1 - e^{-\lambda t}) \tag{4.9}$$

and, thus, the number of nuclei of interest, which were implanted during the $ij$-th implantation part, and, which decayed within this time interval and produced the activity of choice, is given as

$$A_{ij}^{imp} = \int_{t_{ij}^0}^{t_{ij}^0 + T_\mu^{ON}} \lambda n_{ij}^{imp}(t) dt = P_M \left( T_\mu^{ON} - \frac{(1 - e^{-\lambda T_\mu^{ON}})}{\lambda} \right) \tag{4.10}$$

Since this amount is the same for all $N_M N_\mu$ microcycles, we immediately obtain that

$$\sum_{i=1}^{N_M} \sum_{j=1}^{N_\mu} A_{ij}^{imp} = N_M N_\mu P_M \left( T_\mu^{ON} - \frac{(1 - e^{-\lambda T_\mu^{ON}})}{\lambda} \right) \tag{4.11}$$

For each $ij$-th implantation-decay curve the activity of choice accumulated from the nuclei of interest during the decay part can be obtained as a difference

between the number of nuclei that are available for decay at the end of the preceding implantation part ($t_{ij} = (i-1)(T_M^{ON} + T_M^{OFF}) + j(T_\mu^{ON} + T_\mu^{OFF}) = t_{ij}^0 + T_\mu^{ON}$) and the number of nuclei that are still left at the end of the last macrocycle ($t^{N_M} = N_M(T_M^{ON} + T_M^{OFF})$):

$$\begin{aligned} A_{ij}^{dec} &= n_{ij}^{imp}(t_{ij}^0 + T_\mu^{ON})\left(1 - e^{-\lambda[i(T_M^{ON}+T_M^{OFF})-j(T_\mu^{ON}+T_\mu^{OFF})]}\right) \\ &= P_M \frac{(1 - e^{-\lambda T_\mu^{ON}})}{\lambda}\left(1 - e^{-\lambda[i(T_M^{ON}+T_M^{OFF})-j(T_\mu^{ON}+T_\mu^{OFF})]}\right) \end{aligned} \tag{4.12}$$

Finally, using the expressions from Equations 4.11 and 4.12 in Equation 4.7 and performing simple mathematical rearrangements, we get a complete expression for the total number of nuclei of interest that decayed, thus, producing the activity of choice, during $N_M$ successive macrocycles of noncontinuous implantation:

$$\begin{aligned} A_{N_M} &= N_M N_\mu T_\mu^{ON} P_M \\ &- P_M \frac{(1 - e^{-\lambda T_\mu^{ON}})}{\lambda} \sum_{i=1}^{N_M} \sum_{j=1}^{N_\mu} e^{-\lambda[i(T_M^{ON}+T_M^{OFF})-j(T_\mu^{ON}+T_\mu^{OFF})]} \end{aligned} \tag{4.13}$$

For convenience each sum in this expression can be represented as a geometrical series converging as

$$\sum_{n=1}^{N} x^n = \sum_{n=0}^{N} x^n - 1 = \frac{x^{N+1} - 1}{x - 1} - 1 = x\,\frac{x^N - 1}{x - 1} \tag{4.14}$$

This way, the expression in Equation 4.13 finally becomes

$$\begin{aligned} A_{N_M} = N_M N_\mu T_\mu^{ON} P_M - P_M \frac{(1 - e^{-\lambda T_\mu^{ON}})}{\lambda} e^{-\lambda((T_M^{ON}+T_M^{OFF})-(T_\mu^{ON}+T_\mu^{OFF}))} \times \\ \frac{e^{\lambda N_\mu (T_\mu^{ON}+T_\mu^{OFF})} - 1}{e^{\lambda(T_\mu^{ON}+T_\mu^{OFF})} - 1} \cdot \frac{e^{-\lambda N_M (T_M^{ON}+T_M^{OFF})} - 1}{e^{-\lambda(T_M^{ON}+T_M^{OFF})} - 1} \end{aligned} \tag{4.15}$$

As can be seen, when using this expression in Equation 4.6, the unknown production rate $P_M$ of nuclei of interest per one macrocycle is canceled out.

Now, using the correction factors from Equations 4.4, 4.5 and 4.6 we can obtain the total production rate per unit of charge as given in Equation 4.3 for the $^{66}$Fe isotope produced at LISOL in induced fission of $^{238}$U by 30 MeV protons.

The second strongest 470.9 keV $\gamma$-transition from the decay of $^{66}$Fe, see Chapter 5, was taken for this purpose. The resulting value of 0.75±0.08 at/$\mu$C is ∼5.7 times lower than the corresponding value of 4.3 at/$\mu$C, arising from the extrapolation of the neighboring isotopic distributions for Co and Ni isotopes. From this we obtain that the ion-source efficiency in our experiments was ∼0.002%. Clearly, the $^{66,67}$Fe isotopes represent a certain reasonable limit in the current production of neutron-rich Fe isotopes at LISOL. For yet higher-mass isotopes, apart from the dramatically decreasing production cross-section, there will be an additional substantial reduction in production rates due to the decay losses of these shorter-lived isotopes in the gas cell. Nevertheless, provided that the ion-source efficiency is improved and our detection efficiencies are further increased, production of shorter-lived $^{68}$Fe, although being a challenge, becomes rather feasible.

Selective production of neutron-rich Fe isotopes, as well as other nuclei from the neutron-rich Ni region, at LISOL is a considerable achievement, especially when compared with available experimental yields at other laboratories. Large-scale facilities employing the conventional ISOL technique, like, for instance, ISOLDE at CERN, Switzerland, have a clear advantage over LISOL by making use of available high-energy proton beams for producing the whole range of both neutron-rich and neutron-deficient nuclei in proton-induced fission and spallation reactions in various thick targets. But since Fe, Co, and Ni are refractory-type elements and have slow release times, the resulting extraction times for the isotopes of these elements are on the level from tens of seconds to even minutes due to very slow effusion and diffusion processes in the target material. Nevertheless, as an example, the quoted production rate for $^{68}$Ni ($T_{1/2}$=29 s) at ISOLDE is $1{\cdot}10^4$ ions/$\mu$C which is higher than what we can get at LISOL. But due to the fact that the extraction times are very long, the resulting beams have an increasingly high level of contamination with isotopes of surface-ionized atoms, thus, making it difficult to perform extensive spectroscopy studies in $\beta$-decay experiments. Concerning the neutron-rich Fe isotopes, at the moment these beams are not available at ISOLDE. Another possibility is to produce the neutron-rich Mn isotopes, which during the bunching and charge-breeding stages at REX-ISOLDE would decay into corresponding Fe isobars. This is why the first intense beams of neutron-rich Fe isotopes were produced in fragmentation reactions, like, e.g., of the 60.4 MeV/amu $^{86}$Kr$^{+34}$ beam on a $^{58}$Ni target [16] at GANIL, France, or the 500 MeV/amu $^{86}$Kr beam on a $^{9}$Be target [64][35] at GSI, Germany. In both cases the experimental production rates were lower than what we have at LISOL and, as explained in section 4.1, the resulting beams produced with the IF technique have a very broad energy distribution and quite large angular divergence, thus, not allowing a detailed spectroscopy. Finally, it is worth mentioning that the production of neutron-rich Fe isotopes at IGISOL in Jyväskylä, Finland, where a

similar gas-cell configuration is used [65], is not possible at this moment without highly-selective resonant laser ionization.

With our experimental conditions at hand, the fast-release gas-cell configuration coupled with highly-selective laser-ionization provides an essential tool for selective production of radioactive nuclei with the ISOL technique. This also raises once again another important issue to consider, namely the efficiency and sensitivity of our detection set-up, which represent our ability to work with such low-intensity radioactive beams.

## 4.4 The detection set-up

### 4.4.1 Main objectives

The aim of our experiments at LISOL is decay properties and nuclear structure studies, mainly by means of high resolution $\gamma$-ray spectroscopy in $\beta$-decay. In this type of experiments both $\beta$ and $\gamma$ radiation should be registered at the same time to build a level scheme of the nucleus of interest from subsequent $\beta\gamma$-coincidences.

First of all, radioactive beams of a few tens of keV in energy and a few millimeters in spot size should be delivered to the detection point, where they must be stopped to create a point-like source of radiation. Secondly, since we mainly deal with $\gamma$-radiation detection in $\beta$-decay studies, very efficient $\beta$ and $\gamma$ detectors should be placed around the implantation point in a very close geometry. As described in Chapter 3, the true coincidence summing effects will substantially reduce the $\gamma$-ray photopeak efficiency of high multiplicity $\gamma$ cascades. To deal with this, the third objective is to increase the detection sensitivity by implementation of segmented $\beta$ and $\gamma$ detectors. Finally, another important objective is to have an acceptable energy resolution of our detectors and this is especially important for $\gamma$-radiation detection.

With these objectives at hand, a new generation detection set-up was built at LISOL using highly segmented HPGe MINIBALL $\gamma$-ray detectors. A schematic representation of the detection set-up is shown in Fig. 4.10 with a picture of it without shielding. A full description of all components of the detection set-up is given in the coming paragraphs.

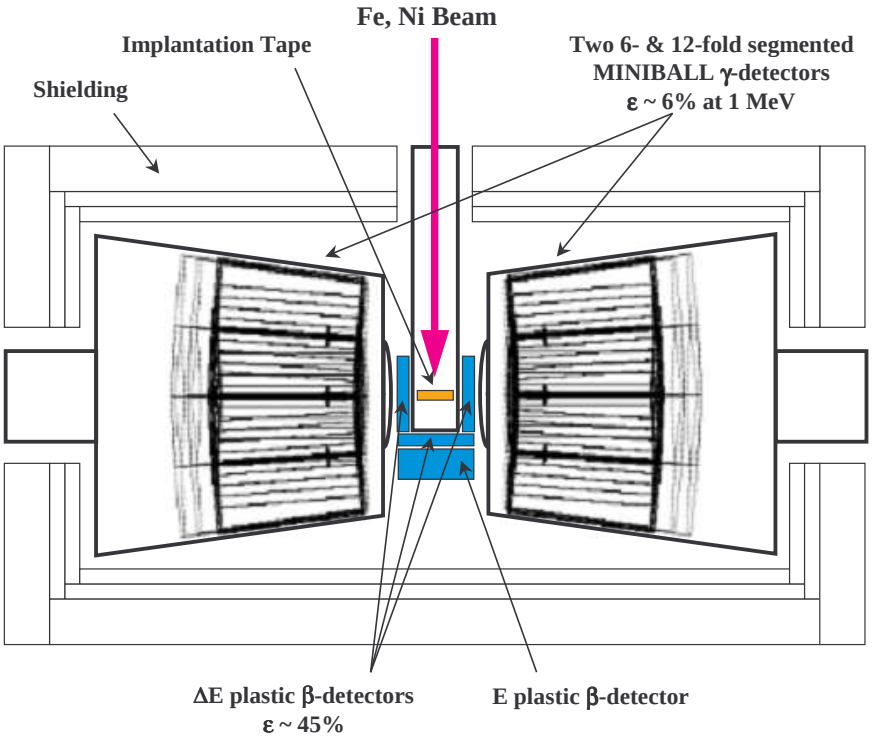


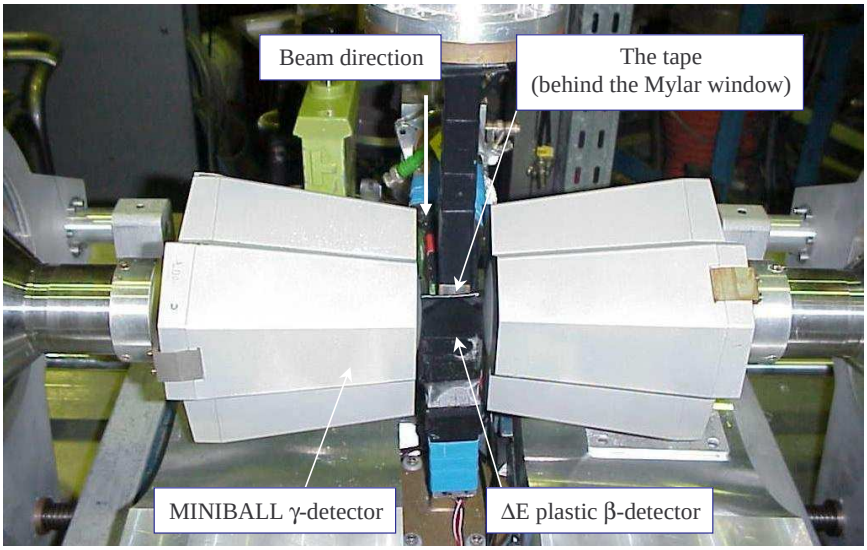


**Figure 4.10:** A schematic top view representation and a photo of the detection set-up at LISOL.

### 4.4.2 The tape system

The nuclei of interest are implanted onto a thin 1.27 cm (0.5 inch) wide aluminum-coated mylar tape. It is thick enough to fully stop the beams of 40 keV in energy. The tape system is positioned down below the detectors. The tape from the first of the two reels goes up, intercepts the beam, extends a bit farther up, and then, turning fully down, comes again below the detection level, finally ending in the second reel.

The implanted radioactive nuclei undergo $\beta$-decay, followed by subsequent $\beta$-decay of daughter nuclei down the isobaric chain. This way, long-lived nuclei closer to the $\beta$-stability line are produced in the tape, adding to the background radiation. To get rid of this long-lived activity, this part of the tape, where nuclei were implanted, is moved down to a certain safe distance of $\sim$40–50 cm away from the detection level by turning the tape reels. The tape movement is triggered after a certain manually-set number of macrocycles. The average time required for one tape move is $\sim$0.8 s. In cases when the macrocycle is not long enough compared to the half-life of nucleus of interest, there may be some activity of interest left from the previous cycle. So, another reason for moving the tape (preferably after each macrocycle) is to have a cleaner implantation-decay time behavior of activity of interest, which leads to a more precise half-life determination. At the end of its length, the tape is rewound in the opposite direction. In case when the half-life of the nucleus of interest is too short, moving the tape after each macrocycle requires more frequent rewinding of the tape, thus reducing the overall duty cycle. Taking into account all these considerations, it is understandable that the choice of the macrocycle time and the number of macrocycles per tape move strongly depends on the half-life of the activity of interest, the half-lives of the daughter isobars, precision required for the half-life determination, and the overall duty cycle.

The whole system is kept under the same vacuum as the beam transport line. There are three thin mylar windows in the structure around the implantation area of the tape to reduce attenuation of radiation of interest.

### 4.4.3 The $\beta$-detectors

Since the registration efficiency is of great concern in our experiments, both $\beta$ and $\gamma$ detectors should be placed as close as possible to the implantation point. In addition to this, we must consider that $\beta$ particles are quickly stopped in a few millimeters of solid material depending on their energies, while $\gamma$-rays can easily penetrate the surrounding structures. This means that $\beta$ detectors should be placed first next to the implantation point with $\gamma$ detectors positioned behind them. To avoid an unwanted decrease in geometrical $\gamma$-ray registration efficiency the $\beta$ detectors should be small in size and compact, thus allowing the $\gamma$ detectors to be also very close to the implantation point. A small thickness

of $\beta$ detectors also helps to substantially reduce their sensitivity to neutrons and $\gamma$-rays. It is achieved best with solid detectors like e.g. semiconductor detectors or plastic scintillators.

The NE104A plastic scintillator detectors, which were readily available from the previous detection set-up [44], were used for registration of $\beta$-particles. Three 1.3 mm thick — two 30×40 and one 19×40 mm$^2$ in area — plastic $\beta$-detectors were placed next to the three mylar windows, thus largely covering the implantation spot, see Fig. 4.10. Originally, the area of each $\beta$ detector was chosen such that it would cover the same solid angle as a coaxial $\gamma$-detector right after it, which is not the case with the MINIBALL $\gamma$-detectors. The plastic detectors were optically glued to light guides. Both plastic and light guides were tightly wrapped in a 15 $\mu$m thick reflective aluminum foil to increase the light collection efficiency and then covered by a light-tight material to avoid penetration of external light. The light guides of each individual detector were in turn glued to two photomultiplier tubes with cathodes of 6 mm in diameter. The signal-to-noise ratio of each photomultiplier tube is rather poor due to small thickness of the plastic, small area of the cathodes, and losses of light in glue junctions. A coincidence condition, set between two photomultipliers of each detector, enormously suppresses the noise, thus allowing us to set signal thresholds very low. The intrinsic efficiency of each $\beta$-detector is close to 100%, but they are slightly sensitive to $\gamma$-rays with the $\gamma$-detection efficiency of about 1–2% according to [44]. The absolute total $\beta$-efficiency in the present configuration is about 45%. The background rate from each $\beta$ detector is approximately 0.4 and 1.0 counts/s with and without the detector shielding, respectively, see paragraph 4.4.8.

In most cases $\beta$ particles deposit only a part of their energy in such a thin plastic material. For this reason, such $\beta$ detectors are also called $\Delta$E detectors. Thus, the extracted signals give information on just a change in the $\beta$-particle original kinetic energy, which is not enough for full energy determination. So, the signals from these detectors were converted to logical signals and then read out by the data-acquisition system. There is a possibility, however, to use a $\Delta$E–E telescope for full energy determination, and as a result for extraction of $Q_\beta$ values. In some runs prior to these experiments, a 5 cm thick NE102A plastic scintillator was used to construct a $\Delta$E–E $\beta$-detector array, as in Fig. 4.10.

As already discussed in Chapter 3, the implementation of segmented $\beta$ and $\gamma$ detectors can substantially increase our detection sensitivity. While having segmented $\gamma$-detectors, the implementation of segmentation for $\beta$-detection is being underway at the moment of writing.

### 4.4.4 The MINIBALL $\gamma$-detectors

To fulfil our objectives for a new $\beta\gamma$-detection set-up, coaxial HPGe $\gamma$-detectors had to be replaced with highly segmented cluster $\gamma$-detectors. Since our group is a member of the MINIBALL Collaboration, the choice for $\gamma$-detectors fell on readily available MINIBALL detectors from Canberra Eurisys [66], one of the leading manufacturers of highly segmented germanium detectors.

The MINIBALL detector in its original design [41][67][68][69] is a cluster of three encapsulated hyper-purity germanium crystals, each being six-fold segmented in the transverse plane, see Fig. 4.11. The crystals and, subsequently, the capsules are tapered to a hexagonal shape at the front to be able to fit three of them side by side to each other in a single cryostat, as in Fig. 4.12, and, thus, to avoid any losses in geometrical efficiency. Originally, the MINIBALL detectors were designed to form a $4\pi$ close-geometry germanium ball with 42 cm inner radius, thus constituting a mini-ball, and this determined the tapering angle. The relative efficiency of the tapered crystal is around 55% at 1.33 MeV. Later on, the Eurisys manufacturers, following the needs of the physicists, moved to production of twelve-fold segmented MINIBALL detectors. The sizes of the crystal and the tapering angle are the same as those for the six-fold segmented detector. Apart from the same radial segmentation into six sectors, there is an additional longitudinal segmentation into two parts of 30 mm long in the front and 48 mm long in the back. The crystals are made of n-type germanium [70][71] with impurity concentrations varying from $0.5\times10^{10}$ cm$^{-3}$ to $2\times10^{10}$ cm$^{-3}$ and exhibiting a radial rise, caused by the crystal growing process. In turn, this determines the value of the high voltage needed for an optimum charge collection. Three capsules are then placed together in the front-end cap and kept in high vacuum. The whole system, constituting a single cryostat, is attached to the liquid nitrogen dewar for cooling down. The most important dimensions of the end-cap configuration of the MINIBALL triple cluster are given in Table 4.2.

A positive high voltage of 3–5 kV, depending on the crystal, is applied to the lithium-diffused center contact, which penetrates deep inside the germanium as in the drawing in Fig. 4.11. The boron-implanted outer sides and the front of the crystal constitute the outer contact. To improve charge collection, the contacts are gold- and aluminum-evaporated for the inner and outer contacts, respectively. The actual "mechanical" contacts are constituted by spring-loaded indium coating. The segmentation is achieved by segmenting the outer contact and electrically separating all of its parts from each other. It must be done properly to avoid any inter-segment currents in the germanium material. An incident $\gamma$-ray deposits a part or all of its energy in the germanium by creating a number of electron-hole pairs, with the latter being proportional to the amount of deposited energy. Within the fully depleted region of germanium between the contacts, the created charges drift to their corresponding

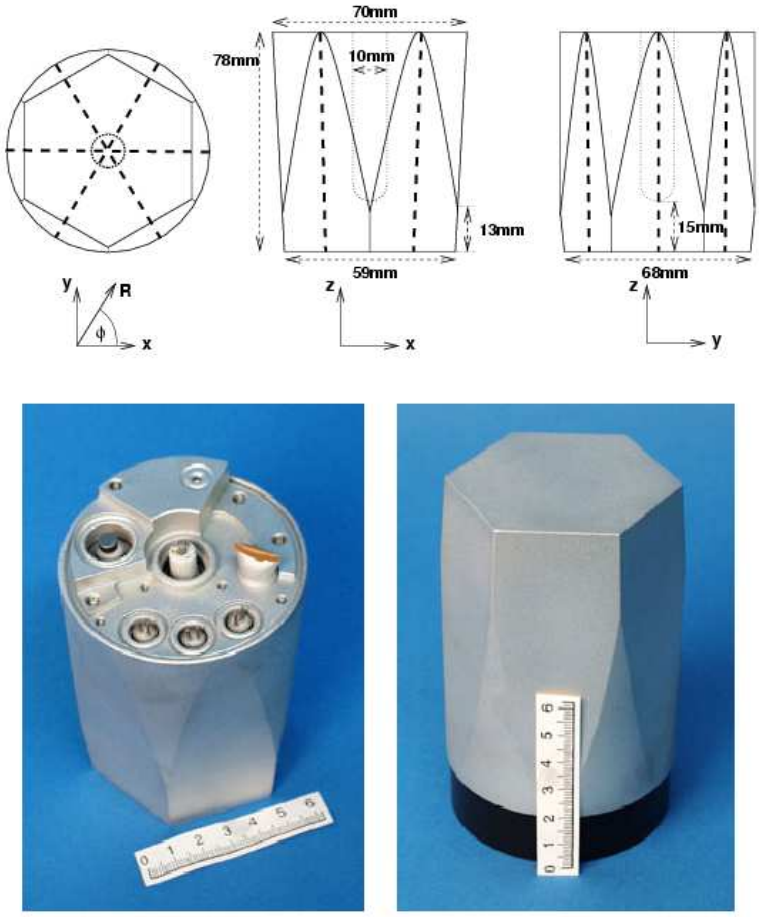


**Figure 4.11:** A picture of the MINIBALL capsule with an exact drawing of the six-fold segmented germanium crystal inside, taken from [41]. The dashed lines in the upper drawing indicate the separation between the outer segment contacts.

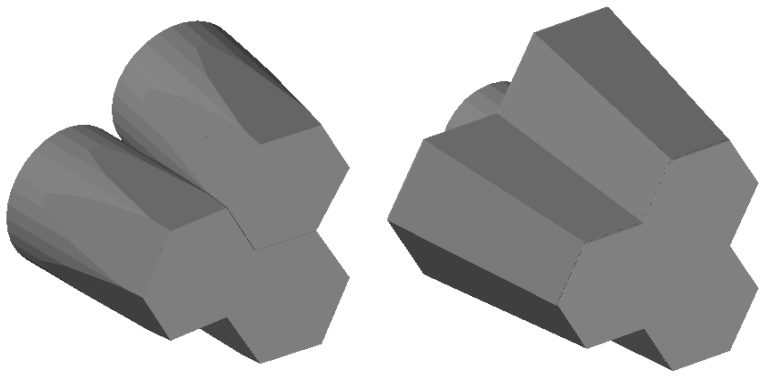

**Figure 4.12:** An arrangement of three MINIBALL capsules constituting a triple cluster in a single cryostat.

**Table 4.2:** The dimensions of the end-cap configuration of the MINIBALL triple cluster.

| Dimension | Length |
|---|---|
| The thickness of the inner contact | ∼500–1000 $\mu$m |
| The thickness of the outer contact | ∼100 $\mu$m |
| The thickness of the back side of the crystal | up to a few millimeters |
| The distance between the crystal and the capsule | 0.7 mm |
| The thickness of the capsule wall | 0.7–0.8 mm |
| The distance between the capsule and the end cap | 2.0 mm |
| The thickness of the end cap | 1.5 mm |

electrodes. This way, electrons are collected on the inner contact, constituting the so-called core signal, and the holes are collected on different segment contacts as in Fig. 4.13. Even at full voltage, which is normally a few times higher than the depletion voltage, the mobility of holes can be up to 30% lower than that of electrons. In addition to this, since the crystal is not strictly of cylindrical shape, and thus the distance between the inner and outer contacts varies, the electric field gradient is not isotropic in any given transverse plane. The electric field lines rather bend to the closest segment contacts, leaving the farthest corners of the crystal hexagon less efficient. It is worth to remember however, that apart from the collected net charge, an amount of induced charge of opposite sign will be present on most neighboring contacts, depending on the distance from the $\gamma$-ray interaction point.

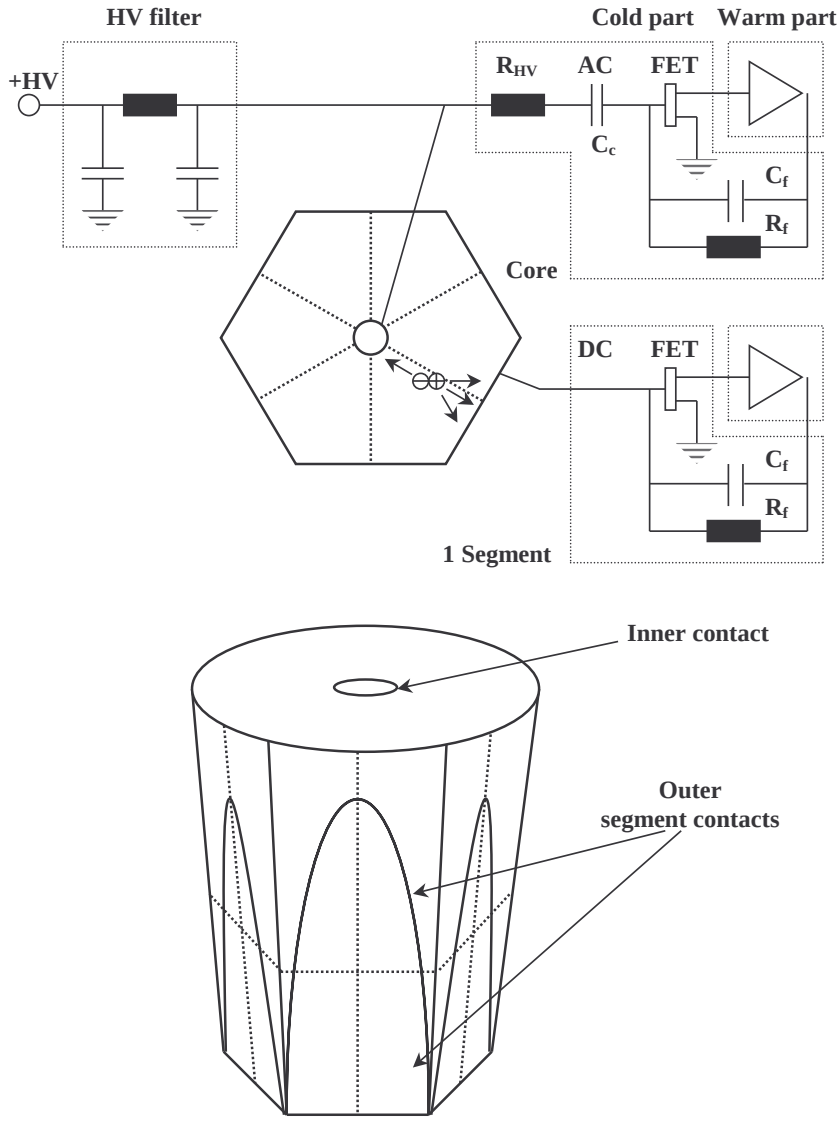


**Figure 4.13:** A schematic representation of charge collection from segmented MINIBALL detectors. The dashed lines indicate the separation between the outer segment contacts.

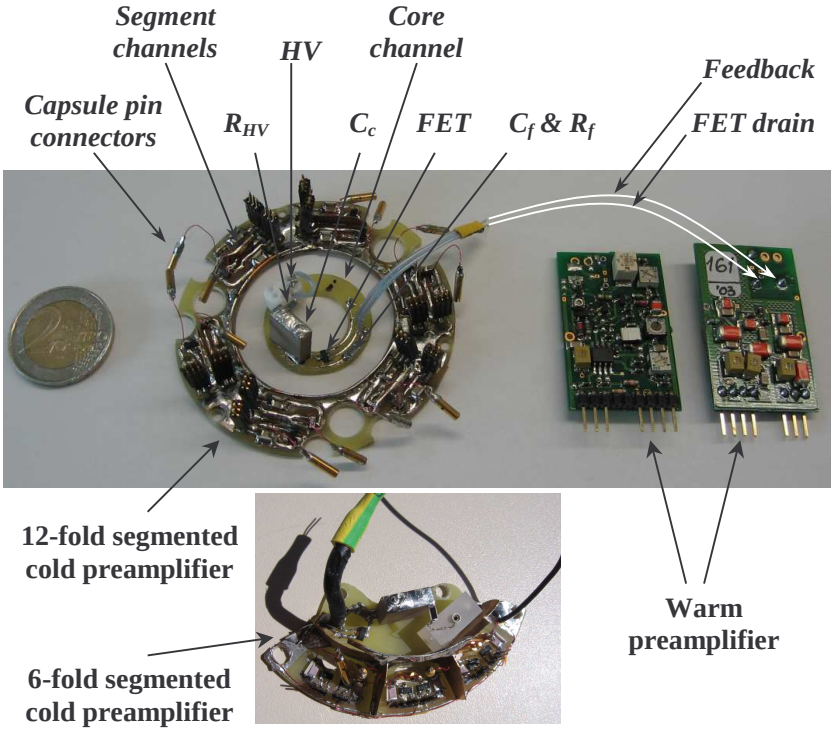


**Figure 4.14:** The MINIBALL preamplifiers.

The current of charge collected on the crystal contacts is integrated by charge-sensitive resistor feedback preamplifiers, developed and produced by one of the members of the MINIBALL Collaboration — the Institute of Nuclear Physics in Cologne, Germany, [72]. In contrast with a coaxial detector, the preamlifier is split into two stages, see Fig. 4.13 and Fig. 4.14. To reduce the thermal noise and achieve an optimum charge collection, the so-called "cold preamlifier" is placed directly on top of the capsule, and thus kept at liquid nitrogen temperature. In case of a segment channel, it consists of the IF1320 field-effect transistor (FET) of low energy consumption and the feedback circuit of 1 GOhm resistor $R_f$ and 1 pF capacitor $C_f$. Concerning the core channel, to separate the signal from the high voltage (HV), the FET is AC-coupled to the

inner contact by means of a 1.2 nF/6 kV coupling capacitor $C_c$. In addition, the 1 GOhm HV resistor $R_{HV}$ is also kept in the cold part, with the HV filter staying outside. The wiring from the contact pins of the capsule to the FETs must be as short as possible to achieve an optimum quality of charge collection, and all the junctions in the preamlifier have to be soldered properly to avoid any parasitic capacitances. It is very important at this stage to avoid any crosstalk between different channels. When the system is improperly handled, the coupling capacitor under high voltage load can spark onto the neighboring structure inside the cryostat, thus leaving a number of very sensitive FETs completely destroyed. At the output of the first stage, the FET drain and feedback signals are then provided outside the cryostat to the so-called "warm preamplifier", which is kept at room temperature. This stage further processes and amplifies the current of collected charge, and finally provides a common collection-decay signal against the ground. Such a compact system of several tens of warm preamplifiers, stacked very close to each other and operating on the same ground, is very much prone to oscillations. These high-amplitude high-frequency standing waves generate a current back to the cold preamplifiers and more often than not destroy the gate–source junction of the FETs. In this case a proper grounding of the preamplifier array becomes a very serious issue.

The charge collection time, determined by the mobility of the charge carriers and the distance between a contact and the interaction point, and thus being a property of the detector, is of the order of a few hundreds of nanoseconds. The decay part of the signal is determined by the feedback circuit of the preamlifier, with the decay time $\tau = C_f \times R_f$. This time constant of 1 ms is then reduced to 50 $\mu$s in the pole-zero cancelation circuit at the very beginning of the second stage of the preamplifier. The information on the energy, deposited by an incident $\gamma$-ray, is retrieved from the height of the output pulse. The optimum energy resolution of the detector is $\leq$2.3 keV at 1.33 MeV for the core channel, and $<$3 keV for the segments, due to an additional capacitance between the outer segment contacts and the wall of the capsule. While the net charge depends only on the amount of deposited energy, the induced charge will also depend on the distance from the corresponding contact to the interaction point, thus affecting the shape of the charge-collection part of the pulse. This gave rise to the pulse-shape analysis technique [41][67][73], which was implemented for the first time by the MINIBALL Collaboration.

The large number of channels, namely 7 or 13 per detector and, thus, 21 or 39 per cluster for the 6-fold and 12-fold segmented detectors, respectively, resulted in a highly compact system. This need for compactness and, in addition, consideration of energy consumption inside the cryostat required a home production of preamplifiers, using very sensitive components. Next to this, since so many channels have to operate against the same ground, just one faulty channel can greatly affect the stability of the whole system. In some cases,

the system has to be opened and repaired several times, before an optimum performance is achieved. Each time this requires to warm up the cluster, to carefully open the front-end configuration, to dismantle the capsules for access to cold preamplifiers, to do the repair work, to close the system, to pump it down to a high vacuum and, if needed, to outgas the interior by careful heating, and then, finally, to cool it down. In normal conditions the whole cycle takes several days to accomplish. All this implicates that to operate such a system and achieve a stable and acceptable performance requires a great deal of work and quite a good amount of certain skills.

In our set-up we use different MINIBALL detectors, depending on their availability. In 2003 our group received a new twelve-fold segmented MINIBALL triple cluster, which was finally assembled here in Leuven. Due to a lack of data-acquisition channels at that time, it was decided to couple each pair of longitudinal segments into one by providing their signals to the same FET. Thus, only the transverse six-fold segmentation was provided. In these specific experiments, presented in this work, apart from our cluster we used MINIBALL detectors from other groups of the collaboration, namely a twelve-fold segmented triple cluster from Munich and during later runs a six-fold segmented triple cluster from Heidelberg. Two six- and twelve-fold segmented MINIBALL triple clusters were placed perpendicular to the beam direction and as close as possible to the implantation spot, see Fig. 4.10. This resulted in a distance of 4.6 cm between the detector end caps.

The absolute full-energy peak efficiency curve of one MINIBALL cluster at the experimental distance is shown in Fig. 4.15. For comparison, an efficiency curve of a 90% coaxial detector, situated at a slightly closer distance, is also given. A $^{152}$Eu source was used in these measurements. It is worth to mention once again, that any multi-line $\gamma$-source introduces a problem of true coincidence summing, which depends on the multiplicity of $\gamma$-ray cascades and the detector–source geometry. Although the $^{152}$Eu source is really a bad choice for efficiency calibration, the two curves comparatively show the ratio of the intrinsic efficiency of three MINIBALL crystals to that of the 90% detector. An absolute full-energy peak efficiency of about 6% at 1 MeV for two MINIBALL clusters at the experimental distances was achieved in our experiments.

Since each MINIBALL cluster has a large number of channels, it operates at a higher liquid nitrogen consumption rate, namely several times that of a standard germanium detector. For this reason an automatic liquid nitrogen filling system had to be built, which fills the detectors every 6 hours. It operates independently and, in case when the temperature of a detector rises above a certain manually set threshold, it performs an emergency fill for that specific channel. It is also very convenient during experiments, especially when the shielding is installed around the detectors.

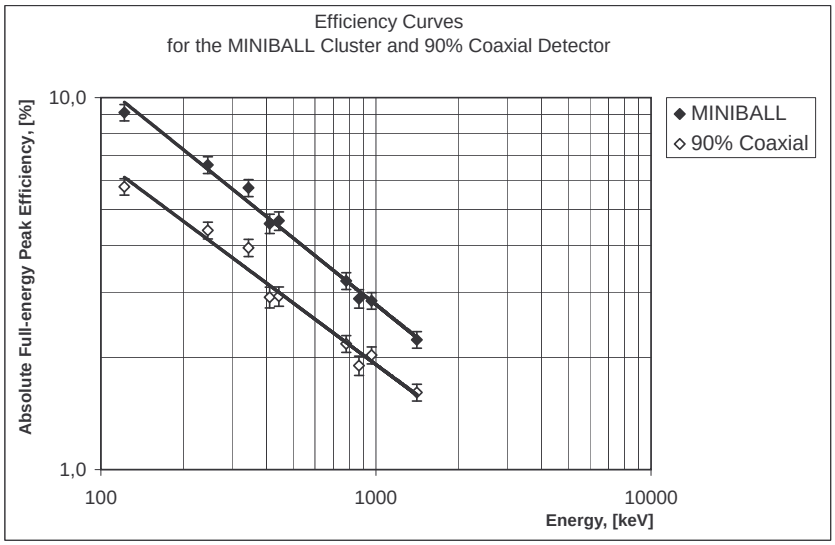


**Figure 4.15:** The absolute full-energy peak efficiencies of the MINIBALL triple cluster at the experimental distance and the 90% coaxial detector at a slightly closer distance.

### 4.4.5 The detector shielding

Apart from the fact that we have to work with low intensity beams, which are in addition contaminated with ions of the same mass-over-charge ratio as the nuclei of interest, we must also deal with the unwanted background radiation. According to its origin and based on the capability of its registration, the ambient radioactivity as a combined source can be subdivided into the following components [71]:

- *Artificial technogenic radioactivity* produced during experiments in nuclear laboratory environments:
  - *Internal* resulting from the long-lived $\beta$-decaying daughters of the nuclei of interest implanted onto, e.g., the tape.
  - *Internal–External* resulting from $\beta$-decaying long-lived radioisotopes created in neutron-capture reactions with nuclei of various materials of and in the close vicinity of the detection set-up when subjected to a neutron flux during experiments.
  - *External* resulting from various experimental activities that may take place in the laboratory as, e.g., Bremsstrahlung radiation or X-rays coming from an accelerator working nearby.

- *Natural terrestrial radioactivity* resulting from $\alpha$-, $\beta$-, and $\gamma$-decays of primordial nuclei, such as $^{40}$K or members of the $^{232}$Th and $^{238}$U chains, and radionuclides of cosmogenic origin, such as $^{60}$Co, $^{116}$In, and $^{207,208}$Bi:
  - *Internal* as being present in the constituent materials of the detection set-up, such as the plastic scintillator or photomultiplier glass of the $\beta$-detectors, various materials in the end-cap configuration of the germanium detectors, the electronic parts of preamplifiers, detector shielding.
  - *External* as resulting from the same nuclei and being present in the materials, which do not constitute the detection set-up, such as the concrete structures of the building or the ambient air. Due to the obvious self-absorption of the source ($\alpha$- and $\beta$-particles are stopped in the material), this part of the background consists almost purely of $\gamma$-radiation.
- *Natural celestial radiation* resulting from or created by the cosmic rays, consisting of the following major components:
  - *Hadronic component*, which consists mainly of neutrons (>99%) at sea level and constitutes up to 20% of the total average cosmic ray flux of $\sim$1.8 cts$\cdot$cm$^{-2}\cdot$min$^{-1}$. The cosmic neutron flux, created in reactions involving mesons and hadrons, depends on the amount of material constituting the detection set-up and various structures in its proximity.
  - *Hard component*, which consists of highly-penetrating muons and almost undetectable neutrinos. At sea level, the muon flux, created in the Earth's atmosphere from the incoming hadronic flux of predominantly (inter-)galactic origin, constitutes 60-80% of the total average cosmic ray flux and is approximately 1 cts$\cdot$cm$^{-2}\cdot$min$^{-1}$ with an average muon energy of $\sim$4 GeV and intensity distribution depending on the zenith angle as $\sim \cos^2\theta$ quite accurately up to $\sim$80° angle. Due to their mass of $\sim$207 electron masses, allowing almost no radiative energy losses via, e.g., Bremsstrahlung, a 4 GeV muon loses its energy predominantly through impact ionization with an average energy loss of 1-1.8 MeV$\cdot$g$^{-1}\cdot$cm$^2$ depending on the ambient medium.
  - *Soft component*, which consists of less-penetrating electrons, positrons, and $\gamma$-rays and at sea level constitutes 20-40% of the total average cosmic ray flux. The e$^{-/+}$, created in $\mu^{-/+}$-decay or through pair production of high-energy $\gamma$-rays, have an average energy of $\sim$70 MeV with a much narrower intensity distribution depending on the zenith angle as $\sim \cos^{8-9}\theta$. Passing through dense layers

of numerous materials of the detection set-up and structures of the laboratory building, such electrons lose their energy through the radiative process of Bremsstrahlung. Involving the subsequent process of pair production, one high-energy primary electron can generate electromagnetic cascades with a multiplicity of up to a few tens of secondary components.

Dealing with the internal part of the background radiation normally requires the use of radioisotope-free pure materials with low neutron-capture cross-section and in as small amounts as possible. During the construction of our set-up, special attention was paid to the amount and choice of materials. To substantially reduce the external background radiation incident onto the detectors, one normally needs to attenuate it by placing a passive shielding. In our case a new multi-layer shielding was constructed that covers the detectors from almost all sides, as in the drawing in Fig. 4.10.

The first outermost layer is dedicated to deal with neutrons. It consists of 50% polyethylene $(H_2C:CH_2)_x$ and 50% borax $Na_2B_4O_5(OH)_4 \cdot 8(H_2O)$ mixed with each other. The layer is at least 17.5 cm thick. Fast neutrons are moderated in the polyethylene by inelastic scattering on hydrogen atoms while thermal[1] neutrons, captured by boron nuclei, get stopped in the borax. As described in [74], there is a quick and relatively precise way to estimate thermal neutron flux within a 30% systematic error, using the 140 keV isomeric transition in $^{75m}$Ge with a half-life of 47 s, created in thermal-neutron capture by $^{74}$Ge of the $\gamma$-detector germanium material:

$$\phi_{th.n.} = \frac{\kappa_d A_{140}}{I_p \Delta t_{meas}} \cdot \frac{980}{(\varepsilon^{\gamma}_{140} + 1.6)V}, \tag{4.16}$$

where $\phi_{th.n.}$ is the thermal neutron flux given in counts$\cdot$cm$^{-2} \cdot \mu$C$^{-1}$; $A_{140}$ is the number of counts in the 140 keV peak corresponding to the isomeric transition in $^{75m}$Ge; $\kappa_d$ is the beam dose correction factor as in Equation 4.5; $I_p$ is the primary proton beam current in $\mu$A; $\Delta t_{meas}$ is the total measuring time in seconds; $V$ is the volume of the $\gamma$-detector germanium material in cm$^3$, which is, for comparison purposes, 273 cm$^3$ and 644 cm$^3$ for a 70% coaxial and one triple MINIBALL cluster detectors, respectively; $\varepsilon^{\gamma}_{140}$ is an estimation of the $\gamma$-detector intrinsic efficiency at 140 keV, given in the same reference by

$$\varepsilon^{\gamma}_{140} = 1 - \frac{1 - e^{-V^{1/3}}}{V^{1/3}} \tag{4.17}$$

[1]The name "thermal" comes from their energy being that of the room-temperature gas or material they are permeating. After a number of collisions, on average 10-20, with nuclei of surrounding materials, the neutrons, provided that they are not absorbed, arrive at this energy level, which corresponds to a speed of approximately 2200 m/s.

**Table 4.3:** The values of the thermal neutron flux in different experiments at LISOL with different detection set-ups and different neutron shieldings. In all three cases the LISOL facility was set for the induced fission of $^{238}$U by 30 MeV protons.

| Experiment Year | $\gamma$-detector | $\phi_{th.n.}$, [counts cm$^{-2}\mu$C$^{-1}$] | Improvement |
|---|---|---|---|
| 1999 | Coaxial | 0.099 ± 0.030 | 1.00 |
| 2004 | MINIBALL | 0.714 ± 0.214 | 0.14 ± 0.06 |
| 2006 | MINIBALL | 0.019 ± 0.006 | 5.23 ± 2.22 |

The extracted values for different experiments in the last several years are summarized in the Table 4.3. The first row represents one of the experiments at LISOL in 1999 when two coaxial HPGe detectors with a compact neutron shielding were used and this value for the thermal neutron flux is taken as a reference for comparison with our new shielding. The second row corresponds to one of the first experiments at LISOL, when the MINIBALL detectors were introduced in the set-up. The larger volume of germanium and by-far less compact $\gamma$-detectors required much more material for the neutron shielding. This value for the thermal-neutron flux was extracted when only a shielding against fast neutrons was installed. This way, bearing in mind that a certain fraction of fast neutrons was thermalized by this shielding, it can be used as an approximate reference to estimate the attenuation of thermal neutrons by any given neutron shielding. The last row represents one of the data sets acquired in this work. As can be seen from this table, the current neutron shielding attenuates the thermal neutron flux by a factor of ∼50 and it is approximately 5 times more efficient than in the previous set-up. As presented later in this chapter in the paragraph 4.4.8, the fraction of fast neutrons out of the total neutron flux was 24% which is more than 2 times lower than the value of 58% [75] for the previous detection set-up.

The next step is to absorb the $\gamma$-radiation in a high density material with high atomic number. The dependence of the half-thickness values for various commonly used shielding materials on the incident $\gamma$-ray energy is given in Fig. 4.16a, from which, evidently, lead represents the best choice. So, the second layer of our shielding consists of lead and is 5.5–11.0 cm thick, which means that 1 MeV $\gamma$-rays will be attenuated by a factor of ∼80–3300, respectively. Still greater thicknesses provide more attenuation of $\gamma$-rays, but also increase the probability of undesired cosmic-ray interaction within the material.

The final step is to absorb the lead $X$-rays created by $\gamma$-rays in the second layer. So, a 1.2 cm thick alloy of 65% copper and 35% zinc was chosen as the third innermost layer. All three layers are placed as close as possible to the detectors and to each other to reduce the amount of material and occupy less space.

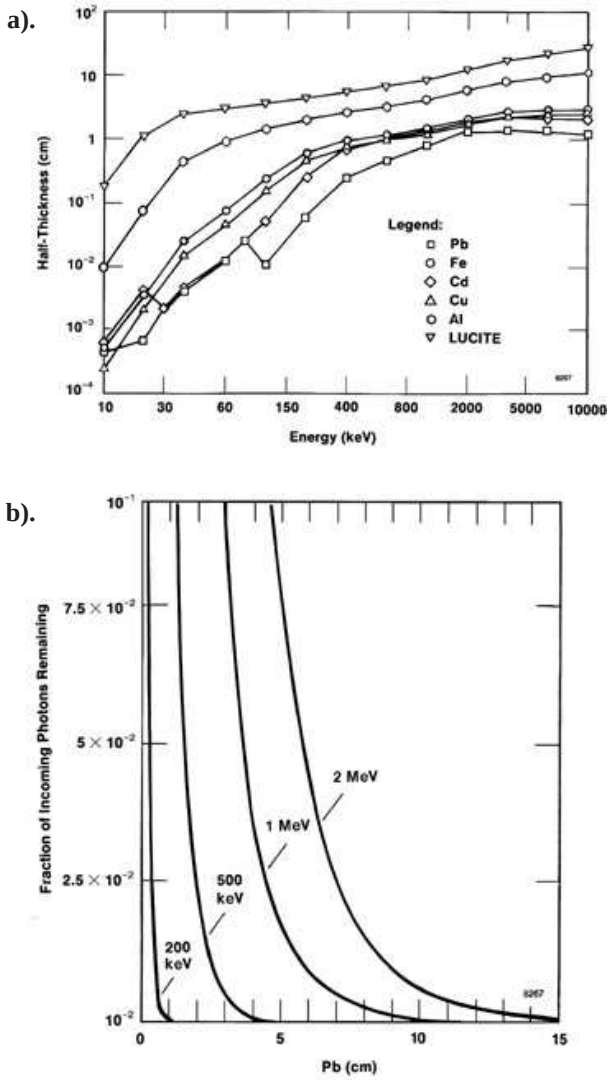


**Figure 4.16:** a). Half-thickness values vs. $\gamma$-ray energy for various commonly used shielding materials. b). The $\gamma$-ray attenuation factor as a function of the lead-shielding thickness for various energies.

The current shielding works as a simple passive attenuator of any external source of radiation except for highly-penetrating cosmic muons. The next logical step would be to implement an active shielding, when thin and compact high-Z $\gamma$-detectors of low resolution but high registration efficiency, like, e.g., bismuth germanate (BGO), would be placed all around the sides and the back of the main $\gamma$-detectors. Although mainly used as an anti-Compton shielding, it can also serve to veto out any incident background $\gamma$-rays. Similarly, large-size plastic scintillator detectors can be placed in an umbrella-like configuration on top of the passive shielding in order to trigger out the incident primary cosmic radiation. Realization of these additional improvements is highly important for the performance of our detection set-up as a low count-rate system, as discussed in the paragraph 4.4.8.

### 4.4.6 The data-acquisition system

To operate our new detection set-up, based on segmented detectors, and fully exploit the additional segment information a completely new data-acquisition system (DAQ) is required. Such system should be based on digital electronics for the following reasons. First of all, having 21 or 39 channels from each $\gamma$-detector, would require a great amount of costly analog electronics. For instance, just one $\gamma$-detector channel would need a standard spectroscopy amplifier plus an analog-to-digital converter (ADC) to extract energy information and a timing filter amplifier plus a constant fraction discriminator to extract timing information. The use of multiplexors in $\gamma$-spectroscopy with segmented detectors does not allow to extract properly the segment information. Instead, the signal from the detector preamplifier can be provided directly to a digital signal processor, where it will be sampled and stored. This way, having a running on-board software, the energy information is extracted directly from the preamplifier pulse hight and the timing information is obtained from a built-in high-precision internal clock upon the event validation. This results in a highly compact system. Secondly, the fully sampled signal preserves the information on the interplay of the collected net and induced charges, as described in 4.4.4. By means of the on-board pulse-shape analysis [41][73][67] the position information of the incident $\gamma$-rays can be extracted. Apart from that, other various on-board tasks can be performed, like, e.g., extraction of timing information by means of constant-fraction algorithms. Thirdly, if there is an additional software-controlled built-in hardware, it becomes much easier to organize a synchronous work of different modules. Finally, most of the tasks are performed by the user-controlled software. This simplifies the control over the whole system, although, on the contrary, making the data analysis more complicated.

Due to the technological progress in electronics manufacturing during the last decade or so, it has become possible to use electronics based on digital

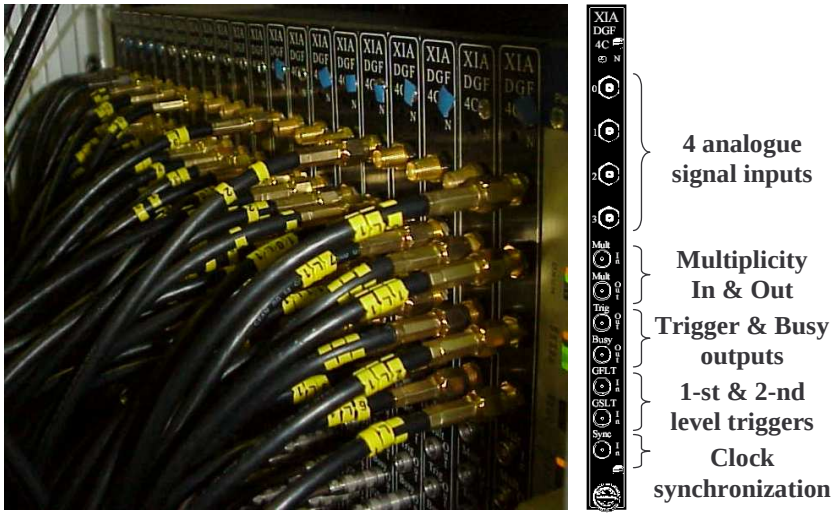


**Figure 4.17:** The array of DGF-4C modules in a single CAMAC crate as a part of the data-acquisition system.

signal processing. The most important specifications are the internal clock precision for proper signal sampling rate and the ADC resolution. The main component of our DAQ is the four channel Digital Gamma-Finder (DGF-4C or DGF) from the X-ray Instrumentation Associates (XIA) [76], which is one of the best suitable options for spectroscopy with multi-segmented HPGe $\gamma$-detectors so far. Moreover, it operates successfully with a wide variety of $\gamma$ and particle detectors using resistor feedback preamplifiers. This was found to be the best option for the MINIBALL detectors and is used extensively in our collaboration. Up to 23 DGF-4C modules can be stacked together in a standard CAMAC crate, see Fig. 4.17. Acquired data is read out from each module via the standard fast CAMAC interface by the Wiener CC32 PCI controller or the Jorway 73A SCSI controller. We found the CC32 controller to be the most suitable choice for our DAQ.

Signals from the detectors are provided to the analogue inputs of the DGFs. During the initialization at start-up, the user-defined software-set parameters, like e.g. signal polarity, baseline offset, pulse decay time, trigger channels, buffer format, as well as pulse shape analysis code are loaded into DGFs. Each DGF channel will have its own individual set of parameters. The DGF-4C incorporates four functional building blocks, which represent four stages of

signal processing as follows:

1. **Analogue Signal Conditioning**. The task of this unit (ASCU) is to adapt incoming signals to the input range of the ADC and adjust for their offsets. There is an additional computer-controlled gain stage. In order to avoid aliasing[2], the high frequency components of the incoming signals are removed in a 4-th order passive Gaussian filter. The signals are then provided to the waveform digitizing 14-bit ADC with the sampling rate of 40 MHz. Each input has its own ASCU.

2. **Real Time Processing**. This unit (RTPU), also one per input channel, consists of a field programmable gate array (FPGA) and a first-in first-out (FIFO) memory. The FIFO memory is continuously filled with the waveform data from the ADC at the full sampling rate. At the same time the signal is digitally filtered by applying a fast trapezoidal filter to detect the arrival of the signal and a slow trapezoidal filter to measure the pulse hight as in Fig. 4.18. The RTPU also contains a pile-up inspector. When a pulse is detected and passed the pile-up inspector, a trigger is issued and an interrupt request is sent to the next stage. The data remain latched until the RTPU is serviced.

3. **Digital Signal Processor**. This unit (DSP) programs the hardware of the ASCUs and RTPUs on initialization and controls the operation of the whole module. It reads raw data from all four RTPUs and stores it in memory, reconstructs true pulse hights, applies time stamps from the internal 40 MHz clock, and finally prepares the data for output to the host computer.

4. **CAMAC Interface**. The host computer communicates with the DGF via the 16-bit level-1 fast CAMAC interface, which supports up to 5 Mbyte/s data transfers.

The fact that all stages operate almost independently from each other allows to digitally process the accepted pulse while the next one is acquired. Additionally, since we deal directly with the preamplifier signal and the decay time parameter is known, we can easily distinguish between the piled-up signals as in Fig. 4.18, which would be normally rejected by the analogue electronics. As a result, one DGF module can operate at up to 200 kHz count rate. The readout from all DGFs and storing to the host computer takes a few milliseconds, and this becomes almost the only source of the total acquisition dead time.

[2]Aliasing is an effect that causes different continuous signals to become indistinguishable (or aliases of one another) when sampled. E.g., improper sampling of the analog signal will cause high-frequency components to be aliased with genuine low-frequency ones, and be incorrectly reconstructed as such. To prevent this problem, the signals must be appropriately filtered, before sampling.

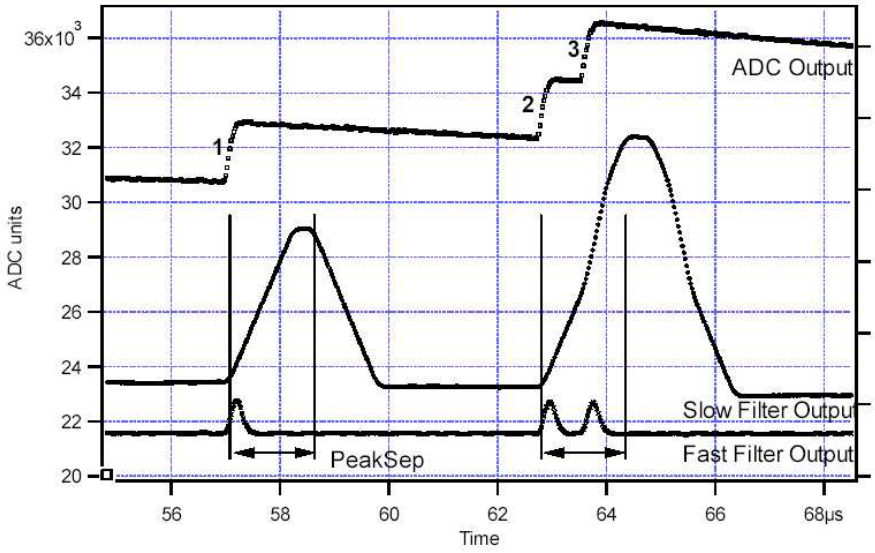


**Figure 4.18:** A sequence of 3 $\gamma$-ray pulses separated by various intervals to show the origin of pile-up and demonstrate how it is detected by the DGF-4C. The picture is taken from [77].

Since an incident $\gamma$-ray is registered by both the core and some of the segments of the same crystal, there is a timing correlation between the signals from one crystal. Further on, there should be no signal from a segment, unless there is a signal from the core of the same crystal. For these reasons, the DGFs, which are used to process the MINIBALL $\gamma$-detector signals, are split into trigger groups, so that one group represents one crystal. This is achieved by the daisy chain connection on the back panel of the modules. This way, 2 or 4 DGF modules are needed for one 6- or 12-fold segmented MINIBALL crystal, respectively. The core channel is set as the main trigger of the group. In case when a number of coaxial detectors is used, their signals can be provided to the same DGF module with their corresponding inputs set as independent triggers. The logical signals from three $\beta$-detectors are provided to one DGF and their inputs are set independently. To estimate the total acquisition live-time a pulser signal feeds one channel of a separate DGF. This value is represented by the ratio of the registered pulser signals to the total number of issued pulses.

When operating many DGFs in a system, it is required to synchronize their

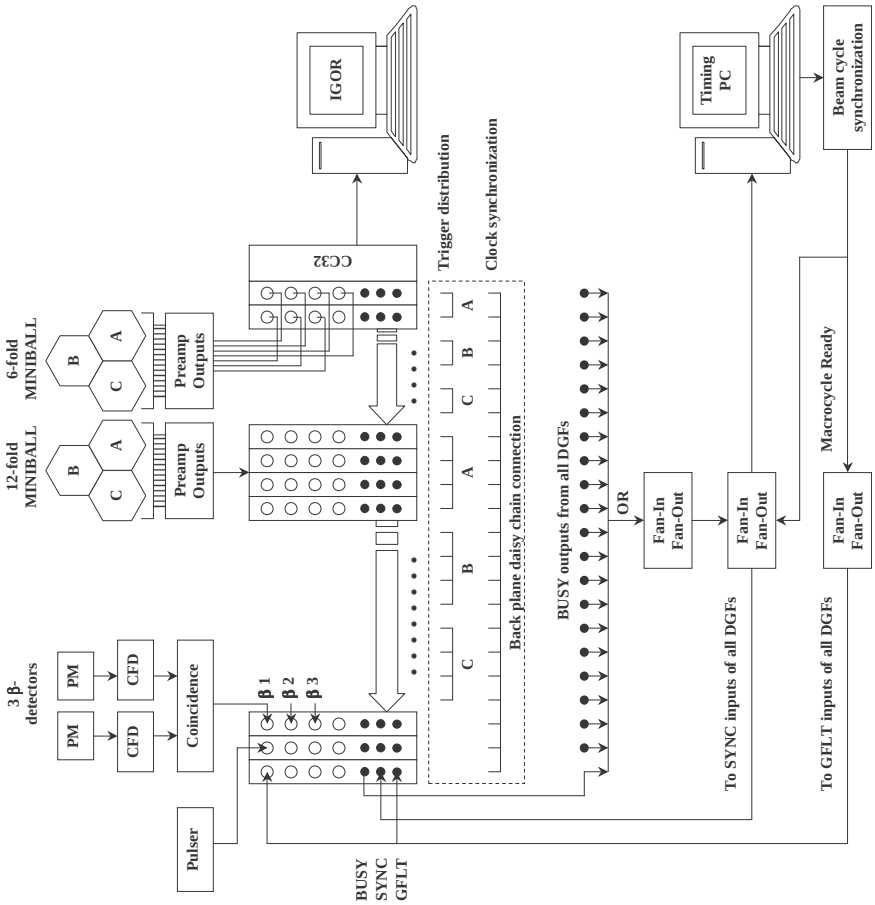


**Figure 4.19:** A schematic representation of the DAQ.

clocks and timers. In addition, the triggers should be distributed between the group modules. As already mentioned, this is achieved by the backplane daisy chain connection. While the clock is distributed between all modules, the trigger distribution should be done only between the members of the trigger group. To ensure that runs start and stop synchronously in all modules, the so called "BUSY-SYNC" loop should be used. The "BUSY" outputs, see Fig. 4.17, from all modules should be OR'ed together and the result should be routed back to the "SYNC" inputs of all modules. This way, when a run is started, the whole system waits until all modules execute their initiation sequence. Conversely, by the same mechanism, the first module to end the run will stop all other modules. This also means that when a buffer of just one module is filled a readout from all DGFs is initiated. The "SYNC" signal is also sent to the timing PC that controls the beam cycle, see 4.2.6, to start the macrocycle at the same time as the run. To have a proper implantation-decay curve of the signals from the activity of interest the DAQ readouts should be synchronized with the beam structure. For this reason, the timing PC issues a Global First Level Trigger (GFLT), which is split to provide it to the GFLT input of each DGF module. The simplest DGF buffer format allows to store 744 events. Usually having a low count rate, this is enough for a macrocycle of the order of several seconds. So, the readout is normally forced after each macrocycle. To have a precise timing information of the beginning of the macrocycle, the GFLT signal is also sent to an input of one dedicated DGF and, thus, is present in the output data. It is worth mentioning that the GFLT trigger from the timing PC also incorporates the signal from the tape system. When the tape needs to be moved, the macrocycle is not started until the tape system is ready.

For further and complete information on the operation of the DGF-4C modules the reader is referred to [77]. A schematic representation of the DAQ is given in Fig. 4.19. To set the DGF parameters and to acquire data we use the IGOR software, which is provided by XIA.

The characteristic distributions of $\beta$-$\gamma$- and $\gamma$-$\gamma$- coincidence events for one of the data sets ([67/Fe/10/0/1]) are shown in Figure 4.20. As can be seen, the ratio of (prompt-)peak-to-random coincidences is 968$\pm$31 and 733$\pm$5, respectively. The timing information was derived by DGFs merely upon signal arrival by means of the leading edge algorithm. This way, the timing resolution depends on i) the signal amplitude, ii) the distance between the interaction point of the incident $\gamma$-ray and the corresponding contact where the created charge is collected or, in other words, pulse shape, and iii) the divergency of the electric field, especially in the weak corner regions of the MINIBALL crystal. All this results in the so-called leading-edge timing "walk" due to pulse amplitude and shape variations [71]. This way, low- and high-amplitude signals result in, respectively, "later" and "earlier" arrival times. For this reason, the FWHM's for the $\beta$-$\gamma$- and $\gamma$-$\gamma$-coincidence distributions are $\sim$95 ns and $\sim$210 ns, respec-

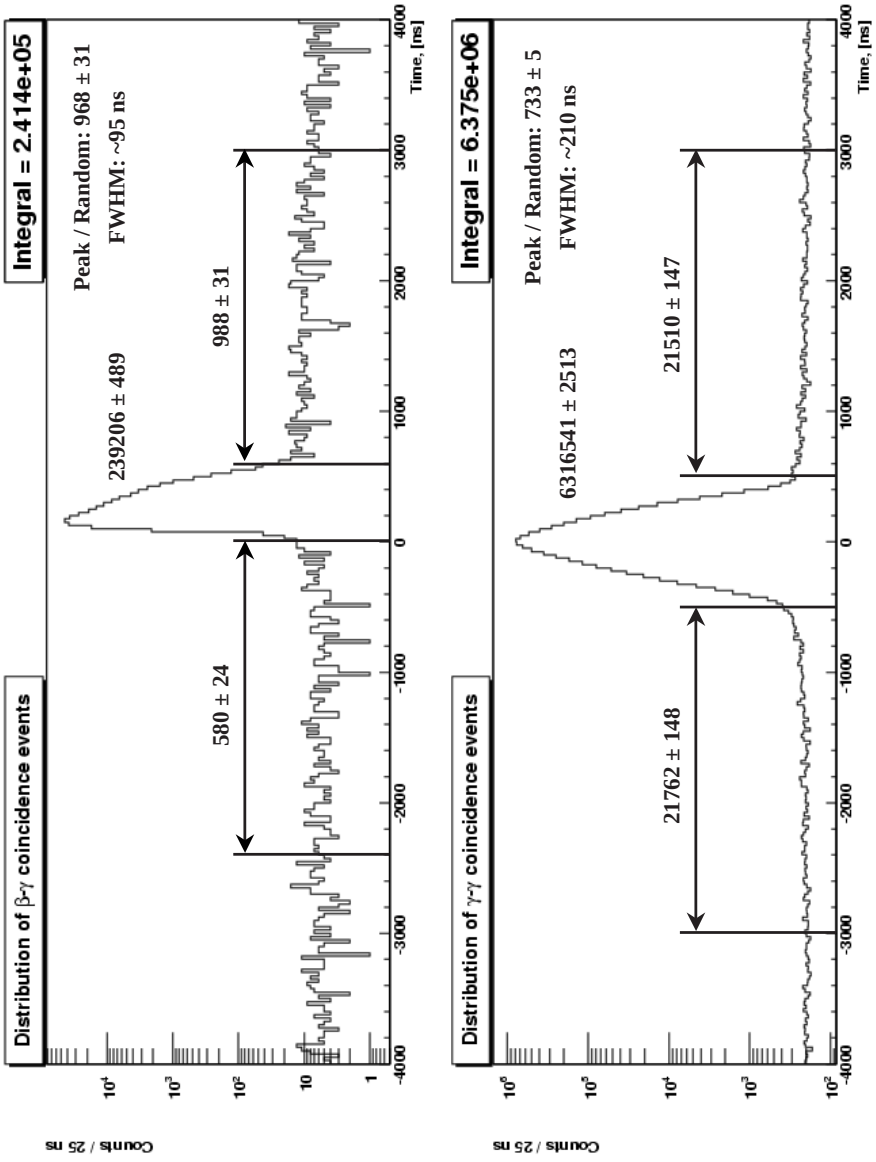


**Figure 4.20:** Time distributions of $\beta\gamma$- (upper plot) and $\gamma\gamma$- (lower plot) coincidence events for the data set [67/Fe/10/0/1].

tively. It is rather obvious that the constant-fraction algorithm must be used instead, which to a rather good approximation depends only on the mobility of the charge carriers, and, as quoted in [67], the DGFs can yield a timing resolution of ∼14 ns. Due to the fact that in our case it failed for low-energy $\gamma$-detector signals, this algorithm was not used in the experiments presented in this work. The current timing resolution for coincidence event distributions can still be more than satisfactory for low count rate activities, resulting in very low rates of random coincidences as in these experiments. But, unquestionably, there will be severe consequences for very high count rate activities. Staying in close contact with the manufacturers from the XIA, further work on the proper implementation of the constant-fraction algorithm was carried out, revealing a bug in the internal code of the DGF-4C modules. As a result, the timing resolution was brought to the level of ∼15 ns.

### 4.4.7 Data analysis

The DGF-4C modules accept all incoming signals unless they are rejected by the external GFLT or GSLT gates. In our case all signals are accepted, except those from the segments in absence of their corresponding core signals. The only signal preconditioning originates from the adaptation of the signals to the ADC range, by means of the baseline offset and gain. This means that there will be a lower and upper energy limits imposed on the signals. Such energy spectra without any external trigger or coincidence conditions are known as singles.

The readout is performed by the CC32 CAMAC controller from all DGF-4C modules in the crate and the content of the DGF buffers is written via a PCI port onto the hard disc of the DAQ computer. Since the fast 16-bit CAMAC interface is used, the data are written in 2-byte words. The DAQ output data format together with the subsequent DGF-4C formats is presented in Fig. 4.21. It is simply a sequence of buffer contents of each DGF-4C module. Each DGF buffer consists of a header and the actual event data. The buffer header contains the information on its length in 2-byte words, the DGF module number, the DGF output data format, and the 48-bit time when the buffer was open for acquiring the data. The DGF buffer data consists of a sequence of acquired events. In turn, each event data consists of a header and channel data and represents the XIA DGF-4C output data format which has four main types. The event header contains the information on when the event was registered (32-bit time) and what channels of this specific DGF module accepted a signal at that time, represented by the so-called hit pattern. In case of a trigger group, the event time is always given by the main trigger channel (in our case a core signal) and the hit pattern represents the channels that were fired during this event (the correlated core and segment signals). Based on the hit pattern, the channel data is a sequence of data from each fired channel of the DGF module.

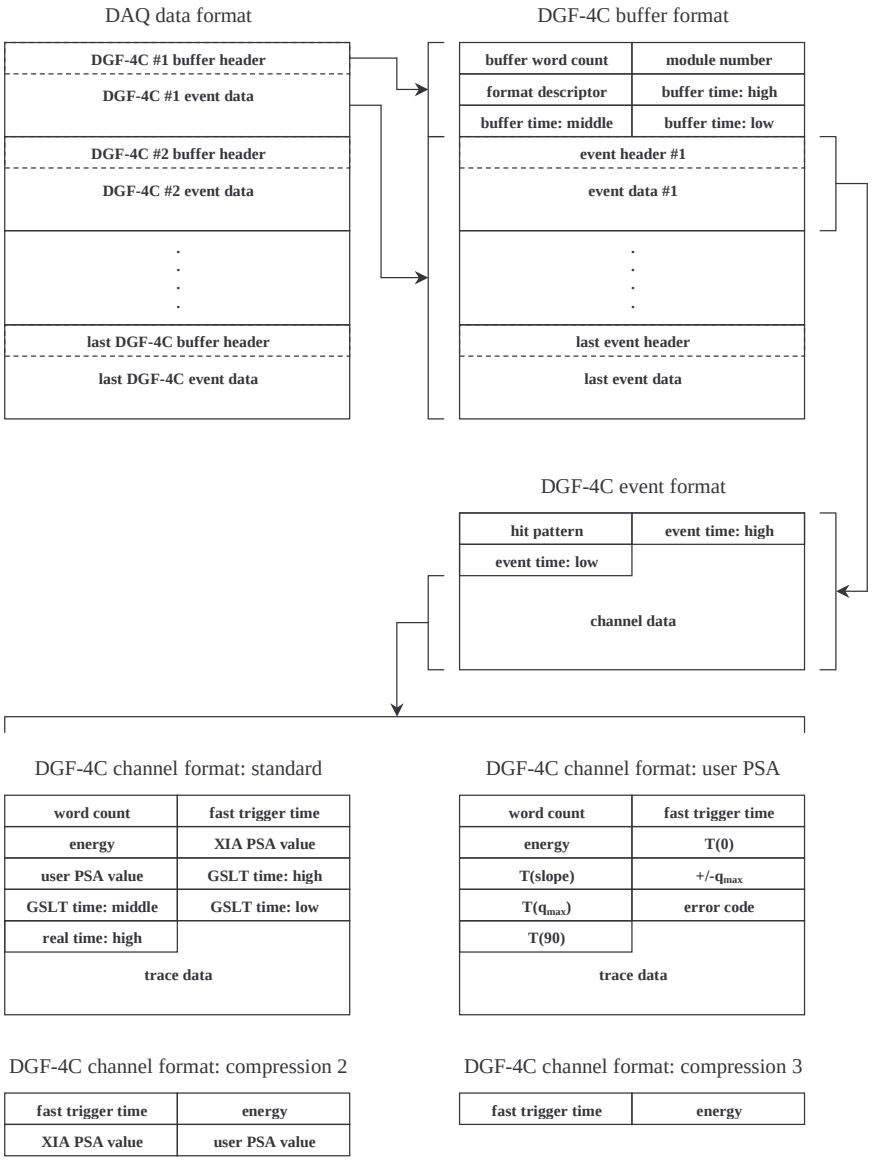


**Figure 4.21:** The DAQ data format with the subsequent DGF-4C formats.

Based on the format descriptor given in the buffer header, it is one of the four main XIA DGF-4C format types. The first two format types are related to the on-line live time determination and off-line pulse-shape analysis (PSA) and have an option of storing the signal traces. In our DAQ the compression level 2 and 3 data formats are used. Both formats contain the information of the 16-bit fast trigger time of signal arrival and signal energy in ADC channels. The compression level 2 format also provides the results of on-line codes, e.g. PSA or constant fraction algorithm.

A new C++ software code was written to read and analyze the data acquired by our new detection set-up. The object oriented ROOT package [78] developed in CERN is used for building the output histograms. While building the singles is a straightforward procedure, the $\beta$-n$\gamma$ and n$\gamma$ coincidences, where n represents the number of $\gamma$-detectors (crystals), are based on the event time stamps. These coincidences are stored in the ROOT trees for further analysis.

### 4.4.8 Performance of the current detection set-up as a low count-rate system

At this moment, it is important to outline various aspects of the performance of our current $\beta\gamma$-detection set-up, in essence, aimed at being a low count-rate detection system.

The characteristic total macro and microcycle distributions of single and coincident events from $\gamma$- and $\beta$-detectors during production of the radioactive beams at LISOL in induced fission of $^{238}$U by protons of 30 MeV in energy and 5 $\mu$A in intensity are shown in Fig. 4.22 for the data set [67/Fe/10/0/1][3]. The corresponding single $\gamma$-spectra during the micro ON and OFF parts of the macrocycle are given in Fig. 4.23 and Fig. 4.24, where the single $\gamma$-spectrum from the background run in the absence of both secondary and primary beams is included for comparison purposes. The corresponding event rates for all four distributions in Fig. 4.22 during different time periods are given in Fig. 4.25. For comparison purposes, the event rates from other data sets are also included.

As can be seen from Fig. 4.22, the count rates from $\beta$- and $\gamma$-detectors are much higher during the proton beam ON parts of the implantation part of the macrocycle, namely by factors of $\sim$2 and $\sim$15, respectively. From the single $\gamma$-spectra in Fig. 4.23 and Fig. 4.24, the count rate of the continuum as well as the 511 keV annihilation peak from the micro ON parts of the macrocycle is more than one order of magnitude higher than the corresponding count rate from the micro OFF parts, resulting in a ratio of $\sim$10 at low energies and growing to $\sim$25 at higher energies above 3 MeV. For comparison, the $\gamma$-event statistics

[3]For the purpose of clarity and conciseness throughout this work, the following abbreviation of the data sets is adopted: ["Separator mass-over-charge ratio"/"Laser-ionized element or OFF if none"/"Macrocycle implantation time"/"Macrocycle decay time"/"Number of macrocycles per tape move"]

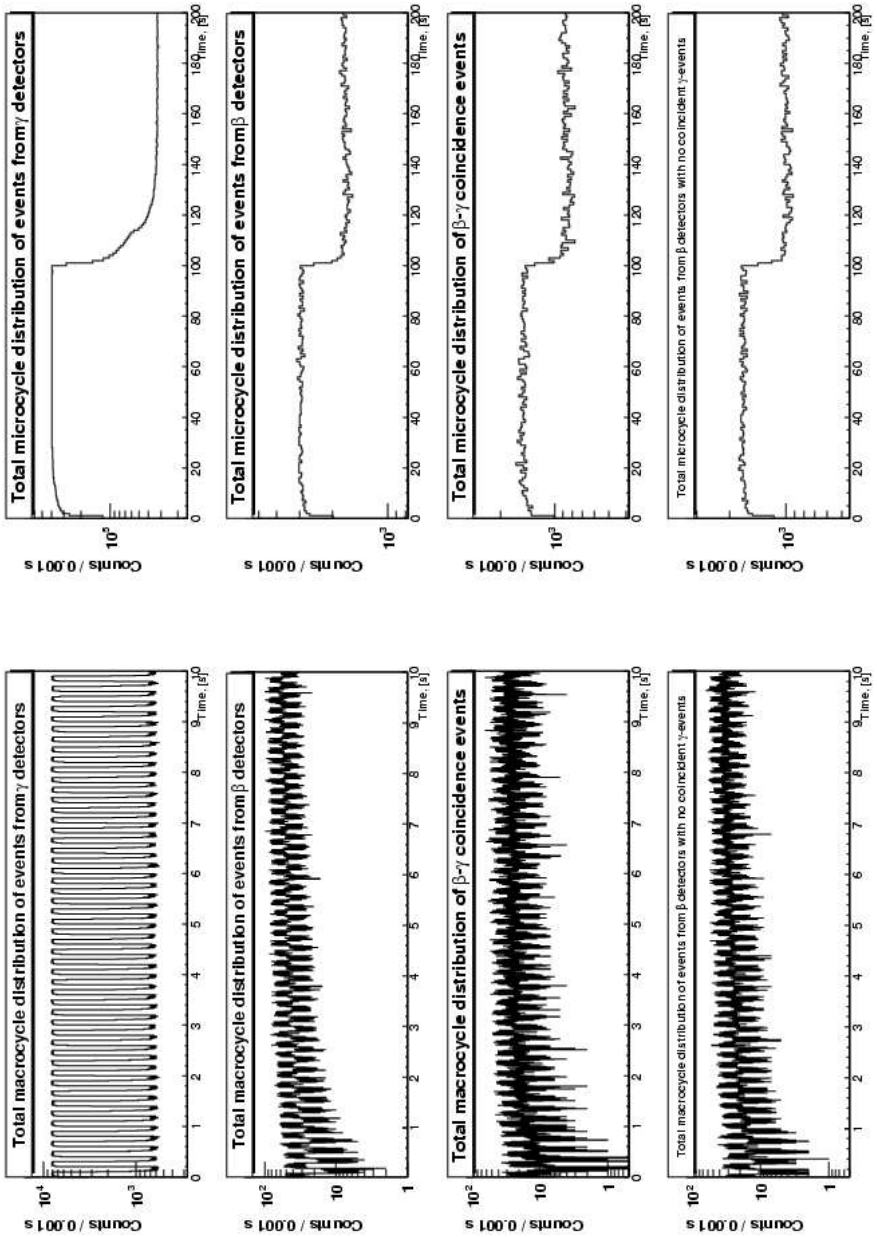


**Figure 4.22:** Total distributions of single and coincident $\beta$- and $\gamma$-events within macro and microcycles for the data set [67/Fe/10/0/1]. The plots on the right represent time distributions of corresponding events from all microcycles summed together.

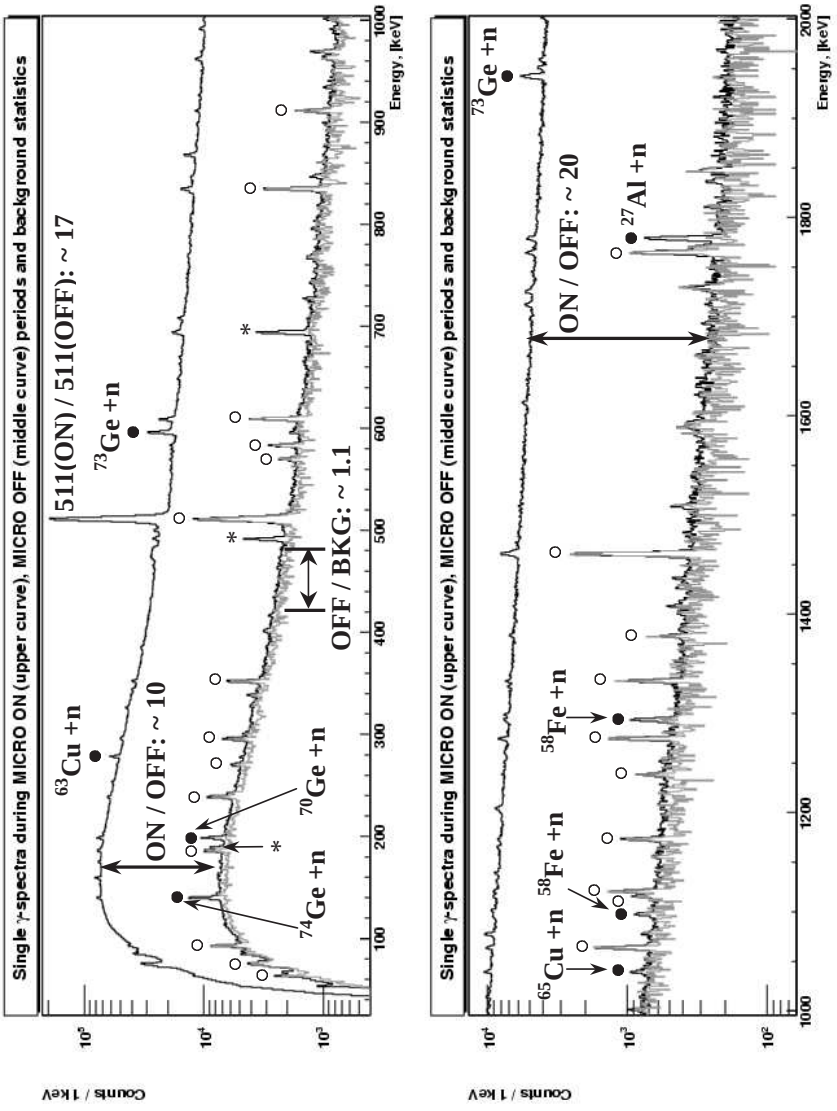


**Figure 4.23:** Single $\gamma$-spectra during the micro ON (upper curve) and OFF (middle curve) parts of the macrocycle for the data set [67/Fe/10/0/1]. Due to the remaining neutron flux after each micro ON part, the first 15 ms of each micro OFF part were excluded. For this reason, the lower curve was up-scaled by a factor of 100/85. For comparison purposes, the single $\gamma$-spectrum from the background run in the absence of both secondary and primary beams (lower curve) is included and up-scaled on the basis of its collection time. Here, the open and closed circles represent most visible $\gamma$-transitions from the natural-radioactivity and neutron-induced background radiations, respectively, while the stars indicate the $\gamma$-transitions originating from the $\beta$-decay of implanted nuclei of the beam.

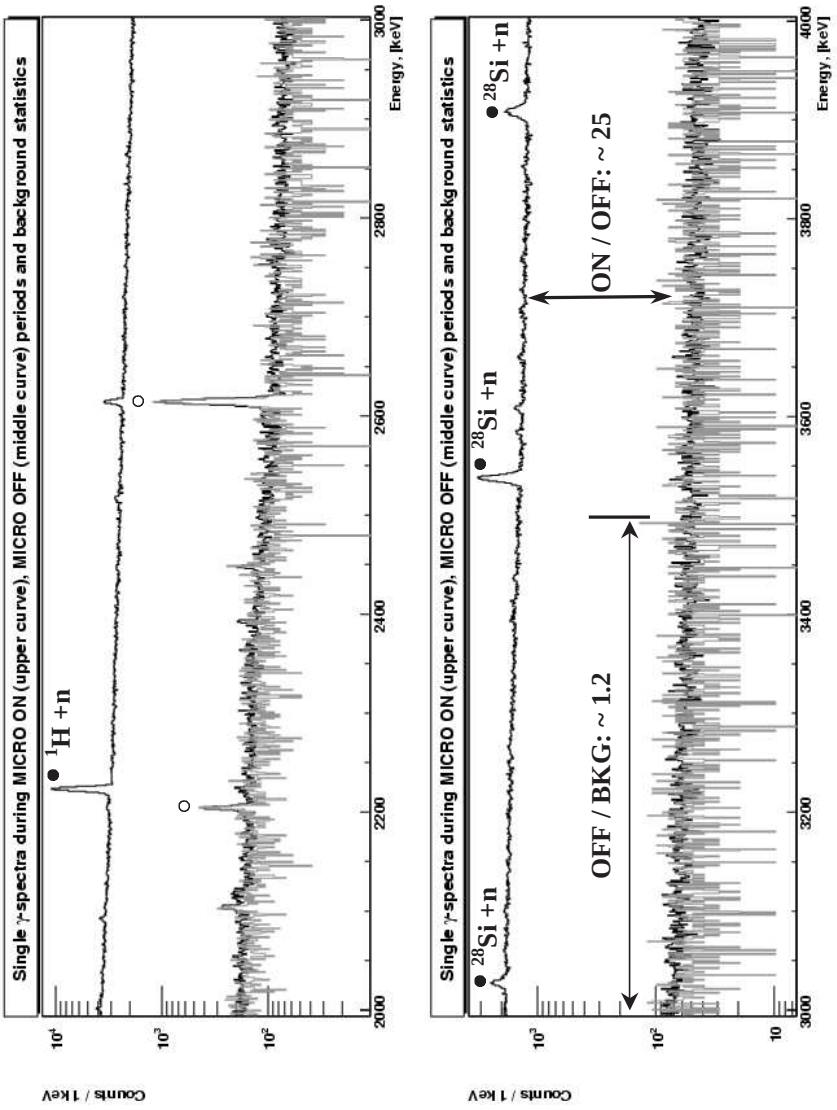


**Figure 4.24:** Continuation of the Fig. 4.23.

| Data Set | Beam Period | Time Slice, [ms] | Event Rate | | | Mγ(β-γ) | Mβ |
|---|---|---|---|---|---|---|---|
| | | | Single γ | Single β | β-Coincident γ | Single β with no γ | | |
| [ 67 / Fe / 10 / 0 / 1 ] Ip = 5 μA | Total | Total | 221,43 (0,03) | 2,44 (0,01) | 1,21 (0,01) | 1,40 (0,01) | 1,35 | 1,04 |
| | MACRO ON Micro ON | 0 - 100 | 398,31 (0,06) | 3,08 (0,01) | 1,53 (0,01) | 1,75 (0,01) | 1,33 | 1,04 |
| | MACRO ON Micro OFF | 100 - 115 | 98,57 (0,08) | 1,91 (0,01) | 0,96 (0,01) | 1,10 (0,01) | 1,37 | 1,03 |
| | MACRO ON Micro OFF | 115 - 200 | 35,02 (0,02) | 1,78 (0,01) | 0,89 (0,01) | 1,04 (0,01) | 1,38 | 1,03 |
| [ 67 / OFF / 10 / 0 / 1 ] Ip = 5 μA | Total | Total | 225,22 (0,09) | 2,02 (0,01) | 0,94 (0,01) | 1,20 (0,01) | 1,36 | 1,04 |
| | MACRO ON Micro ON | 0 - 100 | 406,03 (0,17) | 2,66 (0,01) | 1,24 (0,01) | 1,56 (0,01) | 1,33 | 1,04 |
| | MACRO ON Micro OFF | 100 - 115 | 99,77 (0,21) | 1,47 (0,03) | 0,70 (0,02) | 0,89 (0,02) | 1,44 | 1,04 |
| | MACRO ON Micro OFF | 115 - 200 | 34,63 (0,05) | 1,35 (0,01) | 0,62 (0,01) | 0,84 (0,01) | 1,41 | 1,03 |
| [ 67 / Co / 2 / 2 / 3 ] Ip = 5 μA | Total | Total | 123,48 (0,03) | 1,49 (0,01) | 0,76 (0,01) | 0,86 (0,01) | 1,35 | 1,04 |
| | MACRO ON Micro ON | 0 - 100 | 394,22 (0,12) | 2,67 (0,01) | 1,33 (0,01) | 1,36 (0,01) | 1,32 | 1,05 |
| | MACRO ON Micro OFF | 100 - 115 | 85,76 (0,14) | 1,45 (0,02) | 0,72 (0,01) | 0,76 (0,01) | 1,34 | 1,04 |
| | MACRO ON Micro OFF | 115 - 200 | 31,87 (0,04) | 1,41 (0,01) | 0,71 (0,01) | 0,74 (0,01) | 1,35 | 1,03 |
| | MACRO OFF | 2000 - 4000 | 29,88 (0,02) | 1,05 (0,01) | 0,49 (0,01) | 0,67 (0,01) | 1,39 | 1,04 |
| Ambient Room Background | Total | Continuous | 30,01 (0,05) | 0,42 (0,01) | 0,20 (0,01) | 0,27 (0,01) | 1,63 | 1,08 |

**Figure 4.25:** The cumulative rates of the single and coincident $\beta$- and $\gamma$-events within different time intervals of the macrocycle for various data sets. Here $M_\beta(\beta\gamma)$ and $M_\gamma(\beta\gamma)$ are, respectively, the $\beta$- and $\gamma$-detector multiplicities in $\beta$-$\gamma$-coincidences.

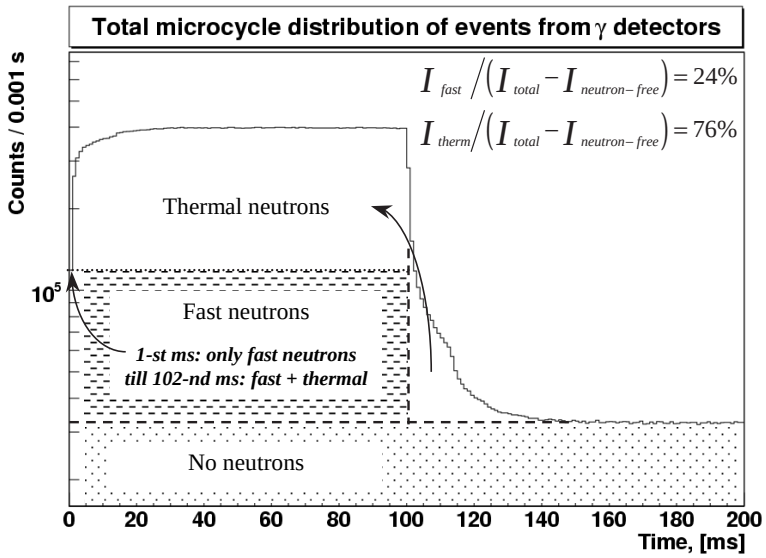


**Figure 4.26:** The microcycle distribution of single $\gamma$-events as on the upper right in Fig. 4.22.

from the micro OFF parts of the macrocycle is at maximum 20% higher than that from the background run. Since the radiation of interest would have half-lives of the order of hundreds of milliseconds or seconds, as clearly seen from the total growing trend of the $\beta$-count rate during the implantation period, such a sudden change in the count rate between the micro ON and OFF parts of the macrocycle can only be attributed to the beam-related activity, namely the neutron-induced $\gamma$-radiation. This way, the statistics during the micro ON parts comes largely from the neutron-induced prompt $\gamma$-rays following the neutron capture by or scattering on various stable nuclides with high neutron-capture or scattering cross-sections, respectively, such as $^{1}$H, $^{27}$Al, $^{28,29,30}$Si, $^{54,56,57,58}$Fe, $^{63,65}$Cu, $^{70,72,73,74,76}$Ge, which constitute some of the most common materials used in our detection set-up. The neutron-induced $\gamma$-transitions in the spectra from the micro OFF parts or even the background run originate from the $\beta$-decay of unstable nuclides, such as $^{28}$Al ($T_{1/2}$=2.246 m), $^{59}$Fe ($T_{1/2}$=44.503 d), $^{66}$Cu ($T_{1/2}$=5.1 m), $^{75m}$Ge ($T_{1/2}$=47 s) formed in neutron-capture by their neighboring stable isotopes. All this shows that in the data analysis the $\beta$-gated $\gamma$-events can be taken from both proton beam ON and OFF parts of the microcycle, while the long-time [$\beta$-$\gamma$]-correlated $\gamma$-events must be

taken only from the macro ON micro OFF and macro OFF parts of the macrocycle with an additional exclusion of the first 15 ms of each micro OFF period.

The presence of the neutron flux is clearly revealed from the behavior of the microcycle time distributions in Fig. 4.22: the rate of the increase at the beginning of each micro ON part and the decrease at the beginning of the following micro OFF parts represents a mean diffusion time of the incoming neutrons. As can be seen best from the microcycle distribution of single $\gamma$-events, there is a substantial remaining thermal-neutron flux after each micro ON part, thus introducing some neutron-related activity in the first 5-15 ms of each micro OFF part. Indeed, with our distance of up to 10 meters from the production stage of LISOL to the detection set-up and with a substantial amount of thermalizing and absorbing material in between, such as concrete walls, creating a scattered "cloud" of thermal neutrons and further increasing their mean scattering range, it will take several milliseconds for thermal neutrons to reach the detectors. By fitting the micro OFF part of the microcycle time distribution of single $\gamma$-events with the exponential function, excluding the first millisecond dominated by fast neutrons and taking into account the flat distribution of radiation of interest, we get a value of $\sim$9.5 ms for the mean diffusion time of the incoming thermal neutron-flux. The appearing delayed time structure most probably represents the complex behavior of the diffusion process inside the experimental hall. It is worth mentioning here that some measurements of the thermal-neutron flux were done in the past [75], which showed a noticeable difference between extracted values at different LISOL beam lines. This seemingly two-component time-structure of the neutron flux may be related to two different diffusion paths. Using the distribution of single $\gamma$-events during the micro ON and OFF parts of the macrocycle we can estimate the fraction of fast neutrons out of the total neutron flux inside the shielding by considering the count rate in the very first 1 ms, see Fig. 4.26. Subtracting the statistics during the micro OFF parts, estimated on the basis of the last 50 ms, we get the total neutron-induced count rate. From here we get that the $\gamma$-detector signals induced by fast neutrons constitute 24% of the total number of $\gamma$-detector events originating from the neutron flux inside the shielding. Since the multiplicity of single $\gamma$-events does not change very much during different parts of the microcycle, see Fig. 4.25, it was not taken into account. In general, this is a very rough estimation. A more detailed analysis would require proper computer simulations, which must take into account the energy distribution of the incoming neutrons and the dimensions of the experimental hall.

It is worth taking a closer look at the event rates in Fig. 4.25, which reveal a true extent of the performance of our detection set-up as a low count-rate system. Since the data-acquisition system collects data from both the $\beta$- and $\gamma$-detectors on event-by-event basis, we are able to establish coincidences of events from any of the detectors in a relatively straightforward way later in the

off-line analysis. This way, we actually deal with $m\beta$-$n\gamma$-coincidences, where $m$=0...$\mathcal{G}_\beta$ and $n$=0...$\mathcal{G}_\gamma$ with $\mathcal{G}_\beta$ and $\mathcal{G}_\gamma$ being the granularity of the $\beta$- and $\gamma$-detectors, respectively. This means that for event rates in Fig. 4.25, we have $I(Single\,\beta) \approx I(\beta\text{-}coincident\,\gamma)\cdot\frac{M_\beta(\beta\gamma)}{M_\gamma(\beta\gamma)} + I(Single\,\beta\,with\,no\,\gamma)$, where $M_\beta(\beta\gamma)$ and $M_\gamma(\beta\gamma)$ are, respectively, the $\beta$- and $\gamma$-detector multiplicities in $\beta$-$\gamma$-coincidences. Using this correction, a careful look reveals that the ratio between single-$\beta$ and $\beta\gamma$-coincidence events stays almost the same — on the level of $\sim$3 for all cases. Since the intrinsic efficiency of both $\beta$- and $\gamma$-detectors to $\beta$- and $\gamma$-radiation, respectively, is close to 100%, this factor represents the ratio between the total geometrical efficiencies of $\beta$- and $\gamma$-detectors. This is supported by the fact that after the correction for $\beta$- and $\gamma$-multiplicities we obtain that the rate of $\beta$-gated $\gamma$-events constitutes approximately one half the rate of single-$\beta$ events with no coincident $\gamma$'s.

Dealing with the background count rates from both $\beta$- and $\gamma$-detectors presents itself as a daunting and tedious task, which, first of all, involves localization and understanding of their main sources, which then must be properly quantified if possible.

The experimental background single and coincident event rates from $\beta$- and $\gamma$-detectors with and without the detector shielding installed are presented in the Table 4.32. Due to low collection times of the background runs with our new $\beta\gamma$-detection set-up using MINIBALL clusters, additional data were acquired with a single-crystal coaxial detector of 75% relative efficiency. The schematic representation and the photo of the $\beta\gamma$-detection set-up with MINIBALL detectors is given in Fig. 4.10, while the two-dimensional drawing of the detectors used in these measurements is presented in Fig. 4.31. The corresponding spectra, representing the event rates in Table 4.32, are given in the following figures: the single $\gamma$-spectra for the coaxial and two MINIBALL clusters in Fig. 4.27, the $\beta$-gated $\gamma$-spectra for the coaxial and two MINIBALL clusters in Fig. 4.28, and the single and $\beta$-gated $\gamma$-spectra from the $^{60}$Co calibration source, positioned at the implantation point, in Fig. 4.29. Being important parameters for further discussions, the total volumes and frontal surface areas of the corresponding detectors scale as 1455 cm$^3$ / 310 cm$^3$ and 180 cm$^2$ / 43 cm$^2$, respectively.

There are a few simple observations to draw from the given numbers:

1. With the detector shielding installed, the number of single $\beta$-detector events is decreased by a factor of $\sim$2;

2. The single $\beta$-detector event rates are almost independent of the presence of the $\gamma$-detectors;

3. The single $\beta$-detector event rates are almost independent of the $\gamma$-detector count rates in case of the background measurements;

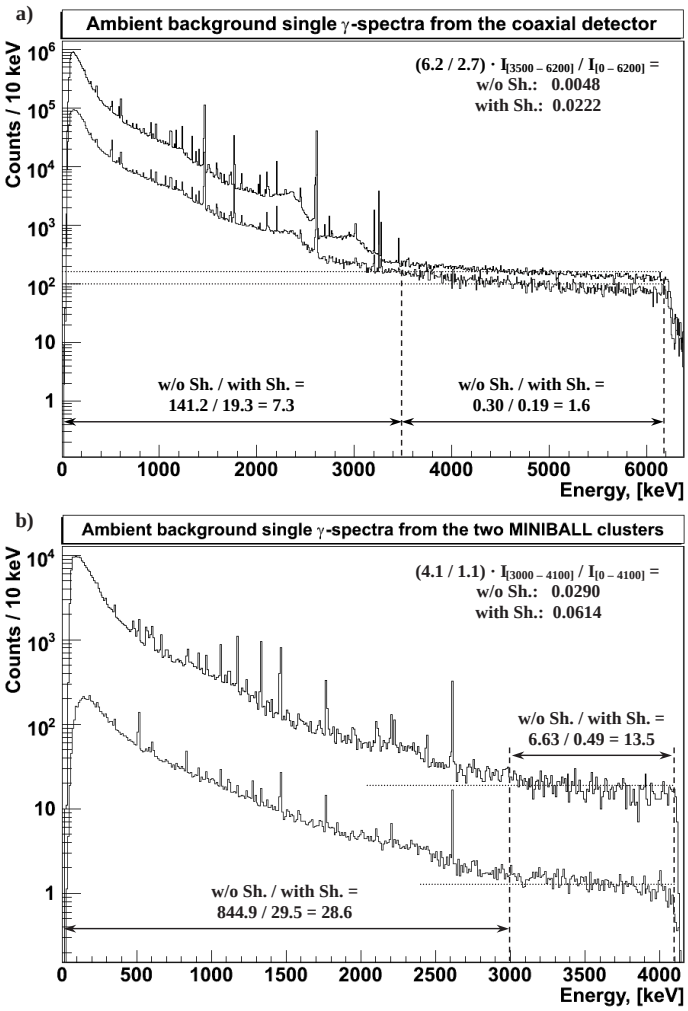


**Figure 4.27:** a) Background single $\gamma$-spectra for the coaxial detector with (lower spectrum) and without (upper spectrum) the shielding. The spectra are normalized for collection times. Both measurements were done in succession and in identical conditions. In contrast to the detection set-up with the MINIBALL detectors, the installed shielding did not cover the back of the coaxial detector. The factor of 6.2/2.7 is introduced to normalize the statistics between 3.5 and 6.2 MeV for the whole energy range. b) Background single $\gamma$-spectra for the two MINIBALL clusters with (lower spectrum) and without (upper spectrum) the shielding. The spectra are normalized for collection times. Both measurements were done in different periods of time and in different conditions. The factor of 4.1/1.1 is introduced to normalize the statistics between 3.0 and 4.1 MeV for the whole energy range.

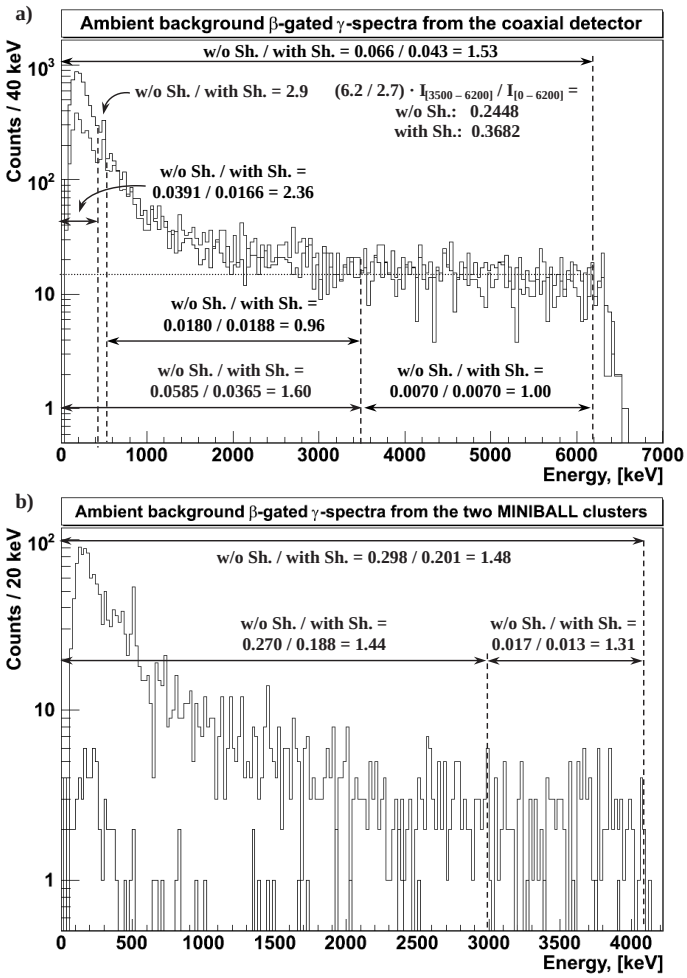


**Figure 4.28:** a) Background $\beta$-gated $\gamma$-spectra for the coaxial detector with (lower spectrum) and without (upper spectrum) the shielding. The spectra are normalized for collection times. Both measurements were done in succession and in identical conditions. The factor of 6.2/2.7 is introduced to upscale the statistics between 3.5 and 6.2 MeV for the whole energy range. b) Background $\beta$-gated $\gamma$-spectra for the two MINIBALL clusters with (lower spectrum) and without (upper spectrum) the shielding. Because of the low statistics the spectra were not normalized with the scaling factor of 0.03 for collection time. Both measurements were done in different periods of time and in different conditions.

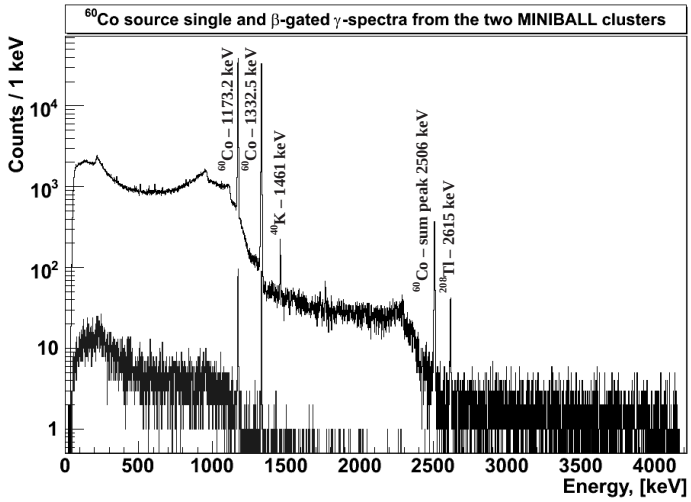


**Figure 4.29:** Single (upper spectrum) and $\beta$-gated (lower spectrum) $\gamma$-spectra for the coaxial detector with the $^{60}$Co source at the implantation point.

4. The single $\gamma$-detector event rate from one coaxial detector and two MINIBALL clusters is decreased by a factor of 7 and 30, respectively, when the shielding is installed;

5. The photopeak-to-total ratio, defined as the ratio of the number of counts in all major $\gamma$-photopeaks to the total number of counts in the spectrum, for single and $\beta$-coincident $\gamma$-detector events in the background spectra is almost independent of the detector shielding and is substantially lower than that with the $^{60}$Co calibration source, pointing to the presence of a pronounced continuum background;

6. The photopeak-to-total ratio for single $\gamma$-events is systematically higher by a factor of $\sim$2.7-4.3 relative to that for the $\beta$-coincident $\gamma$-events;

7. The $\beta$-$\gamma$-coincidence event rates are almost independent of the shielding, scaling between the two MINIBALL clusters and one coaxial detector by almost the same factor of (0.298/0.066=4.52)$\approx$(0.201/0.043=4.67).

Additionally, there are a few remarks to make from the presented spectra:

1. The single $\gamma$-spectra with and without the detector shielding differ mainly in the energy range up to $\sim$3.5 MeV, while:

2. As can be seen best from the statistics for the coaxial detector, there is a considerably smaller change in the event rates above this energy;

3. There are no pronounced $\gamma$-peaks in the single $\gamma$-spectra above $\sim$3.5 MeV in energy, where events constitute a structureless continuum;

4. The $\beta$-$\gamma$-coincidences correspond to prompt events in the coincidence time distributions, excluding any random nature from further discussions;

5. The 511 keV annihilation peak is the only $\gamma$-photopeak in the $\beta$-gated $\gamma$-spectra;

6. The difference in $\beta$-gated $\gamma$-event statistics with and without the detector shielding is almost solely due to the events below and including the 511 keV annihilation peak, while there is virtually no difference in the $\beta$-gated $\gamma$-statistics above the 511 keV photopeak;

7. The shape of the continuum of $\beta$-gated $\gamma$-events below the 511 keV photopeak for the coaxial detector does not appear as that of a Compton continuum from a single-line thin source emitting $\gamma$-rays of 511 keV in energy placed outside the detectors;

8. The ratios between the $\beta$-gated and single $\gamma$-events from the continuum above 3.5 MeV in energy from the spectra taken with the coaxial detector is 0.037 and 0.023 with and without the shielding, respectively, which is considerably higher than the corresponding ratios of 0.0018 and 0.0004 for events below 3.5 MeV;

9. The $\beta$-gated $\gamma$-event statistics for the $^{60}$Co calibration source consists almost purely of the events in the corresponding $\gamma$-peaks at 1173.2 and 1332.5 keV and their Compton continuum, which suggests that:

10. Subtracting the $\beta$-detector background count rate, the remaining majority of single $\beta$-detector events are due to $^{60}$Co $\gamma$-rays. This way, the ratio between the single $\beta$-detector and single $\gamma$-detector events represents the sensitivity of the $\beta$-detectors to incident $\gamma$-rays of 1.1%.

With the knowledge on the possible sources of the ambient background radiation as given in paragraph 4.4.5, considering the experimental observations and remarks as given above, we can now conclude or, if not possible, surmise on the origins of single and coincident background event rates:

- **Single $\gamma$-detector events:**

    1. With the shielding installed, the decrease in the count rate from the coaxial $\gamma$-detector takes place predominantly in the energy range

| Energy, [keV] | Origin | Count Rate, [Hz] | | Pair Production Rate, [Hz] | | Experimental suppression factor | Expected suppression factor | Ratio, [%] |
|---|---|---|---|---|---|---|---|---|
| | | w/o Sh. | with Sh. | w/o Sh. | with Sh. | | | |
| 185,7 | $^{226}$Ra | 0,104 | 0,025 | — | — | 4,2 | 9,9E+22 | 0,0 |
| 238,9 | $^{212}$Pb | 0,354 | 0,036 | — | — | 9,8 | 2,6E+15 | 0,0 |
| 295,4 | $^{214}$Pb | 0,245 | 0,019 | — | — | 12,9 | 1,0E+11 | 0,0 |
| 338,4 | $^{228}$Ac | 0,079 | 0,005 | — | — | 15,8 | 7,5E+08 | 0,0 |
| 352,1 | $^{214}$Pb | 0,487 | 0,038 | — | — | 12,8 | 2,2E+08 | 0,0 |
| 511,0 | $e^+e^-$ | 0,383 | 0,133 | — | — | 2,9 | 41389,8 | 0,0 |
| 569,7 | $^{207}$Bi | 0 | 0,008 | — | — | 0,0 | 7682,3 | 0,0 |
| 583,3 | $^{208}$Tl | 0,240 | 0,023 | — | — | 10,4 | 5530,8 | 0,2 |
| 609,4 | $^{214}$Bi | 0,587 | 0,051 | — | — | 11,5 | 3102,7 | 0,4 |
| 727,2 | $^{212}$Bi | 0,054 | 0,006 | — | — | 9,0 | 434,7 | 2,1 |
| 768,4 | $^{214}$Bi | 0,067 | 0,007 | — | — | 9,6 | 261,4 | 3,7 |
| 846,8 | $^{56}$Co | 0,056 | — | — | — | — | 118,1 | 100,0 |
| 911,5 | $^{228}$Ac | 0,200 | 0,022 | — | — | 9,1 | 69,8 | 13,0 |
| 964,6 | $^{228}$Ac | 0,061 | 0,008 | — | — | 7,6 | 48,5 | 15,7 |
| 968,9 | $^{228}$Ac | 0,123 | 0,013 | — | — | 9,5 | 47,2 | 20,1 |
| 1037,8 | $^{56}$Co | 0,015 | — | — | — | — | 52,4 | 100,0 |
| 1063,7 | $^{207}$Bi | 0 | 0,016 | — | — | 0,0 | 50,2 | 0,0 |
| 1120,3 | $^{214}$Bi | 0,187 | 0,020 | 0,008 | 0,001 | 9,4 | 46,0 | 20,3 |
| 1173,2 | $^{60}$Co | 0,144 | 0,012 | 0,008 | 0,001 | 12,0 | 42,6 | 28,2 |
| 1238,2 | $^{214}$Bi, $^{56}$Co | 0,204 | 0,012 | 0,015 | 0,001 | 17,0 | 39,0 | 43,5 |
| 1332,5 | $^{60}$Co | 0,145 | 0,012 | 0,015 | 0,001 | 12,1 | 34,8 | 34,7 |
| 1460,9 | $^{40}$K | 0,832 | 0,123 | 0,124 | 0,018 | 6,8 | 30,2 | 22,4 |
| 1764,8 | $^{214}$Bi | 0,190 | 0,025 | 0,060 | 0,008 | 7,6 | 23,1 | 32,9 |
| 1770,0 | $^{207}$Bi, $^{56}$Co | 0,038 | 0,002 | 0,012 | 0,001 | 15,7 | 23,0 | 68,1 |
| 2204,2 | $^{214}$Bi | 0,061 | 0,009 | 0,041 | 0,006 | 6,8 | 17,3 | 39,2 |
| 2598,5 | $^{56}$Co | 0,057 | 0,004 | 0,066 | 0,005 | 13,1 | 14,2 | 92,5 |
| 2614,5 | $^{208}$Tl | 0,272 | 0,046 | 0,319 | 0,054 | 5,9 | 14,1 | 42,0 |
| 3202,0 | $^{56}$Co | 0,010 | 0,001 | 0,022 | 0,002 | 11,3 | 13,6 | 82,8 |
| 3253,4 | $^{56}$Co | 0,024 | 0,002 | 0,054 | 0,004 | 12,1 | 13,6 | 88,5 |
| 3273,0 | $^{56}$Co | 0,006 | 0,001 | 0,013 | 0,001 | 10,8 | 13,6 | 79,5 |
| 3500 - 6200 | ? | 0,300 | 0,190 | — | — | 1,6 | 15,2 | 10,4 |
| | **Total Pair Production Rate:** | | | 0,757 | 0,103 | | | |
| | **Total 511 keV:** | | | 0,456 | 0,158 | | | |

**Figure 4.30:** Experimental and expected linear attenuation of incident electromagnetic radiation with the lead shielding of 5.5 cm thickness. The experimental count rates are taken from the measurements with the coaxial detector. All but the last row, giving the continuum event rates, represent the count rates of the most prominent $\gamma$-photopeaks from the terrestrial natural radioactivity. The experimental suppression factors are given as the ratio between the count rates without and with the shielding. The expected suppression factors are calculated using linear attenuation coefficients for given $\gamma$-ray energies in germanium. The values in the last column are obtained by taking the ratio between the experimental and expected suppression factors and representing it in percentage terms. Additionally, the pair production rate is extracted by converting the photopeak rate into the total event rate using the peak-to-total ratio for each given $\gamma$-ray energy. The total rate of 511 keV annihilation radiation is obtained by dividing the photopeak rate by the peak-to-total ratio for this energy and is additionally reduced by the factor of two to account for two annihilation quanta in each process of positron annihilation.

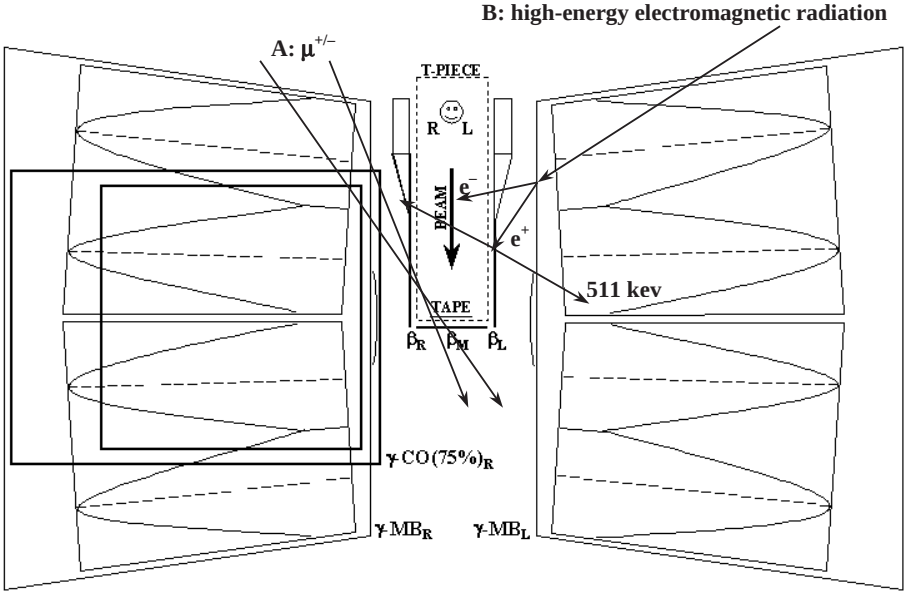


| Detector | Size ([L x H x W] or [D x L]), [mm] | Distance to the implantation point, [mm] |
|---|---|---|
| $\beta_L$ | 30 x 40 x 1.3 | < 20 |
| $\beta_M$ | 19 x 40 x 1.3 | < 20 |
| $\beta_R$ | 30 x 40 x 1.3 | < 20 |
| $\gamma$-$MB_L$ | 59,70 x 78 | 23 + (4 + 1.5 + 2.0 + 0.8 + 0.7) |
| $\gamma$-$MB_R$ | 59,70 x 78 | 23 + (4 + 1.5 + 2.0 + 0.8 + 0.7) |
| $\gamma$-Coax(75%)$_R$ | 74 x 73.5 | 20 + (5) |

**Figure 4.31:** The two-dimensional drawing of the two different detection set-ups used in these measurements. The figure is scaled to fit the page. The exact dimensions of the detectors are given in the table. The following options for $\beta$-$\gamma$-coincidence background events are presented: A) muons from the hard component of the cosmic radiation pass through the edges of the germanium detectors and then get registered by $\beta$-detectors and B) a high energy $\gamma$-ray from the terrestrial natural radioactivity or Bremmstrahlung from the soft component of the cosmic radiation undergo pair production in various materials of the detection set-up with the resulting electrons/positrons being registered by $\beta$-detectors and the 511 keV annihilation radiation being incident on $\gamma$-detectors. See text for more discussion.

| A: 2 MINIBALL Clusters — Background | | | | | | |
|---|---|---|---|---|---|---|
| Count Rate, [Hz] | 2.3 cm, w/o shielding, 300 s | | | 2.3 cm, with shielding, 9999 s | | |
| | γ | β | β–γ | γ | β | β–γ |
| Total | 885 | 0.83 | 0.298 | 30 | 0.42 | 0.201 |
| Photopeaks | 34.43 | | — | 1.43 | | 0.0022 |
| Ph./T., [%] | 3.9 | | — | 4.8 | | 1.1 |
| B: Coaxial Detector — Background | | | | | | |
| Count Rate, [Hz] | 2.0 cm, w/o shielding, 147323 s | | | 2.0 cm, with shielding, 76935 s | | |
| | γ | β | β–γ | γ | β | β–γ |
| Total | 142 | 0.95 | 0.066 | 19 | 0.48 | 0.043 |
| Photopeaks | 5.06 | | 0.0009 | 0.67 | | 0.0006 |
| Ph./T., [%] | 3.6 | | 1.3 | 3.4 | | 1.3 |
| C: 2 MINIBALL Clusters — $^{60}$Co source | | | | | | |
| Count Rate, [Hz] | 2.3 cm, w/o shielding, 300 s | | | | | |
| | γ | β | β–γ | | | |
| Total | 7554 | 81.5 | 53.2 | | | |
| Photopeaks | 1271 | | 4.4 | | | |
| Ph./T., [%] | 16.8 | | 12.0 | | | |

**Figure 4.32:** A,B: Experimental background single and coincident event rates for the two MINIBALL clusters ( 330%) and the coaxial detector (75%) with and without the detector shielding. C: Single and coincident event rates with a $^{60}$Co calibration source, placed as close as possible to the implantation point, at the position of the middle $\beta$-detector. With only two side $\beta$-detectors in place and the middle detector positioned away at a distance, the single $\beta$-detector and $\beta$-$\gamma$-coincidence event rates were upscaled by the factor of 3/2. The detector shielding was not in place in this measurement. Prior to the measurements with the coaxial detector, the total single $\beta$-detector background count rate in the absence of $\gamma$-detectors was 0.95 Hz. The distances given in this table represent the distances between the detector end-caps and the middle of the implantation tape. The collection time is given in seconds for each measurement.

where all major terrestrial natural radioactivity $\gamma$-transitions are situated, indicating that this component of the ambient background radiation plays a major role in constituting the $\gamma$-detector background event rates.

2. With the shielding installed, there is a substantial decrease in the count rate, namely by the factors of $\sim$7 and $\sim$30 for the coaxial

detector and the two MINIBALL clusters, respectively, which suggests that for an unshielded $\gamma$-detector the dominant sources of the background event rates are external. Since the shielding can effectively attenuate only the $\gamma$-rays from the terrestrial natural radioactivity and the soft component of the cosmic radiation, these must be the two major sources of the background event rates. As follows from the numerical evaluations in [71][79], less than 50% of the background events from an unshielded HPGe detector are due to $\gamma$-radiation from the terrestrial natural radioactivity, while the remaining events originate from the soft component of the cosmic radiation.

3. As presented in Table 4.30, considering the reduction in the photopeak event rates when the shielding is installed and comparing it with the expected suppression factors for this shielding at each energy, the internal terrestrial natural radioactivity appears to be one of the major sources of the background event rates from a well-shielded $\gamma$-detector. It is worth drawing attention to the $\gamma$-rays from the $^{56}$Co contaminant present in the gas cell from the previous experiment, which was placed in the experimental hall in close proximity to the detection set-up. Taking into account the fact that there was no shielding installed on the back of the coaxial detector, the experimental suppression factors for $\gamma$-rays from the decay of $^{56}$Co appear to be very close to the corresponding expected suppression factors, indicating that these $\gamma$-rays are completely external. All other activities have differing experimental and expected suppression factors, indicating that the terrestrial natural radioactivity background radiation comes from both external and internal sources. According to [71], the natural radioactivity, being present in various materials constituting the detection set-up (mainly shielding), accounts for more than 60% of the total background event rates from a shielded large-volume HPGe detector, while some 30% or more are due to cosmic radiation.

4. As follows from the crude estimate of the pair production rate in germanium for $\gamma$-rays above 1022 keV in energy in Table 4.30, the count rate of the 511 keV annihilation radiation for both shielded and unshielded $\gamma$-detectors can be explained as originating predominantly from the pair production of high-energy $\gamma$-rays from the terrestrial natural radioactivity. The impact from the $\beta^+$-decaying $^{207,208}$Bi contaminants in the lead shielding is only fractional.

5. A structureless continuum of events above $\sim$3.5 MeV in energy, can originate from single high-energy or otherwise summed electromagnetic radiation in the form of $\gamma$-rays and Bremsstrahlung from cos-

mic electrons or from charged particles, such as cosmic muons and electrons, passing through crystal edges and, thus, leaving only such a small amount of energy. As can be seen from the single $\gamma$-spectra for the coaxial detector in Fig. 4.27a, these events constitute only a small fraction of the total event rates — from 2.2% down to 0.5% with and without the shielding, respectively.

$\Rightarrow$ *Conclusion*

† *The terrestrial natural radioactivity is one of the major sources of the HPGe $\gamma$-detector background events.*

† *From the mentioned references, cosmic radiation with most likely its soft component also plays an important role.*

- **Single $\beta$-detector events:**

1. The plastic $\beta$-detectors can effectively register cosmic muons. Taking an integral over the zenith and azimuth angles, at which muons are incident on infinitesimally thin plastic of given area (in reality just 1.3 mm thick), one gets that the total integrated muon flux on vertically-positioned $\beta$-detectors is by a factor of $\pi$ lower than that for the same detectors in horizontal position. This yields possible count rates of (1 cts$\cdot$cm$^{-2}\cdot$min$^{-1}$)$\cdot$(31.6 cm$^2$)/$\pi\sim$0.17 cts$\cdot$s$^{-1}$ due to muons incident on the vertically positioned $\beta$-detectors of 31.6 cm$^2$ in area. Due to a high penetrability of cosmic muons this value must be independent of the detector shielding. It translates into 35-40% and 18-20% of the total single $\beta$-detector count rate with and without the shielding, respectively.
2. The $\beta$-detector background events can also originate from incident $\gamma$-rays, which may leave some energy in the plastic material predominantly through the mechanism of the Compton scattering. As extracted from the measurement with the $^{60}$Co calibration source, we deal with sensitivity of 0.011 of our $\beta$-detectors to incident $\gamma$-rays of around 1.2-1.3 MeV in energy. This value is slightly higher than the tabulated absorption factor of 0.008 [80] for 1 MeV $\gamma$-ray passing through 1.3 mm of plastic scintillator due to $\gamma$-rays incident on the $\beta$-detectors at an angle. GEANT simulations of similar detectors used in the past [44] showed a value of 1-2%, depending on the incident $\gamma$-ray energy. The fact that the single $\beta$-detector event rates are almost independent of the presence of the $\gamma$-detectors indicates a negligibly small influence of the Compton electrons produced in the $\gamma$-detector end-caps, which then could reach the $\beta$-detectors. The fact that the single $\beta$-detector event rates are almost independent of the $\gamma$-detector event rates indicates that the $\gamma$-radiation from

the terrestrial natural radioactivity is not the major source of the $\beta$-detector background events.

3. One cannot exclude the soft component of the cosmic radiation with its manifold multiplicity as a source of the $\beta$-detector background events. An exact numerical evaluation is not possible without specialized measurements and/or proper computer simulations.
4. Finally, some of the background events can originate from the internal radioactivity within the materials constituting the $\beta$-detectors or the shielding.

$\Rightarrow$ *Conclusion*

† *Cosmic muons can account for 35-40% and 18-20% of the total $\beta$-detector event rates with and without the shielding, respectively, depending on the measurement.*

† *With the detector shielding installed, the electromagnetic radiation of external origin does not appear to play a major role.*

- **$\beta$-$\gamma$-coincidence events:**

1. The fact that the photopeak-to-total ratio for the $\beta$-coincident $\gamma$-events is lower by a factor of $\sim$2.7-4.3 relative to that for single $\gamma$-events suggests that the terrestrial natural radioactivity is not a dominant source of the coincident background events.
2. The ratio between the $\beta$-$\gamma$-coincidence event rates from the two MINIBALL clusters and one coaxial detector of $0.201/0.043 = 4.67$ and $0.298/0.066 = 4.52$ with and without the shielding, respectively, is almost the same as the ratio between the total volumes $1455/310 = 4.69$ and frontal surface areas $180/43 = 4.19$ of the corresponding $\gamma$-detectors. This might indicate that the rate of coincidences between the $\beta$- and $\gamma$-detector events scales as the solid angle coverage of the $\gamma$-detectors relative to the $\beta$-detectors.
3. The fact that the 511 keV annihilation peak is the only photopeak in the $\beta$-gated $\gamma$-spectra indicates that the process of pair production of high-energy electromagnetic radiation plays an important role. Such radiation can only be a $\gamma$-ray from the terrestrial natural radioactivity or Bremsstrahlung from the soft component of the cosmic radiation, see Fig. 4.31. As given in the Table 4.30, although the single $\gamma$-detector event rates of the 511 keV annihilation radiation and the summed pair production rate for all major high-energy $\gamma$-rays are comparable, the electrons and positrons produced in germanium by the $\gamma$-radiation from the terrestrial natural

radioactivity do not have enough energy to reach $\beta$-detectors and thus do not constitute $\beta$-$\gamma$-coincidences. Similarly, if the process of pair production takes place in other materials constituting the detection set-up, produced electrons have too low remaining energies to penetrate even the $\gamma$-detector end-caps. This leaves high-energy Bremsstrahlung radiation of the order of tens of MeV in energy from the soft component of the cosmic radiation as the major source of the 511 keV annihilation radiation in the $\beta$-$\gamma$-coincidence spectra. No $\gamma$-radiation from the $\beta^+$-decaying $^{207,208}$Bi contaminants in the lead shielding is observed in the coincidence spectra. Thus the observed 511 keV annihilation radiation events do not originate from these decays.

4. The fact that there are almost no changes in event rates above the annihilation peak, when the shielding is installed, suggests that these events are due to cosmic muons, which can easily penetrate dense layers of materials. In order to be effectively registered by HPGe detectors, muons must pass through crystal edges, as shown in Fig. 4.31. If considering all events above the 511 keV annihilation peak in Fig. 4.28 as originating from muons, the hard component of the cosmic radiation can account for at least 60% and 38% of the total event rates with and without the shielding, respectively;

5. The fact that the shape of coincidence events below the annihilation peak does not appear as a Compton continuum from a thin single-line source placed outside the detectors, but the rates of these events scale by almost the same factor as the event rates in the 511 keV photopeak, see Fig. 4.28., indicates that the process of pair production does not take place in germanium but rather in various materials constituting the detection set-up.

6. The fact that the ratios of 0.037 and 0.023 with and without the shielding, respectively, between the $\beta$-gated and single $\gamma$-events from the continuum above 3.5 MeV in energy from the spectra for the coaxial detector are considerably higher than the corresponding ratios of 0.0018 and 0.0004 for events below 3.5 MeV, suggests that the high-energy $\beta$-$\gamma$-coincidence events are not due to electromagnetic radiation.

$\Rightarrow$ <u>*Conclusion*</u>

† *The coincident events above the 511 keV annihilation peak, constituting 60% and 38% of the total event rates with and without the shielding, respectively, can be explained by cosmic muons passing through the edges of the HPGe crystals.*

† *The events in the 511 keV annihilation peak and below are due to pair production of high-energy electromagnetic radiation.*

† *The soft component of the cosmic radiation is the most likely source of the $\beta$-$\gamma$-coincidence events at and below 511 keV in energy, when the cosmic electron or positron created in pair production of high-energy Bremsstrahlung is registered by $\beta$-detectors and the annihilation radiation is registered by $\gamma$-detectors.*

Now, considering the event rates from the background run as certain benchmarks of the registration limit, it is clearly seen that we have to deal with rather low experimental count rates: taking the difference of the corresponding rates of "single $\beta$", "$\beta$-coincident $\gamma$", and "single $\beta$ with no $\gamma$" events between the laser ON [67/Fe/10/0/1] and laser OFF [67/OFF/10/0/1] runs results in count rates for $^{67}$Fe as the radiation of interest, being on the same level as those from the background run.

One of the major concerns is a quite substantial sensitivity of the $\gamma$-detectors to the incident $\beta$-particles or associated Bremsstrahlung. The $\beta$-gated $\gamma$-spectra with different directional couplings between $\beta$- and $\gamma$-detectors for the data set [67/Fe/10/0/1] are given in Fig 4.33. Since we have two pairs of $\beta$- and $\gamma$-detectors on each side perpendicular to the beam and a third middle $\beta$-detector in front of the implantation point, see Fig. 4.10, those cases when a remaining energy of a registered $\beta$-particle or the associated Bremsstrahlung was absorbed by a $\gamma$-detector or a $\gamma$-ray was backscattered from a $\gamma$-detector and registered by a neighboring $\beta$-detector, altogether constituting a part of the $\beta\gamma$-coincidences from the same pair of $\beta$- and $\gamma$-detectors, can be removed by using the two side $\beta$-detectors as veto detectors. The middle curve in Fig. 4.33 corresponds to the total statistics of $\beta$-gated $\gamma$-events, whereas the lower curve represents vetoed [$\beta_L$-$\gamma_R$ + $\beta_R$-$\gamma_L$ + $\beta_M$-$\gamma$] $\gamma$-events. For comparison purposes, the single $\gamma$-spectrum (upper curve) is also included. The use of the $\beta$-detectors as triggers in $\beta\gamma$-coincidences represents a highly selective tool for removing a clear majority of unwanted $\gamma$-events originating from the natural-radioactivity and neutron-induced background radiations: the amount of the single $\gamma$-events is reduced by a factor of ∼200–250, while the statistics of the major $\gamma$-transition at 694 keV in $^{67}$Co is decreased only by a factor of ∼2.0–2.5, which represents the reciprocal of the absolute total $\beta$-registration efficiency. From here, taking the ratio of the latter and former factors, the selectivity of the $\beta$-trigger is in the range of 80–130. It is worth noting here, that the absolute total $\beta$-registration efficiency is higher in the absence of the primary beam, resulting in the value of 0.51±0.01, compared to the value of 0.39±0.01 when considering the whole macrocycle. Further on, comparing vetoed and total $\beta$-gated $\gamma$-statistics the amount of photopeak $\gamma$-events is reduced by a factor of ∼1.3 due to a mere exclusion of virtually one $\beta$-detector, while the amount of continuum $\gamma$-events is decreased by a factor of ∼1.4–2.0. By taking again

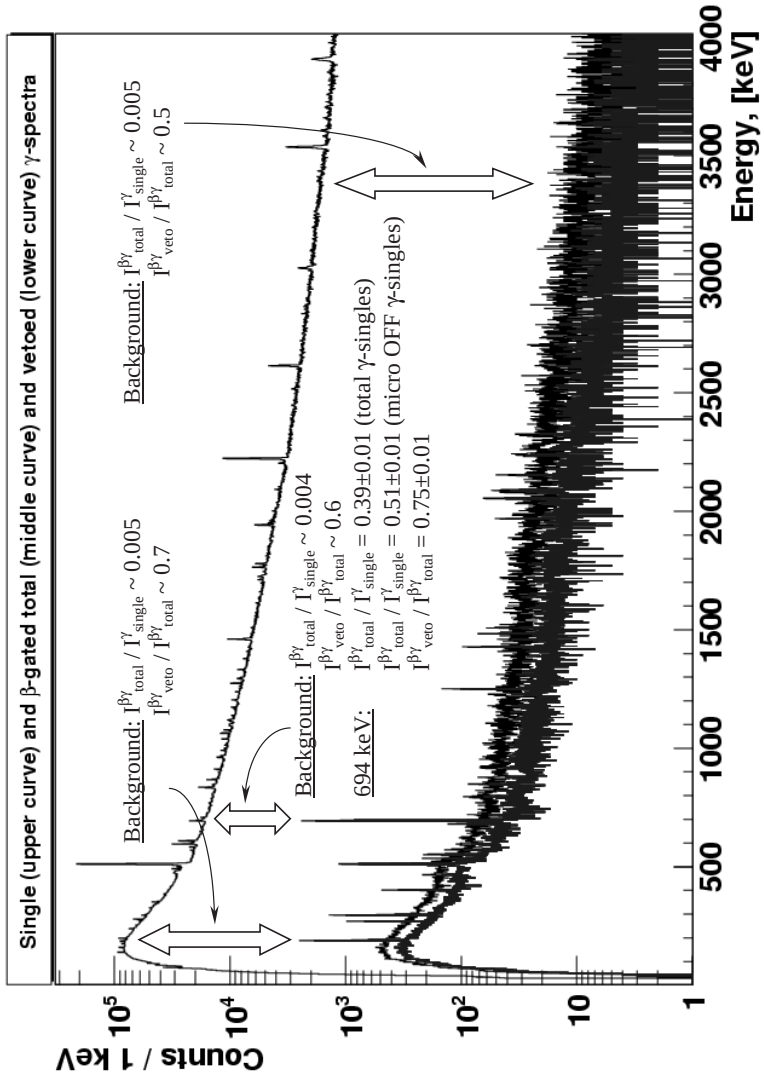


**Figure 4.33:** The total (middle curve) and veto (lower curve) $\beta$-gated as well as single (upper curve) $\gamma$-spectra for the data set [67/Fe/10/0/1]. A detailed explanation is given in the text.

the ratio between the latter and former values we obtain that the selectivity of the $\beta$-trigger is further increased by a factor of $\sim$1.1–1.5. Finally, the adopted values for the $\beta$-registration efficiency for the trigger and veto-trigger cases is 51$\pm$1% and 38$\pm$2%, respectively.

Unfortunately, we could not use the segment information from the MINIBALL detectors. After an exchange of information with the manufacturer of the DGF-4C modules, it was realized that the leading-edge timing information can be extracted correctly only for the main trigger channel, which is always the main core signal from each MINIBALL crystal. Without the segment information, due to the fact that our detectors are situated very close to the source we are not able to distinguish between two or more $\gamma$-rays incident onto the same crystal and, therefore, we cannot perform proper add-back correction that would allow reconstruction of $\gamma$-rays that are scattered between several crystals.

It is worth closing this chapter with a short summary of what was achieved in our new $\beta\gamma$-detection set-up in terms of detection capabilities:

- As a result of the introduction of two HPGe MINIBALL clusters, the $\gamma$-registration efficiency was increased by a factor of $\sim$1.5 at 1 MeV $\gamma$-ray energy. The $\beta$-registration efficiency was only slightly increased from 46% to 51% by substituting one of the detectors.

- The granularity of $\gamma$-detectors was increased from 2 to 6 independent germanium crystals. This allows to avoid a substantial reduction in $\gamma$-registration efficiency when dealing with high-multiplicity $\gamma$-ray cascades.

- New multi-layer detector shielding was installed, improving the attenuation of the neutron flux by a factor of $\sim$5 and more than 2 for thermal and fast neutrons, respectively, compared with the previous detection set-up at LISOL. The attenuation of the background $\gamma$-rays is approximately on the same level as before.

- A new data-acquisition system based on digital electronics was introduced. Having a time stamp for each individual event allows us to collect all data on event-by-event basis and generate $\beta$-$\gamma$- and $\gamma$-$\gamma$ coincidences later in the software. This also gives us more freedom when dealing with long range coincidences, especially between events from different buffer readouts.

All this is a part of, albeit a huge, but still the very first step in the development of our new $\beta$-$\gamma$-detection set-up. It must be finalized by implementing new segmented $\beta$-detectors and using already available segmentation of the $\gamma$-detectors. Only then may we speak of a genuine low-count rate detection system.

### 4.4.9 Computer simulations

It is commonly accepted that an experimental performance of any, whatever sophisticated, experimental set-up that involves a series of complex physical processes, which cannot be rather easily verified analytically in an integral form, must be checked or sometimes even evaluated by comparing it to an idealized performance of a computer model in a transparent differential form.

The current need for computer simulations of our detection set-up can be subdivided into three distinct stages:

- Operation of various hardware components: e.g., charge or light collection in semiconductor or scintillator detectors, respectively;
- Detection of various types of radiation: e.g., interaction of $\gamma$-rays from a specific source with detector material that is a part of the whole structure of the set-up;
- Various external processes, which influence the performance of the set-up: e.g., formation of the beam-related neutron flux in the experimental hall.

With an emphasis on $\gamma$-detectors, the first step was accomplished during the development and introduction stage of the first MINIBALL detectors [41], when such questions as the generation of the electric field and its dependence on the impurity concentrations inside a tapered crystal, creation of net and mirror charges and their mobility in a segmented crystal had to be answered. The second step was started within the framework of the MINIBALL collaboration in its early days as well. Using the GEANT 4 package [81] based on the object-oriented C++ language, the simulation comprises a) reconstruction of the whole technical structure of the detectors within a given geometry, b) simulation of the interaction of $\gamma$-radiation with matter, and c) performance of multi-crystal detector arrays as a whole in order to reproduce certain techniques, such as, e.g., the add-back procedure. The algorithm is based on the Monte-Carlo method, which basically means a successive generation of independent events of isotropically-emitted $\gamma$-radiation from a specified source. As $\gamma$-rays pass through various materials defined in the code, their interaction with matter through various processes, as defined in paragraph 3.2.1, is simulated. Adapting this code to our experimental geometry, we performed similar simulations of $\gamma$-registration by two MINIBALL detectors. The experimental and simulated single $\gamma$-spectra from the two MINIBALL detectors positioned at experimental distances of $\sim$4.6 cm between the two detector end-caps or $\sim$5.1 cm between the crystal front surfaces of the two clusters (a more exact number in the simulations takes into account the tapering angle at which the crystals are aligned into a compact cluster) and with a $^{60}$Co source at the position of the implantation point on the tape are shown in Fig 4.34. The

overall match between the two spectra is quite good — the discrepancy in intensities of the $^{60}$Co peaks is approximately 18%, but as can be immediately seen, there are a few important differences. First of all, since the simulation program deals with an ideal material with no impurities or defects and assumes an ideal charge collection from all regions of the crystal, the resulting spectrum has more events in the peaks and less in the continuum at lower energies. In a real crystal however, charge collection is not ideal and especially in the farthest corners of the tapered crystal — the so-called weak regions, where the electrical field that collects the created charges can be substantially weaker. Secondly, the experimental spectrum contains additional events from the background radiation, thus further increasing statistics of the continuum events. Finally, since a part of the lead shielding was still installed below the detectors and there is a substantial amount of various materials placed behind the germanium crystals and not specified in the simulation code, the amount of continuum events at and around the backscattering edge is much higher in the experimental spectrum. Nevertheless, a rather good match between the experimental and simulated spectra shows that the simulation is reliable and, what is actually more important, that, despite many difficulties associated with operation of highly-segmented detector arrays, the current performance of the MINIBALL detectors is stable and satisfactory. Concerning the third stage of the simulations, it has not been introduced yet.

It is rather clear, that the current simulations of the performance of the detection set-up are far from being complete. First of all, the first stage must be implemented into the existing code in order to have a more realistic evaluation of the registration efficiency. Secondly, the second stage must be properly finalized by including all the existing materials around the detector end-caps, such as the detector cryostats and detector frames, the $\beta$-detectors, the closest parts of the beam line and the tape system, and, finally, the detector shielding. Apart from that, the simulations must be extended to $\beta$-detectors. Finally, a description of the most important external processes, such as the formation of the beam-related neutron flux and the creation of the soft component of the cosmic background radiation, must be developed and included in the simulation code.

The author would like to strongly emphasize, that whatever realistic simulations can never substitute a real experiment and, thus, must be used only as a complimentary tool for comparative purposes. The final task is not only to check the performance of our detection set-up and reveal possible problems, but also to project the simulations into further developments, such as the use of the segment information for the complete add-back procedure and pulse-shape analysis, introduction of new segmented $\beta$-detectors, implementation of an active shielding, and maybe even a change in the existing detector geometry.

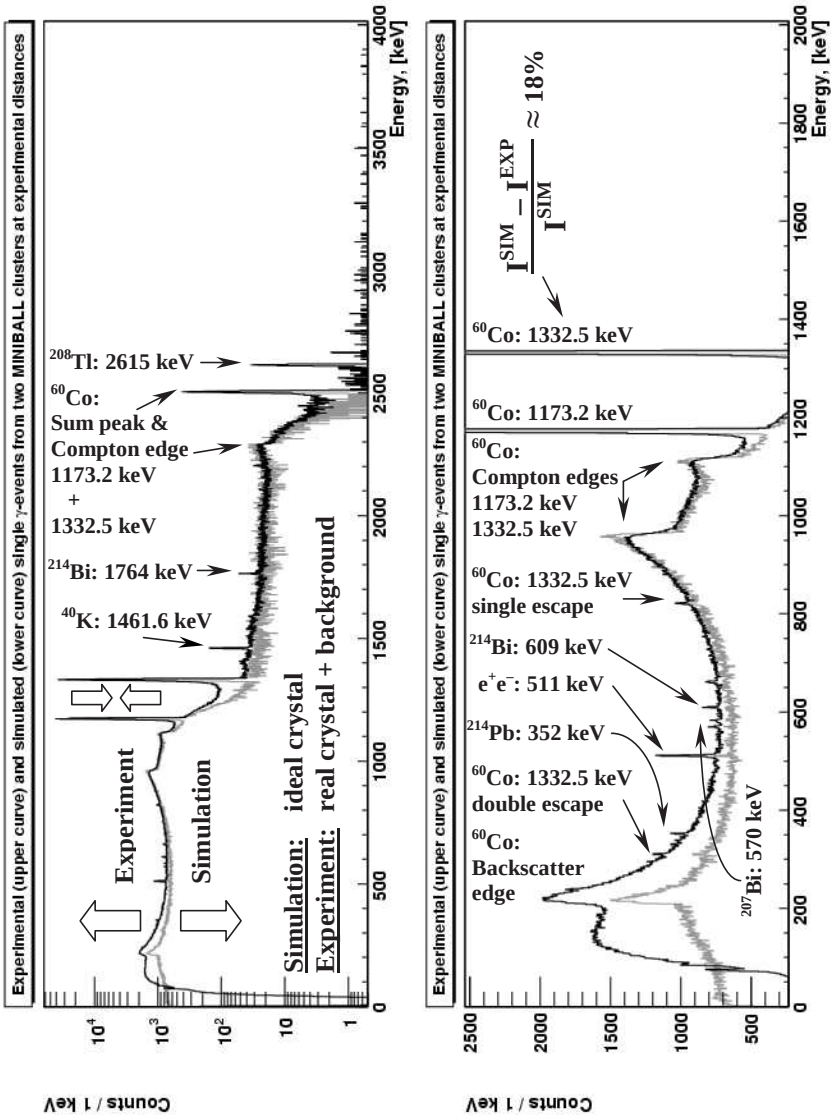


**Figure 4.34:** The experimental and simulated single $\gamma$-spectra from the two MINIBALL detectors positioned at experimental distances with a $^{60}$Co source placed at the implantation point. The experimental statistics is corrected for the data-acquisition dead time. The normalization factor between the two spectra is based on the activity of the $^{60}$Co source.

# Chapter 5

# Nuclear structure of neutron-rich $^{66}$Co studied in the $\beta$-decay of $^{66}$Fe

## 5.1 Experimental results: $\beta$-decay of $^{66}$Fe

### 5.1.1 Short summary of the experiments

The experimental results presented in this chapter were obtained within the scope of the new project, aimed at the nuclear-structure studies of the neutron-rich $^{63-68}$Co isotopes in $\beta$-decay of the corresponding Fe isobars. The whole project consisted of a series of three experiments, carried out at LISOL in November 2005, June 2006, and July 2007. Considering various experimental information available prior to our studies, such as half-life values, expected production rates, quality of the known level schemes, known ground-state $\beta$-feeding, as compiled in Table 5.1, and taking into account the overall progress throughout the project, all three experiments were finally dedicated to the production of $^{65,66,67}$Fe beams. The physics results of this work fully consist of the analysis of the $^{66}$Fe data sets, as given in Table 5.2.

### 5.1.2 Single and $\beta$-gated $\gamma$-spectra

The single and $\beta$-gated $\gamma$-spectra from the $^{66}$Fe laser ON and OFF runs are presented in Fig. 5.1, Fig. 5.2 and Fig. 5.3, Fig. 5.4, respectively. The laser OFF statistics of both types of spectra is normalized on the basis of the measurement time of the two runs, as given in Table 5.2.

**Table 5.1:** A short summary on the feasibility of the nuclear-structure studies of the neutron-rich $^{63-68}$Co isotopes in $\beta$-decay of the corresponding Fe isobars. The half-life values and decay schemes are known from various experiments reported in literature [22], while the expected production rates are taken from Table 4.1.

| Fe isotope | $^{63}$Fe | $^{64}$Fe | $^{65}$Fe | $^{66}$Fe | $^{67}$Fe | $^{68}$Fe |
|---|---|---|---|---|---|---|
| $T_{1/2}$(Fe) | 6.1 s | 2.0 s | 0.45 s | 0.44 s | 0.47 s | 0.1 s |
| $T_{1/2}$(Co) | 27.5 s | 0.3 s | 1.14 s | 0.18 s | 0.43 s | 0.2 s |
| $T_{1/2}$(Ni) | 100 y | stable | 2.52 h | 54.6 h | 21 s | 29 s |
| Production rate, [at/$\mu$C] | 3.3 | 6.0 | 6.6 | 4.3 | 1.7 | 0.4 |
| Number of known $\gamma$-lines | 46 | 9 | — | 3 | 1 | 10 |
| Decay scheme | Yes | Yes | No | No | No | No |
| Ground state $\beta$-feeding | 80% | 95% | ? | ? | ? | ? |
| Feasibility / Objective | No | No | Yes | Yes | Yes | No |

**Table 5.2:** Summary of the experimental specifications of the $^{66}$Fe data sets.

| Data Set | I | II |
|---|---|---|
| Separator mass-over-charge ratio | 66 | 66 |
| Laser ionization | ON | OFF |
| Total measurement time, [h] | 8.1 | 4.9 |
| Macrocycle implantation time, [s] | 1.5 | 1.5 |
| Macrocycle decay time, [s] | 1.5 | 1.5 |
| Number of macrocycles per tape move | 3 | 3 |
| Microcycle period, [ms] | 50 | 50 |
| Average proton beam intensity, [$\mu$A] | 5.0 | 5.0 |

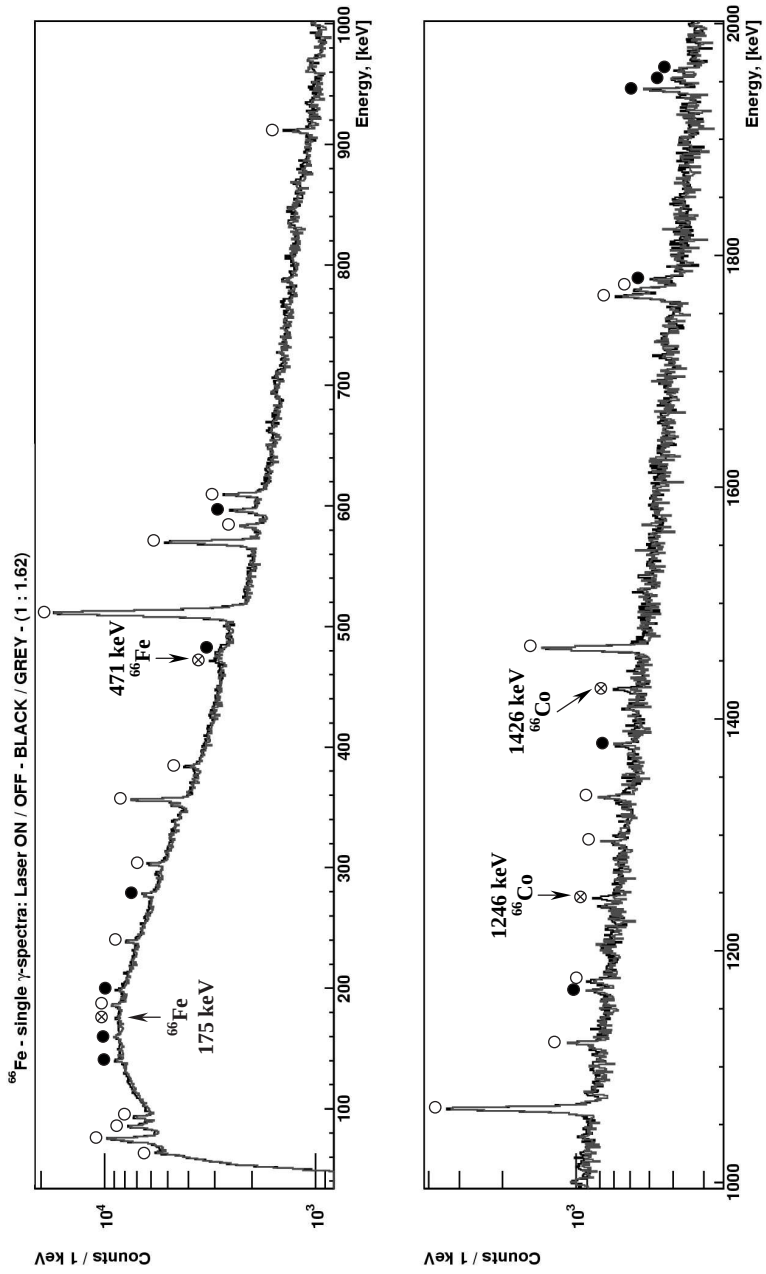


**Figure 5.1:** Single $\gamma$-spectra from the $^{66}$Fe laser ON and OFF runs. The laser OFF statistics is upscaled on the basis of the measurement time of the two runs. $\gamma$-ray photopeaks are marked according to their origin: open circles for the natural radioactivity background, closed circles for the neutron-induced background, and crossed open circles for the nuclei of interest.

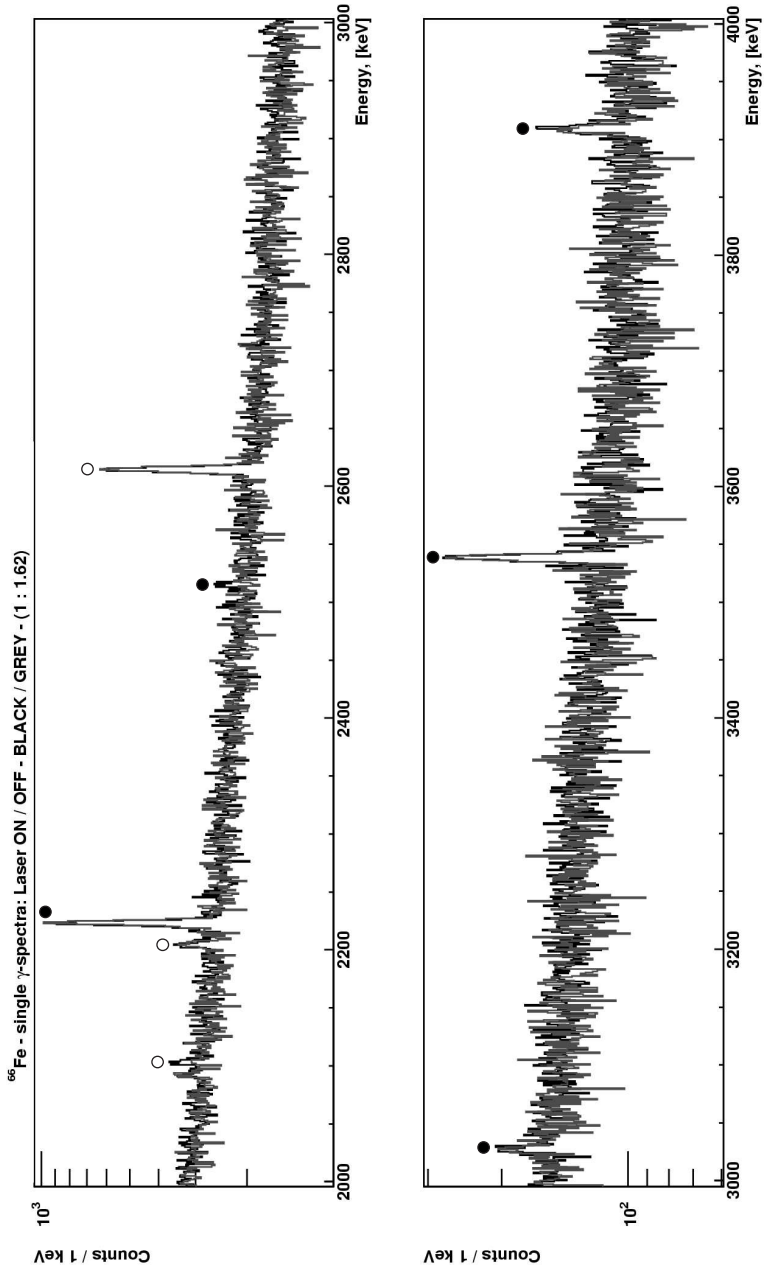


**Figure 5.2:** Continuation of the Fig. 5.1.

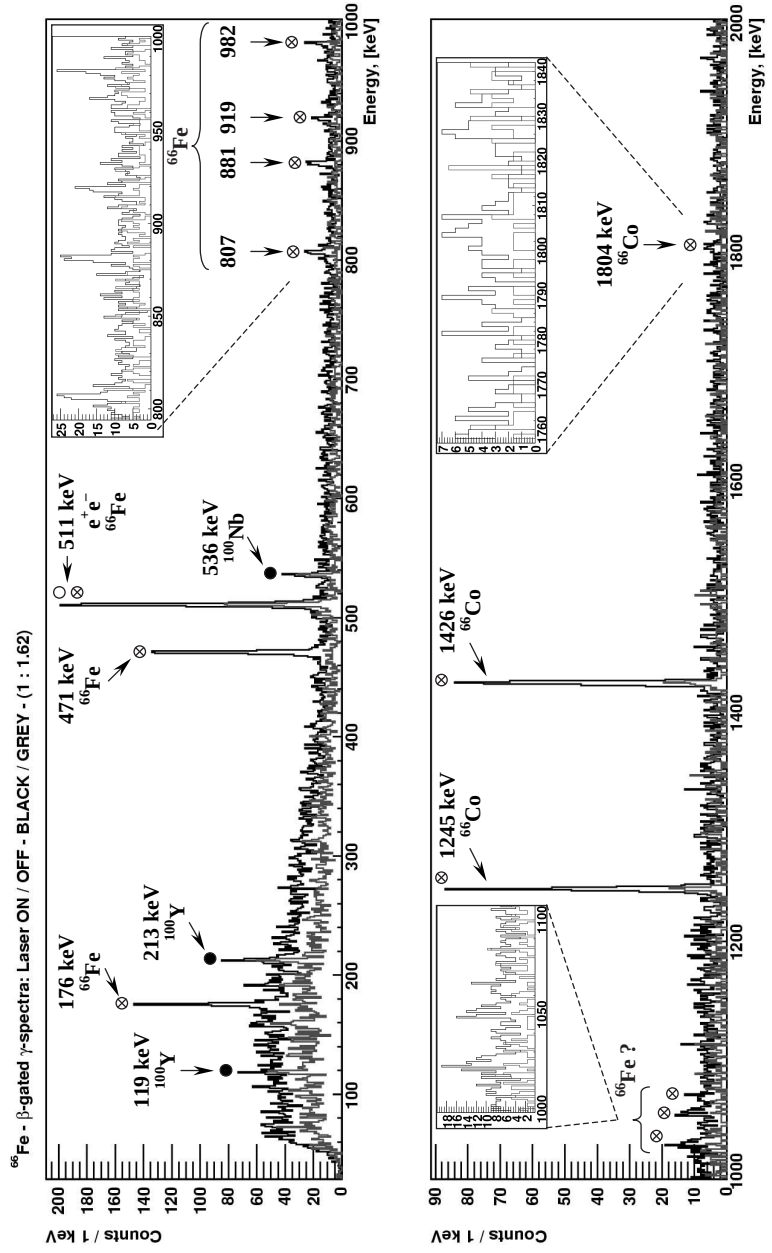


**Figure 5.3:** $\beta$-gated $\gamma$-spectra from the $^{66}$Fe laser ON and OFF runs. The $\beta$-$\gamma$-coincidence time difference, as given in Fig. 5.5, was set in the range from 25 to 5000 ns in order to include the 176 keV $\gamma$-line from the 1.2 $\mu$s isomer in $^{66}$Co. The laser OFF statistics is upscaled on the basis of the measurement time of the two runs. $\gamma$-ray photopeaks are marked according to their source: open circles for the natural radioactivity background, closed circles for the double-mass double-charge contaminants in the beam, and crossed open circles for the neutron-rich $A$=66 isobars.

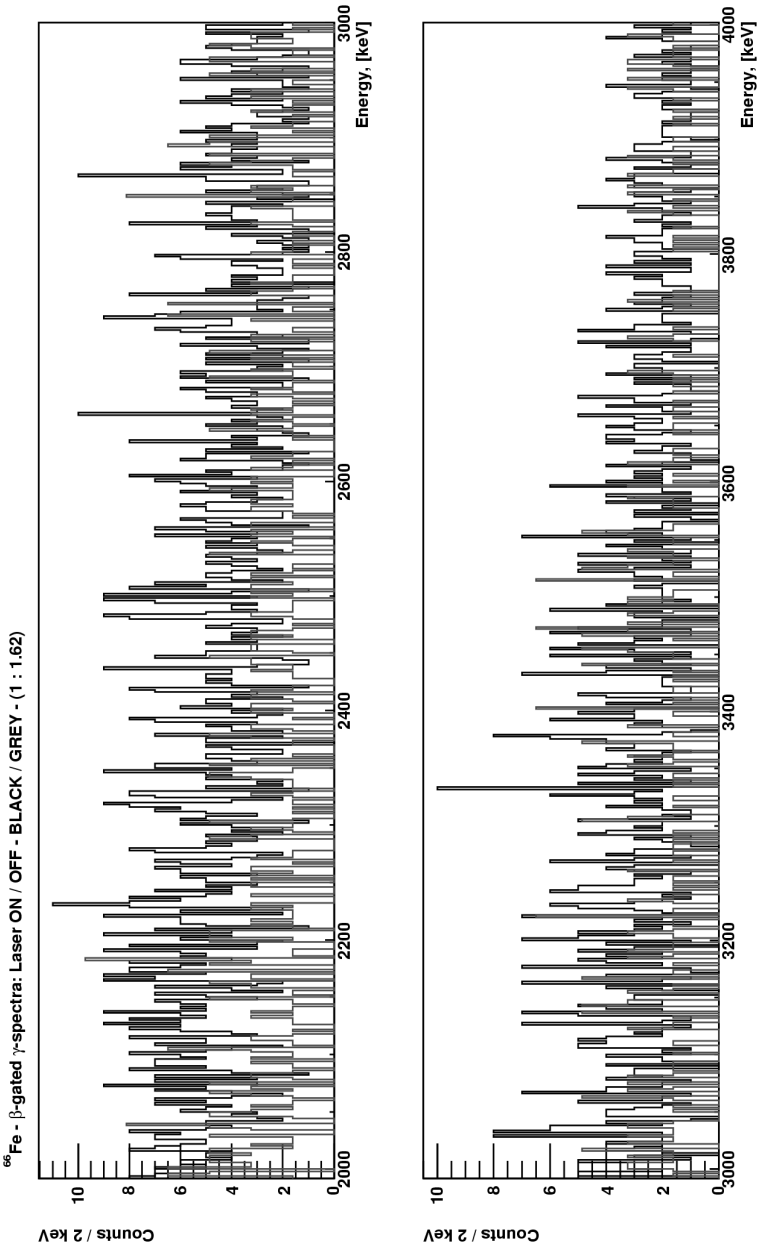


**Figure 5.4:** Continuation of the Fig. 5.3.

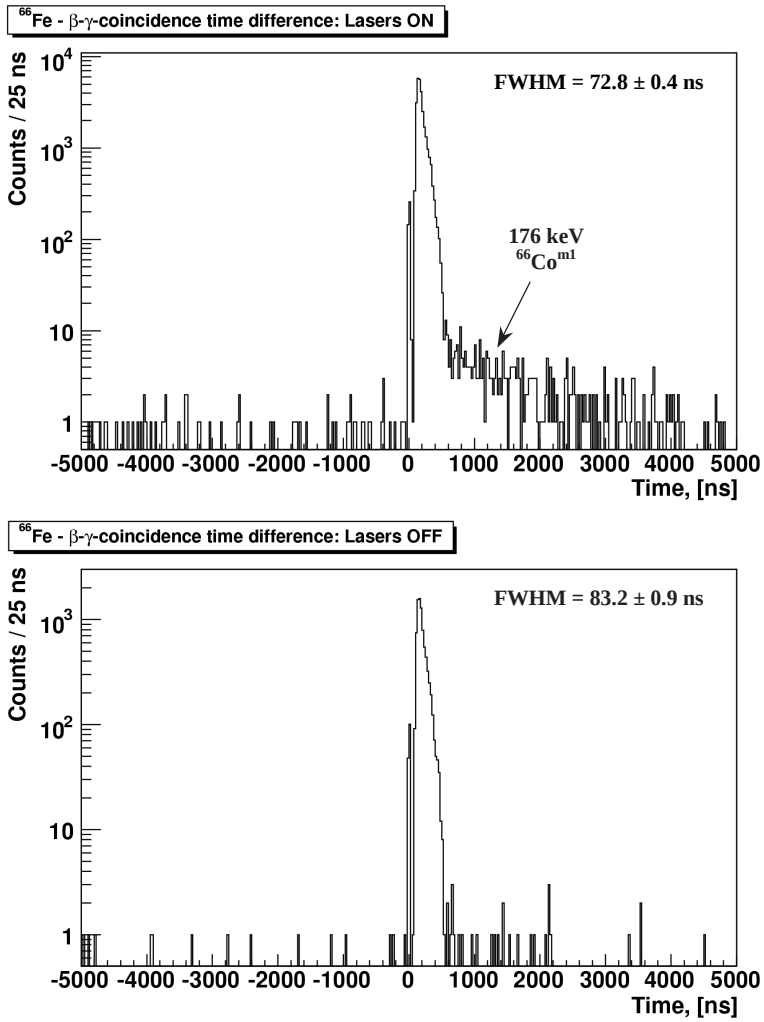


**Figure 5.5:** $\beta$-$\gamma$-coincidence time difference from the $^{66}$Fe laser ON and OFF runs. See text for the discussion on the 176 keV isomer in $^{66}$Co.

**Table 5.3:** The list of all indisputable $\gamma$-ray photopeaks present in the $\beta$-gated $\gamma$-spectra from the $^{66}$Fe laser ON and OFF runs. See text for the discussion on the $\gamma$-ray assignment.

| $\gamma$-line energy, [keV] Laser ON / OFF | Number of counts (Laser ON) measured | Number of counts (Laser OFF) normalized | Assignment |
|---|---|---|---|
| 118.9(3) / 119.1(2) | 36(15) | 50(16) | $^{100}$Y |
| 175.5(1) | 205(24) | — | $^{66}$Fe |
| 212.7(2) / 212.5(2) | 128(25) | 107(19) | $^{100}$Y |
| 470.9(1) | 355(22) | — | $^{66}$Fe |
| 510.6(1) / 511.0(1) | 569(27) | 225(23) | $e^+e^-$, $^{66}$Fe (new) |
| 536.1(2) / 536.1(2) | 81(14) | 45(11) | $^{100}$Nb |
| 806.7(3) | 56(11) | — | $^{66}$Fe (new) |
| 881.2(3) | 66(11) | — | $^{66}$Fe (new) |
| 918.6(3) | 37(10) | — | $^{66}$Fe (new) |
| 981.4(6) | 41(12) | — | $^{66}$Fe (new) |
| 1245.6(1) / 1245.7(3) | 250(17) | 41(10) | $^{66}$Co |
| 1425.1(1) / 1425.1(4) | 294(18) | 49(11) | $^{66}$Co |
| 1804.0(1.2) | 33(10) | — | $^{66}$Co |

As one can see, since we deal with very low count rates from the decay of the produced nuclei of interest as discussed in paragraph 4.4.8, the normalized single $\gamma$-spectrum from the laser OFF run almost fully coincides with the corresponding laser ON statistics, except for the most prominent known $\gamma$-lines in the decay of $^{66}$Fe and the daughter $^{66}$Co isobars. Consequently, the fact that the two spectra follow each other indicates a good stability in performance of both the LISOL facility and the detection set-up, thus ensuring identical conditions for both measurements.

Enhancement of the selectivity for the $\gamma$-radiation of interest through $\beta$-$\gamma$-coincidences presents a distinct difference between the $\beta$-gated $\gamma$-spectra from the laser ON and OFF runs. As follows from the paragraph 4.3.2, out of all $A$=66 isobars, produced in the proton-induced fission of $^{238}$U, $^{66}$Co is expected to have the highest production rate, being 2.1 and 9.3 times higher than those for the closest lying $^{66}$Fe and $^{66}$Ni, respectively. Additionally, the $\beta^-$-decaying $^{66}$Cu and $^{66}$Ni isobars have long half-lives of 5.1 m and 54.6 h, respectively, relative to the period of time of 9 s of three consecutive macrocycles before the tape move, and very large ground-to-ground state $\beta$-decay feeding of 91 and 100%, respectively. All this means that without laser ionization or lasers tuned on Fe virtually only $\gamma$-lines from the decay of the $^{66}$Co and $^{66}$Fe isobars and possible contaminants with the same mass-over-charge ratio must be present in the $\beta$-gated $\gamma$-spectrum. The list of all indisputable $\gamma$-ray photopeaks present in the $\beta$-gated $\gamma$-spectra from the $^{66}$Fe laser ON and OFF runs is given in

Table 5.3. The photopeaks at 118.9, 212.7, and 536.1 keV, being comparable in intensity in both spectra, were assigned to the decay of $^{100}$Y and $^{100}$Nb, which can be present in the beam by forming double-mass double-charge molecules with two atoms of $^{16}$O. The $\gamma$-lines at 1245.6, 1425.1, and 1804.0 keV were firmly assigned to the decay of $^{66}$Co in [4] with a few times higher statistics. On this basis, the rest of the $\gamma$-lines, except for the 511 keV annihilation photopeak, can be assigned to the decay of $^{66}$Fe.

Special attention must be drawn to the 511 keV photopeak, namely to the facts that a) its intensity differs substantially in the laser ON and OFF runs, b) there is a non-overlapping difference in energy, which is not the case for other $\gamma$-lines. Almost certainly being related to the decay of $^{66}$Fe, this could be explained by existence of a high-energy $\gamma$-ray yielding annihilation radiation through pair-production or by a presence of a $\gamma$-ray with an energy close to that of the annihilation photon.

Finally, there might be a few more photopeaks in the $\beta$-gated laser ON $\gamma$-spectrum, as, e.g., possible lines at $\sim$1024, $\sim$1050 and $\sim$1068 keV, which were eventually dismissed through statistical considerations.

It must be mentioned that in one of the first experiments on the decay of $^{66}$Co in [36], two $\gamma$-transitions at 471 and 1020 keV were added to the level scheme. Later on, in the dedicated $\beta$-decay experiment in [4], also carried out at LISOL, these transitions were not observed. Now, we have evidence that the transition at 471 keV follows the decay of $^{66}$Fe. The fact that it was assigned to the decay of $^{66}$Co in [36] can be explained by the use of multi-nucleon transfer reaction of $^{76}$Ge on $^{nat}$W, in which many different nuclei are produced, and a possibly poor $Z$-selection. Additionally, a possible $\gamma$-photopeak at $\sim$1024 keV could also be the $\gamma$-transition 1020 keV seen in the same experiment from [36]. It is worth mentioning here, that a similar discrepancy in assigned $\gamma$-ray energy with the results from that work was also noticed in the analysis of the $^{65}$Fe data sets.

The presence of the $^{66}$Co $\gamma$-lines in the $\beta$-gated laser ON $\gamma$-spectrum is due to the decay of the mother $^{66}$Fe isobar. Since there are no $\gamma$-transitions from the decay of $^{66}$Fe in the laser OFF spectrum, only the lower limit of 24$\pm$11 for the enhancement in production of Fe isotopes due to laser ionization could be determined.

The $\beta$-$\gamma$-coincidence time difference distributions for the laser ON and OFF runs, as given in Fig. 5.5, contain a negligibly small amount of random coincidence events. For this reason, subtraction of random coincidence events is not statistically meaningful. Compared to the laser OFF distribution, there is a considerable amount of events to the right side from the main peak of the laser ON coincidence time distribution, clearly being above the level of the random coincidences. By setting the coincidence time window in this range, literally only the 175.5 keV $\gamma$-line appears in the resulting $\beta$-gated $\gamma$-spectrum.

First observed in [28], this $\gamma$-line corresponds to the transition from one of the isomeric states to the ground state in $^{66}$Co with a half-life of 1.2 $\mu$s. For this reason, in order to fully include this $\gamma$-transition in the data analysis, the $\beta$-$\gamma$-coincidence time window was set to range from 50 to 5000 ns.

### 5.1.3 Half-life values

The process of $\beta$-decay of a mother nucleus of interest results in a population of excited states in a daughter nuclear system, which then subsequently de-excite by emitting $\gamma$-rays or through processes of internal conversion and pair production. This way, the accumulation of the corresponding $\gamma$-ray activity strictly follows the life-time of the mother isobar. By plotting the $\beta$-gated $\gamma$-photopeak intensity within several consecutive time windows of a fixed size, starting from the beginning of each macrocycle, one gets a combined implantation-decay curve, which reproduces the build-up and decay of the corresponding mother nucleus. Provided that the production rate of the mother isobar is constant at least over the period of one macrocycle, the time behavior of the corresponding daughter activity is given by

$$\begin{aligned} A(t) &= A^{ON}(t) + A^{OFF}(t) \qquad (5.1)\\ A^{ON}(t) &= A_0 \left(1 - e^{-\ln 2 \frac{t}{T_{1/2}}}\right), \quad 0 < t < T_M^{ON} \\ A^{OFF}(t) &= A_0 \left(1 - e^{-\ln 2 \frac{T_M^{ON}}{T_{1/2}}}\right) e^{-\ln 2 \frac{t - T_M^{ON}}{T_{1/2}}}, \quad T_M^{ON} < t < T_M^{ON} + T_M^{OFF} \end{aligned}$$

where $A^{ON}(t)$ and $A^{OFF}(t)$ are the registered activities during implantation (macro ON) and decay (macro OFF) parts of the macrocycle, respectively; $A_0$ is the initial activity; $T_M^{ON}$ and $T_M^{OFF}$ are, respectively, implantation and decay periods of the macrocycle; $T_{1/2}$ is the half-life time of the $\beta$-decaying state of the mother nucleus.

The implantation-decay curves for $\beta$-gated $\gamma$-ray activity from the decay of $^{66}$Fe are given in Fig. 5.6, together with a fit with a function from Eq. 5.1. The available statistics allows a feasible half-life fit for only two strongest $\gamma$-lines at 175.5 and 471.0 keV in Fig. 5.6a and Fig. 5.6b, respectively. The half-life time of 1.21(1) $\mu$s of the metastable state, from which the $\gamma$-line at 175.5 keV originates, is by far negligible to distort a much longer resulting half-life value for $^{66}$Fe. In order to improve statistics and, thus, reduce the uncertainty of the half-life fit, the final half-life time for the $\beta$-decay of $^{66}$Fe was obtained from the fit of the sum of the implantation-decay curves for the $\gamma$-lines at 175.5 and 471.0 keV as given in Fig. 5.6c. The resulting value of 830±80 ms is almost two times longer than the previously known half-life of 440±60 ms, reported in [35] and [29]. It can be argued however, that in those experiments the half-life

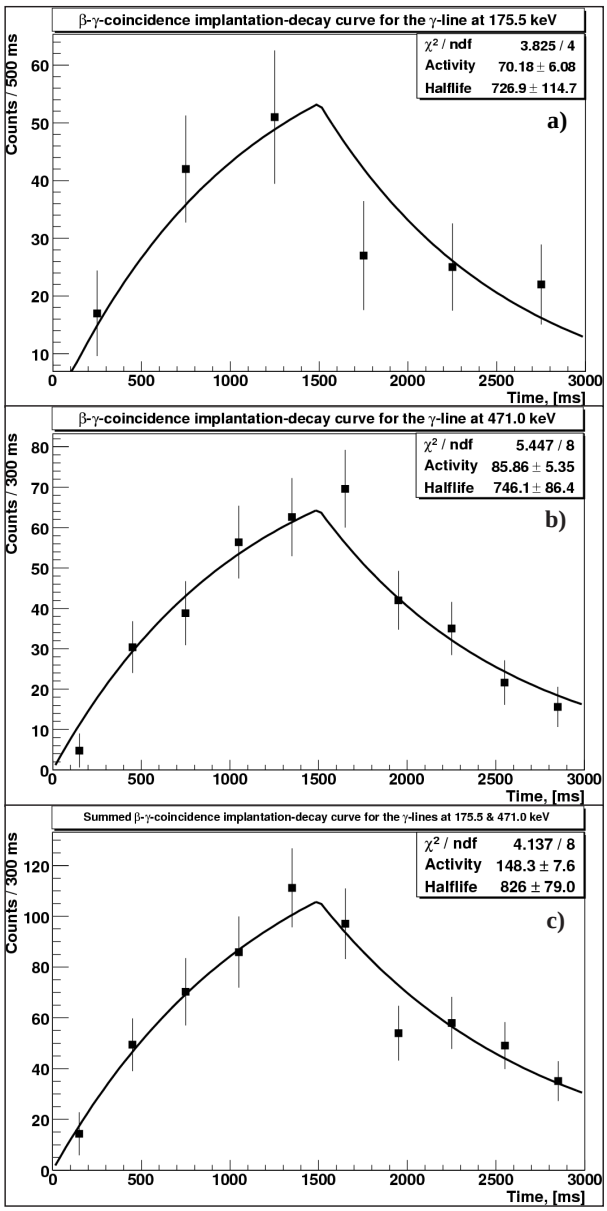


**Figure 5.6:** Extraction of the $\beta$-decay half-life time of $^{66}$Fe from the fit of the implantation-decay curves for the $\beta$-gated 175.5 and 470.9 keV $\gamma$-lines.

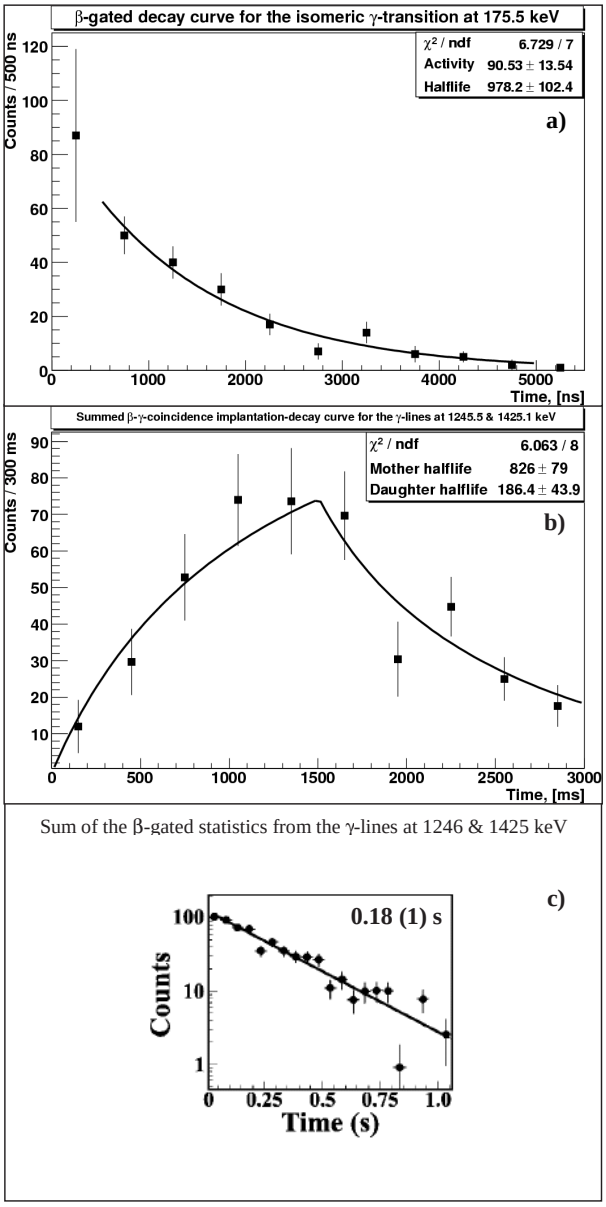


**Figure 5.7:** Half-life values of the ground and metastable states in $^{66}$Co nuclides: a) — extraction of the half-life time of the metastable state at 175.5 keV from the exponential decay fit; b) — consistency check on the $\beta$-decay half-life time of $^{66}$Co from the mother-daughter fit of the summed implantation-decay curve for the $\beta$-gated 1245.5 and 1425.1 keV $\gamma$-lines; c) — the more precise half-life time for the $\beta$-decay of $^{66}$Co obtained previously in a dedicated experiment [4] at LISOL.

values were extracted from the time behavior of single $\beta$-particles correlated with implanted nuclei, while in our case a higher selectivity can be obtained through $\beta$-$\gamma$-coincidences.

The available statistics from the laser OFF run does not allow to obtain a reliable half-life value for the decay of $^{66}$Co from the main two $\gamma$-transitions at 1245.6 and 1425.1 keV. The laser ON statistics can be used instead, by subtracting the upscaled laser OFF events and fitting the resulting implantation-decay curve with a mother-daughter activity function, which can be formulated on the basis of Eq. 5.1. Using the extracted half-life value for the decay of $^{66}$Fe, a consistency check for such mother-daughter implantation-decay curve for the sum of the two main $\gamma$-transitions in the decay of $^{66}$Co is given in Fig. 5.7b. Although our statistics cannot provide a more precise value, the resulting half-life is consistent with the previously known value of 0.18(1) s obtained in the dedicated experiment in [4], see Fig. 5.7c.

### 5.1.4 Isomers

The presence of spin isomers is widely expected in nuclei with prevailing shell-model structure. In our region of interest the spin-isomerism is additionally effectuated by the presence of the unique-parity $g_{9/2}$ state, separated from the $fp$-shell by the semi-magic $N$=40 shell gap. Additionally, through possible shape coexistence, shape isomers can become a distinct feature of nuclei not far from closed shells.

It is highly unlikely that in even-even $^{66}$Fe with a relatively low mass there is a long-lived $\beta$-decaying isomer. For this reason, we can safely presume that the $\beta$-decay of $^{66}$Fe proceeds from its $0^+_1$ ground state. Out of the two known isomers in $^{66}$Co, namely the $(5^+)$ at 176 keV and $(8^-)$ at 642 keV as assigned in [28], only the former one is likely to be seen in $\beta$-decay of $^{66}$Fe, as, indeed, shown in this experiment. However, the fact that the $\gamma$-transition at 175.5 keV from the first isomer is observed with relatively high intensity compared to other $\gamma$-lines, see Table 5.3, might indicate that this metastable state should have a lower value of spin. This issue will be addressed later in the text with more details at hand. The half-life time of this metastable state can be extracted from the time behavior of the $\beta$-gated $\gamma$-events on the right side from the peak of the $\beta$-$\gamma$-coincidence event distribution as shown in Fig. 5.5. By integrating the 175.5 keV photopeak activity within consecutive time windows of fixed size, a decay curve is obtained as shown in Fig. 5.7a. Fitting it with a simple exponential decay function yields a half-life time of 1.0(1) $\mu$s, which is slightly lower than the value of 1.21(1) $\mu$s obtained in [28]. Due to low statistics and insufficient timing resolution for registration of $\gamma$-radiation we cannot provide a better precision and, thus, cannot lay claims for a final value. Nevertheless, it is in a relatively good agreement with the result from [28], thus, pointing to a proper performance of the data-acquisition system.

**Table 5.4:** $\beta$-$\gamma$-$\gamma$-coincidence matrix for the $\gamma$-transitions assigned to the decay of $^{66}$Fe and $^{66}$Co nuclides. The energy gates are given in the leftmost column followed by the statistics of the coincident $\gamma$-photopeaks. Only laser ON statistics was used.

| $\gamma$-photopeak, [keV] | 175.5 | 470.9 | 510.6 | 806.7 | 881.2 | 918.6 | 981.4 |
|---|---|---|---|---|---|---|---|
| 175.5 | — | — | — | 17(4) | — | — | — |
| 470.9 | — | — | 32(6) | — | — | — | — |
| 510.6 | — | 31(6) | — | — | — | — | — |
| 806.7 | 17(4) | — | — | — | — | — | — |
| 881.2 | — | — | — | — | — | — | — |
| 918.6 | — | — | — | — | — | — | — |
| 981.4 | — | — | — | — | — | — | — |

| $\gamma$-photopeak, [keV] | 1245.6 | 1425.1 | 1804.0 |
|---|---|---|---|
| 1245.6 | — | 15(4) | — |
| 1425.1 | 16(4) | — | — |
| 1804.0 | — | — | — |

### 5.1.5 $\beta$-$\gamma$-$\gamma$-coincidences

The $\gamma$-lines from the Table 5.3 represent the $\gamma$-transitions from the excited states populated in $\beta$-decay of the corresponding mother isobars. Nuclear levels can de-excite through a cascade of several $\gamma$-transitions, which would result in registration of several $\gamma$-rays in coincidence with the same registered $\beta$-particle with a probability given as the multiplication of the corresponding registration efficiencies. This way, the final level schemes can be constructed with the use of $\beta$-$\gamma$-$\gamma$-coincidences, provided there is enough statistics for the registered $\gamma$-transitions. Although our statistics for the $\gamma$-transitions from the decay of $^{66}$Co is lower compared to that previously obtained in the dedicated experiment at LISOL [4], the resulting level scheme of $^{66}$Ni can be used as an ultimate check of the performance of our new $\beta$-$\gamma$-detection set-up and, thus, the validity of the new level scheme of $^{66}$Co.

Since our data-acquisition system provides timing information for all incoming events, the search for $m_\beta\beta$-$m_\gamma\gamma$-coincidences within a fixed time window, where $m_\beta$ and $m_\gamma$ are the $\beta$- and $\gamma$-detector event multiplicities, respectively, is performed in the off-line analysis. By requiring the $\gamma$-multiplicity $m_\gamma > 2$ and setting a fixed energy window for any of the coincident $\gamma$-events, the rest of the $\beta$-gated $\gamma$-events constitute the result of $\beta$-$\gamma$-$\gamma$-coincidences. Using only laser ON statistics, the $\beta$-$\gamma$-$\gamma$-coincidence spectra gated on the $\gamma$-lines assigned to the decay of $^{66}$Fe and $^{66}$Co in Table 5.3 are shown in Fig. 5.8, Fig. 5.9 and Fig. 5.10 with the coincidence matrix given in Table 5.4.

There are two possible cascades 175.5(1) + 806.7(3) = 982.2(3) keV and 470.9(1) + 510.6(1) = 981.5(1) keV, most probably originating from the same

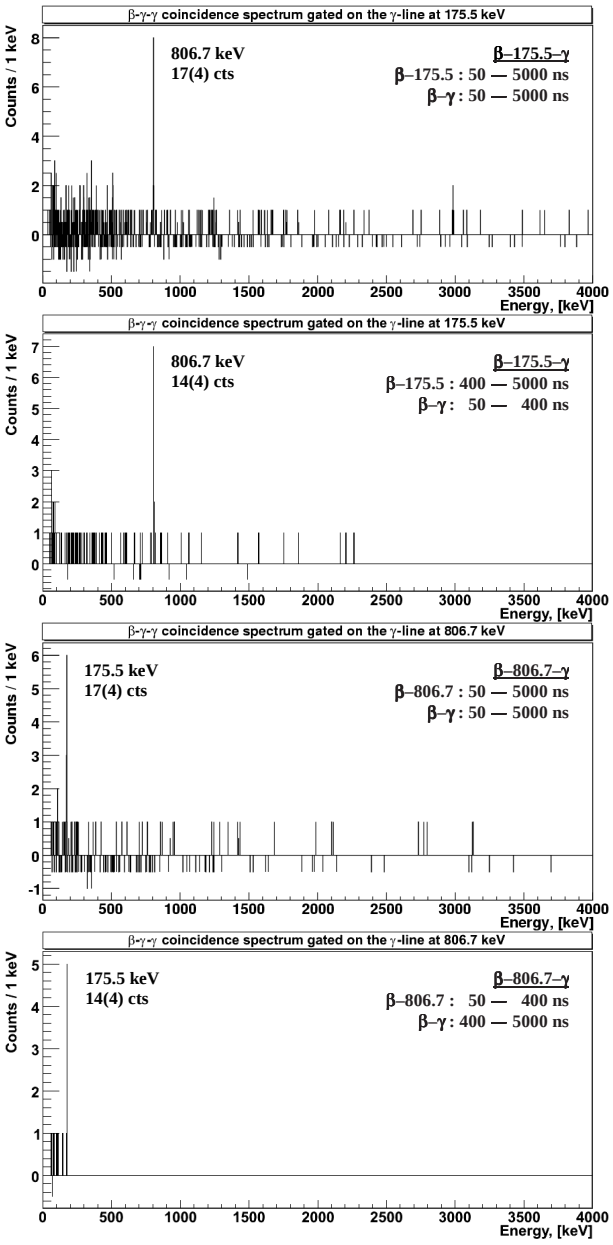


**Figure 5.8:** $\beta$-$\gamma$-$\gamma$-coincidences gated on the $\gamma$-lines from the decay of $^{66}$Fe from the laser ON data set. Similar to the results for the 881.2 and 918.6 keV $\gamma$-lines, the gate on the $\gamma$-transition at 981.4 keV yielded no coincident photopeaks in the resulting spectra and, therefore is not presented here. Subtraction of the continuum events under the $\gamma$-photopeak within the energy gate is performed based on the coincidence statistics from the energy windows on the left and right sides from the main gate, thus yielding negative counts in the final spectra.

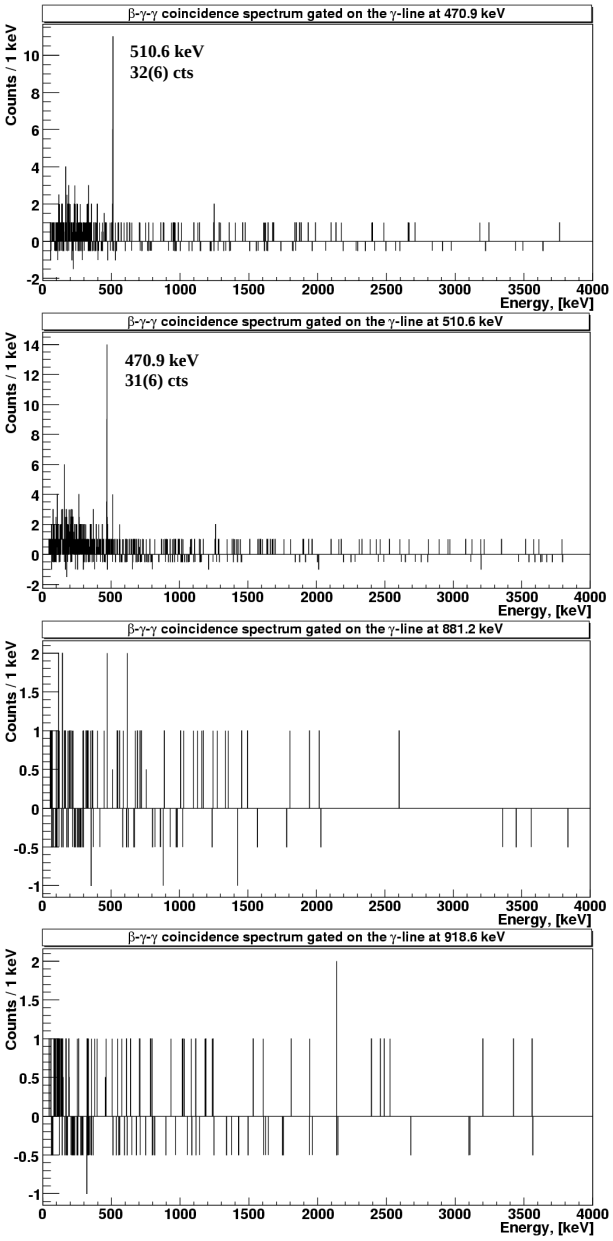


**Figure 5.9:** Continuation of the Fig. 5.8.

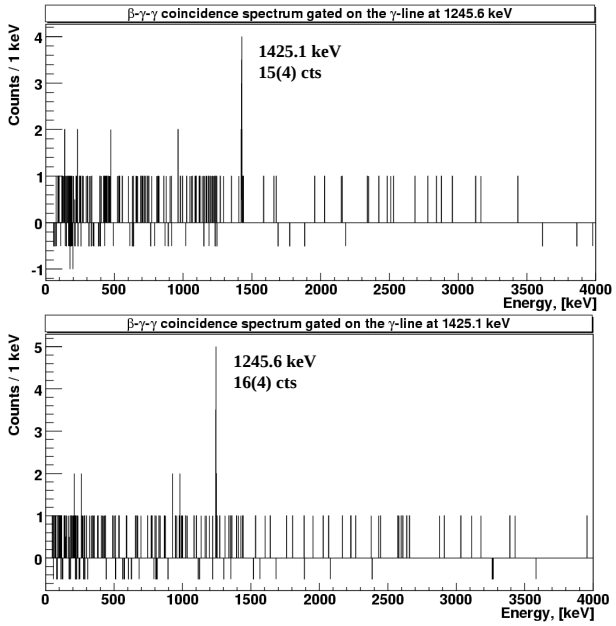


**Figure 5.10:** $\beta$-$\gamma$-$\gamma$-coincidences gated on the $\gamma$-lines from the decay of $^{66}$Co from the laser ON data set. Subtraction of the continuum events under the $\gamma$-photopeak within the energy gate is performed based on the coincidence statistics from the energy windows on the left and right sides from the main gate, thus yielding negative counts in the final spectra.

level at ∼982 keV, which can also cross over by decaying with emission of the 981.4(6) keV $\gamma$-line. Indeed, this is proved by $\beta$-$\gamma$-$\gamma$-coincidences gated on the 175.5, 806.7 and 470.9, 510.6 keV $\gamma$-transitions, as shown in Fig. 5.8 and Fig. 5.9, thus, indicating that these two pairs of $\gamma$-transitions constitute two cascades. The fact that the resulting coincident $\gamma$-photopeak intensities are statistically the same for these cascades, as follows from the coincidence matrix in Table 5.4, shows that the coincidence technique provides valid results. There is no coincidence between any of these four $\gamma$-transitions and the transition at 981.4 keV, being almost the same in intensity in $\beta$-gated spectrum as the 806.7 keV $\gamma$-line. This means that the 981.4 keV $\gamma$-line is most probably a cross-over transition, which must proceed directly to the ground state in $^{66}$Co based on the fact that the level at 175.5 keV was previously assigned to decay to the ground state in [28]. Since the 175.5 keV $\gamma$-transition originates from

the metastable state with the half-life time of 1.21(1) $\mu$s, the $\beta$-$\gamma$-$\gamma$-coincidence statistics gated on the 175.5 and 806.7 keV transitions can be substantially cleaned by requiring that events from the former transition be delayed while events from the latter transition be prompt in time with the corresponding coincident $\beta$-particle in accordance with the $\beta$-$\gamma$-coincidence time distribution in Fig. 5.5. As shown in Fig. 5.8, while the coincident photopeaks at 175.5 and 806.7 keV remain unchanged, there are no weak $\gamma$-lines coincident with these two transitions. The two remaining $\gamma$-transitions at 881.2 and 918.6 keV from the decay of $^{66}$Fe are comparable in intensity in the $\beta$-gated spectrum to the 806.7 keV $\gamma$-line and yield no photopeaks in the resulting $\beta$-$\gamma$-$\gamma$-coincidence spectra, see Fig. 5.9. They are equally not present in the coincidence spectra gated on any of the other available $\gamma$-transitions. No new $\gamma$-lines were found in the resulting spectra of $\beta$-$\gamma$-$\gamma$-coincidences. Any of the seemingly appearing photopeaks could be easily dismissed through statistical considerations, as, e.g., having too large or too small FWHM, or having very little statistical weight amidst the background of continuum events.

When it comes to cross-over transitions, as, in our case, the 981.4 keV $\gamma$-line, it is worth checking if they could simply originate as a result of the true coincidence summing (TCS), described in paragraph 3.3.3. Taking the cascade of the 470.9 and 510.6 keV $\gamma$-lines, the probability that the 981.4 keV $\gamma$-line in the $\beta$-gated spectrum is the sum of these two transitions is given as $\varepsilon_{TCS}^{981.4} = \varepsilon_{ph}^{470.9}/\mathcal{G}_\gamma \cdot \varepsilon_{ph}^{510.6}/\mathcal{G}_\gamma = 0.088/6 \cdot 0.084/6 = 0.00021$, where $\varepsilon_{ph}^{470.9}$ and $\varepsilon_{ph}^{510.6}$ are the photopeak efficiencies of the 470.9 and 510.6 keV $\gamma$-lines, respectively, and $\mathcal{G}_\gamma = 6$ is the granularity of the two MINIBALL cluster $\gamma$-detectors. Applying this factor to the total amount of events from the 470.9 keV $\gamma$-line available for $\gamma$-registration, which is simply the number of counts in the $\beta$-gated photopeak over the absolute $\gamma$-photopeak efficiency for the corresponding $\gamma$-ray energy, yields that only 0.8(0.1) out of 41(12) counts in the $\beta$-gated 981.4 keV photopeak could originate as a result of the TCS between the 470.9 and 510.6 keV $\gamma$-lines. Interestingly, if the granularity of the $\gamma$-detectors were $\mathcal{G}_\gamma = 1$ and $\mathcal{G}_\gamma = 2$ (as in our previous set-up), given that the absolute efficiency stays the same, then the amount of events in the $\beta$-gated 981.4 keV $\gamma$-photopeak due to TCS would be astounding 30(2) and 7(1) counts, respectively. This example clearly shows that with the current granularity $\mathcal{G}_\gamma = 6$ of the two MINIBALL triple-cluster detectors the effects of TCS become almost negligible, thus, almost removing any systematic errors in the counting statistics. For the cascade of the $\gamma$-transitions at 175.5 and 806.7 keV, there must be almost zero probability of TCS due to the simple fact that the state at 175.5 keV is isomeric. Indeed, by gating on any of these two lines with the $\beta$-$\gamma$-coincidence time window set from 50 to 400 ns, the resulting $\beta$-$\gamma$-$\gamma$-coincidences simply cannot reproduce this cascade.

The amount of $\beta$-gated $\gamma$-events in the possible transition at 510.6 keV

can be extracted from the $\beta$-$\gamma$-$\gamma$-coincidences gated on the $\gamma$-transition at 470.9 keV. Then, it must be compared to the difference between the absolute number of counts in the $\beta$-gated laser ON and (upscaled) laser OFF 511 keV photopeaks as follows:

$$\left[I^{510.6}_{\beta-\gamma-\gamma(470.9)}(ON)/\varepsilon^{510.6}_{ph}/\varepsilon^{470.9}_{ph} = 4302(761)\right] \approx$$
$$\left[(I^{510.6}_{\beta-\gamma}(ON) - 1.62 \cdot I^{510.6}_{\beta-\gamma}(OFF))/\varepsilon^{510.6}_{ph} = 4083(807)\right],$$

which simply means that the statistics in the laser ON 510.6 keV photopeak is easily reproduced as the sum of the counts from the possible $\gamma$-transition at 510.6 keV and the background-related statistics equally present in the laser OFF run. This way, the fact the former number is not two times smaller than the latter number indicates that no internal pair creation via $E0$ transition takes place in $^{66}$Co. Additionally, the probability of internal pair formation even for high-energy nuclear states at, e.g., 3–4 MeV is approximately three orders of magnitude lower than the probability of de-excitation through $\gamma$-ray emission. The possibility of the pair production from a high-energy $\gamma$-ray can also be discarded based on the fact that the available statistics in the 510.6 keV photopeak originating from the decay of $^{66}$Fe would require a presence of the full-energy or at least annihilation-radiation-escape photopeaks in the $\beta$-gated $\gamma$-spectrum. Summarizing this discussion, it can be concluded that, with this statistics at hand and limited only up to $\sim$4.3 MeV $\gamma$-registration energy range, the most possible explanation for the extra-statistics in the 510.6 keV $\gamma$-photopeak is that it originates from the $\gamma$-transition in the excitation spectrum of $^{66}$Co.

Out of the three known $\gamma$-transitions from the decay of $^{66}$Co the available statistics allowed to reproduce only the coincidences between the 1245.6 and 1425.1 keV $\gamma$-lines as shown in Fig. 5.10. This is in full agreement with the results from the dedicated experiment on $\beta$-decay of $^{66}$Co carried out at LISOL in the past [4], ensuring the validity of the performance of our new $\beta\gamma$-detection set-up.

## 5.2 Discussion: nuclear structure of $^{66}$Co

### 5.2.1 Level scheme

Based on the $\beta$-$\gamma$-$\gamma$-coincidences, discussed in the previous section, the resulting level scheme of $^{66}$Co is presented in Fig. 5.11 with the final list of all $\gamma$-lines observed in $\beta$-decay of $^{66}$Fe and $^{66}$Co nuclei in this experiment given in Table 5.5.

#### $^{66}$Co

All of the transitions, which were assigned as originating from the decay of $^{66}$Fe in Table 5.3, were placed to the new level scheme of $^{66}$Co. The ordering for the cascade of the 175.5 and 806.7 keV $\gamma$-transitions is obtained from $\beta$-$\gamma$-$\gamma$-coincidences, which clearly showed that the 806.7 keV transition belongs to the prompt part of the $\beta$-$\gamma$-coincidence event distribution while the 175.5 keV transition is delayed. Because of the low energy of the level at 175.5 keV and its isomeric life-time, the intensity of the corresponding 175.5 keV transition was corrected by considering the internal conversion coefficient of 0.06188(87) for the $M2$ transition [22], see the next paragraph for the discussion on the choice of multipolarity (for the $E2$ transition the coefficient is 0.06198(88)). Since no coincidences with other $\gamma$-lines are observed for the cascade of 470.9 and 510.9 keV $\gamma$-transitions, its right ordering cannot be determined. The 510.9 keV $\gamma$-transition is put lowest simply because it has higher energy. Feeding to this level is consistent with zero and therefore only the limits are given. Reversing the cascade results only in a slight change in given values of intensities and branching ratios. The 981.8 keV line is placed as the cross-over transition for the two cascades. The final energy of the considered 510.9(2) keV $\gamma$-transition was extracted from $\beta$-$\gamma$-$\gamma$-coincidences gated on the 470.9(1) keV $\gamma$-line by fitting the corresponding coincident photopeak. The intensity of this line was also extracted from the same coincidence spectrum gated on the 470.9 keV transition as given in the previous paragraph. The energy of 981.8(2) keV of the top level was obtained as an average of the energies of the cross-over 981.4(6) keV transition and two sums — 982.2(3) and 981.8(2) keV — of the 175.5(1), 806.7(3) keV and 470.9(1), 510.9(2) keV $\gamma$-cascades, respectively. Since no coincidences were obtained for the 881.2 and 918.6 keV $\gamma$-transitions, two additional levels at the corresponding energies were placed in the scheme and assigned to decay directly to the ground state. Although being the strongest $\gamma$-transition in the excitation spectrum of $^{66}$Co, the uncertainty for the intensity of the 510.9 keV $\gamma$-line is more than three times larger compared to that for the second-strongest 470.9 keV $\gamma$-line. Therefore, in order to reduce the uncertainty through error propagation the intensities of the $\gamma$-transitions in $^{66}$Co were calculated relative to the intensity of the 470.9 keV transition taken as 100 %.

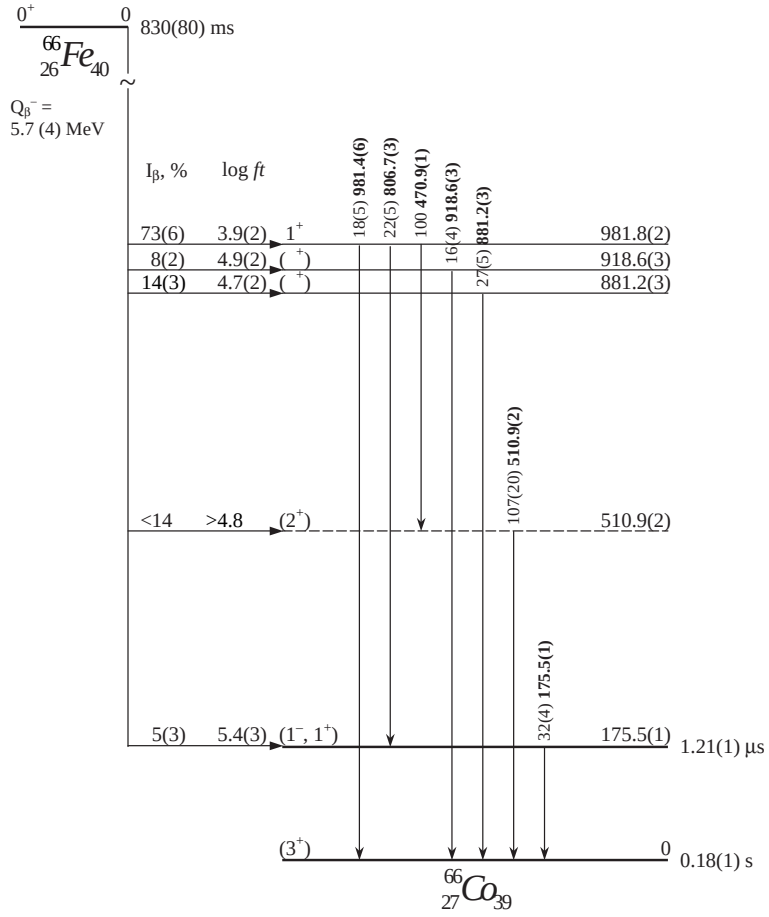


**Figure 5.11:** The resulting level scheme of $^{66}$Co. The absolute intensities of the transitions can be derived by multiplying the given relative intensities by the factor of 0.50. The level at 510.9 keV represents one of the two possibilities for the intermediate level in the cascade of the 470.9 and 510.9 keV transitions. The possibility for a level at 470.9 keV is equally plausible.

**Table 5.5:** The final list of $\gamma$-lines observed in $\beta$-decay of $^{66}$Fe (present experiment) and $^{66}$Co (present experiment / previous experiment at LISOL in [4]) nuclei.

| Nucleus | $E_\gamma$, [keV] | $I_\gamma^{rel}$ | Level, [keV] |
|---|---|---|---|
| $^{66}$Co | 175.5(1) | 32(4) | 175.5(1) |
| $^{66}$Co | 470.9(1) | 100 | 981.8(2) |
| $^{66}$Co | 510.9(2) | 107(20) | 510.9(2) |
| $^{66}$Co | 806.7(3) | 22(5) | 981.8(2) |
| $^{66}$Co | 881.2(3) | 27(5) | 881.2(3) |
| $^{66}$Co | 918.6(3) | 16(4) | 918.6(3) |
| $^{66}$Co | 981.8(2) | 18(5) | 981.8(2) |
| $^{66}$Ni | 1245.6(1) / 1246.1(2) | 79(7) / 69(5) | 2670.7(1) / 2672.0(3) |
| $^{66}$Ni | 1425.1(1) / 1425.9(2) | 100 / 100 | 1425.1(1) / 1425.9(2) |
| $^{66}$Ni | 1804.0(12) / 1804.7(2) | 13(4) / 9(2) | 3229.1(12) / 3230.6(3) |

### $^{66}$Ni

The level scheme of $^{66}$Ni was already known largely from the dedicated experiment on $\beta$-decay of $^{66}$Co [4]. Apart from the three known lines, no additional transitions were observed in the present experiment. As follows from the Table 5.5, the resulting intensities and branching ratios, albeit with lower precision, statistically overlap with the previously known values within given uncertainties. This generally good agreement with the previously known experimental information provides a confirmation of the previous results, also obtained at LISOL, as well as the validity of our new data.

### $^{66}_{26}$Fe$\xrightarrow{\beta^-}{}^{66}_{27}$Co$\xrightarrow{\beta^-}{}^{66}_{28}$Ni

Comparing the total activity of all transitions proceeding to the ground state of $^{66}$Co and the activity of the 1425.1 keV ground state transition in $^{66}$Ni, excluding the direct production of $^{66}$Co and correcting for the tape move after each three macrocycles, the resulting difference provides a $\sim$18(12)% excess of decays of the mother $^{66}$Fe nucleus. This indicates that within experimental uncertainty no ground-state transitions take place in the $\beta$-decay of $^{66}$Fe. Additionally, since no ground-state transitions were observed in the $\beta$-decay of $^{66}$Co in [4], this could also indicate that there might be an additional yet unobserved activity proceeding to the ground state of $^{66}$Ni. In general, this difference is small and can be viewed as an indication that a good consistency is achieved between the observed $\beta$-decays of Fe and Co isobars. However, subtracting the normalized laser OFF statistics from the laser ON single $\beta$ events and comparing the resulting statistics with the available $\gamma$-activity from both

$^{66}$Fe and $^{66}$Co decays, we get:

$$I_\beta = 12910 \pm 114$$

$$I_\gamma = \frac{A_{470.9}}{\varepsilon_{470.9} \cdot I^{abs}_{470.9}} + \frac{A_{1425.1}}{\varepsilon_{1425.1} \cdot I^{abs}_{1425.1}} = 7241 \pm 346$$

where $A_\gamma$ is the activity in the given $\gamma$-peak; $\varepsilon_\gamma$ is the photopeak $\gamma$-registration efficiency at given energy; and $I^{abs}_\gamma$ is the absolute intensity of the given $\gamma$-transition. As one can see, there are almost twice more $\beta$-decays than $\gamma$-activity in the decay of both the mother $^{66}$Fe and daughter $^{66}$Co nuclei. At first, this can be explained by a presence of ground-to-ground state $\beta$-decay transitions. However, as discussed later in the text, the resulting level schemes do not suggest a presence of such transitions. In addition to this, the time behavior of the single-$\beta$-events could not be explained assuming a simple mother-daughter decay. Thus, this issue remains unexplained.

### 5.2.2 Transition probabilities

Before going into any discussion on the nuclear structure of $^{66}$Co, it is important to assess the transition probabilities for different multipolarities, based on the Weisskopf [82] and Moszkowski [83] estimates, for all $\gamma$-transitions from the given level scheme. Provided that a good self-consistency is achieved, this may result in fixing spins and parities for many of the levels even without going into nuclear structure details. The Weisskopf and Moszkowski estimates of the transition probabilities for different multipolarities for all $\gamma$-transitions from the level scheme of $^{66}$Co are given in Table 5.6.

Without reservation, since $^{66}$Fe is an even-even nucleus, the spin $0^+$ can be firmly fixed for its ground state. For the following discussion it is important only in the context of the $\beta$-decay transitions to the excited states of the $^{66}$Co daughter nucleus.

#### The ground state

The spin ($3^+$) for the ground state of $^{66}$Co nucleus is based on the decay studies in [4].

#### The level at 981.8 keV

As follows from Table 3.1 in paragraph 3.1.3, the $\log ft$ value of 3.9(2) for the state at 981.8 keV is a clear indication of the allowed Gamow-Teller $\beta$-decay transition $\Delta I = 0, 1 \quad \Delta\pi = 0$. With spin $0^+$ out of consideration in nuclei far away from the $N = Z$ region, this immediately fixes the spin and parity of

**Table 5.6:** The Weisskopf [82] and Moszkowski [83] estimates of the transition probabilities for different multipolarities for all $\gamma$-transitions from the level scheme of $^{66}$Co. Half-life values for the given states are extracted from the corresponding transition probabilities as $T_{1/2} = \ln 2/\lambda$.

a) 175.5 keV

| Multipolarity | Transition Probability $\lambda$, [s$^{-1}$] | | Half-life Time $T_{1/2}$, [s] | |
|---|---|---|---|---|
| | Weisskopf | Moszkowski | Weisskopf | Moszkowski |
| $E1$ | 8.8E+12 | — | 7.9E-14 | — |
| $M1$ | 1.7E+11 | 1.6E+11 | 4.1E-12 | 4.4E-12 |
| $E2$ | 3.3E+06 | — | 2.1E-07 | — |
| $M2$ | 6.0E+04 | 2.3E+05 | 1.2E-05 | 3.0E-06 |
| $E3$ | 7.8E-01 | — | 8.9E-01 | — |
| $M3$ | 1.5E-02 | 1.2E-01 | 4.6E+01 | 5.8E+00 |
| $E4$ | 1.2E-07 | — | 5.6E+06 | — |
| $M4$ | 2.3E-09 | 3.3E-08 | 3.1E+08 | 2.1E+07 |

b) 214 keV

| Multipolarity | Transition Probability $\lambda$, [s$^{-1}$] | | Half-life Time $T_{1/2}$, [s] | |
|---|---|---|---|---|
| | Weisskopf | Moszkowski | Weisskopf | Moszkowski |
| $E1$ | 1.6E+13 | — | 4.3E-14 | — |
| $M1$ | 3.0E+11 | 2.8E+11 | 2.3E-12 | 2.4E-12 |
| $E2$ | 8.9E+06 | — | 7.8E-08 | — |
| $M2$ | 1.6E+05 | 6.2E+05 | 4.3E-06 | 1.1E-06 |
| $E3$ | 3.1E+00 | — | 2.2E-01 | — |
| $M3$ | 6.0E-02 | 4.8E-01 | 1.1E+01 | 1.5E+00 |
| $E4$ | 7.4E-07 | — | 9.4E+05 | — |
| $M4$ | 1.4E-08 | 2.0E-07 | 5.1E+07 | 3.5E+06 |

c) 252 keV

| Multipolarity | Transition Probability $\lambda$, [s$^{-1}$] | | Half-life Time $T_{1/2}$, [s] | |
|---|---|---|---|---|
| | Weisskopf | Moszkowski | Weisskopf | Moszkowski |
| $E1$ | 2.6E+13 | — | 2.7E-14 | — |
| $M1$ | 5.0E+11 | 4.6E+11 | 1.4E-12 | 1.5E-12 |
| $E2$ | 2.0E+07 | — | 3.5E-08 | — |
| $M2$ | 3.7E+05 | 1.4E+06 | 1.9E-06 | 5.0E-07 |
| $E3$ | 9.8E+00 | — | 7.0E-02 | — |
| $M3$ | 1.9E-01 | 1.5E+00 | 3.7E+00 | 4.6E-01 |
| $E4$ | 3.2E-06 | — | 2.2E+05 | — |
| $M4$ | 5.9E-08 | 8.6E-07 | 1.2E+07 | 8.1E+05 |

d) 470.9 keV

| Multipolarity | Transition Probability $\lambda$, [$s^{-1}$] | | Half-life Time $T_{1/2}$, [s] | |
|---|---|---|---|---|
| | Weisskopf | Moszkowski | Weisskopf | Moszkowski |
| $E1$ | 1.7E+14 | — | 4.1E-15 | — |
| $M1$ | 3.2E+12 | 3.0E+12 | 2.1E-13 | 2.3E-13 |
| $E2$ | 4.6E+08 | — | 1.5E-09 | — |
| $M2$ | 8.3E+06 | 3.2E+07 | 8.3E-08 | 2.2E-08 |
| $E3$ | 7.8E+02 | — | 8.9E-04 | — |
| $M3$ | 1.5E+01 | 1.2E+02 | 4.6E-02 | 5.8E-03 |
| $E4$ | 8.9E-04 | — | 7.8E+02 | — |
| $M4$ | 1.6E-05 | 2.4E-04 | 4.2E+04 | 2.9E+03 |

e) 510.9 keV

| Multipolarity | Transition Probability $\lambda$, [$s^{-1}$] | | Half-life Time $T_{1/2}$, [s] | |
|---|---|---|---|---|
| | Weisskopf | Moszkowski | Weisskopf | Moszkowski |
| $E1$ | 2.2E+14 | — | 3.2E-15 | — |
| $M1$ | 4.1E+12 | 3.9E+12 | 1.7E-13 | 1.8E-13 |
| $E2$ | 6.9E+08 | — | 1.0E-09 | — |
| $M2$ | 1.3E+07 | 4.8E+07 | 5.5E-08 | 1.5E-08 |
| $E3$ | 1.4E+03 | — | 5.0E-04 | — |
| $M3$ | 2.7E+01 | 2.1E+02 | 2.6E-02 | 3.3E-03 |
| $E4$ | 1.9E-03 | — | 3.7E+02 | — |
| $M4$ | 3.4E-05 | 5.0E-04 | 2.0E+04 | 1.4E+03 |

f) 806.7 keV

| Multipolarity | Transition Probability $\lambda$, [$s^{-1}$] | | Half-life Time $T_{1/2}$, [s] | |
|---|---|---|---|---|
| | Weisskopf | Moszkowski | Weisskopf | Moszkowski |
| $E1$ | 8.6E+14 | — | 8.1E-16 | — |
| $M1$ | 1.6E+13 | 1.5E+13 | 4.3E-14 | 4.6E-14 |
| $E2$ | 6.7E+09 | — | 1.0E-10 | — |
| $M2$ | 1.2E+08 | 4.7E+08 | 5.6E-09 | 1.5E-09 |
| $E3$ | 3.4E+04 | — | 2.0E-05 | — |
| $M3$ | 6.5E+02 | 5.2E+03 | 1.1E-03 | 1.3E-04 |
| $E4$ | 1.1E-01 | — | 6.1E+00 | — |
| $M4$ | 2.1E-03 | 3.0E-02 | 3.3E+02 | 2.3E+01 |

g) 881.2 keV

| Multipolarity | Transition Probability $\lambda$, [$s^{-1}$] | | Half-life Time $T_{1/2}$, [s] | |
|---|---|---|---|---|
| | Weisskopf | Moszkowski | Weisskopf | Moszkowski |
| $E1$ | 1.1E+15 | — | 6.2E-16 | — |
| $M1$ | 2.1E+13 | 2.0E+13 | 3.3E-14 | 3.5E-14 |
| $E2$ | 1.0E+10 | — | 6.6E-11 | — |
| $M2$ | 1.9E+08 | 7.3E+08 | 3.6E-09 | 9.5E-10 |
| $E3$ | 6.3E+04 | — | 1.1E-05 | — |
| $M3$ | 1.2E+03 | 9.6E+03 | 5.7E-04 | 7.2E-05 |
| $E4$ | 2.5E-01 | — | 2.8E+00 | — |
| $M4$ | 4.6E-03 | 6.7E-02 | 1.5E+02 | 1.0E+01 |

h) 918.6 keV

| Multipolarity | Transition Probability $\lambda$, [$s^{-1}$] | | Half-life Time $T_{1/2}$, [s] | |
|---|---|---|---|---|
| | Weisskopf | Moszkowski | Weisskopf | Moszkowski |
| $E1$ | 1.3E+15 | — | 5.5E-16 | — |
| $M1$ | 2.4E+13 | 2.2E+13 | 2.9E-14 | 3.1E-14 |
| $E2$ | 1.3E+10 | — | 5.4E-11 | — |
| $M2$ | 2.4E+08 | 9.0E+08 | 2.9E-09 | 7.7E-10 |
| $E3$ | 8.4E+04 | — | 8.2E-06 | — |
| $M3$ | 1.6E+03 | 1.3E+04 | 4.3E-04 | 5.4E-05 |
| $E4$ | 3.6E-01 | — | 1.9E+00 | — |
| $M4$ | 6.7E-03 | 9.7E-02 | 1.0E+02 | 7.1E+00 |

i) 981.8 keV

| Multipolarity | Transition Probability $\lambda$, [$s^{-1}$] | | Half-life Time $T_{1/2}$, [s] | |
|---|---|---|---|---|
| | Weisskopf | Moszkowski | Weisskopf | Moszkowski |
| $E1$ | 1.5E+15 | — | 4.5E-16 | — |
| $M1$ | 2.9E+13 | 2.7E+13 | 2.4E-14 | 2.5E-14 |
| $E2$ | 1.8E+10 | — | 3.8E-11 | — |
| $M2$ | 3.3E+08 | 1.3E+09 | 2.1E-09 | 5.5E-10 |
| $E3$ | 1.3E+05 | — | 5.2E-06 | — |
| $M3$ | 2.6E+03 | 2.0E+04 | 2.7E-04 | 3.4E-05 |
| $E4$ | 6.6E-01 | — | 1.0E+00 | — |
| $M4$ | 1.2E-02 | 1.8E-01 | 5.7E+01 | 3.9E+00 |

$1^+$ for this state. Consequently, this determines the multipolarity $E2$ for the ground-state 981.8 keV transition, see Table 5.6i.

**The level at 175.5 keV**

The spin and parity of $5^+$, assigned in [28], for the first excited state at 175.5 keV is based on the half-life of this isomer, which reduces the character of the 175.5 keV transition to stretched $E2$ or $M2$ transitions, see Table 5.6a. Consequently, the only possible spins are 1 and 5. The $5^+$ assignment was proposed for the first time in [28]. This level is fed by the 806.7 keV transition from the $1^+$ level at 981.8 keV, which also decays through the corresponding 981.8 keV $E2$ transition with equal intensity to the $3^+$ ground state. The prompt character of these $\gamma$-transitions and their intensity ratio will be used to estimate the multipolarity of the 806.7 keV transition. The only possibilities are $M1$,$E2/E1$,$M2$, thus excluding the spin 5 assignment for the level at 175.5 keV and leaving only the spin $1^+$ or $1^-$ possible assignments. Considering positive parity, this would lead to a $M1/E2$ character for the 806.7 keV transition. As can be seen in Table 5.6f, a 806.7 keV transition of $M1$ character is much faster than the 981.8 keV $E2$ transition. There are no known structural reasons, which could change this and, thus, the almost equal intensity of the two lines does not favor the positive-parity assignment. Although from Table 5.6f the same reasoning seems to exclude a $E1$ assignment for the 806.7 keV transition, many cases of strongly retarded $E1$ transitions are known. As an example, the state at 525 keV in $^{71}$Ge de-excites through emission of the 327 keV ($E2$, $I_{rel}$=37%) or much weaker 350 keV ($E1$, $I_{rel}$=4.6%) $\gamma$-transitions, while the Weisskopf estimates of the transition probabilities favor the latter $E1$ transition by almost six orders of magnitude. Together with the lack of strong direct $\beta$-decay feeding to the level at 175.5 keV the most plausible spin and parity assignment for this level is $1^-$.

**The level at 510.9 or 470.9 keV**

The relative intensities of the 510.9 and 470.9 keV transitions do not allow to determine the ordering in this cascade, leaving the possibility for a level at 510.9 or 470.9 keV. This cascade is the strongest de-excitation path of the level at 981.8 keV — five times stronger than the corresponding 981.8 keV transition. As can be seen from Table 5.6d,e, the closest match for the multipolarity of the 470.9 or 510.9 keV transition is $M1$, leading to the $2^+$ spin and parity assignment for this intermediate level. A $2^-$ assignment is not favored as there is no decay to the $1^-$ level at 175.5 keV. The lack of direct $\beta$-decay feeding is also an argument against a $1^+$ assignment for the intermediate level.

#### The levels at 881.2 and 918.6 keV

Since each of these levels is connected directly with the ground state, it is impossible to fix their spins without any additional transitions. Nevertheless, the corresponding $\beta$-decay branching ratios of 14(3) and 8(2)%, respectively, and the log$ft$ values of 4.7(2) and 4.9(2) might be an indication for allowed Gamow-Teller transitions. This would require positive parity assignment for these levels.

#### The levels at 390 and 642 keV

The metastable $8^-$ state at 642 keV and the $6^+$ state at 390 keV, which were not observed through $\beta$-decay in our experiment, were assigned in [28]. With the exclusion of the $5^+$ assignment for the level at 175.5 keV the spins and parities of these states must be re-examined. The fact that these levels are not populated in $\beta$-decay or connected with other states indicates that they must have high spin values. In addition to this, since the level at 642 keV is isomeric it is difficult to reassign its spin and parity without finding another nuclear structure interpretation for its isomeric nature.

### 5.2.3 Interpretation

#### Introductory remarks

As follows from the previous paragraph, the first level scheme of $^{66}$Co with only three excited states observed in [28] cannot be supported by our new and more extensive experimental results. First of all, based on the multipolarity assignments for the newly observed transitions, the isomeric state at 175.5 keV can have only the spin $1^{-/+}$ with most probable choice of negative parity. Secondly, the firm assignment of the spin $1^+$ for the level at 981.8 keV, which de-excites through emission of two independent cascades as well as the cross-over transition directly to the ground state with the spin $3^+$ puts angular momentum restrictions on the intermediate levels. Therefore, the former assignment of the spin $5^+$ from [28] for the level at 175.5 keV is proved to be incorrect. Finally, the levels at 642 and 390 keV from [28] were not observed.

As a consequence, the nuclear structure interpretation for $^{66}$Co nucleus will be given in the context of our new experimental results. Obviously, we must start by considering the connection between the nuclear structure information available for $^{66}$Fe and $^{66}$Ni nuclei.

#### Single-particle configurations

In the shell-model picture of the nucleus with a spherically-symmetric central potential, the ground state of $^{66}$Co, being one proton and one neutron away

from the closed $Z$=28 shell and the $N$=40 sub-shell, respectively, would correspond to the proton hole in the $\pi f_{7/2}$ orbital and the neutron hole in the $\nu p_{1/2}$ orbital, see Fig. 2.3. This configuration yields the $3^+$–$4^+$ spin multiplet, with the $3^+$ member being lowest and, thus, becoming the ground state. This way, with the $N$=40 neutron sub-shell closure being weaker, the lowest excited states in $^{66}$Co must be created through the $\nu f_{5/2}^{-1} p_{1/2}^{+2}$ and $\nu p_{1/2}^{-2} g_{9/2}^{+1}$ neutron particle-hole excitations within the $\nu$fpg-shell.

The most favorable decay channel in $\beta^-$-decay of $^{66}$Mn [19] and $^{66}$Co [4] nuclei as well as in neighboring isotopes, as discussed in the paragraph 3.1.4, is the fast Gamow-Teller $\nu 1f_{5/2} \rightarrow \pi 1f_{7/2}$ transition. The low $\log ft$ value of 3.9(2) for the strongly populated level at 981.8 keV is a clear indication of the allowed Gamow-Teller transition. This suggests the same $\nu 1f_{5/2} \rightarrow \pi 1f_{7/2}$ decay path in the $\beta$-decay of $^{66}$Fe, meaning that the nuclear wave function of this excited state in $^{66}$Co must be dominated by the $\pi f_{7/2}^{-1} \nu f_{5/2}^{-1}$ single-particle configuration. The residual interaction between the protons and neutrons from these two levels should give rise to the multiplet of states with spins ranging from $1^+$ to $6^+$. The $1^+$ level at 981.8 keV must then correspond to the $1^+$ member of this spin multiplet. Since the transitions between the states of the same multiplet are usually favorable, the $(2^+)$ level at 510.9 keV might also be dominated by the $\pi f_{7/2}^{-1} \nu f_{5/2}^{-1}$ single-particle configuration. Through configuration mixing within the whole $fp$-shell the $3^+$ member of this multiplet can constitute a small fraction of the ground state wave function mostly of $\pi f_{7/2}^{-1} \nu p_{1/2}^{-1}$ character.

A positive-parity assignment to the state at 175.5 keV is difficult to explain taking into account spherical single-particle configurations. Presence of deformation so close to $^{68}$Ni, involving proton excitations across the $Z$=28 shell gap, cannot be excluded, but such a discussion falls out of the scope of this work. The negative-parity state at 175.5 keV can be explained only by the presence of the intruder $\pi f_{7/2}^{-1} \nu p_{1/2}^{-2} \nu g_{9/2}^{+1}$ component in the corresponding nuclear wave function. Since there is no configuration mixing between the states of different parity, the energy of this level must be almost independent from other close-lying states. Therefore, the fact that this level is so low in energy close to the ground state clearly points to a very strong residual interaction between the $\pi f_{7/2}$ protons and the $\nu g_{9/2}$ neutrons.

**Proton-neutron coupling**

The occupation of levels within the fpg-shell can be derived from the sequence of states constituting the available spin multiplets. As discussed in paragraph 2.1.3, the proton-neutron residual interaction yields an overall parabolic behavior for the energy distribution of the states within a given multiplet, known as the Paar's rule [84]. The convex of the parabola is directed upward for the particle-particle and hole-hole configurations or, conversely, downward

for the particle-hole configurations. The farthest points on the sides of the parabola correspond to the aligned and anti-aligned spins of the protons and neutrons involved. Within the concept of the seniority scheme the odd number of several valence particles/holes can be considered as a single valence particle/hole. As follows from [84], for a pair of valent proton and neutron in the corresponding orbits with angular momenta $j_p$ and $j_n$, respectively, the total energy shift $\delta E$ of the member of the spin multiplet with the resulting angular momentum $J$ from its original unperturbed position is determined mainly by the energy exchange $\delta E_2$ of the $2^+$ quadrupole phonon and $\delta E_1$ of the $1^+$ spin-vibrational phonon:

$$\begin{gathered}\delta E = \delta E_2 + \delta E_1 \\ \delta E_2 = \frac{\alpha_2 \nu}{12} - \frac{\alpha_2 \nu}{16} \times \\ \frac{[J(J+1) - j_p(j_p+1) - j_n(j_n+1)]^2 + [J(J+1) - j_p(j_p+1) - j_n(j_n+1)]}{j_p(j_p+1) j_n(j_n+1)} \\ \delta E_1 = -\frac{\alpha_1}{4} \cdot \frac{[j_p(j_p+1) + j_n(j_n+1) - \eta J(J+1)]}{(j_p+1)(j_n+1)}\end{gathered} \tag{5.2}$$

where $\nu$ is the occupation number, defined as $\nu$=1 for particle-particle and hole-hole configurations and $\nu$=−1 for particle-hole configurations; $\alpha_2$ and $\alpha_1$ are the corresponding interaction strengths approximated as

$$\begin{aligned}\alpha_2 &\approx 4|(U_{jp}^2 - V_{jp}^2)(U_{jn}^2 - V_{jn}^2)| \\ \alpha_1 &\approx \frac{160}{A} U_{jp} V_{jp} U_{jn} V_{jn}\end{aligned} \tag{5.3}$$

Here, $U_j^2$ and $V_j^2$=1−$U_j^2$ are emptiness and fullness factors, which can be approximated by the relative particle/hole occupations of the orbitals[1]; $A$ is the atomic mass number. Finally, the factor $\eta$ is defined as:

$$\eta = \begin{cases} \frac{(j_n+1)}{j_n}, & \text{if } \mathcal{N} = 0^+ \\ \frac{(j_p+1)}{j_p}, & \text{if } \mathcal{N} = 0^- \\ \frac{(j_p+1)(j_n+1)}{j_p j_n}, & \text{if } \mathcal{N} = 1 \\ 1, & \text{if } \mathcal{N} = -1 \end{cases} \tag{5.4}$$

where $\mathcal{N}$=$j_p - l_p + j_n - l_n$ is the so-called Nordheim number with $\mathcal{N}$=$0^+$ and $\mathcal{N}$=$0^-$ denoting the situations when $j_n - l_n$=$\frac{1}{2}$, $j_p - l_p$=$-\frac{1}{2}$ and $j_n - l_n$=$-\frac{1}{2}$, $j_p - l_p$=$\frac{1}{2}$, respectively.

Based on the given formalism, the resulting energy splitting between the members of the $\pi f_{7/2}^{-1} \nu f_{5/2}^n$ and $\pi f_{7/2}^{-1} \nu g_{9/2}^n$ multiplets for Co isotopes, where $n$ is

[1] For instance, for the level $f_{7/2}$ with 3 out of possible 8 particles, the fullness and emptiness factors are approximated as $U_{j=7/2}^2 \approx 3/8$ and $V_{j=7/2}^2 \approx 5/8$, respectively.

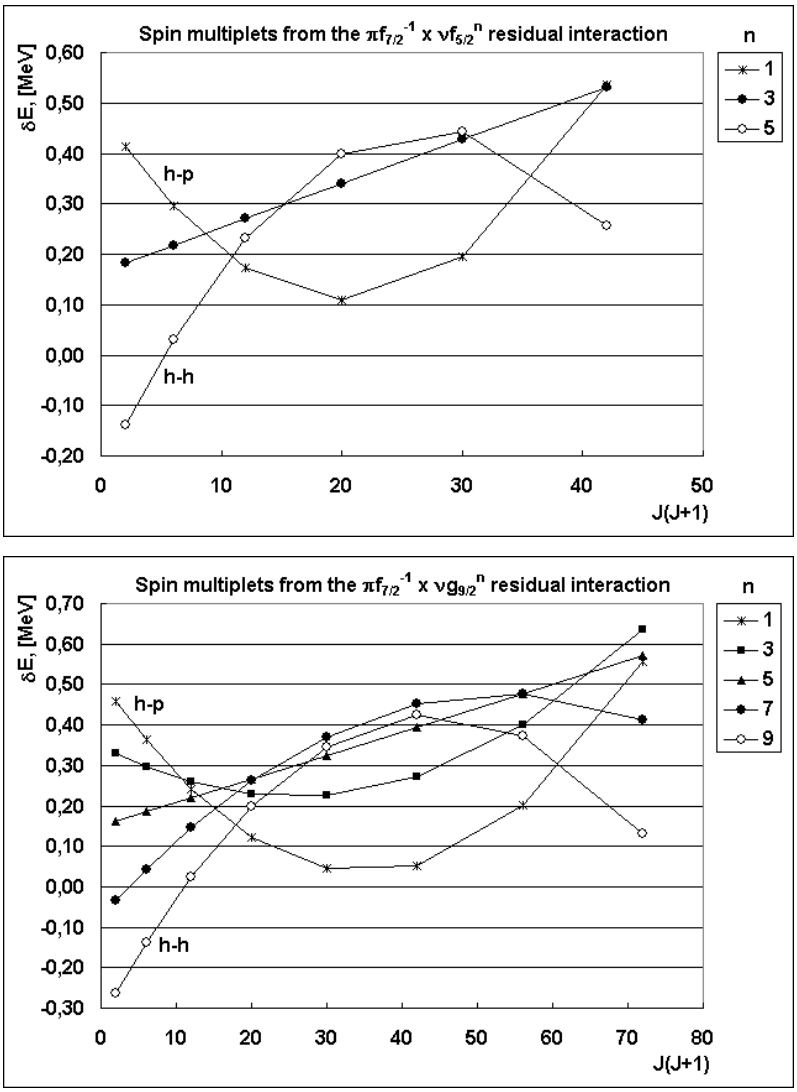


**Figure 5.12:** The calculated energy splitting between the members of the $\pi f_{7/2}^{-1}\nu f_{5/2}^{n}$ and $\pi f_{7/2}^{-1}\nu g_{9/2}^{n}$ spin multiplets, based on the Paar's rule [84]. Here $n$ is an odd number of particles/holes in the corresponding neutron orbitals. The spin multiplets in the upper and lower figures can be related to the ground states of $^{59+n}$Co and $^{67+n}$Co isotopes, respectively.

an odd number of particles/holes in the corresponding neutron orbitals, is presented in Fig. 5.12. Clearly, such estimations consider only the approximated effects of the residual interaction between the valent protons and neutrons and cannot take into account interaction with members of other spin multiplets. In this picture, the $\pi f_{7/2}^{-1}\nu f_{5/2}^{n}$ and $\pi f_{7/2}^{-1}\nu g_{9/2}^{n}$ configurations for the possible excited states in $^{66}$Co must be linked to a ground-state configuration of a Co isotope with the same occupation of the given neutron orbital. As follows from the Fig. 5.12, if the $1^+$ state at 981.8 keV and the $(2^+)$ state at 510.9 keV are members of the same multiplet with the configuration $\pi f_{7/2}^{-1}\nu f_{5/2}^{n}$, then the experimental sequence of these two levels can be reproduced only with $n$=1 particles (5 holes) in the $\nu f_{5/2}$ orbital. Similarly, if the spin and parity assignment for the $(1^-)$ state at 175.5 keV is correct, then the low energy of this state with the most probable $\pi f_{7/2}^{-1}\nu g_{9/2}^{n}$ configuration can be explained only with $n \geq$5 particles in the $\nu g_{9/2}$ orbital. In this simplified picture, five neutrons from the $\nu f_{5/2}$ orbital must be excited across the $N$=40 neutron sub-shell gap into the $\nu g_{9/2}$ orbital. Due to the fact that pairing interaction is stronger in the $\nu g_{9/2}$ orbital (five possible neutron pairs), the $\nu p_{1/2}$ orbital (only one possible pair) may easily remain unoccupied.

**The prevalence of the proton $Z$=28 and neutron $N$=40 shell closures**

As follows from the discussion in paragraph 2.2.3, although $^{68}$Ni cannot be considered as a fully-established (semi-)doubly-magic nucleus, to a large extent the nuclear structure of nuclei in its immediate neighborhood, such as $^{67,69}$Ni and $^{68,69,70}$Cu, with one proton and/or one neutron away from the proton $Z$=28 and/or neutron $N$=40 closed shells, respectively, can still be explained in simple single-particle terms as one or two particles(holes) coupled to the $^{68}$Ni core. For the odd-odd nuclei this means that the lowest energy levels must originate as a result of the residual interaction between the single proton and neutron particles(holes) outside an inert core. As shown in Fig. 2.10, this is indeed the case for the odd-odd $^{68}$Cu and $^{70}$Cu nuclei: the lowest energy levels can be easily explained as members of the spin multiplets arising from the particle-particle $\pi$-$\nu$ residual interaction. It is clear at this point, that the excitation spectrum of the odd-odd $^{66}$Co nucleus cannot be explained in a similar straightforward way. In the $\pi f_{7/2}^{-1}\nu f_{5/2}^{6-n}\nu p_{1/2}^{-2}\nu g_{9/2}^{1+n}$ configuration, the reversed ordering of the $1^+$ and $(2^+)$ levels and the fact that the $(1^-)$ state is situated very close to the ground state can be both explained only if a different sequence of single-particle states, compared to that in $^{68}$Ni, is involved. In simple single-particle terms, the excited states in $^{66}$Co would then correspond to as many as five particle-hole excitations from the $^{68}$Ni core across the neutron $N$=40 subshell gap. It is clear that there must be a serious structural change that would account for such a dramatic disappearance of the neutron $N$=40

subshell closure in the odd-odd $^{66}$Co nucleus. As cautiously pointed out in the paragraph 2.2.3, since there is a much stronger overlap between the radial parts of the nuclear wave-functions for nucleons in $\pi f_{7/2}$ and $\nu f_{5/2}$, $\pi f_{7/2}$ and $\nu g_{9/2}$, compared to that for nucleons in $\pi p_{3/2}$ and $\nu f_{5/2}$, $\pi p_{3/2}$ and $\nu g_{9/2}$ as in neutron-rich Cu isotopes, one might expect more pronounced effects of the $\pi$-$\nu$ residual interaction in neutron-rich Co isotopes. Clearly, this would lead not only to a strong weakening of the neutron $N$=40 subshell closure but also to the partial obliteration of the larger proton $Z$=28 shell gap through additional particle-hole excitations across its reduced length.

It is worth noting here, that the analysis of the $A$=67 data sets revealed an existence of the long-lived ($T_{1/2}$ ≈400 ms) isomer, which was placed firmly in the level scheme of $^{67}$Co [85]. At the moment of writing, there are still serious difficulties in interpretation of the excitation spectrum of this nucleus. The author strongly considers that the enhanced residual interaction between the proton hole(s) in the $\pi f_{7/2}$ orbital and the neutron particles/holes in the $\nu f_{5/2}$ and especially $\nu g_{9/2}$ orbitals might clearly be the reason behind the sudden and unexpected changes in the nuclear structure of both $^{66}$Co and $^{67}$Co nuclei.

**Shell-model calculations**

As shown in paragraph 2.2.3, prior to our experiments at LISOL the nuclear structure of neutron-rich Co nuclei close to $^{68}$Ni had been largely unknown due to a very scarce and limited experimental information. Lack of solid results from experimentalists ensured a subsequent lack of consistent predictions from theoreticians. In order to corroborate and explain the new level scheme of $^{66}$Co, we have performed large-scale shell-model calculations using the computer code based on the formalism described in [86]. In order to fully consider multi-particle excitations in the proton $\pi f_{7/2}$ and neutron $\nu fpg$-shells, the $^{48}$Ca nucleus was chosen as the inert core. In contrast to the Monte-Carlo approach [3], in which the valence space can be effectively truncated based on the occupation probabilities, the large-scale shell-model calculations ideally take into account all possible combinations within the given valence space. Such computations are limited by the computer processing power and memory and, therefore, the valence space had to be truncated. Since neutron excitations are expected to play a dominant role in structuring the excitation spectrum of neutron-rich Co nuclides, the chosen valence space had to contain the neutron $\nu p_{3/2}$, $\nu f_{5/2}$, $\nu p_{1/2}$, and $\nu g_{9/2}$ orbitals and, thus, was limited to only the proton $\pi f_{7/2}$ orbital. It is important to note that the calculations did not contain the monopole interaction [3], which can strongly vary from nucleus to nucleus and, therefore, has to be extracted from various systematics.

The calculated excitation spectra up to 2 MeV in energy for neutron-rich odd-odd $^{56-66}$Co isotopes, representing the whole $\nu fp$-shell, are given in Fig. 5.13 together with the known experimental level schemes. Although, at

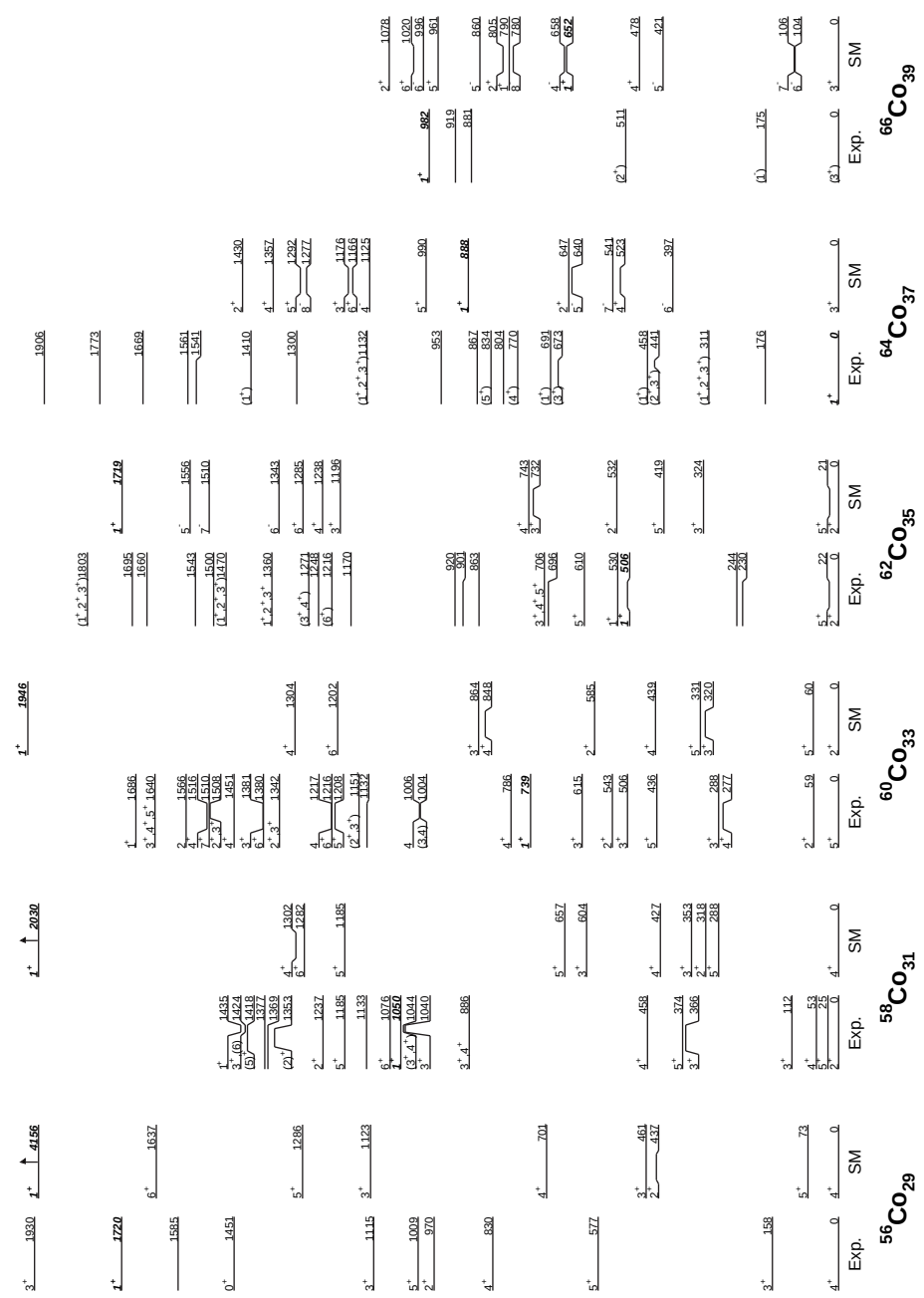


**Figure 5.13:** Results of the performed large-scale shell-model calculations for the neutron-rich odd-odd $^{56-66}$Co isotopes together with the known experimental level schemes. The lowest $1^+$ states are indicated in bold italic.

first, the overall match between the calculated and experimental data is rather poor, there is a reasonable agreement for $^{56}$Co and still some consistency in level energies and ordering at least till $^{64}$Co. A noticeably larger number of experimental levels is due to truncation of the valence space in the calculations and the fact the calculated levels are less compressed in energy and, therefore, many of them are not within the 2 MeV energy cut. In the context of the nuclear structure of $^{66}$Co nucleus special attention must be drawn to the systematics of the $1^+$ states and the position of the spin multiplets of negative-parity states.

In the ideal shell-model picture of the selected valence space, the lowest $1^+$ states in the odd-odd $^{56-66}$Co nuclei must result from the $\pi f_{7/2}^{-1}\nu f_{5/2}^{+1}$ configuration. The next $1^+$ state must be formed by lifting a proton from the $\pi f_{7/2}$ orbital across the $Z$=28 shell gap. From examination of the available experimental levels and transitions between them, the lowest experimental $1^+$ states in the presented Co nuclei, indeed, must be dominated by the $\pi f_{7/2}^{-1}\nu f_{5/2}$ configuration. In accordance with the behavior of the $\pi f_{7/2}^{-1}\nu f_{5/2}^{n}$ spin multiplet in Fig. 5.12, the experimental (lowest) $1^+$ states are at first higher in energy than other members of the multiplet in $^{56,58,60}$Co, corresponding to the downward-directed parabola of the hole-particle type, and then become lower in $^{64,66}$Co nuclei, complying with the reversed upward-directed parabola of the hole-hole type. The first real disagreement between the experiment and calculations takes place in $^{64}$Co, for which the predictions still yield a parabola of the hole-particle type for this spin multiplet, resulting in the ground state of $3^+$ instead of $1^+$. A similar situation is observed in $^{66}$Co. Although the ground state of $3^+$ from the $\pi f_{7/2}\nu p_{1/2}$ configuration is reproduced by calculations, the sequence of the $1^+$ and $2^+$ states is reversed.

The negative-parity states, which must involve the unique-parity $\nu g_{9/2}$ orbital, appear within the 2 MeV energy cut only for the $^{64}$Co and $^{66}$Co nuclei with three and one neutrons, respectively, away from the neutron $N$=40 shell closure. A substantial disagreement takes place in the $^{66}$Co nucleus. In comparison with the experimental results, the calculated level sequence for the $\pi f_{7/2}^{-1}\nu g_{9/2}^{n}$ spin multiplet is reversed. Again, taking also into account the reversed level sequence for the $\pi f_{7/2}^{-1}\nu f_{5/2}^{n}$ spin multiplet, we are coming to the same conclusion that the neutron $\nu g_{9/2}$ orbital is filled by at least five particles at the expense of the underlying $fp$-shell, leaving only one particle in the $\nu f_{5/2}$ orbital.

**Onset of deformation**

As discussed in paragraph 2.2.4, the proton-neutron residual interaction can lead to a sudden onset of deformation. In the presence of the deformed potential, the degeneracy of the orbitals will be removed, resulting in a change in the sequence of single-particle states as shown in Fig. 5.14. As follows from

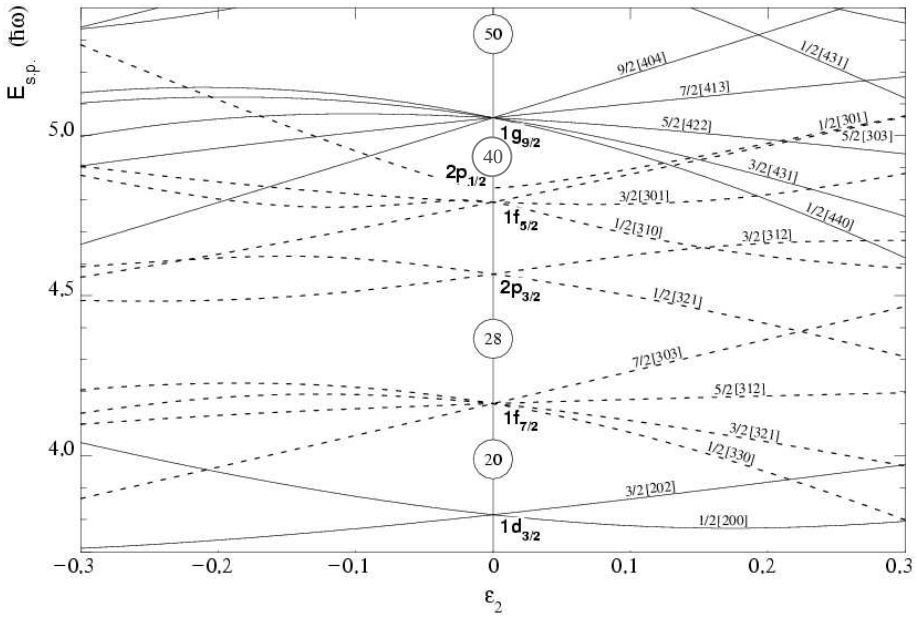


**Figure 5.14:** Nilsson diagram for both proton and neutron single-particle levels, constituting the Fermi level in nuclei from the Ni region. The abscissa is the deformation parameter $\varepsilon$ similar to $\beta$ and the ordinate represents the single-particle energy in units of $\hbar\omega$. The solid and dashed lines represent, respectively, the positive- and negative-parity levels.

the systematics of the quadrupole deformation parameter $\beta$ for nuclei from the neutron-rich Ni region in Fig. 2.11, the $0^+$ ground state in $^{66}$Fe is expected to be strongly deformed with $\beta$=+0.30, while the $3^+$ ground state in $^{66}$Co is close to spherical with $\beta$=+0.09. The fact that there is the negative-parity state observed in the excitation spectrum of $^{66}$Co immediately suggests that the neutron $\nu g_{9/2}$ orbital is occupied. Additionally, as already discussed, the reversed level sequence for both the $\pi f_{7/2}^{-1}\nu f_{5/2}^{n}$ and $\pi f_{7/2}^{-1}\nu g_{9/2}^{n}$ spin multiplets requires that at least five particles be present in the $\nu g_{9/2}$ orbital with five holes in the $\nu f_{5/2}$ orbital. As follows from Fig. 5.14, such scenario might take place at a prolate deformation of $\beta \approx$+0.30, which is in a good agreement with the known deformation for the ground state of $^{66}$Fe. This means that the fast Gamow-Teller $\nu 1f_{5/2} \rightarrow \pi 1f_{7/2}$ transition in $\beta$-decay of $^{66}$Fe takes place

between two deformed states. Additionally, if the $1^+$ state at 981.8 keV in $^{66}$Co is deformed, then the same deformation can be expected for the $2^+$ state at 510.9 keV, being the member of the same spin multiplet. All this suggests that the $1^+$, $(2^+)$, and $(1^-)$ states in $^{66}$Co are most probably strongly deformed with the $(3^+)$ ground state most likely remaining spherical. Additionally, apart from the evident obliteration of the $N$=40 neutron sub-shell closure, one might expect proton excitations across the $Z$=28 proton shell gap. This way, $^{66}$Co can be considered as an example of a shape coexistence in the neutron-rich Ni region.

**Conclusion**

Finally, it is worth drawing a logical conclusion to the overall discussion on the resulting nuclear structure of $^{66}$Co:

- The ground state of $^{66}$Co is suggested to be spherical with the spin $3^+$ arising from the $\pi f_{7/2}\nu p_{1/2}$ spin multiplet [26][28], eventually mixed with the $\pi f_{7/2}^{-1}\nu f_{5/2}^{-1}\nu p_{1/2}^{+2}$ configuration;

- Following the allowed Gamow-Teller $\nu 1f_{5/2} \rightarrow \pi 1f_{7/2}$ transition in $\beta^-$-decay of $^{66}$Fe, the state at 981.8 keV in $^{66}$Co can be firmly assigned with the spin and parity of $1^+$ with the dominant $\pi f_{7/2}^{-1}\nu f_{5/2}^{-1}\nu p_{1/2}^{+2}$ configuration. The level at 510.9 keV (or 470.9 keV) is most probably a $(2^+)$ state, having the same configuration due to the enhanced transition to it from the $1^+$ state;

- The level at 175.5 keV has spin $1^+$ or $1^-$. Taking into account all experimental facts, there is a slight preference for the $1^-$ spin and parity assignment. Within the available shell-model states this can originate only from the occupation of the $\nu g_{9/2}$ orbital;

- However, a Paar's parabola based on the hole-hole configuration cannot have the $1^-$ as the lowest state. Only by considering multi-particle–multi-hole excitations across the $N$=40 neutron sub-shell and possibly $Z$=28 proton shell gaps, unavoidably leading to the onset of deformation, might resolve this issue.

# Chapter 6

# Conclusion and outlook

## 6.1 Conclusion

In this work we reported on the characterization of a new $\beta$-$\gamma$-detection set-up developed and constructed for the study of weak and purified sources of short-lived radioactive nuclei. This set-up was subsequently used to study $\beta$-decay of $^{66}$Fe. Thus, the presented work had two distinctive goals:

1. Technical task — to develop and implement a new $\beta$-$\gamma$-detection set-up based on highly-segmented detectors for our nuclear-structure studies in $\beta$-decay experiments at the LISOL facility;

2. Physics task — using this new and more advanced experimental tool, to perform further nuclear-structure studies of the neutron-rich nuclei from the lower part of the Ni region, namely of the almost unexplored neutron-rich $^{65,66,67}$Co nuclei in $\beta^-$-decay of the corresponding $^{65,66,67}$Fe isobars with the main accent on the $^{66}$Co nucleus.

The achievements of this work on each of the two goals can be summarized separately as follows:

**Development of the new $\beta$-$\gamma$-detection set-up**

- A new twelve-fold segmented HPGe MINIBALL triple-cluster $\gamma$-detector was assembled, successfully tested, and implemented as a basis of the new detection set-up. The detector was wired as six-fold segmented by coupling the longitudinal segments at the preamplifier level;

- Adding a six-fold segmented MINIBALL triple-cluster detector and arranging both detectors at opposite sides perpendicular to the beam, the

close-geometry $\gamma$-detection system was installed at the implantation tape system at the LISOL facility. Compared to the previous detection set-up with two coaxial HPGe single-crystal $\gamma$-detectors, the new system offers the following advantages in $\gamma$-registration:

  - The photopeak $\gamma$-registration efficiency was increased by a factor of $\sim$1.5 — from $\sim$4% to $\sim$6% at 1 MeV $\gamma$-ray energy;
  - The granularity was increased from 2 to 6 separate crystals, which allowed to reduce substantially the effects of true-coincidence summing for $\gamma$-ray cascades. Not only did it diminish the associated systematical errors from the experimental decay schemes, but it also resulted in further increase in the photopeak $\gamma$-registration efficiency depending on the multiplicity of the $\gamma$-cascades involved;

- Although three plastic scintillator $\beta$-detectors from the previous set-up were not substituted with any new detectors, some parallel work has been done in determining the choice of material and providing the basis for construction and implementation of new segmented $\beta$-detectors in the near future;

- New multi-layer detector shielding was constructed and installed, effectively confining the implantation spot and the increased volume of the $\gamma$-detectors. This allowed

  - To keep attenuation of the background $\gamma$-rays on the same level as with the previous set-up;
  - To improve attenuation of the experimental neutron flux by a factor of $\sim$5 for thermal neutrons and more than 2 for fast neutrons;

- New multi-channel data-acquisition system based on digital signal-processing was assembled and implemented in the detection set-up;

- Various technical and logistical developments, such as, e.g., detector tables, frames, and the liquid-nitrogen auto-fill system, have been done to allow for a smooth, controlled, and uninterrupted performance of the new detection set-up;

- New data-analysis code based on the C, C++ programming languages and the ROOT graphics and data-storage package was written;

- New simulation code based on the GEANT package and adapted from the already existing code from the MINIBALL collaboration was introduced, albeit only in its first stages.

**Nuclear-structure studies**

- Using the new $\beta$-$\gamma$-detection set-up, apart from other experiments aimed at nuclear-structure studies of nuclei from other regions of the nuclear chart, two separate experiments on $\beta$-decay of $^{65,66,67}$Fe were successfully performed at LISOL;

- A new detailed level scheme of $^{66}$Co was obtained. A striking feature is the lowest excited state at 175.5 keV, which most probably has the spin and parity of $1^-$ or $1^+$, which is in contrast to the previous $5^+$ assignment prior to this work;

- A new nuclear-structure interpretation of the excitation spectrum of $^{66}$Co is offered. A negative-parity assignment for the 175.5 keV state can only be obtained when neutrons from the fp-shell are excited across the $N$=40 sub-shell gap to the $g_{9/2}$ orbital. Consideration of simple $\pi f_{7/2}^{-1} \otimes \nu g_{9/2}^{+1}$ configurations as well as shell-model calculations do not reproduce such a low-lying $1^-$ state. A more detailed understanding might require consideration of multi-particle–multi-hole excitations across the neutron $N$=40 and proton $Z$=28 shell gaps and thus questions the quasi-doubly-magic character of the $^{68}_{28}Ni_{40}$ nucleus;

- The existence of the low-lying negative-parity isomeric state might indicate a presence of deformation due to a strong proton-neutron residual interaction between the proton hole(s) in the $\pi f_{7/2}$ orbital and the neutron particles in the $\nu$fpg-shell. This way, the onset of deformation can lead to obliteration of both the neutron $N$=40 and proton $Z$=28 shell gaps. The combination of the spherical ground state and deformed excited states suggests shape coexistence in the $^{66}$Co nucleus.

## 6.2 Outlook

The work presented in this thesis naturally leads to possible extensions and improvements:

**Further developments for the new $\beta$-$\gamma$-detection set-up**

- The twelve-fold segmented MINIBALL cluster (with only the six-fold longitudinal transverse segmentation wired up) has to be fully wired to include the two-fold longitudinal segmentation.

- The proper use of the segment information from the MINIBALL clusters. This will allow

  - To increase the full-energy-peak $\gamma$-registration efficiency (by additional more than $\sim$1% at 1 MeV $\gamma$-ray energy) by performing the add-back procedure using the segment hit pattern;
  - Alternatively, to perform the on-board pulse-shape analysis of the incoming $\gamma$-detector signals. Using the longitudinal segmentation may even allow a very crude $\gamma$-ray tracking;
  - To further increase the granularity of the $\gamma$-detectors from 6 to 36 and, thus completely removing the impact of the true-coincidence summing and justifying the use of the add-back procedure.

- Introduction of new segmented $\beta$-detectors. This will allow
  - To increase the selectivity of both $\beta$- and $\gamma$-detectors;
  - To reduce losses in $\gamma$-registration efficiency when the veto procedure has to be performed.

- Introduction of (preferably segmented) active shielding around the MINIBALL clusters;

- Installation of additional active shielding against cosmic radiation on top of the existing passive shielding;

- Possible introduction of additional detectors — $\Delta E$-$E$ detector for measuring full energy of $\beta$-particles or Si detectors for registration of conversion electrons;

- Further development of the simulation code in order to check all feasible detector configurations;

**Further nuclear-structure studies**

- Preferably after all essential work on further developments for the new $\beta$-$\gamma$-detection set-up gets done, to extend the $\beta$-decay studies of neutron-rich Fe isotopes to the $^{63,64}$Fe and possibly $^{68}$Fe nuclei;

- To extend $\beta$-decay studies to neutron-rich nuclei further below the $Z$=28 proton shell — e.g., Mn and Cr isotopes. This can help to asses properly the onset of deformation in this region of the nuclear chart.

# Samenvatting

## Inleiding

Dit werk kadert in een globale studie van de kernstructuur in het neutronrijke gebied rond $^{68}$Ni zoals getoond in Fig. 2.7. In het kader van het schillenmodel worden de nikkel isotopen beschreven als zijnde semi-magisch daar hun protongetal ($Z$=28) een gesloten schillenconfiguratie vormt terwijl het aantal neutronen varieert van de gesloten neutronschillen $N$=20 en $N$=28 aan de protonrijke zijde tot $N$=50 aan de neutronrijke zijde. Tussen $N$=28 en $N$=50 vullen de neutronen de negatieve pariteits orbitalen $p_{3/2}$, $f_{5/2}$, $p_{1/2}$ en het unieke positieve pariteitsorbitaal $g_{9/2}$. Tussen de pf en g orbitalen bevindt zich de $N$=40 sub-schilsluiting en een van de belangrijkste onderzoeksonderwerpen is dan ook de studie van de semi-dubbelmagische $^{68}_{28}Ni_{40}$ kern. De eerst aangeslagen $2^+$ toestand van deze atoomkern ligt op 2033 keV terwijl de gereduceerde elektrische quadrupoolovergangswaarschijnlijkheid $B(E2 : 2^+ \rightarrow 0^+)$ een waarde van 3.2(7) W.u. heeft. Beide kenmerken wijzen op een geslotenschillen karakter voor $^{68}$Ni. In recent onderzoekswerk [24][25] wordt de schijnbare magiciteit van deze kern verklaard aan de hand van kernstructuuroverwegingen waarbij het $\nu g_{9/2}$ unieke pariteitsorbitaal boven de $\nu$fp-schil betrokken is. Verder onderzoek heeft aangetoond dat een goede $N$=40 subschillensluiting enkel beschouwd kan worden voor kernen in de directe omgeving van $^{68}$Ni. Zoals wordt getoond in Fig. 2.10 kunnen de excitatiespectra van deze kernen inderdaad geïnterpreteerd worden als een koppeling van proton- en/of neutrondeeltjes (-gaten) aan de $^{68}$Ni kern. Nochtans verdwijnt de karakteristieke geslotenschillen configuratie van de onderliggende $^{68}$Ni wanneer er twee of meerdere nucleonen van hetzelfde type aan gekoppeld worden. Bovendien is er in kernen onder de $Z$=28 gesloten protonenschil een onverwachte toename in collectief gedrag nabij de $N$=40 neutronensubschil sluiting. Dit volgt uit de energiesystematiek van de neutron rijke ijzer isotopen [19]. Deze aanzet van verhoogd collectief gedrag wordt grotendeels verklaard ten gevolge van de verhoogde proton-neutron residuele interactie waarbij het neutron $g_{9/2}$ orbitaal een belangrijke rol speelt [32], zie ook Fig. 2.11.

Hoewel de neutronrijke kernen op en boven $Z$=28 recent succesvol bestudeerd werden [6][7][10][11][12][13][14], is er slechts zeer weinig geweten over de neutronrijke kernen onder Ni [4][5][17][19][16]. De structuur van de $^{66,67,68}$Co isotopen met $Z$=27 en direct in de buurt van $^{68}$Ni, blijft grotendeels ongekend, zie Fig. 2.10. Excitatiespectra van neutronrijke cobalt kernen kunnen succesvol bestudeerd worden in het $\beta^-$-verval van de corresponderende ijzer isobaren. Er is echter een belangrijk probleem dat te maken heeft met het feit dat ijzer, en ook cobalt en nikkel, elementen van het refractaire[1] type zijn. Dit wil zeggen dat de productie van kortlevende isotopen van deze elementen bijzonder moeilijk is met behulp van hoge temperatuurstrefschijf – ionenbronsystemen die gebruikt worden bij de conventionele Isotope-Separator-On-Line methode (ISOL). Met de In-Flight separatiemethode (IF) daarentegen kunnen deze isotopen wel geproduceerd worden, maar gedetailleerde en accurate $\beta$-vervalspectroscopie wordt bemoeilijkt door de grote energie en energiespreiding van de secundaire bundel.

De doelstellingen van dit werk kunnen als volgt samengevat worden:

- bijdragen tot een beter begrip van de evolutie van de kernstructuur langs de $Z$=28 proton schillensluiting;
- de persistentie van de semi-magische $N$=40 neutron schillensluiting rond $^{68}$Ni bestuderen;
- mogelijke aanwijzingen voor collectief gedrag onderzoeken;
- vervaleigenschappen van de kernen van de geproduceerde isobare ketens onderzoeken;

De productie van radioactieve bundels daalt zienderogen naarmate men zich van de stabiliteitslijn verwijdert. Om gedetailleerde kernstructuurstudies uit te voeren in $\beta$-verval experimenten en om onze doelstellingen te bewerkstelligen, was het technische doel van dit werk het ontwikkelen en implementeren van een nieuwe $\beta$-$\gamma$ detectie-opstelling, gebaseerd op veelvuldig gesegmenteerde detectoren.

## Experimentele opstelling

De experimenten werden uitgevoerd aan de Leuven Isotope Separator On-Line (LISOL) opstelling [8][9] in het Louvain-La-Neuve Cyclotron Research Center (CRC), Belgium. De $^{65,66,67}$Fe isotopen werden geproduceerd in een door 30 MeV protonen geïnduceerde fissie van $^{238}$U. Twee dunne (10 mg/cm$^2$) U trefschijven werden in een gascel [52][53] geplaatst, die gevuld werd met Ar

[1] Deze elementen hebben een lage dampdruk bij grote temperatuur.

gas bij een druk van ∼500 mbar, zodat de reactieproducten gethermalizeerd en geneutralizeerd kunnen worden, zie Fig 4.3. De geproduceerde kernen worden met de constante stroom van het buffergas naar de uitgangsopening van de gascel gevoerd, waar twee-staps laserionisatie [54][9] wordt toegepast met laserbundelfrequenties die afgestemd zijn in resonantie met ijzer. De gemiddelde evacuatietijd is ∼0.5 s. De geproduceerde ionen worden via de SextuPole Ion-Guide (SPIG) [56] geleid naar de 40 kV versnellingsgap van de massaseparator. Omdat er door de impact van de protonenbundel ongewilde ladingen gecreëerd worden, wordt de primaire protonenbundel gepulst met opeenvolgende 100 ms AAN en 100 ms UIT periodes. De ionenextractie wordt uitgevoerd in antifase met de protonenbundel. De ionen worden uiteindelijk geïmplanteerd op een dunne 1.27 cm (0.5") brede met aluminium bedekte mylar tape van de detectie-opstelling. Om de halfwaardetijd te kunnen bepalen van de geïmplanteerde kernen, heeft de secundaire bundel een macrocyclus tijdsstructuur met opeenvolgende implantatie- en vervalperiodes. Na een zeker aantal macrocycli wordt de implantatietape automatisch verderbewogen om de langlevende activiteit te verwijderen. In tegenstelling tot de conventionele ISOL methode, waarbij thermische diffusie uit relatief dikke productietrefschijven gebruikt worden, laat de configuratie van de gascel, gekoppeld met selectieve laserionisatie, een snelle extractie van de beoogde geproduceerde kernen onafhankelijk van de chemische eigenschappen toe.

Een nieuwe $\beta$-$\gamma$ detectie-opstelling, gebaseerd op veelvuldig gesegmenteerde detectoren, werd gebouwd voor de $\beta$-vervalstudies aan LISOL, zie Fig. 4.10. Twee coaxiale High-Purity Germanium (HPGe) $\gamma$-detectoren van de vorige detectie-opstelling [44] werden vervangen door twee zes- en twaalfvoudig gesegmenteerde HPGe MINIBALL triple cluster detectoren [41][67][68], zie Fig. 4.11. Ieder HPGe kristal van ∼55% relatieve efficiëntie op 1.33 MeV is ingekapseld in een dunne aluminium behuizing. Elk kristal, en bijgevolg ook zijn behuizing, gaat over naar een hexagonale vorm aan de voorkant en dit met een zogenaamde taperhoek. Op die manier kunnen de verschillende clusters, zij aan zij, bij elkaar gepast worden in een dichte configuratie om samen een cluster te vormen, zie Fig. 4.12. Aanvankelijk werden de MINIBALL detectoren ontwikkeld om een $4\pi$ dichte geometrie HPGe-bal met 42 cm binnenstraal (een mini-bal) te vormen. Dit legde de taperhoek vast. Drie capsules worden samen bevestigd in een triple-configuratie. Het hele systeem, dat één enkele cryostaat vormt, wordt vervolgens bevestigd aan het vloeibare stikstofvat voor de koeling van het Ge materiaal. Segmentatie wordt bekomen door de buitenste contacten in het transversale vlak te scheiden voor de zesvoudig gesegmenteerde detector met een additionele tweevoudig longitudinale segmentatie voor de twaalfvoudig gesegmenteerde detector. Een absolute piekenergie efficiëntie van ∼6% op 1 MeV werd behaald in onze experimenten voor twee MINIBALL clusters in hun experimentele positie. Voor de registratie van $\beta$-deeltjes werden drie dunne

NE104A plastic scintillatordetectoren gebruikt van de vorige detectie-opstelling [44]. Elke detector is 1.3 mm dik, waarvan twee een oppervlakte hebben van 30×40 en één van 19×40 mm$^2$. De totale absolute $\beta$-detectie efficiëntie in de huidige configuratie is ∼45%. De intrinsieke efficiëntie van elke detector bedroeg ongeveer 100%. De $\beta$-detectoren werden naast de drie mylar vensters rond het implantatiepunt geplaatst. De twee MINIBALL clusters werden achter de beta detectoren gepositioneerd en dit loodrecht op de bundelrichting. Een nieuwe passieve multi-laagafscherming, die de hele detectie-opstelling omgaf tijdens de experimenten, werd gebouwd. Het bestaat uit een buitenste laag van minstens 17.5 cm borax (50%) en polyethyleen (50%) (afscherming voor de neutronen), een 5.5–11.0 cm dikke loodlaag tegen neutron-geïnduceerde $\gamma$-straling en natuurlijke radioactiviteit, en tenslotte een 1.2 cm dikke laag 65% Cu en 35% Zn legering tegen lood X-stralen. Om het grote aantal detectorkanalen te kunnen verwerken — namelijk 21 en 39 van één zes- en één twaalfvoudig gesegmenteerde MINIBALL cluster, respectievelijk, werd een nieuw volledig digitaal data-acquisitiesysteem geïmplementeerd. Het systeem maakt gebruik van de "Four-Channel Digital Gamma-Finder" (DGF-4C) modules van de X-ray Instrumentation Association (XIA) [76]. Om de data van de nieuwe detectie-opstelling te analyzeren, werd een nieuwe data-analysecode geschreven in C++ dat gebruik maakt van het ROOT pakket [78] dat in CERN ontwikkeld werd [87]. Daarnaast werden ook verstelbare detectorhouders en een automatisch vloeibare stikstof vulsysteem gebouwd.

Hoewel de detectie-opstelling nog verder geoptimaliseerd moet worden, werd een reeks substantiele verbeteringen in vergelijking met de vroegere opstelling aangebracht. Deze kunnen samengevat worden in drie hoofdcategorieën volgens detectie-eigenschap:

- *Efficiëntie* — De $\gamma$-fotopiek efficiëntie werd voor een 1 MeV $\gamma$-transitie verhoogd met een factor van ∼1.5 verhoogd, zie Fig. 4.15;

- *Selectiviteit* — De segmentatie van $\gamma$-detectoren werd verhoogd van 2 naar 6 onafhankelijke germanium kristallen. Dit reduceert de kans op het effectief sommeren van verschillende gammastralen die in een cascade worden uitgezonden. Dit kan geïllustreerd worden aan de hand van het niveauschema van $^{66}$Co, zie Fig. 5.11. In dit schema bevindt zich een cascade van de 470.9 and 510.6 keV overgangen met de 981.4 keV cross-over overgang. Met het huidig aantal van 6 afzonderlijke Ge detectoren zijn er slechts 0.8(1) tellingen, van een totaal van 41(12) tellingen in de 981.4 keV fotopiek, een gevolg van het sommeren van de 470.9 en 510.6 keV gammalijnen. Bij het gebruik van slechts 2 Ge detectoren in de vorige opstelling zou dit effect al 7(1) tellingen voor zijn rekening nemen. Bovendien levert een groter aantal afzonderlijke $\gamma$-detectoren een betere selectiviteit in het geval van $\gamma$-$\gamma$-coïncidenties;

- *Sensitiviteit* — De nieuwe multi-laag detectorafscherming verbeterde de attenuatie van de neutronenflux met een factor ∼5 en meer dan 2 voor thermische en snelle neutronen respectievelijk.

## Kernstructuur van $^{66}$Co bestudeerd in $\beta$-verval van $^{66}$Fe

Van de geproduceerde $^{65,66,67}$Fe isotopen concentreert dit werk zich volledig op het $\beta$-verval van $^{66}$Fe. De gegevens werden op twee manieren verzameld: een keer met de lasers afgesteld voor de resonante ionizatie van ijzer (laser AAN) en een keer zonder lasers (laser UIT). Door de lasers AAN en de lasers UIT statistiek te vergelijken werden $\gamma$-overgangen van het $\beta$-verval van $^{66}$Fe, $^{66}$Co en contaminanten met de zelfde massa-over-lading verhouding geïdentificeerd, zie Fig. 5.3 en Fig. 5.4. Een samenvatting van de bekomen gegevens wordt in Tabel 5.5 gegeven. In het verleden werden de $\gamma$-lijnen op 1245.6, 1425.1, en 1804.0 keV toegekend aan het verval van $^{66}$Co uit een experiment aan LISOL [4]. De $\gamma$-lijn op 175.5 keV werd al voor de eerste maal geobserveerd in [28] en geïndentificeerd als een isomere transitie met een halfwaarde tijd van 1.21(1) $\mu$s. De $\gamma$-overgang op 471 keV werd in een vroegere studie toegekend aan het verval van $^{66}$Co in [36]. Nochtans werd deze niet geobserveerd tijdens het experiment in [4]. Nu hebben we echter evidentie dat de 471 keV transitie tot het beta verval van $^{66}$Fe hoort. De vorige toekenning in [36] kan uitgelegd worden door het gebruik van een multi-nucleon transferreactie van $^{76}$Ge op $^{nat}$W, waarbij vele verschillende kernen geproduceerd worden, en een mogelijk minder goede $Z$-selectie. De overgebleven nieuwe $\gamma$-lijnen op 510.6, 806.7, 881.2, 918.6, en 981.4 keV kunnen toegekend worden aan het verval van $^{66}$Fe. Door de $\beta$-$\gamma$-fotopiekintensiteit uit te zetten voor de twee sterkste $\gamma$-lijnen op 175.5 en 471.0 keV, zoals gegeven in Fig. 5.6c, in verscheidene opeenvolgende tijdsvensters met een vaste grootte binnen de macrocyclus en de resulterende distributie te fitten met een gecombineerde implantatie-verval curve, werd een halfwaardetijd bekomen van 830±80 ms voor het $\beta$-verval van $^{66}$Fe. Dit is bijna twee maal langer levend dan de in de literatuur vermeldde halfwaardetijd van 440±60 ms [35] en [29]. Er kan echter aangehaald worden dat in deze experimenten de halfwaardetijden bekomen werden uit het tijdsgedrag van single $\beta$-deeltjes, die gecorreleerd werden met de geïmplanteerde kernen, terwijl in ons geval een grotere selectiviteit kan behaald worden door $\beta$-$\gamma$-coïncidenties. De halfwaardetijd van de isomere toestand op 175.5 keV werd bekomen uit het tijdsgedrag van de $\beta$-$\gamma$-evenementen aan de rechterkant van de piek van de $\beta$-$\gamma$-coïncidentie evenementendistributie, zoals getoond in Fig. 5.5. Door de 175.5 keV fotopiekactiviteit in opeenvolgende tijdsvensters van vaste grootte te integreren, wordt een vervalcurve bekomen zoals getoond

in Fig. 5.7a. Door deze te fitten met een simpele exponentiële vervalfunctie levert dit een halfwaardetijd van 1.0(1) $\mu$s op, wat zeer gelijkaardig is aan de waarde van 1.21(1) $\mu$s bekomen in [28].

Gebaseerd op $\beta\gamma\gamma$-coïncidenties, $\log ft$ waarden, en Weisskopfschattingen van overgangswaarschijnlijkheden [82], werd een nieuw niveauschema van $^{66}$Co gebouwd. Dit schema wordt in Fig. 5.11 getoond. Een aanwijzing voor een sferische grondtoestand met spin $3^+$, vloeit voort uit het $\pi f_{7/2}\nu p_{1/2}$ spin multiplet [26][28], dat eventueel opmengt met de $\pi f_{7/2}^{-1}\nu f_{5/2}^{-1}\nu p_{1/2}^{+2}$ configuratie. Gebruikmakend van de toegelaten Gamow-Teller $\nu 1f_{5/2} \rightarrow \pi 1f_{7/2}$ overgang in het $\beta^-$-verval van $^{66}$Fe, wordt aan de toestand op 981.8 keV in $^{66}$Co een spin en pariteit van $1^+$ met als dominante configuratie $\pi f_{7/2}^{-1}\nu f_{5/2}^{-1}\nu p_{1/2}^{+2}$ toegekend. De toestand op 510.9 keV (of 470.9 keV) is meest waarschijnlijk een $2^+$ toestand, die dezelfde configuratie heeft vanwege de verhoogde overgangsintensiteit vanuit de $1^+$ toestand. De toestand op 175.5 keV kan zowel $1^+$ als $1^-$ als spinwaarde hebben. Op basis van de voedingspatronen van het volledige vervalschema is de meest waarschijnlijke spin en pariteit $1^-$. Binnen de beschikbare schillenmodeltoestanden kan dit enkel voortkomen uit de bezetting van het $\nu g_{9/2}$ orbital. Het vorige gekende niveauschema van $^{66}$Co, dat volledig gebaseerd was op het werk in [28], is eerder summier, zie Fig. 2.12. Enkel de isomere toestand op 175.5 keV kan bevestigd worden. Nochtans past de toekenning van spin en pariteit niet in ons niveauschema en is ze waarschijnlijk fout. De twee andere toestanden vermeld in [28] werden tijdens ons experiment niet geobserveerd.

Schillenmodelberekeningen op grote schaal werden uitgevoerd voor de oneven-oneven $^{56-66}$Co kernen, gebruik makend van de computercode gebaseerd op [86]. De $^{48}$Ca kern werd gekozen als gesloten schil met de valentieruimte beperkt tot de $\pi f_{7/2}$ en $\nu p_{3/2}$, $\nu f_{5/2}$, $\nu p_{1/2}$, en $\nu g_{9/2}$ orbitalen. Een substantieel verschil werd voor de $^{66}$Co kern vastgesteld. Het experimentele niveauschema kon niet gereproduceerd worden door de schillenmodel berekeningen. Hoewel de aanwezigheid van negatieve pariteitstoestanden bekomen werd, was hun ordening omgekeerd. Bovendien resulteerden de berekeningen ook in een omgekeerde volgorde van de $1^+$ en $2^+$ toestanden. Nochtans bieden ruwe schattingen van de opeenvolging van toestanden van dezelfde spin multiplets, gebaseerd op Paars' paraboolwet [84], een mogelijke verklaring. De experimentele sequentie van de $1^+$ en $2^+$ niveaus met de meest waarschijnlijke $\pi f_{7/2}^{-1}\nu f_{5/2}^{n}$ configuratie kan gereproduceerd worden enkel met $n$=1 deeltjes (5 gaten) in het $\nu f_{5/2}$ orbitaal. Op een gelijkaardige manier kan de lage energie van de $1^-$ toestand met de meest waarschijnlijke $\pi f_{7/2}^{-1}\nu g_{9/2}^{n}$ configuratie enkel uitgelegd worden met $n \geq$5 deeltjes in de $\nu g_{9/2}$ orbital. Binnen dit erg vereenvoudigd denkkader moeten vijf neutronen van het $\nu f_{5/2}$ orbitaal geëxciteerd worden over de $N$=40 neutronensubschil sluiting in het $\nu g_{9/2}$ orbitaal. Vanwege het feit dat de paringsinteractie sterker is in het $\nu g_{9/2}$ orbitaal (vijf mogelijke neutronenparen), zou het $\nu p_{1/2}$ orbitaal (enkel één mogelijk paar) gemakkelijk on-

bezet kunnen blijven. Een zeer gelijkaardig beeld ontstaat bij het beschouwen van het collectief gedrag van de cobalt kernen. Uit de systematiek van de quadrupoolvervormingsparameter $\beta$ voor kernen uit het neutronrijke Ni gebied in Fig. 2.11 wordt verwacht dat de $0^+$ grondtoestand in $^{66}$Fe sterk vervormd is met $\beta$=+0.30, terwijl de $3^+$ grondtoestand in $^{66}$Co bijna sferisch is met $\beta$=+0.09. Uit bovenstaande beschouwingen kan men voorlopig besluiten dat de $(1^-)$ toestand in $^{66}$Co hoogstwaarschijnlijk sterk vervormd is, terwijl de $(3^+)$ grondtoestand sferisch blijft. Daarenboven zou men, naast de verdwijning van de $N$=40 neutronensubschil sluiting, misschien protonexcitaties over de $Z$=28 protonenschil opening kunnen verwachten. Zo zou $^{66}$Co beschouwd kunnen worden als een voorbeeld van vormcoëxistentie in het neutronrijke Ni gebied. Dit kan verklaard worden door de aanwezigheid van de sterkere proton-neutron residuele interactie tussen de nucleonen in $\pi f_{7/2}$ en $\nu f_{5/2}$, $\pi f_{7/2}$ en $\nu g_{9/2}$ orbitalen. Dit alles wijst erop dat de invloed van de onderliggende semi-dubbelmagische $^{68}$Ni gesloten schil substantieel verzwakt is voor de kernstructuur van de naburige Co isotopen.

# Conclusie and vooruitzicht

De verwezenlijkingen in dit werk kunnen apart als volgt samengevat worden:

### Ontwikkeling van de nieuwe $\beta$-$\gamma$ detectie-opstelling

De nieuwe $\beta$-$\gamma$ detectie-opstelling, gebaseerd op gesegmenteerde detectoren, werd ontwikkeld en succesvol geïmplementeerd aan LISOL:

- Een nieuwe twaalfvoudig gesegmenteerde HPGe MINIBALL triple cluster $\gamma$-detector werd geassembleerd, succesvol getest, en geïmplementeerd. Een andere zesvoudig gesegmenteerde MINIBALL triple cluster detector werd toegevoegd, zodat een dichte geometrie detectie-opstelling werd bekomen. Deze heeft, in vergelijking met de vorige detectie-opstelling, een grotere efficiëntie en selectiviteit;

- Een nieuwe multi-laag detectorafscherming werd gebouwd, welke resulteerde in een betere reductie van de neutronenflux.

- Een nieuw multi-kanaals data-acquisitiesysteem, gebaseerd op digitale signaalverwerking werd geconfigureerd en geïmplementeerd in de detectie-opstelling;

- Een nieuwe data-analysecode werd geschreven in C++, gebruik makend van het ROOT pakket.

**Kernstructuurstudies aan LISOL**

Gebruik makend van de nieuwe $\beta$-$\gamma$ detectie-opstelling,

- werden twee verschillende experimenten op $\beta$-verval van $^{65,66,67}$Fe succesvol uitgevoerd aan LISOL;
- werd $\beta$-verval van $^{66}$Fe successvol bestudeerd in dit werk:
  - Het eerste vervalschema van $^{66}$Fe en het nieuwe gedetailleerde niveauschema van $^{66}$Co werd opgesteld;
  - Het excitatiespectrum van $^{66}$Co vertoond verrassende structuren die niet met de huidige schillenmodelberekeningen kunnen verklaard worden;
  - De interpretatie voor de bekomen gegevens wijst op het bestaan van vormcoëxistentie in $^{66}$Co.

Het voorgestelde werk leidt automatisch tot verdere mogelijke ontwikkelingen en studies:

**De $\beta$-$\gamma$ detectie-opstelling**

- Verder werk aan de gesegmenteerde MINIBALL $\gamma$-detectoren — het gebruik van segmentatie, wat zal toelaten om on-line pulsvorm analyse of off-line evenementreconstructie uit te voeren.
- Implementatie van gesegmenteerde $\beta$-detectoren, die zullen toelaten om de selectiviteit van het gehele detectiesysteem verder te verhogen;
- Introductie van gesegmenteerde actieve afscherming.

**Kernstructuurstudies**

- Verdere studies aan LISOL — $\beta$-verval van $^{64,68}$Fe en mogelijk neutronrijke Mn isotopen;
- Gebruik van experimentele methoden — zoals bvb., Coulomb excitatie, metingen van kernmomenten, in andere laboratoria, zoals ISOLDE, CERN (Geneve), GANIL (Caen), ILL (Grenoble), en MSU (East Lansing).

# Bibliography


[1] R.F. Casten. *Nuclear Structure from a Simple Perspective.* Oxford University Press, 2000.

[2] K. Langanke, D.J. Dean, P.B. Radha, Y. Alhassid, and S.E. Koonin. *Phys. Rev. C*, 52:718, 1995.

[3] N.A. Smirnova, A. De Maesschalck, A. Van Dyck, and K. Heyde. *Phys. Rev. C*, 69:044306, 2004.

[4] W.F. Mueller, B. Bruyneel, S. Franchoo, M. Huyse, J. Kurpeta, K. Kruglov, Yu. Kudryavtsev, N.V.S.V. Prasad, R. Raabe, I. Reusen, P. Van Duppen, J. Van Roosbroeck, L. Vermeeren, L. Weissman, Z. Janas, M. Karny, T. Kszczot, A. Plochocki, K.-L. Kratz, B. Pfeiffer, H. Grawe, U. Köster, P. Thirolf, and W.B. Walters. *Phys. Rev. C*, 61:054308, 2000.

[5] L. Weissman, A. Andreyev, B. Bruyneel, S. Franchoo, M. Huyse, K. Kruglov, Yu. Kudryavtsev, W.F. Mueller, R. Raabe, I. Reusen, P. Van Duppen, J. Van Roosbroeck, L. Vermeeren, U. Köster, K.-L. Kratz, B. Pfeiffer, P. Thirolf, and W.B. Walters. *Phys. Rev. C*, 59:2004, 1999.

[6] S. Franchoo, M. Huyse, K. Kruglov, Yu. Kudryavtsev, W.F. Mueller, R. Raabe, I. Reusen, P. Van Duppen, J. Van Roosbroeck, L. Vermeeren, A. Wöhr, K.-L. Kratz, B. Pfeiffer, and W.B. Walters. *Phys. Rev. Lett.*, 81:3100, 1998.

[7] S. Franchoo, M. Huyse, K. Kruglov, Yu. Kudryavtsev, W.F. Mueller, R. Raabe, I. Reusen, P. Van Duppen, J. Van Roosbroeck, L. Vermeeren, A. Wöhr, H. Grawe, K.-L. Kratz, B. Pfeiffer, and W.B. Walters. *Phys. Rev. C*, 64:054308, 2001.

[8] M. Huyse, P. Decrock, P. Dendooven, J. Gentens, G. Vancraeynest, P. Van den Bergh, and P. Van Duppen. *Nucl. Instr. and Meth. B*, 70:50, 1992.

[9] Yu. Kudryavtsev, M. Facina, M. Huyse, J. Gentens, P. Van den Bergh, and P. Van Duppen. *Nucl. Instr. and Meth. B*, 204:336, 2003.

[10] J. Van Roosbroeck, H. De Witte, M. Gorska, M. Huyse, K. Kruglov, K. Van de Vel, P. Van Duppen, S. Franchoo, J. Cederkall, V.N. Fedoseyev, H. Fynbo, U. Georg, O. Jonsson, U. Köster, L. Weissman, W.F. Mueller, V.I. Mishin, D. Fedorov, W.B. Walters, N.A. Smirnova, A. Van Dyck, A. De Maesschalck, and K. Heyde. *Phys. Rev. C*, 69:034313, 2004.

[11] J. Van Roosbroeck, C. Guénaut, G. Audi, D. Beck, K. Blaum, G. Bollen, J. Cederkall, P. Delahaye, A. De Maesschalck, H. De Witte, D. Fedorov, V.N. Fedoseyev, S. Franchoo, H.O.U. Fynbo, M. Górska, F. Herfurth, K. Heyde, M. Huyse, A. Kellerbauer, H.-J. Kluge, U. Köster, K. Kruglov, D. Lunney, V.I. Mishin, W.F. Mueller, Sz. Nagy, S. Schwarz, L. Schweikhard, N.A. Smirnova, K. Van de Vel, P. Van Duppen, A. Van Dyck, W.B. Walters, L. Weissman, and C. Yazidjian. *Phys. Rev. Lett.*, 92:112501, 2004.

[12] I. Stefanescu, G. Georgiev, F. Ames, J. Äystö, D.L. Balabanski, G. Bollen, P.A. Butler, J. Cederkäll, N. Champault, T. Davinson, A. De Maesschalck, P. Delahaye, J. Eberth, D. Fedorov, V.N. Fedosseev, L.M. Fraile, S. Franchoo, K. Gladnishki, D. Habs, K. Heyde, M. Huyse, O. Ivanov, J. Iwanicki, J. Jolie, B. Jonson, Th. Kröll, R. Krücken, O. Kester, U. Köster, A. Lagoyannis, L. Liljeby, G. Lo Bianco, B.A. Marsh, O. Niedermaier, M. Oinonen, G. Pascovici, P. Reiter, A. Saltarelli, H. Scheit, D. Schwalm, T. Sieber, N. Smirnova, J. Van De Walle, P. Van Duppen, S. Zemlyanoy, N. Warr, D. Weisshaar, and F. Wenander. *Phys. Rev. Lett.*, N:To be published, 2007.

[13] I. Stefanescu. *private communication*, 2007.

[14] J. Van de Walle. PhD thesis, Katholieke Universiteit Leuven, Leuven, 2006.

[15] isolde.cern.ch. 2007.

[16] O. Sorlin, C. Donzaud, L. Axelsson, M. Belleguic, R. Beraud, C. Borcea, G. Canchel, E. Chabanat, J.M. Daugas, A. Emsallem, D. Guillemaud-Mueller, K.-L. Kratz, S. Leenhardt, M. Lewitowicz, C. Longour, M.J. Lopez, F. de Oliveira Santos, L. Petizon, B. Pfeiffer, F. Pougheon, M.G. Saint-Laurent, and J.E. Sauvestre. *Nucl. Phys. A*, 660:3, 1999.

[17] L. Gaudefroy. PhD thesis, De l'Universite Paris XI Orsay, Paris, 2005.

[18] www.ganil.fr. 2007.

[19] M. Hannawald, T. Kautzsch, A. Wöhr, W. B. Walters, K.-L. Kratz, V.N. Fedoseyev, V.I. Mishin, W. Böhmer, B. Pfeiffer, V. Sebastian, Y. Jading, U. Köster, J. Lettry, H.L. Ravn, and the ISOLDE Collaboration. *Phys. Rev. Lett.*, 82:1391, 1999.

[20] G. Kraus, P. Egelhof, C. Fischer, H. Geissel, A. Himmler, F. Nickel, G. Mnzenberg, W. Schwab, A. Weiss, J. Friese, A. Gillitzer, H.J. Krner, M. Peter, Henning W.F., J.P. Schiffer, J.V. Kratz, L. Chulkov, M. Golovkov, A. Ogloblin, and B.A. Brown. *Phys. Rev. Lett.*, 73:1773, 1994.

[21] T. Otsuka, M. Honma, and T. Mizusaki. *Phys. Rev. Lett.*, 81:1588, 1998.

[22] www.nndc.bnl.gov. 2007.

[23] O. Perru, O. Sorlin, S. Franchoo, F. Azaiez, E. Bouchez, C. Bourgeois, A. Chatillon, J.M. Daugas, Z. Dlouhy, Zs. Dombrádi, C. Donzaud, L. Gaudefroy, H. Grawe, S. Grévy, D. Guillemaud-Mueller, F. Hammache, F. Ibrahim, Y. Le Coz, S.M. Lukyanov, I. Matea, J. Mrazek, F. Nowacki, Yu.-E. Penionzhkevich, F. de Oliveira Santos, F. Pougheon, M.G. Saint-Laurent, G. Sletten, M. Stanoiu, C. Stodel, Ch. Theisen, and D. Verney. *Phys. Rev. Lett.*, 96:232501, 2006.

[24] O. Sorlin, S. Leenhardt, C. Donzaud, J. Duprat, F. Azaiez, F. Nowacki, H. Grawe, Zs. Dombrádi, F. Amorini, A. Astier, D. Baiborodin, M. Belleguic, C. Borcea, C. Bourgeois, D.M. Cullen, Z. Dlouhy, E. Dragulescu, M. Górska, S. Grévy, D. Guillemaud-Mueller, G. Hagemann, B. Herskind, J. Kiener, R. Lemmon, M. Lewitowicz, S.M. Lukyanov, P. Mayet, F. de Oliveira Santos, D. Pantalica, Yu.E. Penionzhkevich, F. Pougheon, A. Poves, N. Redon, M.G. Saint-Laurent, J.A. Scarpaci, G. Sletten, M. Stanoiu, O. Tarasov, and Ch. Theisen. *Phys. Rev. Lett.*, 88:092501–1, 2002.

[25] K. Langanke, J. Terasaki, F. Nowacki, D.J. Dean, and W. Nazarewicz. *Phys. Rev. C*, 67:044314, 2003.

[26] W.F. Mueller, B. Bruyneel, S. Franchoo, H. Grawe, M. Huyse, U. Köster, K.-L. Kratz, K. Kruglov, Yu. Kudryavtsev, B. Pfeiffer, R. Raabe, I. Reusen, P. Thirolf, P. Van Duppen, J. Van Roosbroeck, L. Vermeeren, W.B. Walters, and L. Weissman. *Phys. Rev. Lett.*, 83:3613, 1999.

[27] A.M. Oros-Peusquens and P.F. Mantica. *Nucl. Phys. A*, 669:81, 2000.

[28] R. Grzywacz, R. Béraud, C. Borcea, A. Emsallem, M. Glogowski, H. Grawe, D. Guillemaud-Mueller, M. Hjorth-Jensen, M. Houry, M. Lewitowicz, A.C. Mueller, A. Nowak, A. Plochocki, M. Pfützner,

K. Rykaczewski, M.G. Saint-Laurent, J.E. Sauvestre, M. Schaefer, O. Sorlin, J. Szerypo, W. Trinder, S. Viteritti, and J. Winfield. *Phys. Rev. Lett.*, 81:766, 1999.

[29] O. Sorlin, C. Donzaud, L. Axelsson, M. Belleguic, R. Beraud, C. Borcea, G. Canchel, E. Chabanat, J.M. Daugas, A. Emsallem, D. Guillemaud-Mueller, K.-L. Kratz, S. Leenhardt, M. Lewitowicz, C. Longour, M.J. Lopez, F. de Oliveira Santos, L. Petizon, B. Pfeiffer, F. Pougheon, M.G. Saint-Laurent, and J.E. Sauvestre. *Nucl. Phys. A*, 669:351, 2000.

[30] M. Sawicka, J.M. Daugas, H. Grawe, S. Ćwiok, D.L. Balabanski, R. Béraud, C. Bingham, C. Borcea, M. La Commara, G. de France, G. Georgiev, M. Górska, R. Grzywacz, M. Hass, M. Hellström, Z. Janas, M. Lewitowicz, H. Mach, I. Matea, G. Neyens, C. O'Leary, F. de Oliveira Santos, R.D. Page, M. Pfützner, Zs. Podolyák, K. Rykaczewski, M. Stanoiu, and J. Żylicz. *Eur. Phys. J. A*, 16:51, 2003.

[31] S. Raman, C.W. Nestor Jr., and P. Tikkanen. *adndt*, 78:1, 2001.

[32] Y. Aboussir, J.M. Pearson, A.K. Dutta, and F. Tondeur. *adndt*, 61:127, 1995.

[33] P. Möller, J.R. Nix, and W.J. Swiatecki. *adndt*, 59:185, 1995.

[34] S. Goriely, F. Tondeur, and J.M. Pearson. *adndt*, 77:311, 2001.

[35] F. Ameil, M. Bernas, P. Armbruster, S. Czajkowski, Ph. Dessagne, H. Geissel, E. Hanelt, C. Kozhuharov, C. Miehe, C. Donzaud, A. Grewe, A. Heinz, Z. Janas, M. de Jong, W. Schwab, and S. Steinhäuser. *Eur. Phys. J. A*, 1:275, 1998.

[36] U. Bosch, W.-D. Schmidt-Ott, E. Runte, P. Tidemand-Petersson, P. Koschel, F. Meissner, R. Kirchner, O. Klepper, E. Roeckl, K. Rykaczewski, and D. Schardt. *Nucl. Phys. A*, 477:89, 1988.

[37] I.N. Borzov. *Nucl. Phys. A*, 777:645, 2006.

[38] I.N. Borzov. *Phys. Rev. C*, 71:065801, 2005.

[39] P. Möller, J.R. Nix, and K.-L. Kratz. *adndt*, 66:131, 1997.

[40] T. Tachibana, M. Yamada, and N. Yoshida. *Prog. Theor. Phys.*, 84:111, 1992.

[41] C. Gund. PhD thesis, Ruprecht-Karls-Universität Heidelberg, Heidelberg, 2000.

[42] A. Algora, L. Batist, M.J.G. Borge, D. Cano-Ott, R. Collatz, S. Courtin, Ph. Dessagne, L.M. Fraile, A. Gadea, W. Gelletly, M. Hellström, Z. Janas, A. Jungclaus, R. Kirchner, M. Karny, G. Le Scornet, Ch. Miehé, F. Maréchal, F. Moroz, E. Nácher, E. Poirier, E. Roeckl, B. Rubio, K. Rykaczewski, J.L. Tain, O. Tengblad, and V. Wittmann. *Eur. Phys. J. A*, 20:199, 2004.

[43] H. Mach, P.M. Walker, R. Julin, M. Leino, S. Juutinen, M. Stanoiu, Zs. Podolyak, R. Wood, A.M. Bruce, T. Bäck, J.A. Cameron, B. Cederwall, J. Ekman, B. Fogelberg, P.T. Greenless, M. Hellström, P. Jones, W. Klamra, K. Lagergren, A-P. Leppänen, P. Nieminen, R. Orlandi, J. Pakarinen, P. Rahkila, D. Rudolph, G. Simpson, J. Uusitalo, and C. Wheldon. *J. Phys. G*, 31:S1421, 2005.

[44] L. Weissman, J. Van Roosbroeck, K. Kruglov, A. Andreyev, B. Bruyneel, S. Franchoo, M. Huyse, Yu. Kudryavtsev, W.F. Mueller, R. Raabe, I. Reusen, P. Van Duppen, and L. Vermeeren. *Nucl. Instr. and Meth. A*, 423:328, 1999.

[45] I.Y. Lee, M.A. Deleplanque, and K. Vetter. *Rep. Prog. Phys.*, 66:1095, 2003.

[46] D.J. Morrissey and B.M. Sherrill. *Lecture Notes in Physics*, 651:113, 2004.

[47] M. Huyse. *Lecture Notes in Physics*, 651:1, 2004.

[48] S. Franchoo. PhD thesis, Katholieke Universiteit Leuven, Leuven, 1999.

[49] I. Reusen. PhD thesis, Katholieke Universiteit Leuven, Leuven, 1999.

[50] S. Dean. PhD thesis, Katholieke Universiteit Leuven, Leuven, 2004.

[51] J. Ärje, J. Äystö, H. Hyvönen, P. Taskinen, V. Koponen, J. Honkanen, A. Hautojärvi, and K. Vierinen. *Phys. Rev. Lett.*, 54:99, 1985.

[52] M. Facina. PhD thesis, Katholieke Universiteit Leuven, Leuven, 2004.

[53] M. Huyse, M. Facina, Yu. Kudryavtsev, and P. Van Duppen. *Nucl. Instr. and Meth. B*, 187:535, 2002.

[54] Yu. Kudryavtsev, J. Andrzejewski, N. Bijnens, S. Franchoo, J. Gentens, M. Huyse, A. Piechaczek, J. Szerypo, I. Reusen, P. Van Duppen, P. Van den Bergh, L. Vermeeren, J. Wauters, and A. Wöhr. *Nucl. Instr. and Meth. B*, 114:350, 1996.

[55] P. Van Duppen, B. Bruyneel, M. Huyse, Yu. Kudryavtsev, P. Van den Bergh, and L. Vermeeren. *Hyp. Int.*, 127:401, 2000.

[56] P. Van den Bergh, S. Franchoo, J. Gentens, M. Huyse, Yu. Kudryavtsev, A. Piechaczek, R. Raabe, I. Reusen, P. Van Duppen, L. Vermeeren, and A. Wöhr. *Nucl. Instr. and Meth. B*, 126:194, 1997.

[57] M. Huyse, P. Van Duppen, P. Van den Bergh, Yu. Kudryavtsev, and J. Gentens. *private communication*, 2006.

[58] C. Wagemans. *The Nuclear Fission Process*. CRC Press, 1991.

[59] G. Savard and R. Pardo. *Proposal*. Physics Division, Argonne National Laboratory, 2005.

[60] S. Baba, H. Umezawa, and H. Baba. *Nucl. Phys. A*, 175:177, 1971.

[61] K. Kruglov, A. Andreyev, B. Bruyneel, S. Dean, S. Franchoo, M. Huyse, Yu. Kudryavtsev, W.F. Mueller, N.V.S.V. Prasad, R. Raabe, I. Reusen, K.-H. Schmidt, K. Van de Vel, P. Van Duppen, J. Van Roosbroeck, L. Weissman, and ISOLDE collaboration. *Nucl. Phys. A*, 701:145c, 2002.

[62] K. Kruglov, A. Andreyev, B. Bruyneel, S. Dean, S. Franchoo, M. Gorska, K. Helariutta, M. Huyse, Yu. Kudryavtsev, W.F. Mueller, N.V.S.V. Prasad, R. Raabe, K.-H. Schmidt, P. Van Duppen, J. Van Roosbroeck, K. Van de Vel, and L. Weissman. *Eur. Phys. J. A*, 14:365, 2002.

[63] J. Benlliure, A. Grewe, M. de Jong, K.-H. Schmidt, and S. Zhdanov. *Nucl. Phys. A*, 628:458, 1998.

[64] M. Weber, C. Donzaud, J.P. Dufour, H. Geissel, A. Grewe, D. Guillemaud-Mueller, H. Keller, M. Lewitowicz, A. Magel, A.C. Mueller, G. Münzenberg, F. Nickel, M. Pfützner, A. Piechaczek, M. Pravikoff, E. Roeckl, K. Rykaczewski, M.G. Saint-Laurent, I. Schall, C. Stephan, K. Sämmerer, L. Tassan-Got, D.J. Vieira, and B. Voss. *Z. Phys. A*, 343:67, 1992.

[65] I.D. Moore, A. Nieminen, J. Billowes, P. Campbell, Ch. Geppert, A. Jokinen, T. Kessler, B. Marsh, H. Penttil, S. Rinta-Antila, B. Tordoff, K.D.A. Wendt, and J. Äystö. *J. Phys. G*, 31:1499, 2005.

[66] www.canberra.com. 2006.

[67] D. Weisshaar. PhD thesis, Universität zu Köln, Köln, 2003.

[68] J. Eberth, G. Pascovici, H.G. Thomas, N. Warr, D. Weisshaar, D. Habs, P. Reiter, P. Thirolf, D. Schwalm, C. Gund, H. Scheit, M. Lauer, P. Van Duppen, M. Huyse, R.M. Lieder, W. Gast, J. Gerl, K.P. Lieb, and the MINIBALL Collaboration. *Prog. Part. Nucl. Phys.*, 46:389, 2001.

[69] P. Reiter, H. Eberth, J.and Faust, S. Franchoo, J. Gerl, C. Gund, D. Habs, M. Huyse, A. Jungclaus, K.P. Lieb, H. Scheit, D. Schwalm, H.G. Thomas, P. Van Duppen, and D. Weisshaar. *Nucl. Phys. A*, 701:209c, 2002.

[70] G. Gilmore and J. Hemingway. *Practical Gamma-ray Spectroscopy.* John Wiley & Sons Ltd., 1995.

[71] G.F. Knoll. *Radiation Detection and Measurement.* John Wiley & Sons Inc., 2000.

[72] G. Pascovici. *private communication*, 2006.

[73] M. Lauer. PhD thesis, Max-Plank-Institut für Kernphysik, Heidelberg, 2005.

[74] G.P. Skoro, I.V. Anicin, A.H. Kukoc, Dj. Krmpotic, P. Adzic, R. Vukanovic, and M. Zupancic. *Nucl. Instr. and Meth. A*, 316:333, 1992.

[75] J. Van Roosbroeck. *Master Thesis, Katholieke Universiteit Leuven, Leuven*, 1997.

[76] www.xia.com. 2006.

[77] X-Ray Instrumentation Associates. *DGF-4C User's Manual*, 2004.

[78] root.cern.ch. 2006.

[79] F. Sanchez, E. Navarro, J.L. Ferrero, A. Bacza, and J.M. Barrigon. *Nucl. Instr. and Meth. A*, 339:297, 1994.

[80] V.R. Bom and R.W. Hollander. *Photon Absorption Graphs, 1 keV – 10 MeV.* Technische Hogeschool Delft, 1983.

[81] geant4.cern.ch. 2006.

[82] V.F. Weisskopf. *Phys. Rev.*, 83:1073, 1951.

[83] S.F. Moszkowski. *Phys. Rev.*, 83:1071, 1951.

[84] V. Paar. *Nucl. Phys. A*, 331:16, 1979.

[85] D. Pauwels, O. Ivanov, P. Van Duppen, and M. Huyse. *private communication*, 2006.

[86] M. Hjorth-Jensen, T. T.S. Kuo, and E. Osnes. *Phys. Reports*, 261:125, 1995.

[87] www.cern.ch. 2006.